



Universiteit Gent
Faculteit Wetenschappen
Vakgroep Fysica en Sterrenkunde

² No title yet

³ No sub-title neither, obviously...

⁴ Alexis Fagot

5



Thesis to obtain the degree of
Doctor of Philosophy in Physics
Academic years 2012-2017





Universiteit Gent
Faculteit Wetenschappen
Vakgroep Fysica en Sterrenkunde

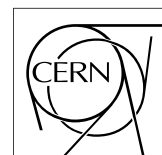
Promotoren: Dr. Michael Tytgat
Prof. Dr. Dirk Ryckbosch

Universiteit Gent
Faculteit Wetenschappen
Vakgroep Fysica en Sterrenkunde
Proeftuinstraat 86, B-9000 Gent, België
Tel.: +32 9 264.65.28
Fax.: +32 9 264.66.97

17



Thesis to obtain the degree of
Doctor of Philosophy in Physics
Academic years 2012-2017



Acknowledgements

¹⁹ Ici on remerciera tous les gens que j'ai pu croiser durant cette aventure et qui m'ont permis de passer
²⁰ un bon moment

Gent, ici la super date de la mort qui tue de la fin d'écriture
22 *Alexis Fagot*

Table of Contents

24	Acknowledgements	i
25	Nederlandse samenvatting	vii
26	English summary	ix
27	1 Introduction	1-1
28	1.1 A story of High Energy Physics	1-1
29	1.2 Organisation of this study	1-1
30	2 Investigating the TeV scale	2-1
31	2.1 The Standard Model of Particle Physics	2-2
32	2.1.1 A history of particle physics	2-2
33	2.1.2 Construction and test of the model	2-11
34	2.1.3 Investigating the TeV scale	2-12
35	2.2 The Large Hadron Collider & the Compact Muon Solenoid	2-14
36	2.2.1 LHC, the most powerful particle accelerator	2-14
37	2.2.1.1 Particle acceleration	2-15
38	2.2.2 CMS, a multipurpose experiment	2-18
39	2.2.2.1 The silicon tracker, core of CMS	2-20
40	2.2.2.2 The calorimeters, measurement of particle's energy	2-20
41	2.2.2.3 The muon system, corner stone of CMS	2-22
42	3 Muon Phase-II Upgrade	3-1
43	3.1 High Luminosity LHC and muon system requirements	3-2
44	3.2 Necessity for improved electronics	3-5
45	3.3 New detectors and increased acceptance	3-8
46	3.3.1 Improved forward resistive plate chambers	3-9
47	3.3.2 Gas electron multipliers	3-12
48	3.3.3 Installation schedule	3-16
49	3.4 Implications of the different upgrades on the Level-1 Trigger. Improvement of physics performance.	3-16
50	3.5 Ecofriendly gas studies	3-16
51	3.5.1 Status of the studies and potential candidates	3-16
52	3.5.2 Implications in case of no suitable ecofriendly mixture	3-16
53		
54	4 Physics of Resistive plate chambers	4-1
55	4.1 Principle	4-1
56	4.1.1 Electron drift velocity	4-4
57	4.2 Rate capability and time resolution of Resistive Plate Chambers	4-4
58	4.2.1 Operation modes	4-4

59	4.2.2	Detector designs and performance	4-6
60	4.2.2.1	Double-gap RPC	4-7
61	4.2.2.2	Multigap RPC (MRPC)	4-8
62	4.2.2.3	Charge distribution and performance limitations	4-9
63	4.3	Signal formation	4-12
64	4.4	Gas transport parameters	4-12
65	5	Longevity studies and Consolidation of the present CMS RPC subsystem	5-1
66	5.1	Resistive Plate Chambers at CMS	5-1
67	5.1.1	Overview	5-1
68	5.1.2	The present RPC system	5-2
69	5.1.3	Pulse processing of CMS RPCs	5-3
70	5.2	Testing detectors under extreme conditions	5-4
71	5.2.1	The Gamma Irradiation Facilities	5-6
72	5.2.1.1	GIF	5-6
73	5.2.1.2	GIF++	5-8
74	5.3	Preliminary tests at GIF	5-10
75	5.3.1	Resistive Plate Chamber test setup	5-10
76	5.3.2	Data Acquisition	5-12
77	5.3.3	Geometrical acceptance of the setup layout to cosmic muons	5-12
78	5.3.3.1	Description of the simulation layout	5-13
79	5.3.3.2	Simulation procedure	5-15
80	5.3.3.3	Results	5-16
81	5.3.4	Photon flux at GIF	5-16
82	5.3.4.1	Expectations from simulations	5-16
83	5.3.4.2	Dose measurements	5-21
84	5.3.5	Results and discussions	5-22
85	5.4	Longevity tests at GIF++	5-23
86	5.4.1	Description of the Data Acquisition	5-26
87	5.4.2	RPC current, environmental and operation parameter monitoring	5-27
88	5.4.3	Measurement procedure	5-28
89	5.4.4	Longevity studies results	5-28
90	6	Investigation on high rate RPCs	6-1
91	6.1	Rate limitations and ageing of RPCs	6-1
92	6.1.1	Low resistivity electrodes	6-1
93	6.1.2	Low noise front-end electronics	6-1
94	6.2	Construction of prototypes	6-1
95	6.3	Results and discussions	6-1
96	7	Conclusions and outlooks	7-1
97	7.1	Conclusions	7-1
98	7.2	Outlooks	7-1
99	A	A data acquisition software for CAEN VME TDCs	A-1
100	A.1	GIF++ DAQ file tree	A-1
101	A.2	Usage of the DAQ	A-2
102	A.3	Description of the readout setup	A-3
103	A.4	Data read-out	A-3
104	A.4.1	V1190A TDCs	A-4

105	A.4.2 DataReader	A-6
106	A.4.3 Data quality flag	A-10
107	A.5 Communications	A-12
108	A.5.1 V1718 USB Bridge	A-13
109	A.5.2 Configuration file	A-13
110	A.5.3 WebDCS/DAQ intercommunication	A-17
111	A.5.4 Example of inter-process communication cycle	A-18
112	A.6 Software export	A-18
113	B Details on the offline analysis package	B-1
114	B.1 GIF++ Offline Analysis file tree	B-1
115	B.2 Usage of the Offline Analysis	B-2
116	B.2.1 Output of the offline tool	B-3
117	B.2.1.1 ROOT file	B-3
118	B.2.1.2 CSV files	B-5
119	B.3 Analysis inputs and information handling	B-6
120	B.3.1 Dimensions file and IniFile parser	B-6
121	B.3.2 TDC to RPC link file and Mapping	B-7
122	B.4 Description of GIF++ setup within the Offline Analysis tool	B-9
123	B.4.1 RPC objects	B-9
124	B.4.2 Trolley objects	B-10
125	B.4.3 Infrastructure object	B-11
126	B.5 Handeling of data	B-12
127	B.5.1 RPC hits	B-13
128	B.5.2 Clusters of hits	B-14
129	B.6 DAQ data Analysis	B-15
130	B.6.1 Determination of the run type	B-16
131	B.6.2 Beam time window calculation for efficiency runs	B-17
132	B.6.3 Data loop and histogram filling	B-18
133	B.6.4 Results calculation	B-19
134	B.6.4.1 Rate normalisation	B-19
135	B.6.4.2 Rate and activity	B-21
136	B.6.4.3 Strip masking tool	B-23
137	B.6.4.4 Output CSV files filling	B-25
138	B.7 Current data Analysis	B-29

139

Nederlandse samenvatting –Summary in Dutch–

140

141 Le resume en Neerlandais (j'aurais peut-être pu apprendre la langue juste pour ça...).

English summary

¹⁴³ Le meme résume mais en Anglais (on commencera par la hein!).

List of Figures

144

145	2.1	Through the gold foil experiment Rutherford could show that most of the mass of atoms was contained in a positively charged nucleus and could then propose a more accurate atomic model than that of Thomson.	2-3
146	2.2	Figure 2.2a: Meson octet. Figure 2.2b: Baryon octet. Figure 2.2c: Baryon decuplet.	2-8
147	2.3	The elementary particles of the Standard Model are showed along with their names and properties. Their interactions with the strong, weak and electromagnetic forces have been explicated using color squares. In the left column, the scalar higgs boson is depicted, while the central is focused on the matter particles, the fermions, and the right on the force carriers, the gauge bosons. The role of the Higgs boson in electroweak symmetry breaking is highlighted, and the corresponding way properties of the various particles differ in the (high-energy) symmetric phase (top) and the (low-energy) broken-symmetry phase (bottom) are showed.	2-11
148	2.4	CERN accelerator complex.	2-15
149	2.5	Pictures of the different accelerators. From top to bottom: first the LINAC 2 and the <i>Pb</i> source of LINAC 3. Then the Booster and the LEIR. Finally, the PS, the SPS and the LHC.	2-16
150	2.6	Figure 2.6a: schematics of the LHC cryodipoles. 1: Superconducting Coils, 2: Beam pipe, 3: Heat exchanger Pipe, 4: Helium-II Vessel, 5: Superconducting Bus-bar, 6: Iron Yoke, 7: Non-Magnetic Collars, 8: Vacuum Vessel, 9: Radiation Screen, 10: Thermal Shield, 11: Auxiliary Bus-bar Tube, 12: Instrumentation Feed Throughs, 13: Protection Diode, 14: Quadrupole Bus-bars, 15: Spool Piece Bus-bars. Figure 2.6b: magnetic field and resulting motion force applied on the beam particles.	2-17
151	2.7	Figure 2.7a: picture of the LHC quadrupoles. Figure 2.7b: magnetic fields and resulting focussing force applied on the beam by 2 consecutive quadrupoles.	2-18
152	2.8	Picture of the CMS barrel. The red outer layer is the muon system hosted into the red iron return yokes. The calorimeters are the blue cylinder inside in magnet solenoid and the tracker is the inner yellow cylinder built around the beam pipe.	2-19
153	2.9	View of the CMS apparatus and of its different components.	2-19
154	2.10	Slice showing CMS sub-detectors and how particles interact with them.	2-20
155	2.11	CMS tracker.	2-20
156	2.12	Figure 2.12a: picture of the ECAL. Figure 2.12b: picture of the lead tungstate crystals composing the ECAL.	2-21
157	2.13	CMS hadron calorimeter barrel.	2-21
158	2.14	A quadrant of the muon system, showing DTs (yellow), RPCs (blue), and CSCs (green).	2-22
159	2.15	Figure 2.15a: Barrel wheel with its detector rings and return yokes. Figure 2.15b: CSC endcap disk with the 2 CSC stations. The outer station is made of 10 deg detectors while the inner station is made of 20 deg detectors. Figure 2.15c: RPC endcap disk. The inner station is not equipped and the inner CSC station can be seen.	2-23
160			
161			
162			
163			
164			
165			
166			
167			
168			
169			
170			
171			
172			
173			
174			
175			
176			
177			
178			
179			
180			
181			
182			
183			

- 184 2.16 Figure 2.16a: Cross section of a DT module showing the two superlayers measur-
 185 ing the ϕ coordinate, perpendicular to the cross section plane, and the superlayer
 186 measuring the η coordinate, placed in between the two others with honeycomb and
 187 parallel to the cross section plane. The DT detector is sandwiched in between 2
 188 RPCs whose readout strips are perpendicular to the cross section plane, measuring
 189 the ϕ coordinate. Figure 2.16b: A DT cell is shown together with its electric field.
 190 The path of a muon through a superlayer is shown. 2-23
- 191 2.17 Figure 2.17a: cathode strips and anode wire layout of a CSC panel. Figure 2.17b
 192 avalanche development and charge collection by anode wires and induction on cath-
 193 ode strips inside of a CSC panel. 2-24
- 194 2.18 Muon track reconstruction through the 6 panels of a CMS CSC using the infor-
 195 mation of anode wire groups and cathode strip charge distribution combined with
 196 comparator bits to decide on which half strip the muon is more likely to have passed. 2-24
- 197 2.19 Double gap layout of CMS RPCs. Muons passing through the gas volumes will cre-
 198 ate electron-ions pairs by ionising the gas. this ionisation will immediately translate
 199 into a developing avalanche. 2-25
- 200 3.1 Detailed timeline projection of for LHC and HL-LHC operation until 2039 show-
 201 ing the evolution of the instantaneous and integrated luminosity as designed (Fig-
 202 ure 3.1a) and in the ultimate case where the instantaneous luminosity is increased to
 203 $7.5 \times 10^{34} \text{ cm}^{-2}\text{s}^{-1}$ (Figure 3.1b) [20, 22]. 3-2
- 204 3.2 Absorbed dose in the CMS cavern after an integrated luminosity of 3000 fb. Using
 205 the interaction point as reference, R is the transverse distance from the beamline and
 206 Z is the distance along the beamline. 3-3
- 207 3.3 A quadrant of the muon system, showing DTs (yellow), RPCs (blue), and CSCs
 208 (green). The locations of new forward muon detectors for Phase-II are contained
 209 within the dashed box and indicated in red for GEM stations (ME0, GE1/1, and
 210 GE2/1) and dark blue for improved RPC (iRPC) stations (RE3/1 and RE4/1). 3-4
- 211 3.4 Figure 3.4a: Extrapolated fraction of failing channels of the present DT MiC1 elec-
 212 tronics as a function of the integrated luminosity for different scenari until LS4. Fig-
 213 ure 3.4b: Comparison of the current (left) and upgraded (right) DT data processing.
 214 So far, the data is sent to service cavern of CMS facility via copper-to-optical-fiber
 215 translators (CuOF) by each MiC1. There, data including RPCs and outer hadron
 216 calorimeter is combined into trigger primitives (TPG) and transmitted by the Twin-
 217 Mux system to CMS Track Finder. The time-to-digital converter (TDC) data is col-
 218 lected and sent to the CMS data acquisition system (DAQ) by the micro read-out
 219 server (μ ROS). After the upgrade, the TDC data will be sent via optical links to
 220 a patch panel inside the experimental cavern by each MiC2, and transferred to the
 221 back-end, where triggering and event building will be performed. 3-6
- 222 3.5 Figure 3.5a: The event loss fractions as a function of the instantaneous luminosity is
 223 compared for CFEBs (Phase-1) and DCFEBs (Phase-II) at different CSC locations.
 224 HL-LHC luminosity is marked with the dashed brown line. Figure 3.5b: Comparison
 225 of the current (left) and upgraded (right) CSC data processing. A part of the con-
 226 nections in between ALCTs and DCFEBs, and the trigger mother boards (TMBs)
 227 and data acquisition mother boards (DMBs) will be upgraded toward optical data
 228 transfer. The detector dependent units (DDUs) used as interface in between CSCs'
 229 front-end electronics and the CMS DAQ will be replaced by new FED boards. 3-7
- 230 3.6 Comparison of the simulated time residuals in between reconstructed and true muon
 231 times without (blue) and with (red) the upgraded RPC link system. 3-8

232	3.7 RMS of the multiple scattering displacement as a function of muon p_T for the proposed forward muon stations. All of the electromagnetic processes such as bremsstrahlung and magnetic field effect are included in the simulation.	3-9
233		
234		
235	3.8 Simulation of the impact of RPC hit inclusion onto the local trigger primitive efficiency in station 3 (left) and station 4 (right). The contribution of iRPC starts above $ \eta = 1.8$	3-9
236		
237		
238	3.9 Expected hit rate due to neutrons, photons, electrons and positrons at HL-HLC instantaneous luminosity of $5 \times 10^{34} \text{ cm}^{-2}\text{s}^{-1}$ in RE3/1 chambers covering the region $1527 \text{ mm} < R < 3192 \text{ mm}$. In the upper part of the figure the sensitivities of RPCs used in the simulation for each particle are reported. The hit rates are expected to be similar in RE4/1 covering the region $1770 \text{ mm} < R < 3140 \text{ mm}$	3-10
239		
240		
241		
242		
243	3.10 Measured average charge per avalanche as a function of the effective electric field for different gas gap thickness in double gap RPCs using HPL electrodes.	3-11
244		
245	3.11 The PETIROC time jitter as a function of the input signal amplitude, measured with and without internal clocks.	3-12
246		
247	3.12 Schematics of a GEM showing the cathode on top, the GEM foil separating the gas volume into the drift region, in between the cathode and foil, and the induction region, in between the GEM foil and the anode, and the anode on which a 2D read-out is installed. A negative voltage is applied on the cathode while the anode is connected to the ground.	3-13
248		
249		
250		
251		
252	3.13 Left: Picture of a CMS GEM foil provided by a scanning electron microscope. Right: Representation of the electric field lines in a GEM hole and of the amplification that electrons and ions undergo in the hole's volume due to the very intense electric field.	3-14
253		
254		
255	3.14 Schematic representation of CMS triple GEMs. The gas volume is divided into 4 areas. The drift area is the region where the primary electrons are created before being amplified a first time while passing through the first GEM foil. Then the process of drift and amplification is repeated twice in following two transfer areas and GEM foils. Finally, the charges have been amplified enough to induce current in the read-out strips while in the last drift area. The dimensions, potentials and electric fields are provided.	3-14
256		
257		
258		
259		
260		
261		
262	3.15 Simulated efficiency and rate of the standalone Level-1 muon trigger using tracks reconstructed in CSCs and all GEM stations compared with Phase-I values in the case where only CSCs are used or CSCs+GE1/1. The zones of inefficiency of the CSC subsystem are compensated by the addition of GEMs during Phase-II and the trigger rates is kept from increasing due to the high luminosity.	3-15
263		
264		
265		
266		
267	3.16 Figure 3.16a: Simulated resolution of the muon direction measurement $\Delta\phi$ with Phase-II conditions. In the second endcap station, the resolution is compared in the case of CSCs (ME2/1) alone and CSCs+GEMs (GE2/1+ME2/1) while a similar resolution measurement is given in the case of the first station (GE1/1+ME1/1). Figure 3.16b: The addition of GEM detectors on stations 1 and 2 (ME0 is considered to contribute to station station 1) as redundant system to CSCs allows to improve the muon momentum improvement through a more accurate measurement of the local bending angles ϕ_1 and ϕ_2	3-15
268		
269		
270		
271		
272		
273		
274		

275	4.1	Different phases of the avalanche development in the RPC gas volume subjected to a constant electric field E_0 . a) An avalanche is initiated by the primary ionisation caused by the passage of a charged particle through the gas volume. b) Due to its growing size, the avalanche starts to locally influence the electric field. c) The electrons, lighter than the cations reach the anode first. d) The ions reach the cathode. While the charges have not recombined, the electric field in the small region around the avalanche stays affected and locally blind the detector.	4-2
282	4.2	Effeciency (circles and stars with 30 mV and 100 mV thresholds respectively) and streamer probability (opened circles) as function of the operating voltatge of a 2 mm single gap HPL RPC flushed with a gas mixture containing (a) 5%, (b) 2%, (c) 1% and (d) no SF_6 [38].	4-3
286	4.3	Movement of the charge carriers in an RPC. Figure 4.3a: Voltage across an RPC whose electrode have a relative permittivity of 5 at the moment the tension s applied. Figure 4.3b: After the charge carriers moved, the electrodes are charged and there is no voltage drop over the electrodes anymore. The full potential is applied on the gas gap only. Figure 4.3c: The streamer discharge initiated by a charged particle transports electrons and cations towards the anode and cathode respectively.	4-5
292	4.4	Typical oscilloscope pulses in streamer mode (Figure 4.4a) and avalanche mode(Figure 4.4b). In the case of streamer mode, the very small avalanche signal is visible.	4-5
294	4.5	Rate capability comparison for the streamer and avalanche mode of operation. An order of magnitude in rate capability for a maximal efficiency drop of 10% is gained by using the avalanche mode over the streamer mode.	4-6
297	4.6	Possible double-gap RPC layouts: a) "standard" 1D double-gap RPC, as used in CMS experiment, where the anodes are facing each other and a 1D read-out plane is sandwiched in between them, b) double read-out double-gap RPC as used in AT-LAS experiment, where the cathodes are facing each other and 2 read-out planes are used on the outer surfaces. This last layout can offer the possibility to use a 2D reconstruction by using orthogonal read-out planes.	4-7
303	4.7	Comparison of performance of CMS double and single gap RPCs using cosmic muons [49]. Figure 4.7a: Comparison of efficiency sigmoids. Figure 4.7b: Voltage distribution at 95% of maximum efficiency. Figure 4.7c: $\Delta_{10\%}^{90\%}$ distribution.	4-7
306	4.8	Presentation of ALICE MRPC using 250 μm gas gaps, 620 μm outer glass electrodes and 550 μm inner floating electrodes. More details on the labels are given in [50].	4-8
308	4.9	Particle identification applied to electrons in the STAR experiment. The identifica- tion is performed combining ToF and dE/dx measurements [55].	4-9
310	4.10	Comparison of the detector performance of ALICE ToF MRPC [56] at fixed applied voltage (in blue) and at fixed effective voltage (in red). The effective voltage is kept fixed by increasing the applied voltage accordingly to the current drawn by the detector.	4-9
313	4.11	Ratio between total induced and drifting charge have been simulated for single gap, double-gap and multigap layouts [57]. The total induced charge for a double-gap RPC is a factor 2 higher than for a multigap.	4-10
316	4.12	Charge spectra have been simulated for single gap, double-gap and multigap lay- outs [57]. It appears that when single gap shows a decreasing spectrum, double and multigap layouts exhibit a spectrum whose peak is detached from the origin. The detachment gets stronger as the number of gaps increases.	4-11
320	4.13	The maximal theoretical efficiency is simulated for single gap, double-gap and multi- gap layouts [57] at a constant gap thickness of 2 mm and using an effective Townsend coefficient of 9 mm^{-1}	4-11

323	5.1	Signals from the RPC strips are shaped by the FEE described on Figure 5.1a. Output LVDS signals are then read-out by a TDC module connected to a computer or converted into NIM and sent to scalers. Figure 5.1b describes how these converted signals are put in coincidence with the trigger.	5-3
327	5.2	Description of the principle of a CFD. A comparison of threshold triggering (left) and constant fraction triggering (right) is shown in Figure 5.2a. Constant fraction triggering is obtained thanks to zero-crossing technique as explained in Figure 5.2b. The signal arriving at the input of the CFD is split into three components. A first one is delayed and connected to the inverting input of a first comparator. A second component is connected to the noninverting input of this first comparator. A third component is connected to the noninverting input of another comparator along with a threshold value connected to the inverting input. Finally, the output of both comparators is fed through an AND gate.	5-4
336	5.3	Figure 5.3a: The integrated charge per region (Barrel, Endcap) is extrapolated to HL-LHC integrated luminosity (3000 fb^{-1}) using the data accumulated in 2016 in every HV channels. Figure 5.3b: The hit rate per region (Barrel, Endcap) is linearly extrapolated to HL-LHC highest instantaneous luminosity ($5 \times 10^{34} \text{ cm}^{-2}\text{s}^{-1}$) using the rate as a function of instantaneous luminosity recorded by RPCs in 2017 showing a linear dependence.	5-5
342	5.4	Background Fluka simulation compared to 2016 Data at $L = 10^{34} \text{ cm}^{-2}\text{s}^{-1}$ in the fourth endcap disk region. A mismatch in between simulation and data can be observed. [To be understood.]	5-6
345	5.5	Layout of the test beam zone called X5c GIF at CERN. Photons from the radioactive source produce a sustained high rate of random hits over the whole area. The zone is surrounded by 8 m high and 80 cm thick concrete walls. Access is possible through three entry points. Two access doors for personnel and one large gate for material. A crane allows installation of heavy equipment in the area.	5-7
350	5.6	^{137}Cs decays by β^- emission to the ground state of ^{137}Ba (BR = 5.64%) and via the 662 keV isomeric level of ^{137}Ba (BR = 94.36%) whose half-life is 2.55 min.	5-8
352	5.7	Floor plan of the GIF++ facility. When the facility downstream of the GIF++ takes electron beam, a beam pipe is installed along the beam line (z-axis). The irradiator can be displaced laterally (its center moves from $x = 0.65 \text{ m}$ to 2.15 m), to increase the distance to the beam pipe.	5-8
356	5.8	Simulated unattenuated current of photons in the xz plane (Figure 5.8a) and yz plane (Figure 5.8b) through the source at $x = 0.65 \text{ m}$ and $y = 0 \text{ m}$. With angular correction filters, the current of 662 keV photons is made uniform in xy planes.	5-9
359	5.9	Description of the RPC setup. Dimensions are given in mm. A tent containing RPCs is placed at 1720 mm from the source container. The source is situated in the center of the container. RE-4-2-BARC-161 chamber is 160 mm inside the tent. This way, the distance between the source and the chambers plan is 2060 mm. Figure 5.9a provides a side view of the setup in the xz plane while Figure 5.9b shows a top view in the yz plane.	5-10
365	5.10	RE-4-2-BARC-161 chamber is inside the tent as described in Figure 5.9. In the top right, the two scintillators used as trigger can be seen. This trigger system has an inclination of 10° relative to horizontal and is placed above half-partition B2 of the RPCs. PMT electronics are shielded thanks to lead blocks placed in order to protect them without stopping photons from going through the scintillators and the chamber.	5-11

370	5.11 Hit distributions over all 3 partitions of RE-4-2-BARC-161 chamber is showed on 371 these plots. Top, middle and bottom figures respectively correspond to partitions A, 372 B, and C. These plots show that some events still occur in other half-partitions than 373 B2, which corresponds to strips 49 to 64, in front of which the trigger is placed, con- 374 tributing to the inefficiency of detection of cosmic muons. In the case of partitions 375 A and C, the very low amount of data can be interpreted as noise. On the other hand, 376 it is clear that a little portion of muons reach the half-partition B1, corresponding to 377 strips 33 to 48.	5-12
378	5.12 Results are derived from data taken on half-partition B2 only. On the 18 th of June 379 2014, data has been taken on chamber RE-2-BARC-161 at building 904 (Prevessin 380 Site) with cosmic muons providing us a reference efficiency plateau of $(97.54 \pm$ 381 $0.15)\%$ represented by a black curve. A similar measurement has been done at GIF 382 on the 21 st of July with the same chamber giving a plateau of $(78.52 \pm 0.94)\%$ 383 represented by a red curve.	5-13
384	5.13 Representation of the layout used for the simulations of the test setup. The RPC is 385 represented as a yellow trapezoid while the two scintillators as blue cuboids looking 386 at the sky. A green plane corresponds to the muon generation plane within the sim- 387 ulation. Figure 5.9a shows a global view of the simulated setup. Figure 5.9b shows 388 a zommed view that allows to see the 2 scintillators as well as the full RPC plane.	5-14
389	5.14 γ flux $F(D)$ is plot using values from table 5.1. As expected, the plot shows similar 390 attenuation behaviours with increasing distance for each absorption factors.	5-17
391	5.15 Figure 5.15a shows the linear approximation fit done via formulae 5.7 on data from 392 table 5.2. Figure 5.15b shows a comparison of this model with the simulated flux 393 using a and b given in figure 5.15a in formulae 5.4 and the reference value $D_0 =$ 394 50cm and the associated flux for each absorption factor F_0^{ABS} from table 5.1	5-19
395	5.16 Dose measurements has been done in a plane corresponding to the tents front side. 396 This plan is 1900 mm away from the source. As explained in the first chapter, a 397 lens-shaped lead filter provides a uniform photon flux in the vertical plan orthogonal 398 to the beam direction. If the second line of measured fluxes is not taken into account 399 because of lower values due to experimental equipments in the way between the 400 source and the tent, the uniformity of the flux is well showed by the results.	5-21
401	5.17	5-22
402	5.18 Evolution of the maximum efficiency for RE2 (5.18a) and RE4 (5.18b) chambers 403 with increasing extrapolated γ rate per unit area at working point. Both irradiated 404 (blue) and non irradiated (red) chambers are shown.	5-24
405	5.19 Evolution of the working point for RE2 (5.19a) and RE4 (5.19b) with increasing 406 extrapolated γ rate per unit area at working point. Both irradiated (blue) and non 407 irradiated (red) chambers are shown.	5-24
408	5.20 Evolution of the maximum efficiency at HL-LHC conditions, i.e. a background hit 409 rate per unit area of 300 Hz/cm^2 , with increasing integrated charge for RE2 (5.20a) 410 and RE4 (5.20b) detectors. Both irradiated (blue) and non irradiated (red) chambers 411 are shown. The integrated charge for non irradiated detectors is recorded during test 412 beam periods and stays small with respect to the charge accumulated in irradiated 413 chambers.	5-25
414	5.21 Comparison of the efficiency sigmoid before (triangles) and after (circles) irradiation 415 for RE2 (5.21a) and RE4 (5.21b) detectors. Both irradiated (blue) and non irradiated 416 (red) chambers are shown.	5-25
417	5.22 Evolution of the Bakelite resistivity for RE2 (5.22a) and RE4 (5.22b) detectors. Both 418 irradiated (blue) and non irradiated (red) chambers are shown.	5-26

419	5.23 Evolution of the noise rate per unit area for the irradiated chamber RE2-2-BARC-9 only.	5-26
421	A.1 (A.1a) View of the front panel of a V1190A TDC module [63]. (A.1b) View of the 422 front panel of a V1718 Bridge module [64]. (A.1c) View of the front panel of a 6U 423 6021 VME crate [65].	A-3
424	A.2 Module V1190A <i>Trigger Matching Mode</i> timing diagram [63].	A-4
425	A.3 Structure of the ROOT output file generated by the DAQ. The 5 branches (<code>EventNumber</code> , 426 <code>number_of_hits</code> , <code>Quality_flag</code> , <code>TDC_channel</code> and <code>TDC_TimeStamp</code>) are visible on 427 the left panel of the ROOT browser. On the right panel is visible the histogram cor- 428 responding to the variable <code>nHits</code> . In this specific example, there were approximately 429 50k events recorded to measure the gamma irradiation rate on the detectors. Each 430 event is stored as a single entry in the <code>TTree</code>	A-10
431	A.4 The effect of the quality flag is explained by presenting the content of <code>TBranch</code> 432 <code>number_of_hits</code> of a data file without <code>Quality_flag</code> in Figure A.4a and the con- 433 tent of the same <code>TBranch</code> for data corresponding to a <code>Quality_flag</code> where all TDCs 434 were labelled as <code>GOOD</code> in Figure A.4b taken with similar conditions. It can be noted 435 that the number of entries in Figure A.4b is slightly lower then in Figure A.4a due 436 to the excluded events.	A-12
437	A.5 Using the same data as previously showed in Figure A.4, the effect of the quality 438 flag is explained by presenting the reconstructed hit multiplicity of a data file with- 439 out <code>Quality_flag</code> in Figure A.5a and the reconstructed content of the same RPC 440 partition for data corresponding to a <code>Quality_flag</code> where all TDCs were labelled as 441 <code>GOOD</code> in Figure A.5b taken with similar conditions. The artificial high content of bin 442 0 is completely suppressed.	A-12
443	A.6 WebDCS DAQ scan page. On this page, shifters need to choose the type of scan 444 (Rate, Efficiency or Noise Reference scan), the gamma source configuration at the 445 moment of data taking, the beam configuration, and the trigger mode. These in- 446 formation will be stored in the DAQ ROOT output. Are also given the minimal 447 measurement time and waiting time after ramping up of the detectors is over before 448 starting the data acquisition. Then, the list of HV points to scan and the number of 449 triggers for each run of the scan are given in the table underneath.	A-14
450	B.1 Example of expected hit time distributions in the cases of efficiency (Figure B.1a) 451 and noise/gamma rate per unit area (Figure B.1b) measurements as extracted from 452 the raw ROOT files. The unit along the x-axis corresponds to ns. The fact that 453 "the" muon peak is not well defined in Figure B.1a is due to the contribution of all 454 the RPCs being tested at the same time that don't necessarily have the same signal 455 arrival time. Each individual peak can have an offset with the ones of other detectors. 456 The inconsistancy in the first 100 ns of both time distributions is an artefact of the 457 TDCs and are systematically rejected during the analysis.	B-16
458	B.2 The effect of the quality flag is explained by presenting the reconstructed hit multi- 459 plicity of a data file without <code>Quality_flag</code> . The artificial high content of bin 0 is the 460 effect of corrupted data.	B-19

- 461 B.3 Display of the masking tool page on the webDCS. The window on the left allows the
462 shifter to edit `ChannelsMapping.csv`. To mask a channel, it only is needed to set the
463 3rd field corresponding to the strip to mask to 0. It is not necessary for older mapping
464 file formats to add a 1 for each strip that is not masked as the code is versatile and
465 the default behaviour is to consider missing mask fields as active strips. The effect
466 of the mask is directly visible for noisy channels as the corresponding bin turns red.
467 The global effect of masking strips will be an update of the rate value showed on the
468 histogram that will take into consideration the rejected channels. B-24

List of Tables

469

470	4.1	Properties of the most used electrode materials for RPCs.	4-4
471	5.1	Total photon flux ($E\gamma \leq 662$ keV) with statistical error predicted considering a ^{137}Cs activity of 740 GBq at different values of the distance D to the source along the x-axis of irradiation field [60].	5-16
472	5.2	Correction factor c is computed thanks to formulae 5.5 taking as reference $D_0 = 50$ cm and the associated flux F_0^{ABS} for each absorption factor available in table 5.1.	5-18
473	5.3	The data at D_0 in 1997 is taken from [60]. In a second step, using Equations 5.8 and 5.9, the flux at D can be estimated in 1997. Then, taking into account the attenuation of the source activity, the flux at D can be estimated at the time of the tests in GIF in 2014. Finally, assuming a sensitivity of the RPC to γ $s = 2 \cdot 10^{-3}$, an estimation of the hit rate per unit area is obtained.	5-20
474	A.1	Inter-process communication cycles in between the webDCS and the DAQ through file string signals.	A-19
475			
476			
477			
478			
479			
480			
481			
482			

List of Acronyms

A

489 AFL

Almost Full Level

490 ALCTs

anode local charged track boards

B

495 BARC

Bhabha Atomic Research Centre

496 BLT

Block Transfer

497 BNL

Brookhaven National Laboratory

498 BR

Branching Ratio

C

503 CAEN

Costruzioni Apparecchiature Elettroniche Nucleari S.p.A.

504 CERN

European Organization for Nuclear Research

505 CFD

Constant Fraction Discriminator

506 CFEBs

cathode front-end boards

507 CMB

Cosmic Microwave Background

508 CMS

Compact Muon Solenoid

509 CSC

Cathode Strip Chamber

510 CuOF

copper-to-optical-fiber translators

D

515 DAQ

Data Acquisition

516 DCS

Detector Control Software

517 DQM

Data Quality Monitoring

518 DT

Drift Tube

519		
520	E	
521		
522		
523	ECAL	electromagnetic calorimeter
524		
525	F	
526		
527		
528	FCC	Future Circular Collider
529	FEE	Front-End Electronics
530	FEB	Front-End Board
531		
532	G	
533		
534		
535	GE-/-	Find a good description
536	GE1/1	Find a good description
537	GE2/1	Find a good description
538	GEANT	GEometry ANd Tracking - a series of software toolkit platforms developed by CERN
539		
540	GEM	Gas Electron Multiplier
541	GIF	Gamma Irradiation Facility
542	GIF++	new Gamma Irradiation Facility
543		
544	H	
545		
546		
547	HCAL	hadron calorimeter
548	HL-LHC	High Luminosity LHC
549	HPL	High-pressure laminate
550	HV	High Voltage
551		
552	I	
553		
554		
555	iRPC	improved RPC
556	IRQ	Interrupt Request
557	ISR	Intersecting Storage Rings
558		
559		
560	L	
561		

562	LEIR	Low Energy Ion Ring
563	LEP	Large Electron-Positron
564	LHC	Large Hadron Collider
565	LS1	First Long Shutdown
566	LS2	Second Long Shutdown
567	LS3	Third Long Shutdown
568	LV	Low Voltage
569	LVDS	Low-Voltage Differential Signaling

570

571

M

573

574	MiC1	first version of Minicrate electronics
575	MC	Monte Carlo
576	MCNP	Monte Carlo N-Particle
577	ME-/	Find good description
578	ME0	Find good description
579	MRPC	Multigap RPC

580

581

N

583

584	NIM	Nuclear Instrumentation Module logic signals
-----	-----	--

585

586

P

588

589	PMT	PhotoMultiplier Tube
590	PS	Proton Synchrotron
591	PU	pile-up

592

593

Q

595

596	QCD	Quantum Chromodynamics
597	QED	Quantum Electrodynamics

598

599

R

601

602	RE-/	Find a good description
603	RE2/2	Find a good description
604	RE3/1	Find a good description

605	RE3/2	Find a good description
606	RE4/1	Find a good description
607	RE4/2	Find a good description
608	RE4/3	Find a good description
609	RMS	Root Mean Square
610	ROOT	a framework for data processing born at CERN
611	RPC	Resistive Plate Chamber

612

613

S

615

616	SC	Synchrocyclotron
617	SLAC	Stanford Linear Accelerator Center
618	SM	Standard Model
619	SPS	Super Proton Synchrotron
620	SUSY	supersymmetry

621

622

T

624

625	TDC	Time-to-Digital Converter
626	TDR	Technical Design Report
627	ToF	Time-of-flight
628	TPG	trigger primitives

629

630

W

632

633	webDCS	Web Detector Control System
-----	--------	-----------------------------

634

635

Y

637

638	YETS	Year End Technical Stop
-----	------	-------------------------

1

Introduction

639

640

⁶⁴¹ **1.1 A story of High Energy Physics**

⁶⁴² **1.2 Organisation of this study**

2

643

644

Investigating the TeV scale

645 „We may regard the present state of the universe as the effect of the
646 past and the cause of the future. An intellect which at any given mo-
647 ment knew all of the forces that animate nature and the mutual posi-
648 tions of the beings that compose it, if this intellect were vast enough
649 to submit the data to analysis, could condense into a single formula
650 the movement of the greatest bodies of the universe and that of the
651 lightest atom; for such an intellect nothing could be uncertain and
652 the future just like the past would be present before its eyes.”

653

654 - Pierre Simon de Laplace, *A Philosophical Essay on Probabilities*, 1814

Throughout history, physics experiment became more and more powerful in order to investigate finer details of nature and helped understanding the elementary blocks of matter and the fundamental interactions that bond them in the microscopic world. Nowadays, the Standard Model (SM) of particle physics is the most accurate theory designed to explain the behaviour of particles and was able to make very precise predictions that are constantly verified, although some hints of new physics are visible as bricks are still missing to have a global comprehension of the Universe.

To highlight the limits of the SM and test the different alternative theories, ever more powerful machines are needed. This is in this context that the Large Hadron Collider (LHC) has been thought and built to accelerate and collide particles at energies exceeding anything that had been done before. Higher collision energies and high pile-up imply the use of enormous detectors to measure the properties of the interaction products. The Compact Muon Solenoid (CMS) is a multipurpose experiment that have been designed to study the proton-proton collisions of the LHC and give answers on various high energy physics scenari. Nevertheless, the luminosity delivered by the collider will in the future be increased to levels beyond the original plans to improve its discovery potential giving no choice to experiments such as CMS to upgrade their technologies to cope with the increased radiation levels and detection rates.

2.1 The Standard Model of Particle Physics

In this early 21st century it is now widely accepted that matter is made of elementary blocks referred to as *elementary particles*. The physics theory that classifies and describes the best the behaviour and interaction of such elementary particles is the so called Standard Model that formalizes 3 of the 4 fundamental interactions (electromagnetic, weak and strong interactions). It's development took place during the 20th century thanks to a strong collaboration in between the theoretical and experimental physicists.

2.1.1 A history of particle physics

The idea that nature is composed of elementary bricks, called *atomism*, is not contemporary as it was already discussed by Indian or Greek philosophers during antiquity. In Greece, atomism has been rejected by Aristotelianism as the existance of *atoms* would imply the existance of a void that would violate the physical principles of Aristotle philosophy. Aristotelianism has been considered as a reference in the european area until the 15th century and the italian *Rinascimento* where antic text and history started to be more deeply studied. The re-discovery of Platon's philosophy would allow to open the door to alternative theories and give a new approach to natural sciences where experimentation would become central. A new era of knowledge was starting. By the begining of the 17th century, atomism was re-discovered by philosophers and the very first attempt to estimate an *atom* size would be provided by Magnetus in 1646. Although his *atoms* correspond to what would nowadays be called *molecules*, Magnetus achieved feats by calculating that the number of molecules in a grain of incense would be of the order of 10^{18} simply by considering the time necessary to smell it everywhere in a large church after the stick was lit on. It is now known that this number only falls short by 1 order of magnitude.

An alternative philosophy to atomism popularized by Descartes was corpuscularianism. Built on ever divisible corpuscles, contrary to atoms, it's principles would be mainly used by alchemists like Newton who would later develop a corpuscular theory of light. Boyle would combine together ideas of both atomism or corpuscularianism leading to mechanical philosophy. The 18th century have

seen the development of engineering providing philosophical thought experiments with repeatable demonstration and a new point of view to explain the composition of matter and Lavoisier would greatly contribute to chemistry and atomism by publishing in 1789 a list of 33 chemical elements corresponding to what is now called *atoms*. In the early 19th century Dalton would summarize the knowledge on composition of matter and Fraunhofer would invent the spectrometer and discover the spectral lines. The rise of atomic physics, chemistry and mathematical formalism would unravel the different atomic elements and ultimately, the 20th century would see the very first sub-atomic particles.

Discovery of the inner structure of the atom

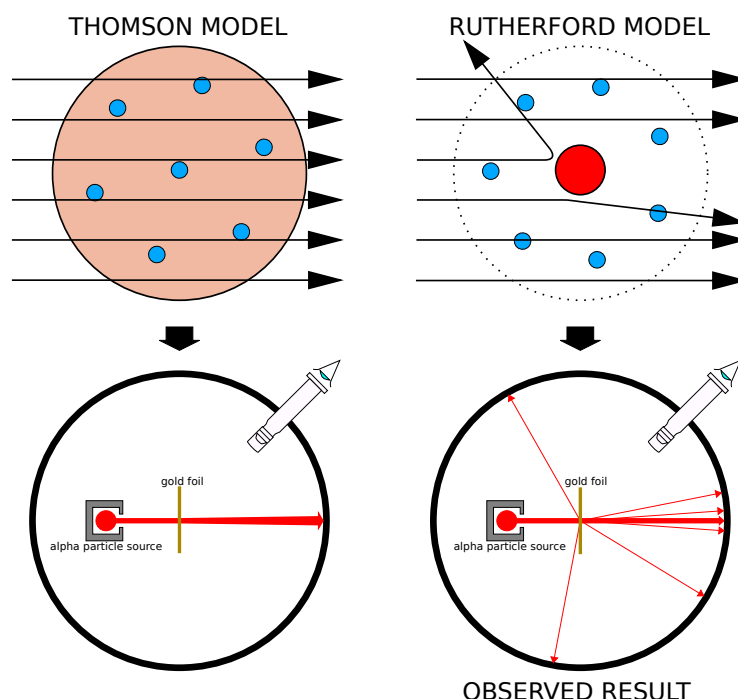


Figure 2.1: Through the gold foil experiment Rutherford could show that most of the mass of atoms was contained in a positively charged nucleus and could then propose a more accurate atomic model than that of Thomson.

The negative *electron* would be the first to be discovered in 1897 by Thomson after 3 decades of research on cathode rays by proving that the electrification observed in an electroscope, as reported by Perrin, was due to the rays themselves and that they had to be composed of electrically charged particles. In 1900, Becquerel would show the *beta rays* emitted by radium had the same charge over mass ratio than what measured by Thomson for cathode rays, pointing to electrons as a constituent of atoms. In 1907, Rutherford and Royds showed that *alpha* particles, once captured in a tube and subjected to an electric spark causing an electron avalanche, where helium ions as they could combine with 2 electrons to form a ${}^4\text{He}$. This discovery was directly followed by the constraint of the atom structure in 1909 through the gold foil experiment in which the deflection angle of alpha particles fired at a very thin gold foil was measured and highlighted atoms where mainly empty with

716 nearly all its mass contained into a tiny positively charged *nucleus*. With these two observations,
 717 he could formulate the Rutherford model of the atom in 1911, shown together with the Thomson
 718 plum pudding model in Figure 2.1. The link in between atomic number and number of positive and
 719 negative charges contained into the atoms would fast be understood and the different kind of element
 720 transmutation appeared to be purely nuclear processes making clear that the electromagnetic nature
 721 of chemical transformation could not possibly change nuclei. Thus a new branch in physics appeared
 722 to study nuclei exclusively: the nuclear physics.

723 Moreover, in 1913 quantum physics would be introduced into the atomic model by Bohr based
 724 on the assumptions of Plank to explain spectral lines, and other observed quantum effects. The same
 725 year, Moseley would confirm Bohr's model and Debye would extend it by introducing elliptical
 726 orbits.

727 By studying alpha emission and the product of their interaction with nitrogen gas, Rutherford
 728 reported in 1919 the very first nuclear reaction leading to the discovery that the hydrogen nucleus was
 729 composed of a single positively charged particle that was later baptised *proton*. This idea came from
 730 1815 Prout's hypothesis proposing that all atoms are composed of "*protyles*" (i.e. hydrogen atoms).
 731 By using scintillation detectors, Rutherford could highlight typical hydrogen nuclei signature and
 732 understand that the impact of alpha particles with nitrogen would knock out an hydrogen nucleus
 733 and produce an oxygen 17, as explicated in Formula 2.1 and would then postulate that protons are
 734 building bricks of all elements.



735 With this assumption and the discovery of isotopes together with Aston, elements with identical
 736 atomic number but different masses, Rutherford would propose that all elements' nuclei but hydrogen's are composed of both charged particles, protons, and of chargeless particles, which he called
 737 *neutrons*, and that these neutral particles would help maintaining nuclei as one, as charged protons
 738 were likely to electrostatically repulse each other, and introduced the idea of a new force, a *nuclear*
 739 force. Though the first idea concerning neutrons was a bond state of protons and electrons as it was
 740 known that the beta decay, emitting electrons, was taking place in the nucleus, it was then showed
 741 that such a model would hardly be possible due to Heisenberg's uncertainty principle and by the
 742 recently measured *spin* of both protons and electrons. The spin, discovered through the study of
 743 the emission spectrum of alkali metals, would be understood as a "two-valued quantum degree of
 744 freedom" and formalized by Pauli and extended by Dirac, to take the relativist case into account.
 745 Measured to be $\frac{1}{2}\hbar$ for both, it was impossible to arrange an odd number of half integer spins and
 746 obtain a global nucleus spin that would be integer. Finally, in 1932, following the discovery of a new
 747 neutral radiation, Chadwick could discover the neutron as an uncharged particle with a mass similar
 748 to that of the proton whose half integer spin would reveal to be the solution to explain the nuclear
 749 spin.
 750

751 Development of the Quantum Electrodynamics

752 Historically, the development of the quantum theory revolved around the question of emission and
 753 absorption of discrete amount of energy through light. Einstein used the initial intuition of Plank
 754 about the black-body radiation to develop in 1905 a model to explain the photoelectric effect in
 755 which light was described by discrete quanta now called *photons*. For this model, Einstein introduced
 756 the concept of wave-particle duality as classical theory was not able to describe the phenomenon.
 757 With the new understanding of atoms and of their structure, classical theories also proved unable

758 to explain atoms stability. Indeed, using classical mechanics, electrons orbiting around a nucleus
 759 should radiate an energy proportional to their angular momentum and thus lose energy through
 760 time and the spectrum of energy emission should then be continuous, but it was known since the
 761 19th century and the discovery of spectral lines that the emission spectrum of material was discrete.

762 This was Bohr who first suggested that a quantum description of the atom was necessary in 1913.
 763 Using the correspondence principle stating that at large enough numbers the quantum calculations
 764 should give the same results than the classical theory, he proposed the very first quantum model
 765 of the hydrogen atom explaining the line spectrum by introducing the principal quantum number
 766 n describing the electron shell. This model would then be improved by Sommerfeld that would
 767 quantize the z-component of the angular momentum, leading to the second and third quantum
 768 numbers, or azimuthal and magnetic quantum number, l and m defining for the second the orbital
 769 angular momentum of the electrons on their shells and thus, the shape of the orbital, and for the third
 770 the available orbital on the subshell for each electron. Nevertheless, although the model was not only
 771 limited to spherical orbitals anymore, making the atom more realistic, the Zeeman effect couldn't be
 772 completely explained by just using n , l and m . A solution would be brought after the discovery of
 773 Pauli in 1924, as Uhlenbeck, Goudsmit, and Kramers proposed in 1925 the idea of intrinsic rotation
 774 of the electron, introducing a new angular momentum vector associated to the particle itself, and
 775 not to the orbital, and associated to a new quantic number s , the *spin* projection quantum number
 776 explaining the lift of degeneracy to an even number of energy levels.

777 The introduction of the *spin* happened 1 year after another attempt of improvement of the theory
 778 was made by De Broglie in his PhD thesis. The original formulation of the quantum theory only
 779 considered photons as energy quanta behaving as both waves and particles. De Broglie proposed
 780 that all matter are described by waves and that their momentum is proportional to the oscillation of
 781 quantized electromagnetic field oscillators. This interpretation was able to reproduce the previous
 782 version of the quantum energy levels by showing that the quantum condition involves an integer
 783 multiple of 2π , as shown by Formula 2.2.

$$p = \hbar k \Leftrightarrow \int pdx = \hbar \int kdx = 2\pi\hbar n \quad (2.2)$$

784 Although the intuition of De Broglie about the wave-particle duality of all matter, his interpretation
 785 was semiclassical and it's in 1926 that the first fully quantum mechanical wave-equation would
 786 be introduced by Schrödinger to describe electron-like particles, reproducing the previous semiclassical
 787 formulation without inconsistencies. This complexe equation describes the evolution of the
 788 wave function Ψ of the quantum system, defined by its position vector \mathbf{r} and time t as an energy
 789 conservation law, in which the hamiltonian of the system \hat{H} is explicit, by solving the Equation 2.3.

$$i\hbar \frac{\partial}{\partial t} |\Psi(\mathbf{r}, t)\rangle = \hat{H} |\Psi(\mathbf{r}, t)\rangle \quad (2.3)$$

790 In 1927, Dirac would go further in his paper about emission and absorption of radiation by
 791 proposing a second quantization not only of the physical process at play but also of the electromagnetic
 792 field, providing the ingredients to the first formulation of *Quantum Electrodynamics (QED)*
 793 and the description of photon emission by electrons dropping into a lower energy state in which the
 794 final number of particles is different than the initial one. To complete this model to the many-body
 795 wave functions of identical particles, Jordan included creation and annihilation operators for fields
 796 obeying Fermi-Dirac statistics leading to a model describing particles that would be referred to as
 797 *fermions*. Nevertheless, in order to properly treat electromagnetism, the incorporation of the relativ-

ity theory developed by Einstein. Including gravity into quantum physics still is a challenge nowadays, but in 1928 Pauli and Jordan would show that special relativity's coordinate transformations could be applied to quantum fields as the field commutators were Lorentz invariant. Finally derived the same year, the Dirac equation, shown as Equation 2.4, similarly to Schrödinger's equation, is a single-particle equation but it incorporates special relativity in addition to quantum mechanics rules. It features the 4×4 gamma matrices γ^μ built using 2×2 Pauli matrices and unitary matrix, the 4-gradient ∂_μ , the rest mass m of any half integer spin massive particle described by the wave function $\psi(x, t)$, also called a Dirac spinor, and the speed of light c . In addition to perfectly reproduce the results obtained with quantum mechanics so far, it also provided with *negative-energy solutions* that would later be interpreted as a new form of matter, *antimatter* and give a theoretical justification to the Pauli equation that was phenomenologically constructed to account for the spin as in the non-relativistic limit, the Dirac equation is similar.

$$i\hbar\gamma^\mu\partial_\mu\psi - mc\psi = 0 \quad (2.4)$$

The successes of the QED was soon followed with theoretical problems as computations of any physical process involving photons and charged particles were showed to be only reliable at the first order of perturbation theory. At higher order of the theory, divergent contributions were appearing giving nonsensical results. Only two effects were contributing to these infinities.

- The self-energy of the electron (or positron), the energy that the particle has due its own interaction with its environment.
- The vacuum polarization, virtual electron–positron pairs produced by a background electromagnetic field in the vacuum which is not an "empty" space. These virtual pairs affect the charge and current distributions generated by the original electromagnetic field.

Solving this apparent problem was done by carefully defining the concepts of each observables, for example mass or charge, as these quantities are understood within the context of a non-interacting field equation, and that from the experiment point of view, they are abstractions as what is measured are "renormalized observables" shifted from there "bare" value by the interaction taking place in the measuring process. The infinities needed to be connected to corrections of mass and charge as those are fixed to finite values by experiment. This was the intuition of Bethe in 1947 who successfully computed the effect of such *renormalization* in the non-relativist case. Fully covariant formulations of QED including renormalization was achieved by 1949 by Tomonaga, Schwinger, Feynman and Dyson and Feynman is now famous for his association of diagrams to the term of the scattering matrix, greatly simplifying the representation and computation of interactions as the diagrams directly corresponded the measurable physical processes and would then be used in every quantum field theories. With the resolution of infinities, QED had mostly reached its final form, being still today the most accurate physical theory and would serve as a model to build all other quantum field theories.

Development of the quark model and Quantum Chromodynamics

To explain the nuclear force that holds *nucleons* (protons and neutrons) together, Yukawa theoretically proposed in 1934 the existence of a force carrier called *meson* due to it's predicted mass in the range in between the electron and nucleon masses. Discovered in 1936 by Anderson and Neddermeyer, and confirmed using bubble chambers in 1937 by Street and Stevenson, a first meson

838 candidate was observed in the decay products of cosmic rays. Assuming it had the same electric
 839 charge than electrons and protons, this particle was observed to have a curvature due to magnetic
 840 field that was sharper than protons but smoother than electrons resulting in a mass in between that
 841 of electrons and protons. But its properties were not compatible with Yukawa's theory, which was
 842 emphasized by the discovery of a new candidate in 1947, again in cosmic ray products using photo-
 843 graphic emulsions.

844 This new candidate, although it had a similar mass than the already believed *meson*, would rather
 845 decay into it. For distinction, the first candidate would then be renamed "*mu meson*" when the second
 846 would be the "*pi meson*". The *mu meson* was behaving like a heavy electron and didn't participate
 847 in the strong interaction whereas the pion was believed to be the carrier of the nuclear interaction.
 848 This lead to classify the *mu* in a new category of particles called *leptons* together with the electron
 849 that shared similar properties and *the neutrino*, and be renamed *muon*. The *pi meson* was finally
 850 found to be a triplet of particles: a positively charged, a negatively charged, and a neutral particle.
 851 The neutral *pi meson* has been more difficult to identify as it wouldn't leave tracks on emulsions nor
 852 on bubble chambers and needed to be studied via it's decay products. It was ultimately identified in
 853 University of California's cyclotron in 1950 through the observation of its decay into 2 photons.

854 Also discovered in 1947 but in cloud chamber photographs, the *K meson* as also been an im-
 855 portant step towards the establishment of the Standard Model. A triplet of particle, 2 charged and a
 856 neutral, with a mass roughly half that of a proton, were reported. These particles were baptised *K*
 857 *meson* in contrast to the "light" *pi* and *mu* "L-mesons". The particularity of the *K* were there very
 858 slow decays with a typical lifetime of the order of 10^{-10} s much greater than the 10^{-23} s of *pi*-proton
 859 reactions. The concept of *strangeness*, a new quantum number was then introduced by Pais as an
 860 attempt to explain this phenomenon as *strange* particles appeared as a pair production of a strange
 861 and anti-strange particle.

862 With the development of synchrotrons, the particle *zoo* would grow to several dozens during the
 863 1950s as higher energies were reachable through acceleration. In 1961, a first classification system,
 864 called Eightfold Way, was proposed by Gell-Mann and finding its roots in the Gell-Mann–Nishijima
 865 formula, which relates the electric charge Q , the third component of the isospin I_3 , the *baryon*
 866 number B and the strangeness S , as explicitated in Formula 2.5. The isospin was a quantum number
 867 introduced in 1932 to explain symmetries of the newly discovered neutron using representation
 868 theory of SU(2). The baryon number, was introduced by Nishijima as a quantum number for baryons,
 869 i.e. particles of the same family as nucleons. The mesons were classified in an octet and baryons of
 870 spin $\pm \frac{1}{2}$ and $\pm \frac{3}{2}$ were respectively classified into an octet and a decuplet, as shown in Figure 2.2. To
 871 complete the baryon decuplet, Gell-Mann predicted the existance of baryon Ω^- which would later
 872 be discovered in 1964.

$$Q = I_3 + \frac{1}{2}(B + S) \quad (2.5)$$

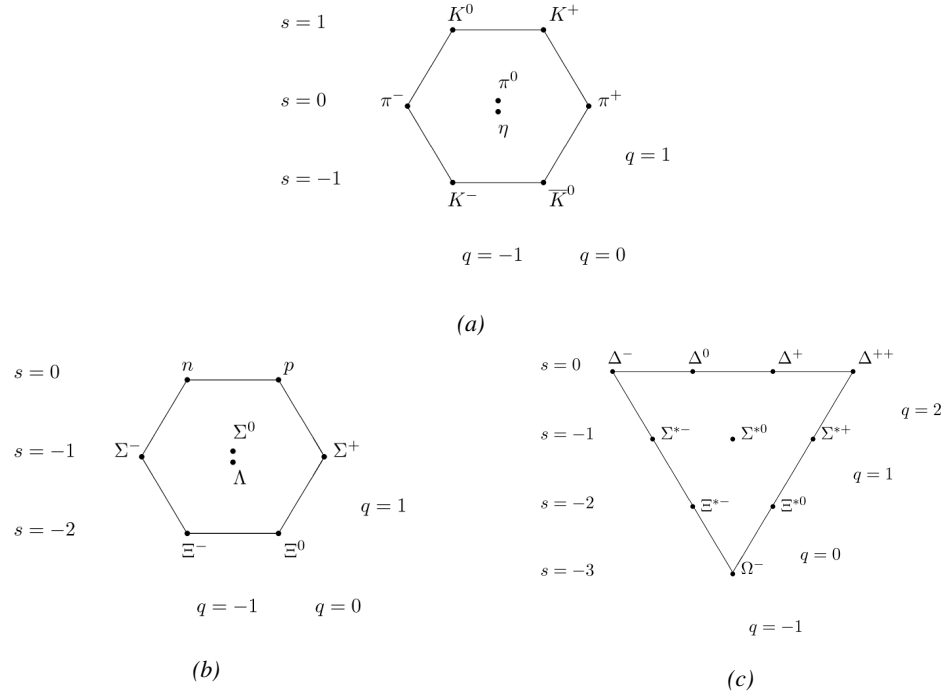


Figure 2.2: Figure 2.2a: Meson octet. Figure 2.2b: Baryon octet. Figure 2.2c: Baryon decuplet.

Strong of this classification using an SU(3) flavor symmetry, Gell-Mann, and independently Zweig, would propose a full theoretical model in which *hadrons* (strongly interacting particles, i.e. mesons and baryons) were not elementary particles anymore. They would rather be composed with 3 flavors of particles called *quarks* and there anti-particles. The 3 flavors were called *up*, *down* and *strange*. *Up* and *down* would be used to explain the nucleons and non-strange mesons, while *strange* would come into the composition of hadrons showing strangeness. *Up* and *down* flavors would be discovered in 1968 thanks to the deep inelastic scattering experiments conducted at the Stanford Linear Accelerator Center (SLAC), and *strange* could only be indirectly validated even though it provided a robust explanation to *kaon* (K) and *pion* (π). However, in the decade following the Gell-Mann-Zweig quark model proposition, several improvement to the model were brought, first by Glashow and Bjorken the same year that predicted the existence of a fourth quark flavor, the *charm*, that would equalize the then known number of quarks and leptons and finally in 1973 by Kobayashi and Maskawa that would increase the number of quarks to 6 to explain the experimental observation of CP violation. These two quarks would be referred to as *top* and *bottom* for the first time in 1975. It's only after these additions to the quark model that finally the *charm* would be discovered in 1974 at both SLAC and Brookhaven National Laboratory (BNL). A meson where the *charm* was bound with an *anti-charm*, called J/ψ , would help convince the physics community of the validity of the model. The *top* would be discovered soon after in 1977 in Fermilab and indicate the existence of the *bottom* that would resist to discovery until Fermilab's experiments CDF and D \emptyset in 1995 due its very large mass and the energy needed to produce it.

As remarked by Struminsky, the original quark model proposal composed of 3 quarks should possess an additional quantum number due to mesons such as Ω^- or Δ^{++} . Indeed, these mesons are composed of 3 identical quarks, respectively 3 *strange* and *up* quark, with parallel spins, which

should be forbidden by the exclusion principle. Independentle, Greenberg and Han-Nambu proposed an additional SU(3) degree of freedom possessed by the quarks, that would later be refered to as *color charge gauge*, that could interact through *gluons*, the gauge boson octet corresponding to this degree of freedom. Nevertheless, as observing free quarks proved to be impossible, two visions of the quarks were argued mainly due to the failures to observe these particles free to prove their existence. On one side, Gell-Mann proposed to see quarks as mathematical construct instead of real particles, as they are always confined, implying that quantum field theory would not describe entirely the strong interaction. Opposed to this vision, Feynman on the contrary argued that quarks were real particles, that he would call *partons*, that should be described as all other particles by a distribution of position and momentum. The implications of quarks as point-like particles would be verified at SLAC and the concept of *color* would be added to the quark model in 1973 by Fritzsch and Leutwyler together with Gell-Mann to propose a description of the strong interaction through the theory of Quantum Chromodynamics (QCD). The discovery the same year of asymptotic freedom within the QCD by Groos, Politzer and Wilczek, allowed for very precise predictions thanks to the perturbation theory. Nowadays, the confinement of quarks is studied in experiments such as ALICE, through exploration of the quark-gluon plasma.

912 **The Weak interaction, spontaneous symmetry breaking, the Higgs mechanism and the Elec- 913 troweak unification**

914 The weak interaction is the process that causes radioactive decays. Thanks to the neutron discovery,
 915 Fermi could explain in 1934 the beta radiations through the beta decay process in which the neutron
 916 decays into a proton by emitting an electron. Though the missing energy observed during this
 917 process triggered a huge debate about the apparent non conservation of energy, momentum and spin
 918 of the process, Fermi, as Pauli before him, proposed that the missing energy was due to a neutral
 919 not yet discovered particle that would then be baptised *neutrino*. The impossibility to detect such
 920 a particle would leave some members of the scientific community sceptical, but hints of energy
 921 conservation and of the existence of the neutrino were provided by measuring the energy spectrum
 922 of electrons emitted through beta decay, as there was a strict limit on their energy. It's only 30 years
 923 later in 1953 that it would be discovered by the team of Cowan and Reines using the principle of
 924 inverse beta decay described through Formula 2.6. The experiment consisted in placing water tanks
 925 sandwiched in between liquid scintillators near a nuclear reactor with an estimated neutrino flux of
 926 $5 \times 10^{13} \text{ s}^{-1} \text{ cm}^{-2}$. However, in order to explain the absence of some reactions in the experiment
 927 of Cowan and Reines, and constraint the beta decay theory of Fermi and extend it to the case of
 928 the muon, Konopinski and Mahmoud proposed in 1953 that the muon decay would eject a particle
 929 similar to the neutrino and thus predicted the existence of a muon neutrino that would be different
 930 than the one involved in the beta decay, related to the electron. With this, the idea of lepton number
 931 would arise. The muon neutrino would successfully be detected in 1962 by Lederman, Schwartz and
 932 Steinberger.

$$\bar{\nu} + p \rightarrow n + e^+ \quad (2.6)$$

933 The theory could not be valid though as the probability of interaction, called cross-section, would
 934 have been increasing without bond with the square of the energy. Fermi assumed in a two vector
 935 current coupling but Lee and Yang noted that an axial current could appear and would violate parity.
 936 The experiment of Wu in 1956 would confirm the parity violation and Gamow and Teller would try to
 937 account for it by describing Fermi's interaction through allowed (parity-violating) and superallowed

938 (parity-conserving) decays. But the success of QED as a quantum field theory would spark the
939 development of such a theory to describe the weak interaction.

940 As previously discussed, the great success of QED was built on an underlying symmetry, inter-
941 preted as a gauge invariance so that the effect of the force is the same in all space-time coordinates,
942 and of the possibility to renormalize it in order to absorb the infinities. Independently in 1958,
943 Glashow, and Salam and Ward used 1957 Schwinger ideas about vector intermediary for the decay
944 processes, could find a way to unite both the electromagnetic and weak interaction into a gauge
945 theory involving 4 gauge bosons, 3 of which were massive and carried out the weak interaction and
946 a massless boson carrying the electromagnetic interaction. Among the 3 massive bosons, 2 were
947 charged and 1 was neutral, similarly to the previously theorized *pi meson* vector of the Yukawa
948 model and all have a mass much greater than nucleons and thus a very short life time implying a
949 finite very short range contrary to the contact interaction originally proposed by Fermi.

950 Breakthrough in other fields of physics contributed in giving theoretical support and interpreta-
951 tion to the unified electroweak theory. The stepping stone would be the use of spontaneous symmetry
952 breaking that was inspired to Nambu at the end of the 1950s following the development of the BCS
953 superconductivity mechanism in 1957. Cooper had shown that BCS pairs, pairs of electrons bound
954 together at low temperature, could have lower energy than the Fermi energy and where responsi-
955 ble for superconductivity. This lead to the discovery of Goldstone-Nambu bosons as a result of the
956 spontaneous breaking of the chiral symmetry in a theory describing nucleons and mesons devel-
957 opped by Nambu and Jona-Lasinio in 1961, and now understood as a low-energy approximation of
958 QCD. Similarly to mechanism of energy gap appearance in superconductivity, the nucleon mass
959 is suggested to the result of a self-energy of a fermion field and is studied through a four-fermion
960 interaction in which, as a consequence of the symmetry, bound states of nucleon-antinucleon pairs
961 appear and can be regarded as virtual pions. Though the symmetry is maintained in the equations,
962 the ground state is not preserved. Goldstone would later the same year show that the bound states
963 corresponds to spinless bosons with zero mass.

964 Although the model in itself didn't revolutionize particle physics, spontaneous symmetry break-
965 ing would be generalized to quantum field theories. As all fundamental interactions are described
966 using gauge theories based on underlying symmetries, processes such as the chiral symmetry break-
967 ing would be introduced soon after the publication of Nambu and Jona-Lasinio. In 1962, Anderson,
968 following an idea of Schwinger who suggested that zero-mass vector bosons were not necessarily
969 required to describe the conservation of baryons contrary to the bosons emerging from chiral sym-
970 metry breaking, discussed the implications of spontaneous symmetry breaking in particles physics.
971 A model was finally independently built in 1964 by Brout and Englert, Higgs, and Guralnik, Hagen,
972 and Kibble, who discovered that combining an additional field into a gauge theory in order to break
973 the symmetry, the resulting gauge bosons acquire a nonzero mass. Moreover, Higgs stated that this
974 implied the existence of at least one new massive, i.e. self-interacting, scalar boson, that are now
975 known as *Higgs bosons* corresponding to this additional field. The Higgs mechanism today specifi-
976 cally refers to the process through which the gauge bosons of the weak interaction acquire mass. In
977 1968, Weinberg could point to the Higgs mechanism to integrate a Higgs field into a new version
978 of the electroweak theory in which the spontaneous symmetry breaking mechanism of the Higgs
979 field would explicitly explain the masses of the weak interaction gauge bosons and the zero-mass
980 of photons.

2.1.2 Construction and test of the model

The Standard Model of particle physics was built in the middle of the 1970s after the experimental confirmation of the existence of quarks. It is based on the assembly of the models previously introduced and describing the fundamental interactions, except for gravitation, and their gauge bosons as well as the way elementary "matter" particles interact with the fields associated with these force carriers. In this sense, the development of QED and the unification of the electroweak interaction, of the Yukawa interaction and of QCD, and of the Higgs mechanism made it possible to explain most of contemporary physics.

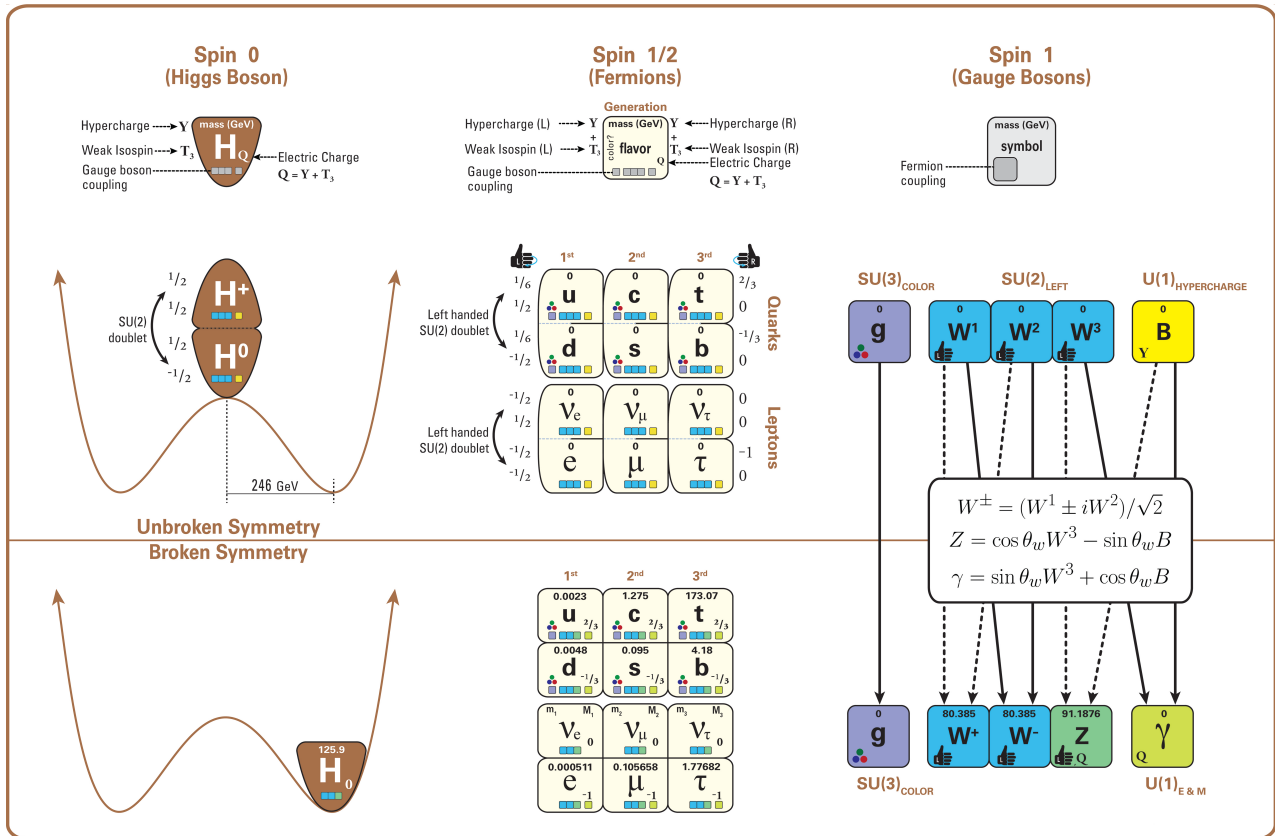


Figure 2.3: The elementary particles of the Standard Model are showed along with their names and properties. Their interactions with the strong, weak and electromagnetic forces have been explicited using color squares. In the left column, the scalar higgs boson is depicted, while the central is focused on the matter particles, the fermions, and the right on the force carriers, the gauge bosons. The role of the Higgs boson in electroweak symmetry breaking is highlighted, and the corresponding way properties of the various particles differ in the (high-energy) symmetric phase (top) and the (low-energy) broken-symmetry phase (bottom) are showed.

In the SM, "matter" particles, are described by 12 fermion fields of spin $\frac{1}{2}$ obeying the Fermi-Dirac statistics, i.e. subjected to the Pauli exclusion principle. To each fermion is associated its corresponding antiparticle. The fermions are classified according to the way they interact and, thus, according to the charges they carry. 6 of them are classified as quarks (u, d, c, s, t , and b) and are subjected to all interactions and the 6 others as leptons ($e^-, \mu^-, \tau^-, \nu_e, \nu_\mu$, and ν_τ). Leptons

994 are not subjected to the strong interaction and among them, the 3 neutrinos only interact weakly as
 995 they are neutral particles, which explains why they are so difficult to detect. The gauge boson fields
 996 are the gluons g for the strong interaction, the photon γ for the electromagnetic interaction and the
 997 weak bosons W^+ , W^- , and Z^0 for the weak interaction. Finally, the Higgs field H^0 is responsible,
 998 through the spontaneous symmetry breaking, of the mixing of the massless electroweak boson fields
 999 W_1 , W_2 , W_3 , and B leading to the observable states γ , W^+ , W^- , and Z^0 that can gain mass while
 1000 interacting with the Higgs field. This picture of the SM is summarized through Figure 2.3 where the
 1001 antifermions are not showed.

1002 When the model was first finalized, the existence of the weak gauge bosons, of the charm, of the
 1003 third quark generation composed of top and bottom quarks to explain the observed CP violation was
 1004 not proven but the predictions were measured with good precision in the years following. First, the
 1005 charm quark would be discovered in 1974, followed by the bottom quark in 1977. The weak bosons
 1006 would be discovered during the next decade in 1983. The top quark would resist until 1995 due to
 1007 its very large mass but would offer the last piece of the elementary QCD particles. The very last
 1008 predicted elementary particle of the model that was not observed yet would prove to be very difficult
 1009 to observe. the Higgs boson needed the start of the LHC to finally be observed in 2012. A few years
 1010 more of tests were necessary to measure its properties to confirm the observation of a scalar boson
 1011 compatible with the predicted Higgs boson H^0 . Eventhough only quark-antiquark (mesons) and 3
 1012 quark states (baryons) were observed, exotic hadrons were not forbidden by QCD and no limit of
 1013 quark is imposed by the theory. Moreover, gluons could form bond states by themselves and with
 1014 quarks. These two types of states are called *glueballs* and *hybrid hadrons*. For decades, experi-
 1015 ments have been conducted without confirmation of such possible states existing. Nevertheless, in
 1016 2014, tetraquarks were observed by LHCb, one of LHC's main experiments, and in 2015, the same
 1017 experiment reported the discovery of pentaquarks making the SM one of the best tested theories of
 1018 physics.

1019 2.1.3 Investigating the TeV scale

1020 Even though the SM is a well tested theory, several hints of physics going beyond its scope have
 1021 been observed. First of all, gravity is not explained through this model and huge difficulties are en-
 1022 countered when trying to include gravitation. The strength of gravitational interaction is expected to
 1023 be negligible at the scale of elementary particles, nevertheless, adding gravitation in the perspective
 1024 of developing a "theory of everything" leads to divergent integrals that could not be fixed through
 1025 renormalization.

1026 Moreover, the SM considers neutrinos to be massless but it was shown in the late 1960s by the
 1027 Homestake experiment that the flux of solar neutrinos (i.e. ν_e) measured didn't match the predicted
 1028 values due to neutrino oscillations, confirmed in the early 2000s by the Sudbury Neutrino Obser-
 1029 vatory. This oscillation implies that neutrinos that can be observed are a superposition of massive
 1030 neutrino states. The research on neutrino oscillation is already quite advanced with experiments
 1031 looking at atmospheric, reactor or beam neutrinos in order to determine the elements of the mixing
 1032 matrix similar to the CKM matrix describing the mixing of quarks. Nevertheless, no answer to the
 1033 origin of neutrino mass is provided.

1034 Another intriguing fact is that the universe is dominated by matter. However, the SM predicted
 1035 that matter and antimatter should have been created in equal amounts and no mechanism is able to
 1036 explain this matter-antimatter asymmetry. Although this asymmetry is seen from the visible uni-
 1037 verse, it may be possible that other unknown regions of the Universe are dominated by antimatter.

1038 Another possibility to explain the apparent asymmetry would be the existence of a electric dipole
1039 in any fundamental particle that would permit matter and antimatter particles to decay at different
1040 rates.

1041 The discrepancy of velocity dispersion of stars in galaxies with respect to the visible mass they
1042 contain is known since the end of the 19th century where Kelvin proposed that this problem could
1043 be solved if a "*great majority of [the stars] would be dark bodies*". Throughout the 20th century,
1044 physicists like Kapteyn, Zwicky, showed the first hints of a "*dark matter*" by studying star veloc-
1045 ities and galactic clusters, followed by robust measurements of galaxy rotation curves by Babcock
1046 which suggested that the mass-to-luminosity ratio was different from what would be expected from
1047 watching the visible light. Later in the 1970s, Rubin and Ford from direct light observations and
1048 Rogstad and Shostak from radio measurements showed that the radial velocity of visible objects in
1049 galaxies was increasing with increasing distance to the center of the galaxy. Finally observation of
1050 lensing effect by galaxy clusters, temperature distribution of hot gas in galaxies and clusters, and
1051 the anisotropies in the Cosmic Microwave Background (CMB) kept on pointing to a "*dark matter*".
1052 From all the data accumulated, the visible matter would only account to no more than 5% of the total
1053 content on the visible universe. Alternative theories have tried to investigate modified versions of
1054 the General Relativity as this theory is only well tested at the scale of the solar system but is not suf-
1055 ficiently tested on wider ranges or even theories in which gravitation is not a fundamental force but
1056 rather an emergent one, but so far, such theories have difficulties to reproduce all the experimental
1057 observations as easily as through dark matter.

1058 A possible theory to offer dark matter candidates would be supersymmetry (SUSY) which pro-
1059 poses a relationship in between bosons and fermions. In this model, each elementary particle,
1060 through a spontaneous spacetime symmetry breaking mechanism would have a *super partner* from
1061 the other family of particles. On top of providing heavy dark matter candidates, supersymmetry
1062 could also help solving the *Hierarchy problem*, the very large scale difference in between the weak
1063 interaction and gravity, although, as mentioned before, in the case gravity is found not to be a funda-
1064 mental force, this problem would automatically fade.

1065

1066 All these different aspects of physics beyond the Standard Model of particle physics and the
1067 Standard model itself can be tested through the use of very energetic and intense hadron and ion col-
1068 liders. The LHC at CERN is a perfect tool to seek answers to these open questions except maybe for
1069 the gravity as gravity is extremely weak at particles level. For example, one of LHCb experiment's
1070 goal is to investigate CP-violation and thus baryonic asymmetry. In 2017, the collaboration has an-
1071 nounced to have so far a 3.3σ statistical significance over a CP-violation through the study of the
1072 decays of Λ_b^0 and $\overline{\Lambda}_b^0$ into a proton (or antiproton) and 3 pions. Many analysis teams are also working
1073 hard on supersymmetry both in ATLAS and CMS collaborations, the two multipurpose experiments
1074 of LHC, even though no evidence of a supersymmetrical theory was seen, the few hint having the
1075 tendency to confirm the standard model. These experiments also have the possibility to investigate
1076 ways to explain Majorana neutrino mass through Yukawa interactions of scalar particles.

1077 The higher the center-of-mass energy, the smaller details the experiments will be able to see, the
1078 heavier the potential particle creation barrier will be, the stronger the cross-section of certain rare
1079 decay channels will be. As a comparison, with collisions happening at 14 TeV, the LHC is approxi-
1080 mately 2 orders of magnitude more sensitive to the Higgs than the Tevatron was with its already very
1081 powerful 2 TeV. All these advantages eventually lead to new discoveries and deeper understanding
1082 of the models describing our Universe. But the LHC only is a step forward to gather more precise
1083 tests of the Standard Model and new knowledge about the physics beyond it. A successful physics

1084 campaign will probably serve to justify the building of new accelerators with even greater discovery
 1085 potential like for example the Future Circular Collider (FCC) that would push even further the study
 1086 of the unanswered questions of contemporary physics.

1087 2.2 The Large Hadron Collider & the Compact Muon Solenoid

1088 Throughout its history, CERN has played a leading role in high energy particle physics. Large re-
 1089 gional facilities such as CERN were thought after the second world war in an attempt to increase
 1090 international scientific collaboration and allows scientists to share the forever increasing costs of
 1091 experiment facilities required due to the need for increasing the energy in the center of mass to
 1092 deeper probe matter. The construction of the first accelerators at the end of the 50s, the Synchro-
 1093 cyclotron (SC) and the Proton Synchrotron (PS), was directly followed by the first observation of
 1094 antinuclei in 1965 [1]. Strong from the experience of the Intersecting Storage Rings (ISR), the very
 1095 first proton-proton collider that showed hints that protons are not elementary particles, the Super
 1096 Proton Synchrotron (SPS) was built in the 70s to investigate the structure of protons, the preference
 1097 for matter over antimatter, the state of matter in the early universe or exotic particles, and lead to
 1098 the discovery in 1983 of the W and Z bosons [2–5]. These newly discovered particles and the elec-
 1099 troweak interaction would then be studied in details by the Large Electron-Positron (LEP) collider
 1100 that will help to prove in 1989 that there only are three generations of elementary particles [6]. The
 1101 LEP would then be dismantled in 2000 to allow for the LHC to be constructed in the existing tunnel.

1102 2.2.1 LHC, the most powerful particle accelerator

1103 The LHC has always been considered as an option to the future of CERN. At the moment of the
 1104 construction of the LEP beneath the border between France and Switzerland, the tunnel was built in
 1105 order to accomodate what would be a Large Hadron Collider with a dipole field of 10 T and a beam
 1106 energy in between 8 and 9 TeV [7] directly followed in 1985 with the creation of a 'Working Group
 1107 on the Scientific and Technological Future of CERN' to investigate such a collider [8]. The decision
 1108 was finally taken almost 10 years later, in 1994, to construct the LHC in the LEP tunnel [9] and the
 1109 approval of the 4 main experiments that would take place at the 4 interaction points would come in
 1110 1997 [10] and 1998 [11]:

- 1111 • ALICE [12] has been designed in the purpose of studying quark-gluon plasma that is believed
 1112 to have been a state of matter that existed in the very first moment of the universe.
- 1113 • ATLAS [13] and CMS [14] are general purpose experiments that have been designed with
 1114 the goal of continuing the exploration of the Standard Model and investigate new physics.
- 1115 • LHCb [15] has been designed to investigate the preference of matter over antimatter in the
 1116 universe through the CP violation.

1117 These large scale experiments, as well as the full CERN accelerator complex, are displayed on
 1118 Figure 2.4. The LHC is a 27 km long hadron collider and the most powerful accelerator used for
 1119 particle physics since 2008 [16]. The LHC was originally designed to collide protons at a center-
 1120 of-mass energy of 14 TeV and luminosity of $10^{34} \text{ cm}^{-2}\text{s}^{-1}$, as well as Pb ions at a center-of-mass
 1121 energy of 2.8 TeV/A with a peak luminosity of $10^{27} \text{ cm}^{-2}\text{s}^{-1}$. Run 1 of LHC, when the center-of-
 1122 mass energy only was half of the nominal LHC energy, was enough for both CMS and ATLAS to

discover the Higgs boson [17] and for LHCb to discover pentaquarks [18] and confirm the existance of tetraquarks [19]. Nevertheless, after the Third Long Shutdown (LS3) (2024-2026), the accelerator will be in the so called High Luminosity LHC (HL-LHC) configuration [20], increasing its instantaneous luminosity to $10^{35} \text{ cm}^{-2}\text{s}^{-1}$ for pp collisions and to $4.5 \times 10^{27} \text{ cm}^{-2}\text{s}^{-1}$, boosting the discovery potential of the LHC. The HL-LHC phase should last at least another 10 years depending on the breakthrough this machine would lead to. Already a new accelerating device, the FCC, as been proposed to prepare the future of high energy physics after the LHC.

CERN's Accelerator Complex

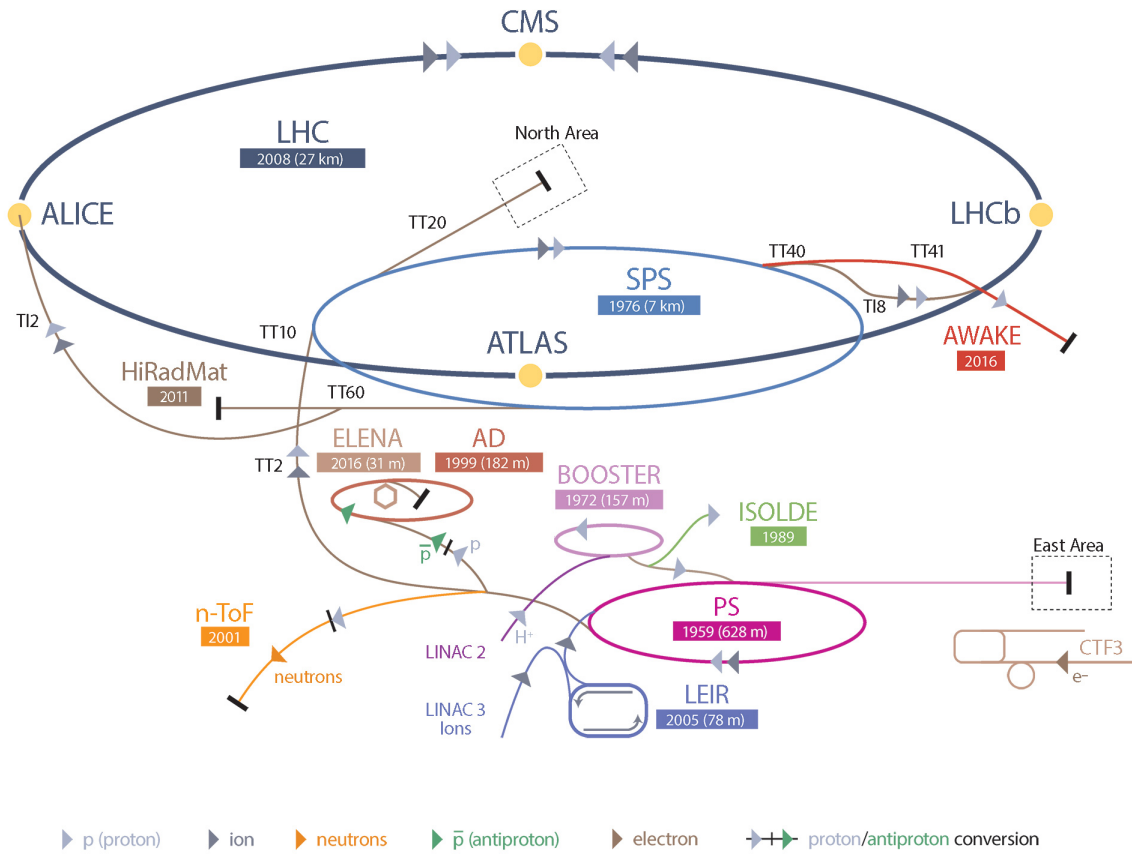


Figure 2.4: CERN accelerator complex.

2.2.1.1 Particle acceleration

The LHC is the last of a long series of accelerating devices. Before being accelerated by the LHC, the particles need to pass through different acceleration stages. All these acceleration stages are visible on Figure 2.4 and pictures of the accelerators are showed in Figure 2.5.

The story of accelerated protons at CERN starts with a bottle of hydrogen gas injected into the source chamber of the linear particle accelerator *LINAC 2* in which a strong electric field strips the

1137 electron off the hydrogen molecules only to keep their nuclei, the protons. The cylindrical conductors,
 1138 alternatively positively or negatively charged by radiofrequency cavities, accelerate protons by
 1139 pushing them from behind and pulling them from the front and ultimately give them an energy of
 1140 50 MeV, increasing their mass by 5% in the process.

1141

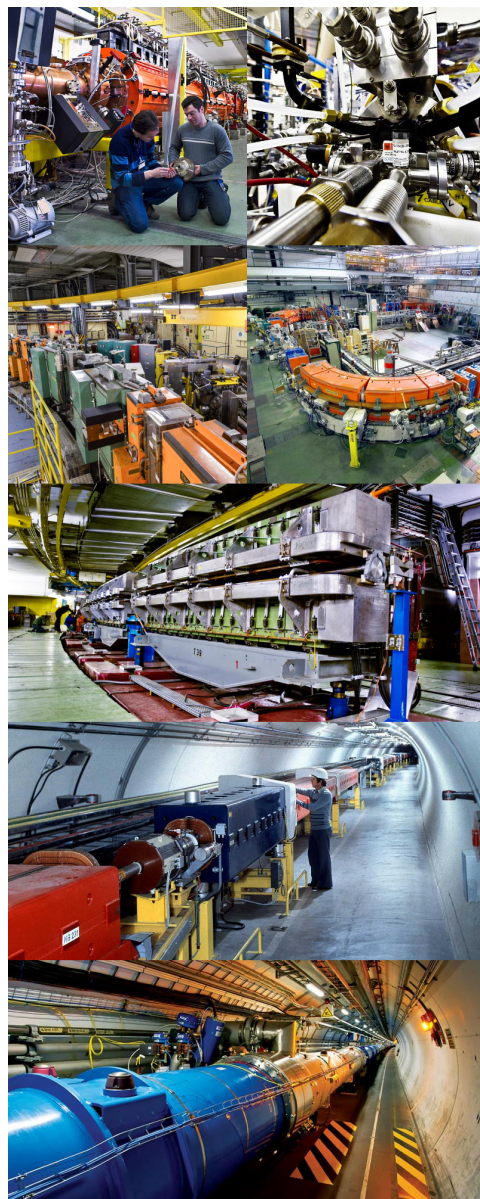


Figure 2.5: Pictures of the different accelerators. From top to bottom: first the LINAC 2 and the Pb source of LINAC 3. Then the Booster and the LEIR. Finally, the PS, the SPS and the LHC.

1142 When exiting the LINAC 2, the protons are divided into 4 bunches and injected into the 4 su-
 1143 perimposed synchrotron rings of the *Booster* where they are then accelerated to reach an energy of

1144 1.4 GeV before being injected into the PS. Before the Booster was operational in 1972, the protons
 1145 were directly injected into the PS from the LINAC 2 but the low injection energy limited the amount
 1146 of protons that could be accelerated at once by the PS. With the Booster, the PS accepts approxi-
 1147 mately 100 times more particles.

1148

1149 The 4 proton bunches are thus sent as one to the PS where their energy eventually reaches
 1150 26 GeV. Since the 70s, the main goal of this 628 m circumference synchrotron has been to sup-
 1151 ply other machines with accelerated particles. Nowadays, not only the PS accelerates protons, it also
 1152 accelerates heavy ions from the *Low Energy Ion Ring (LEIR)*. Indeed, the LHC experiments are not
 1153 only designed to study *pp*-collisions but also *Pb*-collisions. Lead is first injected into the dedicated
 1154 linear collider *LINAC 3*, that accelerate the ions using the same principle than LINAC 2. Electrons
 1155 are striped off the lead ions all along the acceleration process and eventually, only bare nuclei are
 1156 injected in the LEIR whose goal is to transform the long ion pulses received into short dense bunches
 1157 for LHC. Ions injected and stored in the PS were aceelerated by the LEIR from 4.2 MeV to 72 MeV.

1158

1159 Directly following the PS, is finally the last acceleration stage before the LHC, the 7 km long
 1160 *SPS*. The SPS accelerates the protons to 450 GeV and inject proton in both LHC accelerator rings
 1161 that will increase their energy up to 7 TeV. When the LHC runs with heavy lead ions for ALICE
 1162 and LHCb, ions are injected and accelerated to reach the energy of 2.8 TeV/A.

1163

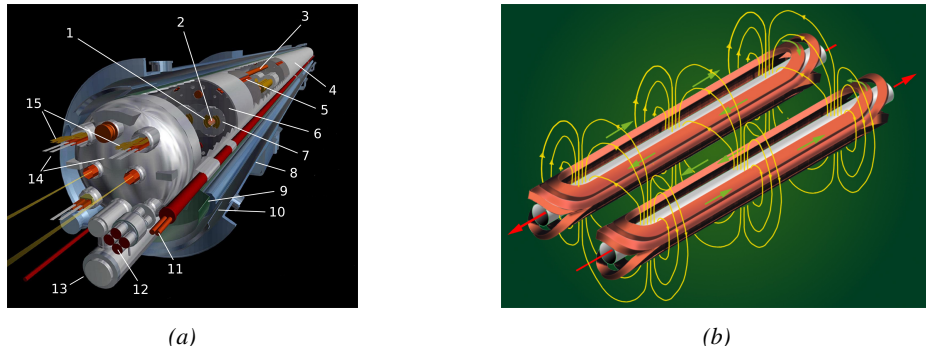


Figure 2.6: Figure 2.6a: schematics of the LHC cryodipoles. 1: Superconducting Coils, 2: Beam pipe, 3: Heat exchanger Pipe, 4: Helium-II Vessel, 5: Superconducting Bus-bar, 6: Iron Yoke, 7: Non-Magnetic Collars, 8: Vacuum Vessel, 9: Radiation Screen, 10: Thermal Shield, 11: Auxiliary Bus-bar Tube, 12: Instrumentation Feed Throughs, 13: Protection Diode, 14: Quadrupole Bus-bars, 15: Spool Piece Bus-bars. Figure 2.6b: magnetic field and resulting motion force applied on the beam particles.

1164

1165 The LHC beams are not continuous and are rather organised in bunch of paticles. When in *pp*-
 1166 collision mode, the beams are composed of 2808 bunches of 1.15×10^{11} protons separated by 25 ns.
 1167 When in *Pb* collision mode, the 592 *Pb* bunches are on the contrary composed of 2.2×10^8 ions
 1168 separated by 100 ns. The two parrallel proton beams of the LHC are contained in a single twin-
 1169 bore magnet due to the space restriction in the LEP tunnel. Indeed, building 2 completely separate
 1170 accelerator rings next to each other was impossible. The dipoles of the 1232 twin-bore magnets are
 1171 showed in Figure 2.6 alongside the magnetic field generated along the dipole section to accelerate the
 1172 particles. The dipoles generate a nominal field of 8.33 T, needed to give protons and lead nucleons
 their nominal energy. Some 392 quadrupoles, presented in Figure 2.7, are also used to focus to the

¹¹⁷³ beams, as well as other multipoles to correct smaller imperfections.

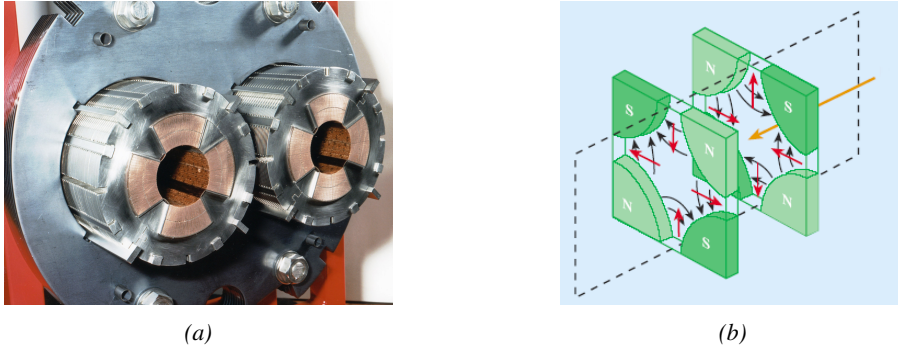


Figure 2.7: Figure 2.7a: picture of the LHC quadrupoles. Figure 2.7b: magnetic fields and resulting focussing force applied on the beam by 2 consecutive quadrupoles.

¹¹⁷⁴ 2.2.2 CMS, a multipurpose experiment

¹¹⁷⁵ Among the four main LHC experiments is the Compact Muon Solenoid used as a multipurpose tool to
¹¹⁷⁶ investigate the SM and physics beyond its scope. Proposed through a letter of intention in 1992 [14],
¹¹⁷⁷ and as its name suggests, this very compact detector's uses the muons as a clear tag of most of SM
¹¹⁷⁸ and new physics interesting channels. In the original 1997 Technical Design Report (TDR) [21], the
¹¹⁷⁹ very first sentences were stating that "*Muons are an unmistakable signature of most of the physics*
¹¹⁸⁰ *LHC is designed to explore. The ability to trigger on and reconstruct muons at the highest lumi-*
¹¹⁸¹ *nosities is central to the concept of CMS, the Compact Muon Solenoid.*" CMS participated in the
¹¹⁸² discovery of the Higgs boson and the measurement of its properties and couplings together with
¹¹⁸³ ATLAS and is also actively involved in the search for SUSY and heavy ion collisions. Other exotic
¹¹⁸⁴ physics are also being investigated using the data collected by CMS.

¹¹⁸⁵ The CMS apparatus in itself is the heaviest detector ever built starring a SI15m diameter and a
¹¹⁸⁶ 29 m length for a total weight of 14 kT. A thick 4 T solenoid magnet located at the beam interaction
¹¹⁸⁷ point hosts trackers and calorimeters. Extending in all directions around the magnet, heavy iron
¹¹⁸⁸ return yokes are installed to extend the magnetic field and support a muon system. The apparatus
¹¹⁸⁹ consists of a barrel, referring to the magnet and the detectors contained in it and the part of the muon
¹¹⁹⁰ system built directly in the cylinder around the magnet, and of 2 endcaps in the forward and back-
¹¹⁹¹ ward region of the detector that closes the apparatus and complete the detection coverage along the
¹¹⁹² beam line. A front view on the barrel is provided in Figure 2.8 while a detailed view of the apparatus
¹¹⁹³ is given in Figure 2.9.

¹¹⁹⁴

¹¹⁹⁵ In order to efficiently detect all long leaving particles and measure their properties with good
¹¹⁹⁶ precision, the CMS detector uses an onion like layout around of the interaction point in order to
¹¹⁹⁷ maximize the covered solid angle. As detailed in Figure 2.10, in the innermost region of the detector,
¹¹⁹⁸ closest to the interaction point, the silicon tracker records the trajectory of charged particles. Around
¹¹⁹⁹ it, the electromagnetic calorimeter (ECAL) stops and measure the energy deposition of electrons
¹²⁰⁰ and photons. In the next layer, the hadron calorimeter (HCAL), hadrons are stopped and their energy
¹²⁰¹ measured. These layers are contained inside of the magnet of CMS, the superconducting solenoid.
¹²⁰² Outside of the magnet are the muon chambers embedded into iron return yokes used to control the

1203 magnetic field and gives muons, the only particles traveling completely through the whole detector, a
 1204 double bending helping in reconstructing their energy and trajectory. Note that photons and neutral
 1205 hadrons are differentiated from electrons and charged hadrons in the calorimeters by the fact that
 1206 don't interact with the silicon tracker and that they are not influenced by the magnetic field.

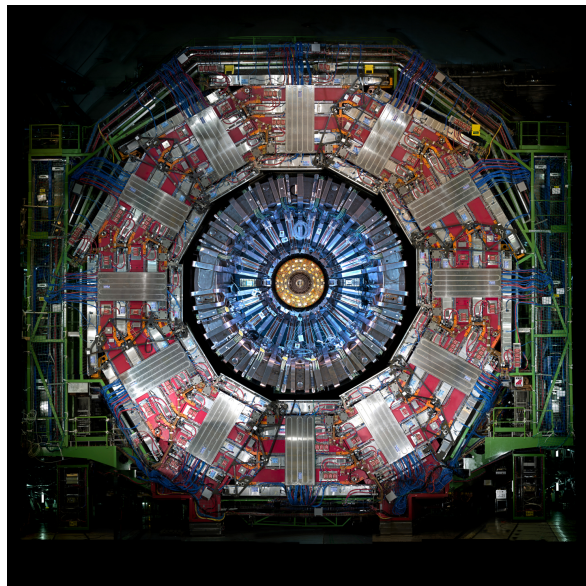


Figure 2.8: Picture of the CMS barrel. The red outer layer is the muon system hosted into the red iron return yokes. The calorimeters are the blue cylinder inside in magnet solenoid and the tracker is the inner yellow cylinder built around the beam pipe.

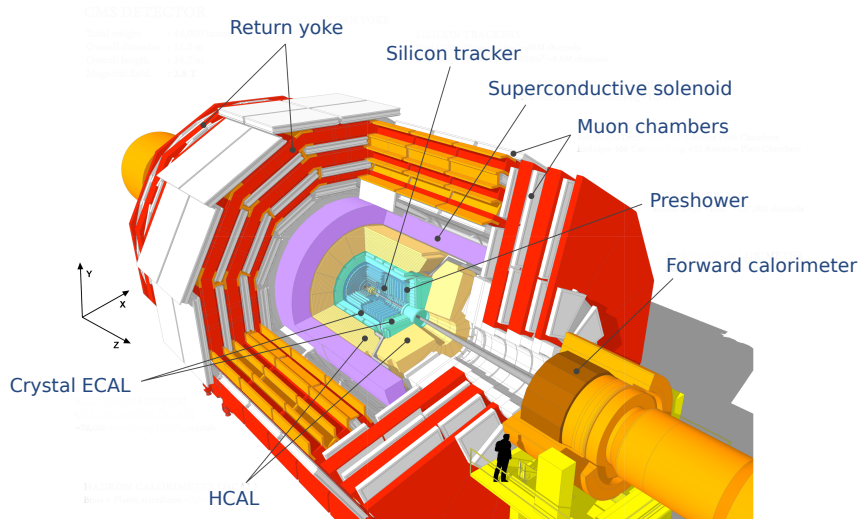


Figure 2.9: View of the CMS apparatus and of its different components.

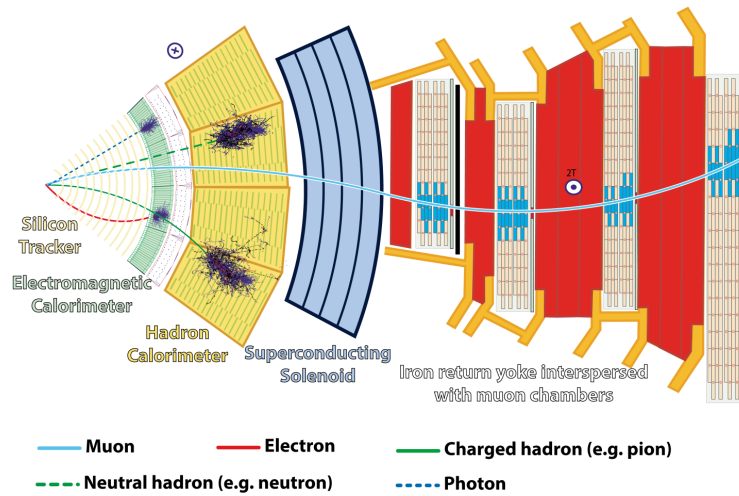


Figure 2.10: Slice showing CMS sub-detectors and how particles interact with them.

2.2.2.1 The silicon tracker, core of CMS

The silicon tracker visible on Figure 2.11 is divided into 2 different sub-systems: the *pixel detector* at the very core and the *microstrip detector* around it. This system is composed of 75 million individual readout channels with up to 6000 channels per squared centimeter for the pixels making it the world's biggest silicon detector. This density allows for measurements of the particle tracks with a precision of the order of $10\ \mu\text{m}$. This is necessary to reconstruct all the different interaction vertices with precision and have a precise measure of the curvature of the charged particles traveling through the magnetic field to estimate their charge and momentum.

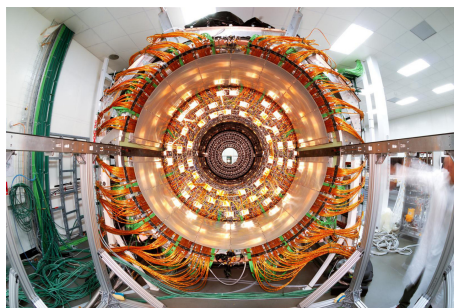


Figure 2.11: CMS tracker.

2.2.2.2 The calorimeters, measurement of particle's energy

The ECAL directly surrounding the tracker is composed of crystals of lead tungstate, PbWO_4 , a very dense but optically transparent material used to stop high energy electrons and photons. These crystal blocks basically are extremely dense scintillators which scintillate in fast, short light bursts proportionally to the energy deposition. The light is yielded rapidly and contained at 80% in the corresponding 25 ns lasting bunch crossing. Each crystal is isolated from the other by the carbon fiber matrix they are embedded in. It is composed of a barrel containing more than 60,000 crystals

and of closing endcaps containing another 15,000 crystals. In front of the ECAL endcap is installed a preshower detector made out of two layers of lead and silicon strip detectors to increase the spatial resolution close to the beam line for pion-photon and single-double photon discrimination purposes. Figure 2.12 shows the calorimeter inside of the magnet and the crystals.

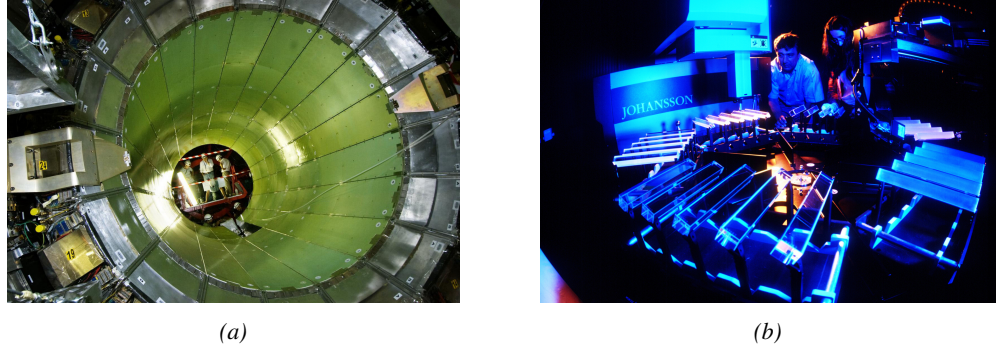


Figure 2.12: Figure 2.12a: picture of the ECAL. Figure 2.12b: picture of the lead tungstate crystals composing the ECAL.

The next layer is the HCAL measuring the hadrons momentum and providing indirect hints of non interacting neutral particles, such as neutrinos, as missing transverse momentum. Several layers of brass or steel are interleaved with plastic scintillators readout by photodiodes using wavelength-shifting fibers. The HCAL is also composed of a barrel, showed in Figure 2.13 and of endcaps. It also features forward calorimeters on both sides of CMS in the region very close to the beam line at high pseudorapidity ($3.0 < |\eta| < 5.0$). The role of these forward calorimeters, made using steel and quartz fibers, is to measure very energetic hadrons.



Figure 2.13: CMS hadron calorimeter barrel.

Finally, in the outer region of the apparatus, a muon system is used to trigger on potentially interesting event by identifying muons. Indeed, the muon system is a very important part of the CMS trigger infrastructure designed to efficiently select data from the enormous data flow received by the detectors as the LHC delivers collisions at a rate of 40 MHz with a pile-ip of 20 to 30 collisions per bunch crossing during Phase-I and up to 200 during Phase-II, representing billions of interactions per second among which a large quantity are low energy collisions that are not likely to produce new reactions, and which is physically impossible for nowadays technologies to cope with. Working at a maximum rate of 100 kHz, the trigger system is able to select the 100,000 more interesting events

by looking at the energy distribution of the interaction products and clear signatures like muons reconstructed by the muon system. the vast majority of these events will not finally be stored after physics tests are applied.

2.2.2.3 The muon system, corner stone of CMS

The challenge for the muon system is to provide a robust and fast measurement of muons. Three different subsystems, and soon 4 after LS2, compose the muon system as showed in Figure 2.14 in which a quadrant of the CMS detector focused on muon system. Drift Tube (DT) are found in the barrel region covering the low pseudorapidity region where particles transverse momentum is lower and Cathode Strip Chamber (CSC) are found in the endcap region covering higher pseudorapidity region closer to beam line where particles have a stronger momentum. The redundancy of the system is insured by Resistive Plate Chamber (RPC) in both the barrel and endcap region. Nevertheless, the region closest to the beam line ($|\eta| > 1.8$) was not equipped with RPCs. This lack of redundancy in the high pseudo rapidity region will be solved during LS2, the following Year End Technical Stop (YETS) in 2021 and 2022, and LS3 where the necessary services, detectors and Link System, that collects the data and synchronizes them, will be installed.

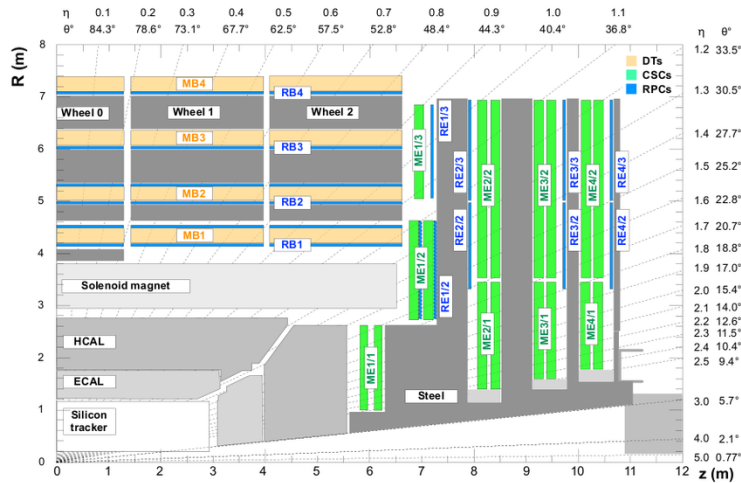


Figure 2.14: A quadrant of the muon system, showing DTs (yellow), RPCs (blue), and CSCs (green).

The barrel region is divided into 5 *wheels* made out of 4 *rings* of detectors with iron return yokes in between them whereas the endcaps are made out of 4 disks, each divided into pseudorapidity stations, 2 for CSCs (except for the first disk where 3 stations are equipped) and 3 for RPCs, although only 2 RPCs stations are equipped at present. The wheels and disks are showed in Figure 2.15. So far, each subsystem was dedicated to a particular task. DTs, in the barrel, and CSCs, in the endcaps, are used mainly for their spatial resolution. Indeed, DTs' resolution is of the order of 100 μm along both the $(r - \phi)$ and $(r - z)$ components while the resolution of CSCs is similar but varies in a range from 50 μm to 140 μm depending on the distance to the beamline. On the other hand, RPCs are used for their time resolution as they can deliver an information on the muon tracks within 1.5 ns.

The 250 CMS DTs, found in the barrel covering the pseudorapidity region $0 < |\eta| < 1.2$ and whose structure is shown in Figure 2.16, are composed of 3 *superlayers* of DT cells. Two of these superlayers are dedicated to measuring the ϕ coordinate of the muons and while the last one

measures the η (or z) coordinate. Each superlayer consists on 4 layers of 60 to 70 DT cells arranged in quincunx to allow for a precise reconstruction of the muon path through the DT layers. Each DT cell is a rectangular aluminium gas volume with a central anode wire. Cathode strips are placed on the narrow surface of the cells and electrode strips are placed on the wide surface to help shaping the electric field to ensure a consistent drift velocity of electrons in the drift volume. These detectors are operated using a 85/15 mixture of Ar and CO_2 .

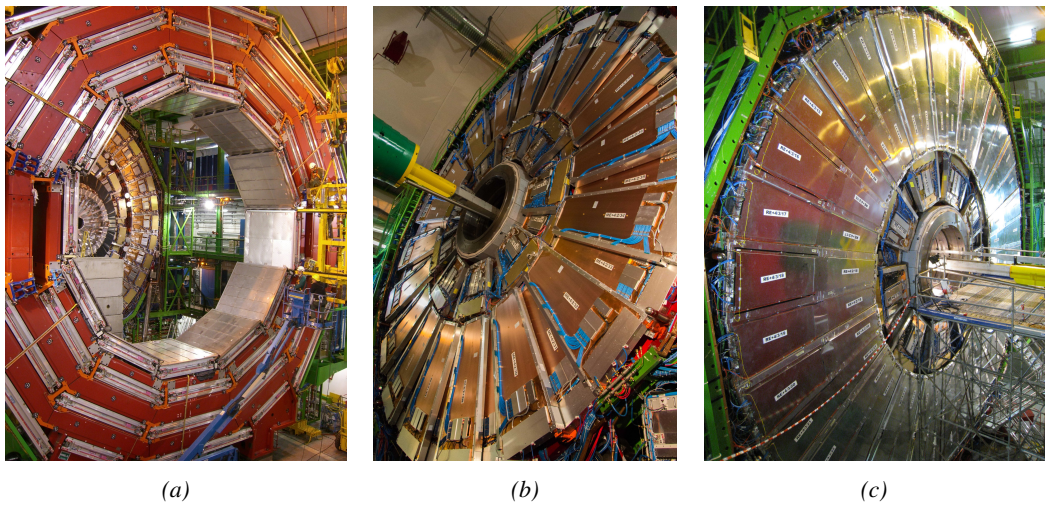


Figure 2.15: Figure 2.15a: Barrel wheel with its detector rings and return yokes. Figure 2.15b: CSC endcap disk with the 2 CSC stations. The outer station is made of 10 deg detectors while the inner station is made of 20 deg detectors. Figure 2.15c: RPC endcap disk. The inner station is not equipped and the inner CSC station can be seen.

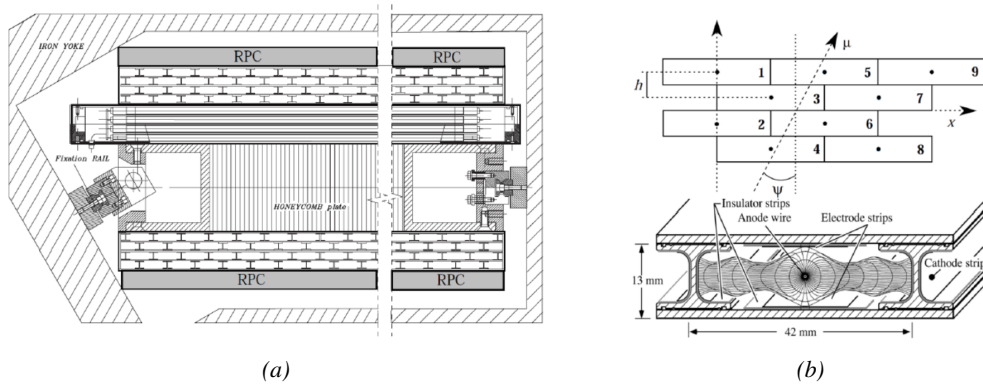


Figure 2.16: Figure 2.16a: Cross section of a DT module showing the two superlayers measuring the ϕ coordinate, perpendicular to the cross section plane, and the superlayer measuring the η coordinate, placed in between the two others with honeycomb and parallel to the cross section plane. The DT detector is sandwiched in between 2 RPCs whose readout strips are perpendicular to the cross section plane, measuring the ϕ coordinate. Figure 2.16b: A DT cell is shown together with its electric field. The path of a muon through a superlayer is shown.

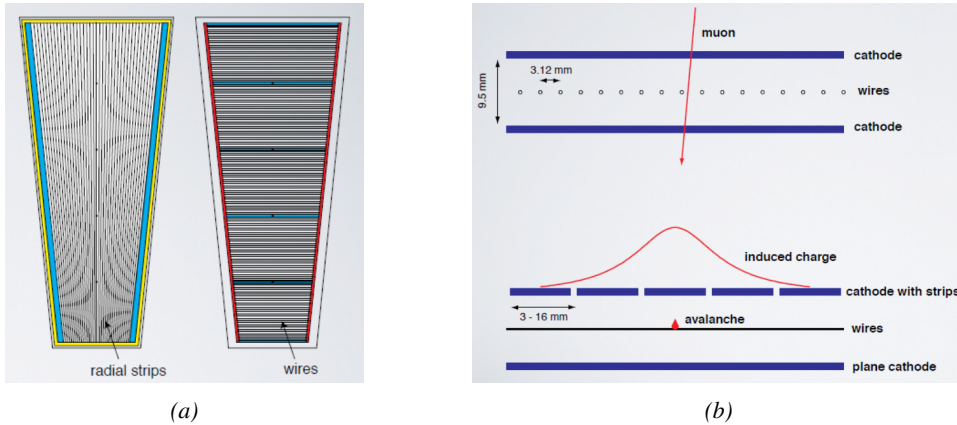


Figure 2.17: Figure 2.17a: cathode strips and anode wire layout of a CSC panel. Figure 2.17b avalanche development and charge collection by anode wires and induction on cathode strips inside of a CSC panel.

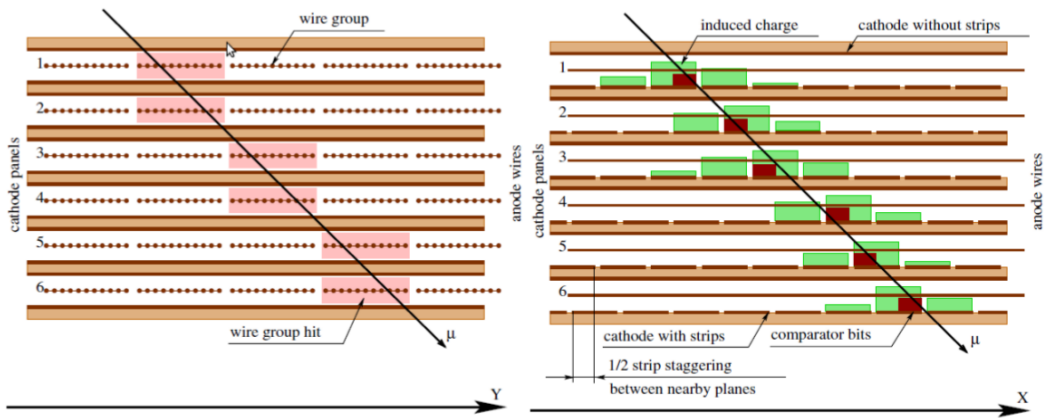


Figure 2.18: Muon track reconstruction through the 6 panels of a CMS CSC using the information of anode wire groups and cathode strip charge distribution combined with comparator bits to decide on which half strip the muon is more likely to have passed.

The 540 CMS CSCs, found in the endcaps covering the pseudorapidity region $0.9 < |\eta| < 2.5$ and described through Figure 2.17, are composed of 6 panels of CSC, each panel consisting in a wide gas volume of 9.5 mm (7 mm in the case of ME1/1 station) containing anode wires and whose surfaces are cathodes. The top cathode is a wide copper plane of the size of the gas volume. The bottom cathode is divided into thin trapezoidal copper strips radially arranged to measure the azimuthal coordinate ϕ with a pitch ranging from 8 to 16 mm. The $0.50 \mu\text{m}$ anode wires are placed perpendicularly to the strips to measure radial coordinate r and are grouped by 10 to 15 with a wire to wire space of 3.2 mm. In the specific case of ME1/1 placed against the HCAL endcap, the $0.30 \mu\text{m}$ anode wires have a wire to wire distance of 2.5 mm and are not disposed perpendicularly to the strips but slightly tilted by an angle of 29 deg to compensate for the lorentz force due to the very strong local magnetic field of 4 T. These detectors are operated with a 40/50/10 mixture of Ar, CO₂ and CF₄. Combining the information of the multiple CSC panels, the detectors achieve a very precise measurement of the muon track.

Despite their excellent spatial resolution, the wire chambers (DTs and CSCs) are limited in terms of time resolution by the fact that the charge needs to drift towards the anode wire and be collected before having the confirmation that a particle was detected as the drift volume is not used to develop avalanches. Indeed, the stronger electric field close to the anode wire triggers the avalanche and the gain of the detector. Due to the drift, the time resolution is thus limited at best to approximately 2 to 3 ns. In addition, even though the intrinsic time resolution of the tracking chambers is rather good compared to the 25 ns in between successive collisions, the processing time of the trigger system doesn't allow for very fast triggering as it provides a time precision of only 12.5 ns. Thus, detectors fully dedicated to timing measurement have been installed as a redundant system. These detectors are RPCs, also gaseous detectors but that use current induction instead of charge collection allowing for a time resolution of the order of 1.5 ns only. Theoretically, depending on the design used, RPCs could reach a time resolution of the order of 10 ps but in the context of LHC where bunch crossing happen every 25 ns, a time resolution of 1.5 ns is sufficient to accurately assign the right bunch crossing to each detected muon.

The 1056 RPCs equipping the CMS muon system both in the barrel and endcap regions and covering the pseudorapidity region $0 < |\eta| < 1.6$ are composed of two layers of RPC *gaps* as described in Figure 2.19. Each gap consists in two resistive electrodes made out of 2 mm thick Bakelite enclosing a 2 mm thick gas volume containing a 95.2/4.5/0.3 mixture of $C_2H_2F_4$, $i - C_4H_{10}$ and SF_6 . Due to this geometry, the electric field inside of a gap is homogeneous and linear at every point in the gas translating into a uniform development of avalanches in the gas volume as soon as a passing muon ionises the gas. The two gaps sandwich a readout copper strip plane. A negative voltage is applied on the outer electrodes, used as cathodes, and the inner electrodes, the anodes, are simply connected to the ground as well as the readout panel that picks up the current induced by the accumulated charge of the growing avalanches in one or both of the gas gaps. This OR system allows for a lower gain (i.e. a lower electric field) on both gaps to reach the maximal efficiency of such a detector.

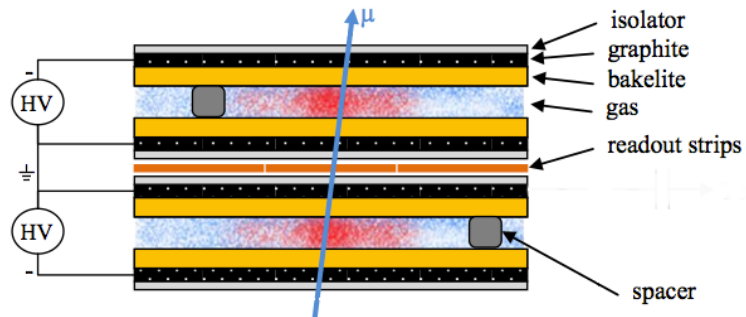


Figure 2.19: Double gap layout of CMS RPCs. Muons passing through the gas volumes will create electron-ion pairs by ionising the gas. this ionisation will immediately translate into a developing avalanche.

3

1313

1314

Muon Phase-II Upgrade

1315 The very first proton beam successfully circulated in the LHC in September 2008 directly followed
1316 by an incident leading to mechanical damage that would delay the LHC program for a year until
1317 November 2009, the very first collisions at a center-of-mass energy of 7 TeV taking place in March
1318 2010. The energy of the beam would be increased after a First Long Shutdown (LS1) starting early
1319 2013 after less than 3 years of data taking. Nevertheless, this first data taking period at only 7 TeV
1320 was sufficient to claim the discovery of a new particle compatible with the Higgs boson in July 2012.
1321 During the 2 years of shutdown, the upgrade of the accelerator allowed for several maintainances
1322 along the beam pipes, repair and consolidation of magnet connection and high-current splices. But
1323 not only the LHC was upgraded. Indeed, the experiments at the 4 collision points also took the
1324 advantage of this time to upgrade their system in prevision of the next LHC run (Run-II) until
1325 2018 and the Second Long Shutdown (LS2) as the luminosity and energy of the beam would be
1326 continuously increasing. By the end of Run-II, the luminosity will have reached twice its nominal
1327 value when the center-of-mass energy has already got close to its nominal value by reaching an
1328 historical 13 TeV for the first time in 2017.

1329 The next long shutdown will occur at the end of this year and will again be the occasion for sim-
1330 ilar maintenance and consolidation in prevision of Run-III and the future upgrade of LS3. Still, the
1331 main occupation of LS2 on LHC side will be the upgrade of LHC injectors. On the experiments side,
1332 LHCb and ALICE will, in a very tight schedule, implement major upgrades while ATLAS and CMS
1333 will wait until LS3 to upgrade their detectors in prevision of high luminosity *LHC-Phase-II*. ALICE
1334 main challenge is an upgrade of their apparatus to cope with the 50 kHz $Pb - Pb$ collisions. Simi-
1335 larly, LHCb will upgrade their frontend readout electronics to cope with the full 40 MHz collisions
1336 delivered by LHC. ATLAS will perform standard maintenance and CMS will focus on the urgent up-
1337 grade of the pixel detector and on the installation of new muon detectors in order to take profit of LS2
1338 time to mitigate the upgrade of detectors foreseen during LS3. Run-III will start in 2021 with the LHC
1339 at its nominal center-of-mass energy and will bring LHC-Phase-I to an end at the end of 2023. By
1340 then the luminosity will only increase to reach 2.5 times the nominal luminosity but during these 3
1341 years of run, the LHC will deliver as much integrated luminosity as what what brought during the al-

¹³⁴² most 7 years of both Run-I and II of data taking. Phase-I will end with an overall 300 fb^{-1} delivered.
¹³⁴³

¹³⁴⁴ 3.1 High Luminosity LHC and muon system requirements

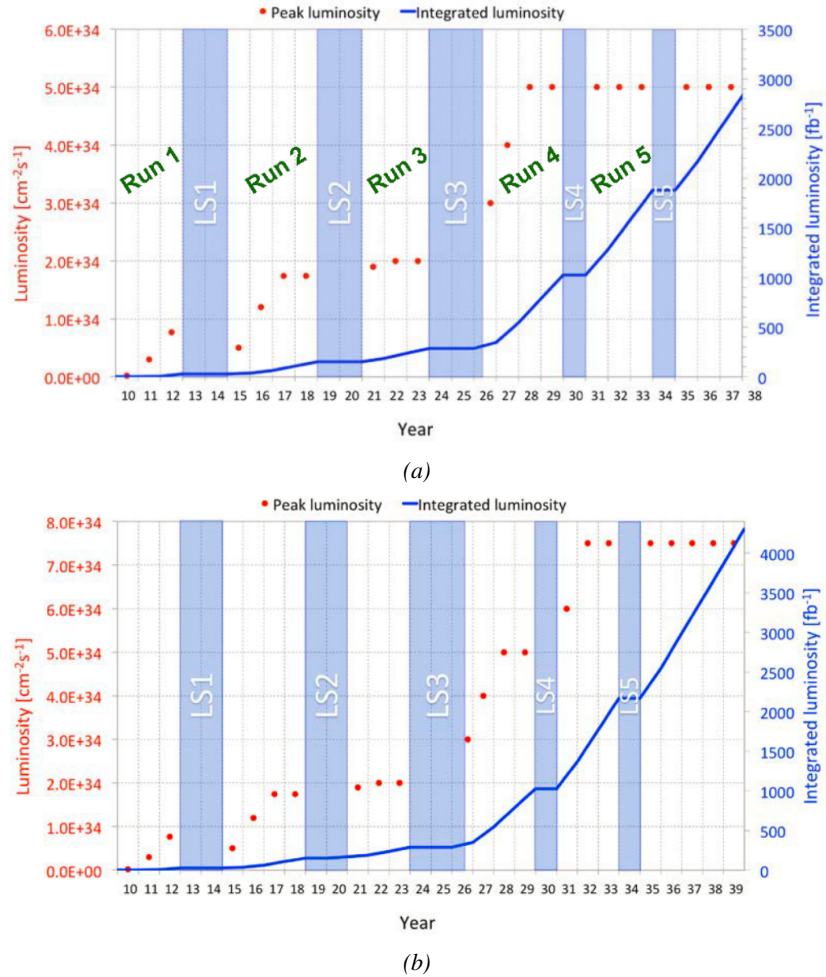


Figure 3.1: Detailed timeline projection of for LHC and HL-LHC operation until 2039 showing the evolution of the instantaneous and integrated luminosity as designed (Figure 3.1a) and in the ultimate case where the instantaneous luminosity is increased to $7.5 \times 10^{34} \text{ cm}^{-2}\text{s}^{-1}$ (Figure 3.1b) [20, 22].

¹³⁴⁵ After approximately 15 years of operation, the LHC will undergo a new series of upgrade during
¹³⁴⁶ the LS3 in order to boost its discovery potential as showed in Figure 3.1. This moment onward is
¹³⁴⁷ what is referred to HL-LHC or Phase-II. The goal is to aim for a luminosity 5 to 7 times stronger
¹³⁴⁸ than the nominal one trying to reach even 10 times this value if possible. Increasing the luminosity
¹³⁴⁹ means that the beam size at the collision points needs to be reduced to boost the number of collisions
¹³⁵⁰ per bunch crossing. For this purpose, new focusing and bending magnets, and collimators will be
¹³⁵¹ installed at the collision points as well as newly developed "crab cavities" that will tilt the particle

1352 bunched just prior to the collisions by giving them transverse momentum and thus increasing their
 1353 meeting area. In addition, the full proton injection line will be upgraded.

1354 Over its full lifetime, the HL-LHC is expected to deliver an outstanding integrated luminosity of
 1355 3000 fb^{-1} leading, in the case of Higgs studies to measuring the couplings of the boson to a precision
 1356 of 2 to 5% thanks to the estimated 15 millions of Higgs created every year providing a more precise
 1357 measurement of potential deviations from the theoretical predictions. SUSY and heavy gauge boson
 1358 studies would also see their mass range limits pushed away by at least 1 TeV and could lead to a new
 1359 breakthrough. SUSY is a particularly important topic as it could give an answer to why the Higgs
 1360 boson can stay so light while coupled to heavy particles by introducing the contributions of the super
 1361 partners on top of providing dark matter candidates. Finally, the increase of luminosity will give the
 1362 possibility to investigate "exotic" mode like for example the models introducing extra dimensions to
 1363 explain the hierarchy problem.

1364 On the experiments side, the pile-up (PU) will be increased up to 150 to 200 interactions per
 1365 bunch crossing in ATLAS and CMS, making necessary an strong upgrade of the trigger system and
 1366 of the inner trackers and of the calorimeters. Both ATLAS and CMS will also need to upgrade
 1367 the muon trigger at the level of the endcaps mainly focusing on the coverage near the beam line in
 1368 order to increase the detection acceptance and event selection. Moreover, the increased luminosity
 1369 will also lead to an increased background rate and a faster ageing of the detectors. This PhD work
 1370 takes place into this very specific context of muon detector consolidation and certification for the
 1371 HL-LHC period in order to provide the CMS experiment with robust new detectors and confirm that
 1372 the present system will survive through the next 20 years of HL-LHC.

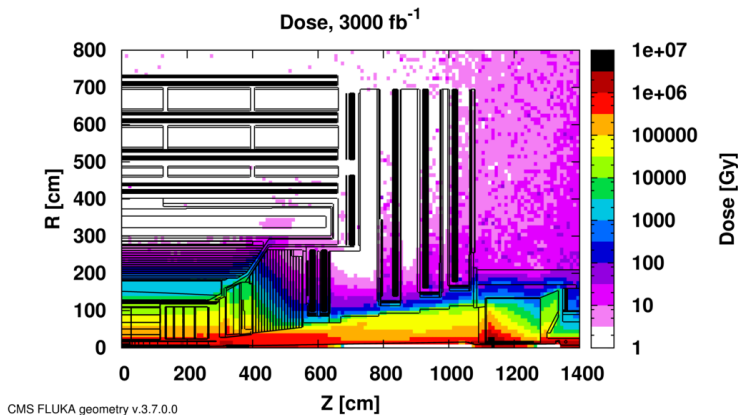


Figure 3.2: Absorbed dose in the CMS cavern after an integrated luminosity of 3000 fb^{-1} . Using the interaction point as reference, R is the transverse distance from the beamline and Z is the distance along the beamline.

1373 The end of 2018 will mark the beginning of LS2 and the start of Phase-II upgrade activities.
 1374 From the HL-LHC period onwards, i.e. past LS3, the performance degradation due to integrated
 1375 radiation as well as the average number of inelastic collisions per bunch crossing, seen as pile-up
 1376 into the detectors' readout that far exceeds this of the original LHC plans, will rise substantially and
 1377 become a major challenge for all of the LHC experiments, like CMS, that were forced to address
 1378 an upgrade program for Phase-II [23]. Dealing with the data from the muon detectors will force
 1379 to upgrade the detectors and electronics towards the most recent technologies. Simultaneously, this
 1380 will push new latency requirements onto the Level-1 trigger and the Data Acquisition (DAQ) that

will only be fulfilled by upgrading the system with electronics having deeper buffering and faster processing. Simulations of the expected distribution of absorbed dose in the CMS detector under HL-LHC conditions show, in Figure 3.2, that detectors placed close to the beam line will have to withstand high irradiation, the radiation dose being of the order of a few tens of Gy.

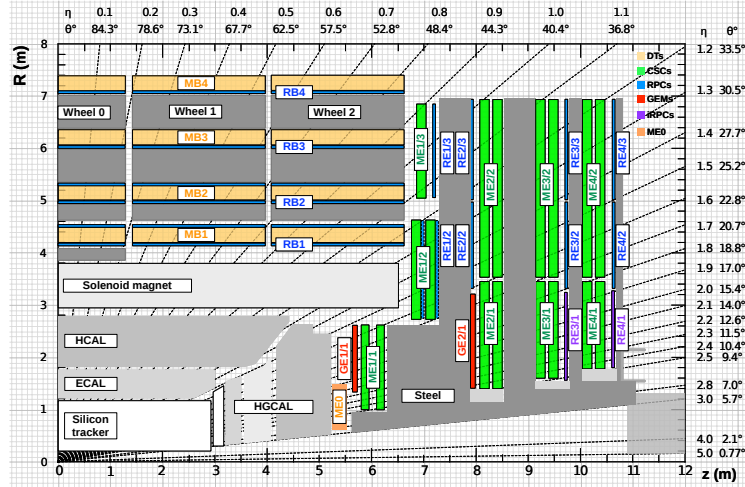


Figure 3.3: A quadrant of the muon system, showing DTs (yellow), RPCs (blue), and CSCs (green). The locations of new forward muon detectors for Phase-II are contained within the dashed box and indicated in red for GEM stations (ME0, GE1/1, and GE2/1) and dark blue for improved RPC (iRPC) stations (RE3/I and RE4/I).

The increase of irradiation close to the beam line will affect the background rate seen by the muon detectors in this area and tracking muons will prove to be difficult as this region is not yet equipped with all the detectors that were already foreseen for Phase-I. Improving this situation will come with the increase of hit numbers recorded along the particle track to reduce the ambiguity on muon versus background detection. Moreover, the measurement of small production cross-section and/or decay branching ratio processes, such as the Higgs boson coupling to charge leptons, and in particular to muons, or the $B_s \rightarrow \mu^+ \mu^-$ decay, is of major interest and specific upgrades in the forward regions of the detector will be required to maximize the physics acceptance to the largest possible solid angle.

To ensure proper trigger performance within the present coverage, the muon system will be completed with new chambers and the electronics of the present system will need to be upgraded to ensure an efficient triggering. Figure 3.3 shows the addition of Gas Electron Multiplier (GEM) and improved RPC (iRPC) in the pseudo-rapidity region $1.6 < |\eta| < 2.4$ to complete the redundancy of the already existing CSCs as originally scheduled in the CMS Technical Proposal [24]. A first step into this direction will be taken by installing GEMs on the first endcap disk in position GE1/1 during LS2, during which preparations for the future installation of more GEMs and RPCs will take place by installing the needed services. During the YETS following LS2, iRPCs will be installed on the third and fourth endcap disks in position RE3/I and RE4/I, and more GEMs will equip the second endcap in position GE2/1 and the inner layer, closest to the HCAL endcap called ME0 during LS3, finally completing the redundant coverage of the muon system and extending it a little by extending the reach to $|\eta| = 2.8$, the redundancy in the region $2.4 < |\eta| < 2.8$ being maintained by the 6 GEM layers contained in each ME0 detector that provide enough tracking points to efficiently reject

¹⁴⁰⁷ neutron-induced background.

¹⁴⁰⁸ Nevertheless, the region beyond $|\eta| > 2.8$ and extending to $|\eta| = 5.0$ only is covered by the
¹⁴⁰⁹ forward HCAL detectors and lack redundant muon detector coverage. Extensions of the tracker in
¹⁴¹⁰ the context of HL-LHC will increase its coverage up to $|\eta| = 4.0$ but the identification of muons and
¹⁴¹¹ measurement of their energy with reasonable precision only using the tracker is nearly impossible.
¹⁴¹² Thus, this increased tracker coverage range needs to be put in parallel with a matching muon detector
¹⁴¹³ and will open doors to multi-lepton final states in which leptons are likely to have a low transverse
¹⁴¹⁴ momentum and to be found near the beam line.

¹⁴¹⁵

¹⁴¹⁶ Finally, as the muon system is composed only of gaseous detectors, strong environmental con-
¹⁴¹⁷cerns have risen over the last years as the European directives will restrict the use of fluorine based
¹⁴¹⁸gas mixtures. Both the CSC and RPC subsystems, using CF_4 , $C_2H_2F_4$, or SF_6 , will need to adapt
¹⁴¹⁹their working gas in order to strongly reduce the greenhouse potential of the mixtures released into
¹⁴²⁰the atmosphere due to gas leaks.

¹⁴²¹ 3.2 Necessity for improved electronics

¹⁴²² Drift Tubes and Cathode Strip Chambers are important components used to identify and measure
¹⁴²³muons, especially thanks to their spatial resolution of the order of $100\text{ }\mu\text{m}$. Nevertheless, the lumi-
¹⁴²⁴nosity and irradiation during HL-LHC will cause serious event loss and ageing on the electronics of
¹⁴²⁵these subsystems that will comprise the triggering and data transferring needs of CMS. Thus, elec-
¹⁴²⁶tronics upgrade are foreseen to address these expected problems. While only the RPCs' electronic
¹⁴²⁷system is able to operate under Phase-II requirements, DTs and CSCs will need to improve their
¹⁴²⁸trigger accept rate and latency to ensure that Level-1 trigger threshold stays at the same level [25],
¹⁴²⁹and DAQ data transfer rate, that respectively need to achieve a minimum of 500 kHz , get down to
¹⁴³⁰ $12.5\text{ }\mu\text{s}$ [26], and increase to 1082 Gbit/s DTs and to 1026 Gbit/s for CSCs. As of today, the Level-
¹⁴³¹1 trigger accept rate of DTs doesn't reach 300 kHz while this of CSCs is below 250 kHz but the
¹⁴³²foreseen upgrades are expected to increase the rate way beyond the requirement in the of DTs and
¹⁴³³up to 4 MHz for CSCs [23].

¹⁴³⁴ The first version of Minicrate electronics (MiC1) used by DTs don't allow for high enough
¹⁴³⁵trigger rate. In addition to this problem, it was showed that these electronics contain components
¹⁴³⁶that are not radiation hard enough to sustain HL-LHC conditions and thus, a too large number of
¹⁴³⁷channels may fail due to radiations. Considering the most optimistic scenario, at least 19% of the
¹⁴³⁸channels could have failed by LS4, as explicitated in Figure 3.4, far before the end of the HL-LHC
¹⁴³⁹campain. The MiC1 will be replaced on each detector by an improved version referred to as MiC2
¹⁴⁴⁰while front-end electronics and high-voltage modules will not need any replacement. On the other
¹⁴⁴¹hand, CSCs showed that there electronics would be able to live through the 10 years of Phase-II but
¹⁴⁴²the limited buffer depth might cause memory overflows and readout inefficiencies with a fraction
¹⁴⁴³of event loss ranging from 5 to more than 10% at an instantaneous luminosity similar to which of
¹⁴⁴⁴HL-LHC depending on the expected background, as showed on Figure 3.5 through the different
¹⁴⁴⁵detector positions. Thus the replacement of CSCs' cathode front-end boards (CFEBs) by digital
¹⁴⁴⁶ones, DCFEBS, with deeper buffer would permit to make event loss negligible and satisfy HL-LHC
¹⁴⁴⁷requirements [23].

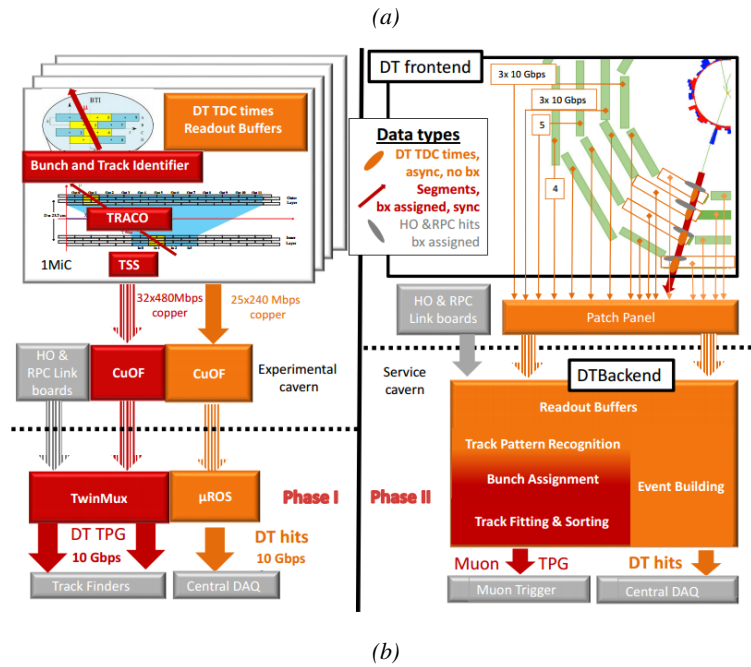
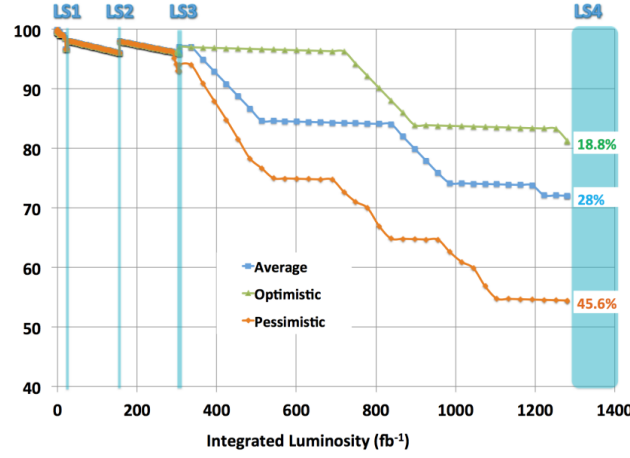


Figure 3.4: Figure 3.4a: Extrapolated fraction of failing channels of the present DT MiC1 electronics as a function of the integrated luminosity for different scenari until LS4. Figure 3.4b: Comparison of the current (left) and upgraded (right) DT data processing. So far, the data is sent to service cavern of CMS facility via copper-to-optical-fiber translators (CuOF) by each MiC1. There, data including RPCs and outer hadron calorimeter is combined into trigger primitives (TPG) and transmitted by the TwinMux system to CMS Track Finder. The time-to-digital converter (TDC) data is collected and sent to the CMS data acquisition system (DAQ) by the micro read-out server (μ ROS). After the upgrade, the TDC data will be sent via optical links to a patch panel inside the experimental cavern by each MiC2, and transferred to the back-end, where triggering and event building will be performed.

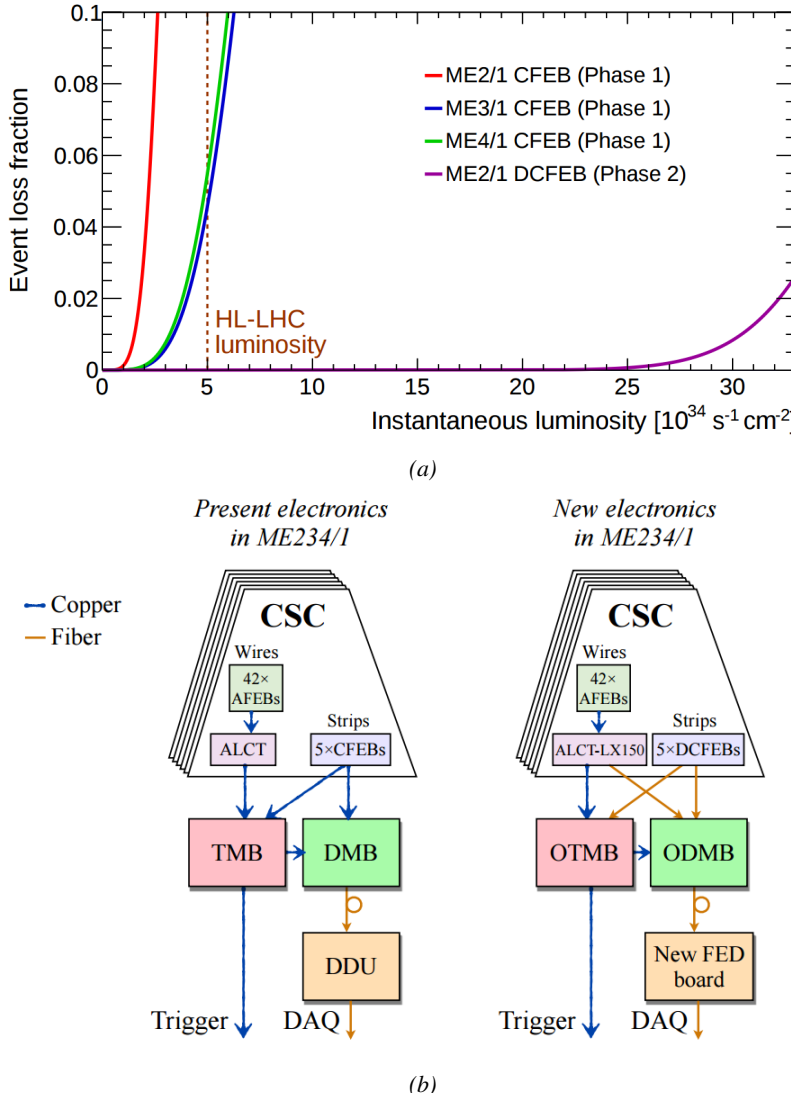


Figure 3.5: Figure 3.5a: The event loss fractions as a function of the instantaneous luminosity is compared for CFEBs (Phase-1) and DCFEBs (Phase-II) at different CSC locations. HL-LHC luminosity is marked with the dashed brown line. Figure 3.5b: Comparison of the current (left) and upgraded (right) CSC data processing. A part of the connections in between ALCTs and DCFEBs, and the trigger mother boards (TMBs) and data acquisition mother boards (DMBs) will be upgraded toward optical data transfer. The detector dependent units (DDUs) used as interface in between CSCs' front-end electronics and the CMS DAQ will be replaced by new FED boards.

All these new DT and CSC electronics will be connected to the trigger electronics via optical links to ensure a faster communication. The main change will come from the new DT minicrate modules which will not anymore be responsible for trigger and event building logic which will be transferred to the back-end electronics instead located in the service cavern via the patch pannels to which the Time-to-Digital Converter (TDC) data will be sent. The trigger and data transfer logic will barely change for CSCs. The existing copper cable connections of cathode and anode FEBs (CFEBs,

1454 and AFEBs which data is transmitted through the ALCTs) toward the trigger and data mother boards
 1455 (TMBs and DMBs) will simply be replaced by optical fibers and the TMBs and DMBs upgraded with
 1456 optical versions (OTMBS and ODMBs). As a new feature, the full anode wire data from ALCTs
 1457 will be sent to the ODMBs causing a lack of FPGA memory resources in these ALCT boards that
 1458 will thus need replacement.

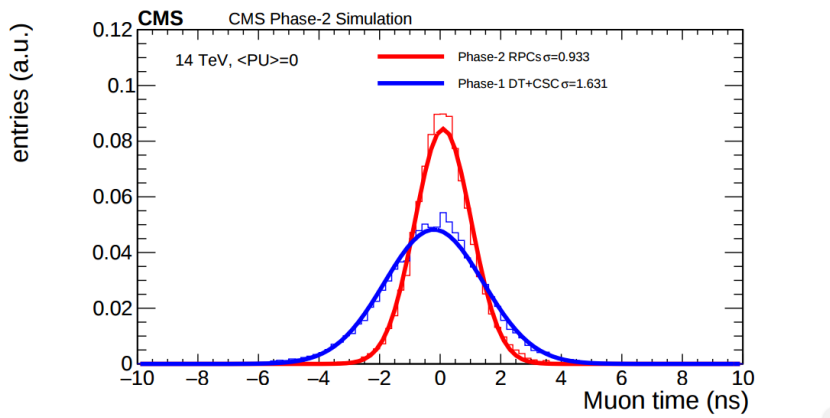


Figure 3.6: Comparison of the simulated time residuals in between reconstructed and true muon times without (blue) and with (red) the upgraded RPC link system.

1459 The upgrade on the side of Resistive Plate Chambers will then not come from their on-board
 1460 electronics but from the Link System located in the service cavern of CMS and that connects the
 1461 front-end electronics data of RPCs into CMS trigger processors. The main motivation for such an
 1462 upgrade is that the electronic board composing the link system are built using obsolete components
 1463 and weak components that can easily suffer from the electromagnetic noise. These components may
 1464 be the source of failing channels throughout Phase-II. Moreover, these link boards were originally
 1465 designed only to match RPC digitized signals with the corresponding bunch crossing. Due to this
 1466 feature, the time resolution of the full RPC chain is thus limited to 25 ns and does not exploit the full
 1467 time resolution of the detectors. This would make the synchronization of the RPC system easier and
 1468 allow to have a finer offline background removal within the 25 ns in between bunch crossings thanks
 1469 to the order of magnitude gained in terms of time resolution.

1470 Upgrading RPC link system will require the installation of 1376 new link boards and 216 control
 1471 boards. The new boards will make use of the recent progress made with fast FPGAs and will be a
 1472 great improvement to the ASICs formerly used as they will be able to process signals from several
 1473 detectors in parallel. The benefit from using the full RPC time resolution thanks to the upgraded
 1474 link system can be seen through Figure 3.6 where the resolution of the RPC system itself is better
 1475 than that of DTs and CSCs that was used until now.

1476 **3.3 New detectors and increased acceptance**

1477 In the present muon system, the redundancy was assured by RPCs used for their good timing per-
 1478 formances. The extension of the muon system towards higher pseudo-rapidity in order to complete
 1479 the redundancy in this very region and to contribute to the precision of muon momentum measure-
 1480 ments will require muon chambers with a spatial resolution less or comparable to the contribution

¹⁴⁸¹ muon of multiple scattering through the detector volume [21]. Most of the plausible physics is
¹⁴⁸² covered only considering muons with $p_T < 100$ GeV thus, in order to match CMS requirements,
¹⁴⁸³ a spatial resolution of $\mathcal{O}(\text{few mm})$ will be necessary for the proposed new RPC stations while the
¹⁴⁸⁴ GEMs will need a resolution better than 1 mm, as showed by the simulation in Figure 3.7.

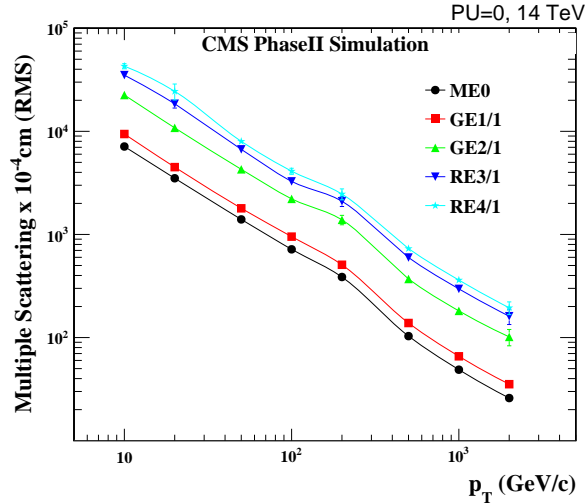


Figure 3.7: RMS of the multiple scattering displacement as a function of muon p_T for the proposed forward muon stations. All of the electromagnetic processes such as bremsstrahlung and magnetic field effect are included in the simulation.

¹⁴⁸⁵ 3.3.1 Improved forward resistive plate chambers

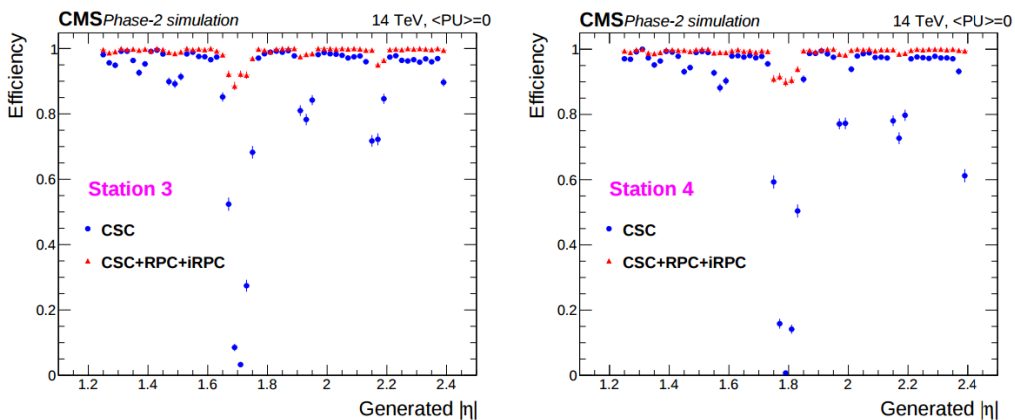


Figure 3.8: Simulation of the impact of RPC hit inclusion onto the local trigger primitive efficiency in station 3 (left) and station 4 (right). The contribution of iRPC starts above $|\eta| = 1.8$.

¹⁴⁸⁶ Figure 3.3 shows that the iRPCs that will equip the third and fourth endcap disks in position RE3/1
¹⁴⁸⁷ and RE4/1 will finally be the partners of the CSCs in position ME3/1 and ME4/1 and complete
¹⁴⁸⁸ Phase-I plans but bringing the needed upgrades in the scope of Phase-II as the older chambers are

not suitable to equip the forward region of CMS due to HL-LHC rates and charge deposition. By completing the redundancy, more track along the muon trajectory will be available and the lever arm will be improved. The benefits from extending the redundancy of the muon system with iRPCs to the forward most region is showed in Figure 3.8 in which the trigger efficiency is showed with and without RPCs in which it is possible to see that the efficiency of CMS trigger with the complete redundancy is improved is above 95% in the region $|\eta| > 1.8$ as the iRPCs help filling the holes in the CSC system.

1496

The detectors that will be installed in the coming years will be similar to the already existing RPC system. 18 of the new chambers, each spanning 20° in φ around the beam axis with 96 radially oriented trapezoidal read-out strips, will cover each muon endcap disk leading to the production of 72 iRPCs. The main difference with the old RPC chambers is that these detectors will not have readout strips segmented in η as by using fast front-end electronics the strips will be read-out on both sides allowing for a radial spatial resolution of the order of 2 cm in order to contribute to the better reconstruction of muon in the forward region where the bending of muons by the magnetic field is low. This is motivated by the fact that, in the case a η segmentation was used, at least 5 pseudorapidity partitions would have been necessary to reach the minimal radial spatial resolution (≈ 20 cm). Having only one strip read-out from both along the chamber reduces by 60% the total number of channels and the necessary cabling and allows for a better spatial resolution. The strip pitch will range from 6.0 mm (5.9 mm) on the high pseudo-rapidity end to 12.3 mm (10.9 mm) on the low one on position RE3/1 (RE4/1). The spatial resolution in the direction perpendicular to the strips should reach approximately 3 mm, better than the minimal needed resolution (Figure 3.7), and the overall time resolution of the new installation will be equally 1.5 ns, as for the present due to the same link system being used.

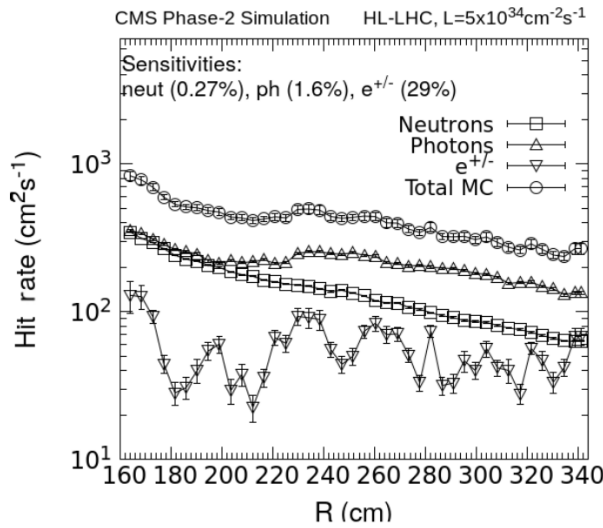


Figure 3.9: Expected hit rate due to neutrons, photons, electrons and positrons at HL-HLC instantaneous luminosity of $5 \times 10^{34} \text{ cm}^{-2} \text{ s}^{-1}$ in RE3/1 chambers covering the region $1527 \text{ mm} < R < 3192 \text{ mm}$. In the upper part of the figure the sensitivities of RPCs used in the simulation for each particle are reported. The hit rates are expected to be similar in RE4/1 covering the region $1770 \text{ mm} < R < 3140 \text{ mm}$.

Nevertheless, having only a single strip instead of pseudo-rapidity segmentation will increase the probability of double hits in the same channel. This probability was estimated to be low enough as it shouldn't exceed 0.6%. This estimation was made assuming an average hit rate per unit area of 500 Hz/cm^2 in the iRPCs (see Figure 3.9), a cluster size (average number of strips fired per muon) of 2, a strip active area of $158.4 \times 0.87 \text{ cm}^2$ and a safety factor 3 leading to an estimated rate per strip of 380 kHz corresponding to an average time interval of 2600 ns in between 2 consecutive hits. The time for a signal to go through the full strip length is about 10 ns to which can be added 1 ns of dead time and 2 TDC clock cycles of 2.5 ns for a minimal time interval of 16 ns necessary to avoid ambiguities. The probability of having ambiguous double hits in a strip is then the ratio in between this minimal time interval in between 2 consecutive hits and the average time interval estimated from the rate the detectors are subjected to.

The instantaneous luminosity at HL-LHC being very high, the rates at the level of the new chambers needed to be simulated in order to understand the necessary requirements for these detectors. The simulated results for different background components (neutrons, photons, electrons and positrons) are showed in Figure 3.9 assuming known sensitivities to these particles. It is showed that in the hottest area, the rates could increase beyond 700 Hz/cm^2 . Thus, taking into account a safety factor of about 3, it was decided that improved RPCs should at least be certified for rates reaching 2 kHz/cm² which would be achieved thanks to several improvements on the design and on the electronics. The detectors design will be based on the existing RPC design as they will be double gaps. Similarly to the existing RPC system, the electrode material will be HPL although the thickness of the electrodes and of the gas gap will be reduced to 1.4 mm as a thinner gas gap leads to a decrease of deposited charge per avalanche as showed in Figure 3.10. The smaller the gas gap, the more the detector becomes sensitive to gap non-uniformities across the electrode planes making a gap of 1.4 mm a good compromise in between these two competing factors.

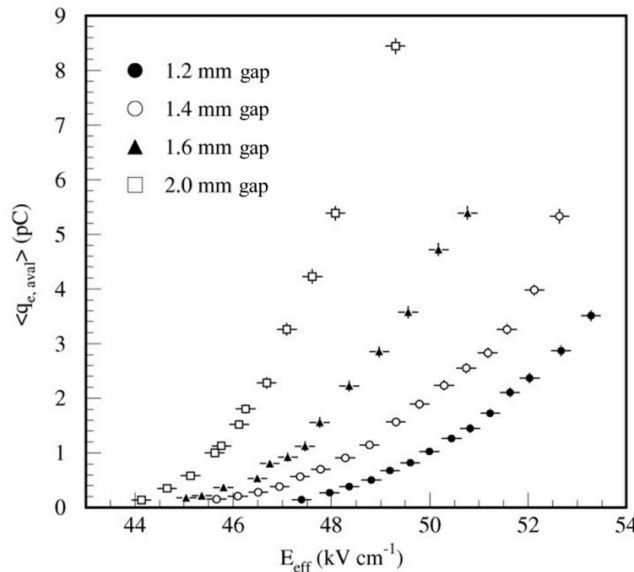


Figure 3.10: Measured average charge per avalanche as a function of the effective electric field for different gas gap thickness in double gap RPCs using HPL electrodes.

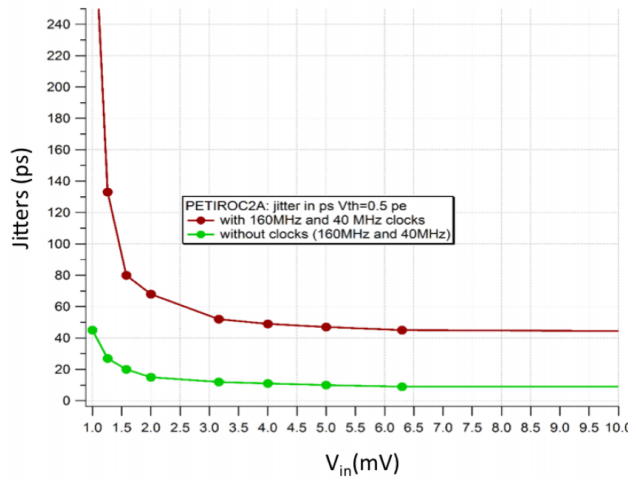


Figure 3.11: The PETIROC time jitter as a function of the input signal amplitude, measured with and without internal clocks.

1537 A lower charge deposition inside of the detector volume means a slower ageing and a longer life-
 1538 time for detectors subjected to high irradiation. But, in order to take advantage of the lower detector
 1539 gain, more sensitive electronics are required so that the part of gain that was formerly done in the gas
 1540 volume can be moved to the electronics. Achieving this with the technology developed more than
 1541 10 years ago for the present system is not possible as the signal over noise ratio of such electronics
 1542 doesn't allow to detect charges as low as 10 fC. Moreover, the new front-end electronics will need
 1543 to be radiation hard to survive to more than 10 years of HL-LHC conditions. The new technology
 1544 that has been chosen is based on the PETIROC ASIC manufactured by OMEGA and is a 64-channel
 1545 ASIC called CMS RPCROC on which the original SiGe technology will be replaced by CMOS to
 1546 increase its radiation hardness while keeping fast pre-amplification and discrimination with a very
 1547 low jitter that can reach less than 20 ps if no internal clock is used, as can be seen from Figure 3.11.
 1548 The ASIC is associated with an FPGA which purpose is to measure time thanks to a TDC with a
 1549 time resolution of 50-100 ps developed by Tsinghua University and that will provide a measurement
 1550 of the signal position along the strip with a precision of a few cm by measuring the signal timing
 1551 on both ends of the strips. In order to read-out all 96 strips, 3 ASICs and 3 TDCs, each having 64
 1552 channels, are hosted on a front-end board attached to the chamber.

1553
 1554 [Wait for the analysis of 2018 GIF++ data to add interesting information about the time and
 1555 spatial resolution measured during test beam periods.]
 1556

1557 3.3.2 Gas electron multipliers

1558 In the region closer to the interaction point where the spatial resolution is requested to be better
 1559 than 1 mm for the new detectors (at least for GE1/1 and ME0, GE2/1 being in the same order of
 1560 requested spatial resolution than the new iRPCs that will equip the third and fourth endcaps), the
 1561 choice has been made to use triple GEMs, micro pattern gaseous detectors, in the place of RPCs.
 1562 The GE1/1 project had been the first to be approved and demonstrators had been installed in CMS

already during LS1. The rest of the detectors will be installed during LS2 while the GE2/1 and ME0 projects are still under development. ME0, GE1/1 and GE2/1 will be installed respectively next to the HCAL endcap, on the first and on the second muon endcap disks as can be seen from Figure 3.3.

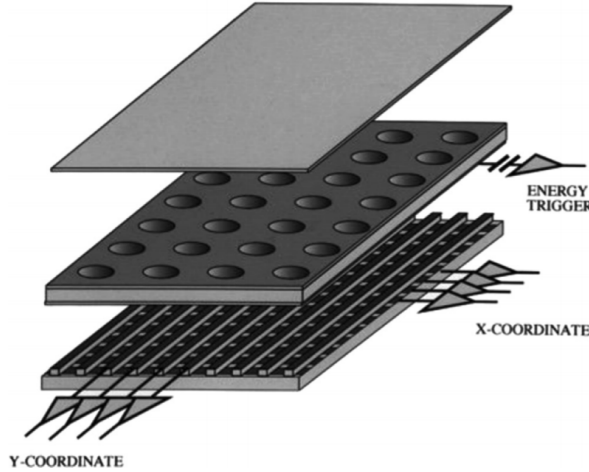


Figure 3.12: Schematics of a GEM showing the cathode on top, the GEM foil separating the gas volume into the drift region, in between the cathode and foil, and the induction region, in between the GEM foil and the anode, and the anode on which a 2D read-out is installed. A negative voltage is applied on the cathode while the anode is connected to the ground.

Gas Electron multipliers are gaseous detectors [27] which gas volume is confined in between 2 planar electrodes, the anode serving as read-out panel. The gas volume is divided in 2 or more regions by a single or multiple *GEM foils* as showed in Figure 3.12. These foils are very thin, of the order of a few tens of μm , and are pierced with holes as can be seen in Figure 3.13. Both surfaces of the GEM foils are clad with copper in order to apply a strong electric field in between each side that will generate very strong potentials in the holes. The gas region contained in between the cathode and the GEM foil is called the drift region as the electric field is not strong enough to cause avalanches and thus start an amplification. The primary electrons drift toward the foil and are accelerated and amplify by the very high potential within the holes, as showed in Figure 3.13. Then the electrons reach the second drift region in which they will induce signal on the read-out located on the anode. By restraining the amplification process at the level of the holes, the electrons can stay in a very confined space and thus induce a very localized current, providing the GEMs with a very good spatial resolution.

In order to achieve a stronger amplification, the amplification process can be repeated several times in a row. The GEMs that will be used in CMS are triple GEM detectors operated with a 70/30 gas mixture of Ar/CO_2 . They contain 3 GEM foils and thus 3 electron amplifications, as can be seen in Figure 3.14. The GEM foils used in CMS are 50 μm foils clad with 5 μm of copper on each side. The foils are pierced with double-canonical holes which inner and outer diameters are respectively 50 and 70 μm which are placed 140 μm from each other in an hexagonal pattern, as showed in Figure 3.13. These detectors have a time resolution better than 10 ns and reach very good spatial resolutions of less than 300 μm with an angular precision of less than 200 μrad .

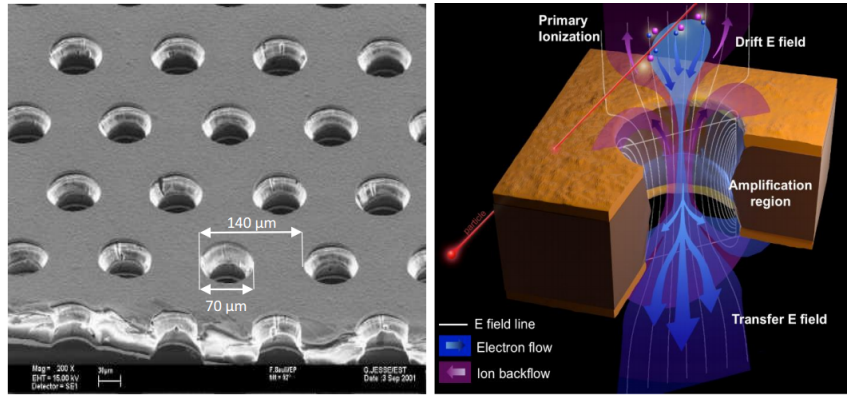


Figure 3.13: Left: Picture of a CMS GEM foil provided by a scanning electron microscope. Right: Representation of the electric field lines in a GEM hole and of the amplification that electrons and ions undergo in the hole's volume due to the very intense electric field.

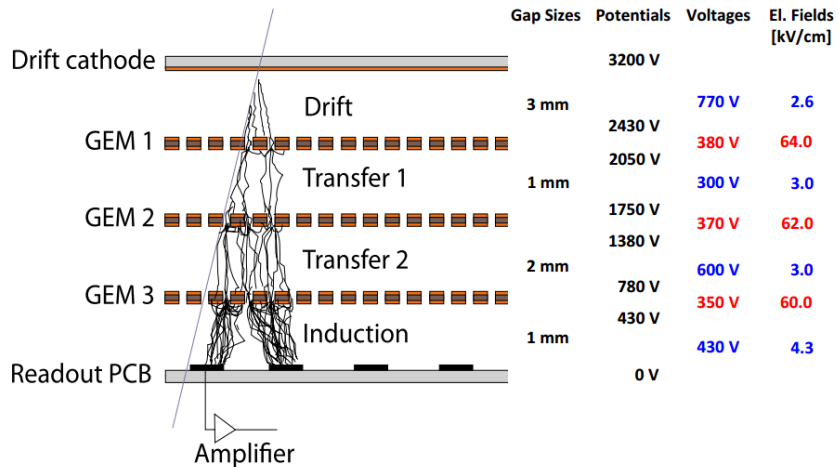


Figure 3.14: Schematic representation of CMS triple GEMs. The gas volume is divided into 4 areas. The drift area is the region where the primary electrons are created before being amplified a first time while passing through the first GEM foil. Then the process of drift and amplification is repeated twice in following two transfer areas and GEM foils. Finally, the charges have been amplified enough to induce current in the read-out strips while in the last drift area. The dimensions, potentials and electric fields are provided.

1587 The GEM Upgrade is divided into 3 subsystems as GE1/1 was the first approved project [28]
1588 and that the detectors will already be installed during LS2. GE2/1 and ME0, on the other hand,
1589 will profit of the R&D knowledge and skills developed for GE1/1 while the requirements for each
1590 subsystem are different as they are not placed at the same distance from the interaction point. In this
1591 very forward region, a different position with respect to the center of the detector can change dra-
1592 matically the conditions in which the detectors will have to be operated. In terms of rate capability,
1593 GE2/1, which is the furthest, is required to withstand 2.1 kHz/cm² while GE1/1 needs to be better
1594 than 10 kHz/cm² and ME0, better than 150 kHz/cm². In terms of ageing with respect to charge
1595 deposition, ME0 needs to be certified to 840 mC/cm², GE1/1 to 200 mC/cm² and GE2/1 only to

1596 9 mC/cm². All 3 detectors need to have a time resolution better than 10 ns and an angular resolution
 1597 better than 500 µrad.

1598 Adding the GEMs into the forward region of the muon system will allow to strongly enhance
 1599 the Level-1 Trigger performance by reducing the inefficiency regions and the trigger rate as showed
 1600 in Figure 3.15. Moreover, benefiting from the good spatial and angular resolution of the GEMs,
 1601 the precision into the muon measurement will also be greatly improved by the addition of GEMs as can
 1602 be seen from the simulation presented in Figure 3.16.

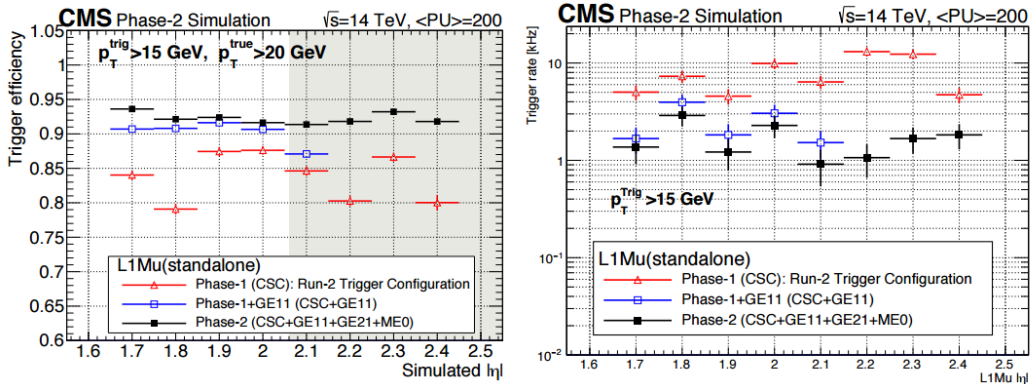


Figure 3.15: Simulated efficiency and rate of the standalone Level-1 muon trigger using tracks reconstructed in CSCs and all GEM stations compared with Phase-I values in the case where only CSCs are used or CSCs+GE1/1. The zones of inefficiency of the CSC subsystem are compensated by the addition of GEMs during Phase-II and the trigger rates is kept from increasing due to the high luminosity.

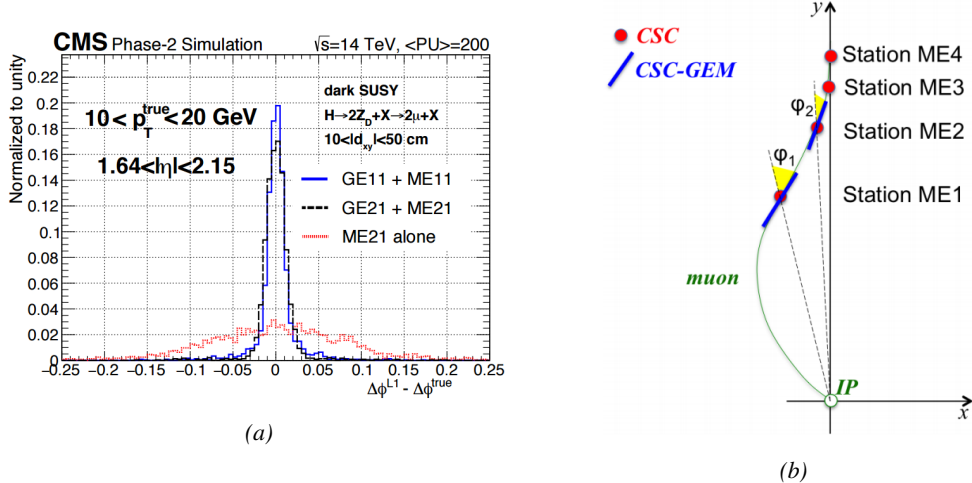


Figure 3.16: Figure 3.16a: Simulated resolution of the muon direction measurement $\Delta\phi$ with Phase-II conditions. In the second endcap station, the resolution is compared in the case of CSCs (ME2/1) alone and CSCs+GEMs (GE2/1+ME2/1) while a similar resolution measurement is given in the case of the first station (GE1/1+ME1/1). Figure 3.16b: The addition of GEM detectors on stations 1 and 2 (ME0 is considered to contribute to station station 1) as redundant system to CSCs allows to improve the muon momentum improvement through a more accurate measurement of the local bending angles ϕ_1 and ϕ_2 .

¹⁶⁰³ **3.3.3 Installation schedule**

¹⁶⁰⁴ **3.4 Implications of the different upgrades on the Level-1 Trig-**
¹⁶⁰⁵ **ger. Improvement of physics performance.**

¹⁶⁰⁶ **3.5 Ecofriendly gas studies**

¹⁶⁰⁷ **3.5.1 Status of the studies and potential candidates**

¹⁶⁰⁸ **3.5.2 Implications in case of no suitable ecofriendly mixture**

4

1609

1610

Physics of Resistive plate chambers

1611 A Resistive Plate Chamber (RPC) is a gaseous detector using the same physical processes described
1612 in Chapter 3. It has been developed in 1981 by Santonico and Cardarelli [29], under the name of
1613 *Resistive Plate Counter*, as an alternative to the local-discharge spark counters proposed in 1978
1614 by Pestov and Fedotovich [30, 31]. Working with spark chambers implied using high-pressure gas
1615 and high mechanical precision which the RPC simplified by formerly using a gas mixture of argon
1616 and butane flowed at atmospheric pressure and a constant and uniform electric field propagated
1617 in between two parallel electrode plates. Moreover, a significant increase in rate capability was
1618 introduced by the use of electrode plate material with high bulk resistivity, preventing the discharge
1619 from growing throughout the whole gas gap. Indeed, the effect of using resistive electrodes is that
1620 the constant electric field is locally canceled out by the development of the discharge, limiting its
1621 growth.

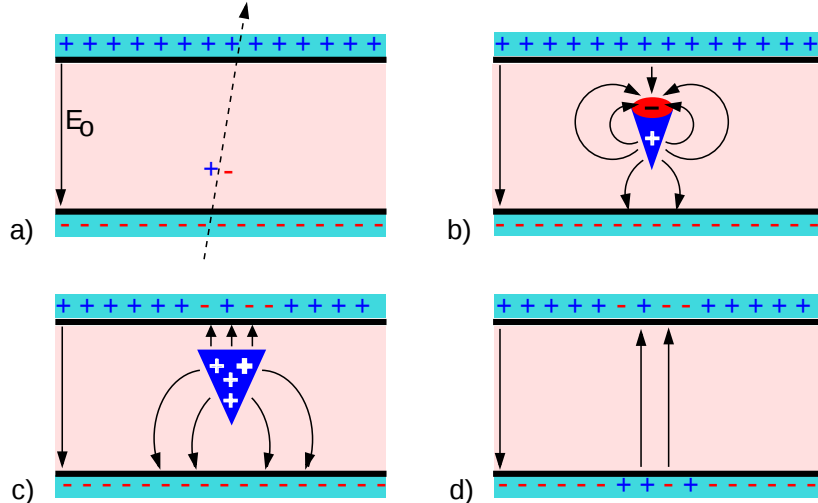
1622 Through its development history, different operating modes [32–34] and new detector designs [35–
1623 37] have been discovered, leading to further improvement of the rate capability of such a detector.
1624 Moreover, the addition of SF_6 into the gas mix improved the stability of operation of the RPC [38,
1625 39].

1626 The low developing costs and easily achievable large detection areas offered by RPCs, as well as
1627 the wide range of possible designs, made them a natural choice to as muon chambers and/or trigger
1628 detectors in multipurpose experiments such as CMS [21] or ATLAS [40], time-of-flight detectors in
1629 ALICE [41], calorimeter with CALICE [42] or even detectors for volcanic muography with ToMu-
1630 Vol [43].

1631 4.1 Principle

1632 RPCs are ionisation detectors composed of two parallel resistive plate electrodes in between which
1633 a constant electric field is set. The space in between the electrodes, referred as *gap*, is filled with a
1634 dense gas that is used to generate primary ionization into the gas volume. The free charge carriers
1635 (electrons and cations) created by the ionization of the gas molecules are then accelerated towards

1636 the electrodes by the electric field, as shown in Figure 4.1 [44].



1637 *Figure 4.1: Different phases of the avalanche development in the RPC gas volume subjected to a constant*
 1638 *electric field E_0 . a) An avalanche is initiated by the primary ionisation caused by the passage of a charged*
 1639 *particle through the gas volume. b) Due to its growing size, the avalanche starts to locally influence the electric*
 1640 *field. c) The electrons, lighter than the cations reach the anode first. d) The ions reach the cathode. While*
 1641 *the charges have not recombined, the electric field in the small region around the avalanche stays affected and*
 1642 *locally blind the detector.*

1643 RPCs being passive detectors, a current on pick-up copper read-out placed outside of the gas
 1644 volume is induced by the charge accumulation during the growth of the avalanche. As a result,
 1645 the time resolution of the detector is substantially increased as the output signal is generated while
 1646 the electrons are still in movement. The advantage of a constant electric field, over multi-wire
 1647 proportional chambers, is that the electrons are being fully accelerated from the moment charge
 1648 carriers are freed and feel the full strength of the electric field that doesn't depend on the distance to
 1649 the readout and that the output signal doesn't need for the electrons to be physically collected.

1644 The typical gas mixture RPCs are operated with is generally composed of 3 gas compounds.

- 1645 • Tetrafluoroethane ($C_2F_4H_2$), also referred to as *Freon*, is the principal compound of the RPC
 1646 gas mixtures, with a typical fraction above 90%. It is used for it's high effective Townsend
 1647 coefficient and the great average fast charge that allows to operate the detector with a high
 1648 threshold with respect to argon, for example, that has similar effective Townsend coefficient
 1649 but suffers from a lower fast charge. To operate with similar conditions, argon would require a
 1650 higher electric field leading to a higher fraction of streamers, thus limiting the rate capability
 1651 of the detector [45].
- 1652 • Isobutane (i- C_4H_{10}), only present in a few percent in the gas mixtures, is used for its UV
 1653 quenching properties [46] helping to prevent streamers due to UV photon emission during the
 1654 avalanche growth.
- 1655 • Sulfur hexafluoride, (SF_6), referred to simply as *SF6*, is used in very little quantities for its
 1656 high electronegativity. Excess of electrons are being absorbed by the compound and streamers

are suppressed [39]. Nevertheless, a fraction of SF_6 higher than 1% will not bring any extra benefit in terms of streamer cancelation power but will lead to higher operating voltage [38], as can be understood through Figure 4.2.

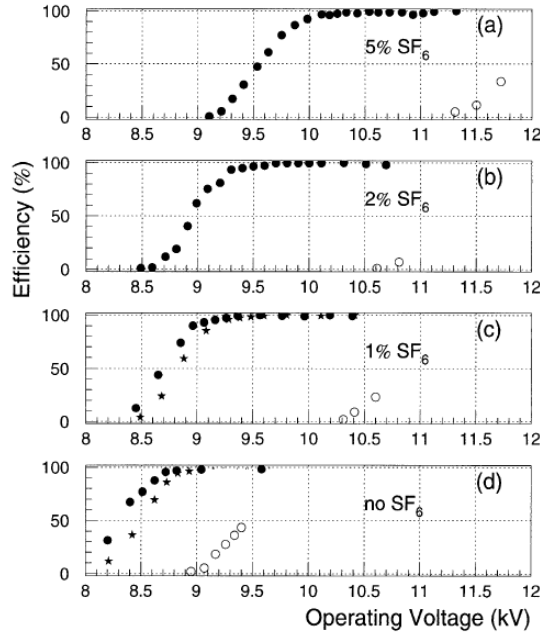


Figure 4.2: Effeciency (circles and stars with 30 mV and 100 mV thresholds respectively) and streamer probability (opened circles) as function of the operating voltatge of a 2 mm single gap HPL RPC flushed with a gas mixture containing (a) 5%, (b) 2%, (c) 1% and (d) no SF_6 [38].

After an avalanche developed in the gas, a time long compared to the development of a discharge is needed to recombine the charge carriers in the electrode material due to their resistivity. This property has the advantage of affecting the local electric field and avoiding sparks in the detector but, on the other hand, the rate capability is intrinsically limited by the time constant τ_{RPC} of the detector. Using a quasi-static approximation of Maxwell's equations for weakly conducting media, it can be shown that the time constant τ_{RPC} necessary to the charge recombination at the interface in between the electrode and the gas volume is given by the Formula 4.1 [47].

$$\tau_{RPC} = \frac{\epsilon_{electrode} + \epsilon_{gas}}{\sigma_{electrode} + \sigma_{gas}} \quad (4.1)$$

A gas can be assimilated to vacuum, leading to $\epsilon_{gas} = \epsilon_0$ and $\sigma_{gas} = 0$, and the electrodes permittivity and conductivity can be written as $\epsilon_{electrode} = \epsilon_r \epsilon_0$ and $\sigma_{electrode} = 1/\rho_{electrode}$, showing the strong dependence of the time constant to the electrodes resistivity in Formula 4.2.

$$\tau_{RPC} = (\epsilon_r + 1)\epsilon_0 \times \rho_{electrode} \quad (4.2)$$

Very few materials with a low enough resistivity exist in nature. The resistivity targeted to build RPCs ranges from 10^9 to $10^{12} \Omega \cdot \text{cm}$. The most common RPC electrode materials are displayed in Table 4.1. When the doped glass and ceramics can offer short time constants of the order of 1 ms,

¹⁶⁷³ the developing cost of such materials is quite high due to the very low demand. Thus, High-pressure
¹⁶⁷⁴ laminate (HPL) is often the choice for high rate experiments using very large RPC detection areas.
¹⁶⁷⁵ Other experiments working at cosmic muon fluxes can safely operate with ordinary float glass.

Material	$\rho_{electrode}$ ($\Omega \cdot \text{cm}$)	ϵ_r	τ_{RPC} (ms)
Float glass	10^{12}	~ 7	~ 700
High-pressure laminate	10^{10} to 10^{12}	~ 6	~ 6 to 600
Doped glass (LR S)	10^9 to 10^{11}	~ 10	~ 1 to 100
Doped ceramics (SiN/SiC)	10^9	~ 8.5	~ 1
Doped ceramics (Ferrite)	10^8 to 10^{12}	~ 20	~ 0.2 to 2000

Table 4.1: Properties of the most used electrode materials for RPCs.

¹⁶⁷⁶ 4.1.1 Electron drift velocity

¹⁶⁷⁷ Talk about the electron drift velocity and mention the time resolution of RPCs.

¹⁶⁷⁸ 4.2 Rate capability and time resolution of Resistive Plate Chambers

¹⁶⁸⁰ As already previously discussed, the electrode material plays a key role in the max intrinsic rate
¹⁶⁸¹ capability of RPCs. R&D is being done to develop at always cheaper costs material with lower
¹⁶⁸² resistivity. Nevertheless, the amount of charge released, i.e. the size of the discharge, if reduced
¹⁶⁸³ leads to a smaller blind area in the detector, increasing the rate capability of the detector.

¹⁶⁸⁴ 4.2.1 Operation modes

¹⁶⁸⁵ RPCs where developed early 1980s. At that time it was using an operating mode now referred to
¹⁶⁸⁶ as *streamer mode*. Streamers are large discharges that develop in between the 2 electrodes enough
¹⁶⁸⁷ to locally discharge the electrodes. If the electric field inside of the gas volume is strong enough,
¹⁶⁸⁸ with electrons being fast compared to ions, a large and dense cloud of positive ions will develop
¹⁶⁸⁹ nearby the anode and extend toward the cathode while the electrons are being collected, eventually
¹⁶⁹⁰ leading to a streamer discharge due to the increase of field seen at the cathode. the field is then strong
¹⁶⁹¹ enough so that electrons are pulled out of the cathode. Electrodes, though they are a unique volume
¹⁶⁹² of resistive material, can be assimilated to capacitors. At the moment an electric field is applied in
¹⁶⁹³ between their outer surfaces, the charge carriers inside of the volume will start moving leading to
¹⁶⁹⁴ a situation where there is no voltage across the electrodes and a higher density of negative charges,
¹⁶⁹⁵ i.e. electrons, on the inner surface of the cathode. Finally, when a streamer discharge occurs, these
¹⁶⁹⁶ electrons are partially released in the gas volume contributing to increase the discharge strength until
¹⁶⁹⁷ the formation of a conductive plasma, the streamer. This can be understood through Figure 4.3 [32].
¹⁶⁹⁸ Streamer signals are very convenient in terms of read-out as no amplification is required with output
¹⁶⁹⁹ pulses amplitudes of the order of a few tens to few hundreds of mV as can be seen on Figure 4.4.

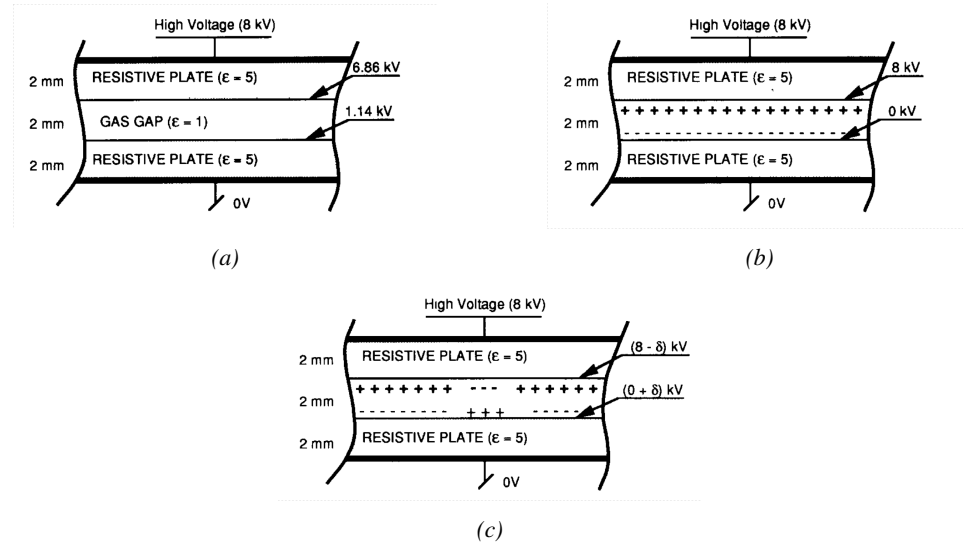


Figure 4.3: Movement of the charge carriers in an RPC. Figure 4.3a: Voltage across an RPC whose electrode have a relative permittivity of 5 at the moment the tension s applied. Figure 4.3b: After the charge carriers moved, the electrodes are charged and there is no voltage drop over the electrodes anymore. The full potential is applied on the gas gap only. Figure 4.3c: The streamer discharge initiated by a charged particle transports electrons and cations towards the anode and cathode respectively.

When the electric field is reduced though, the electronic gain is small until the electrons get close enough to the anode and the positive ion cloud is much smaller. The electric field cannot rise to the point a field emission of electrons on the cathode is possible. The resulting signal is weak, of the order of a few mv as shown on Figure 4.4, and requires amplification. This is the *avalanche mode* of RPC operation.

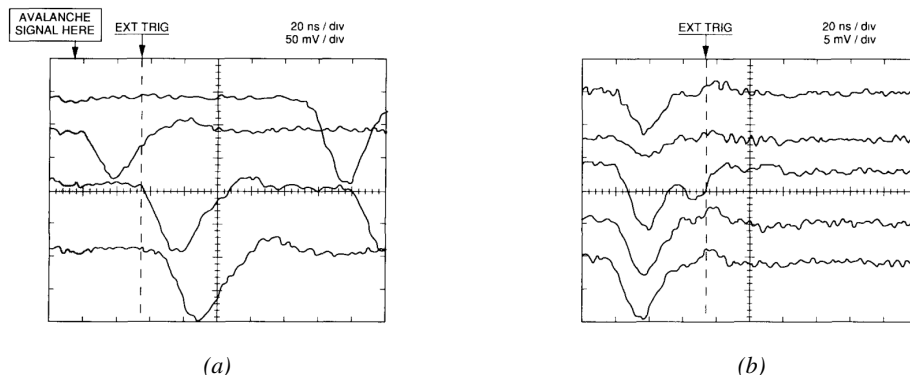


Figure 4.4: Typical oscilloscope pulses in streamer mode (Figure 4.4a) and avalanche mode(Figure 4.4b). In the case of streamer mode, the very small avalanche signal is visible.

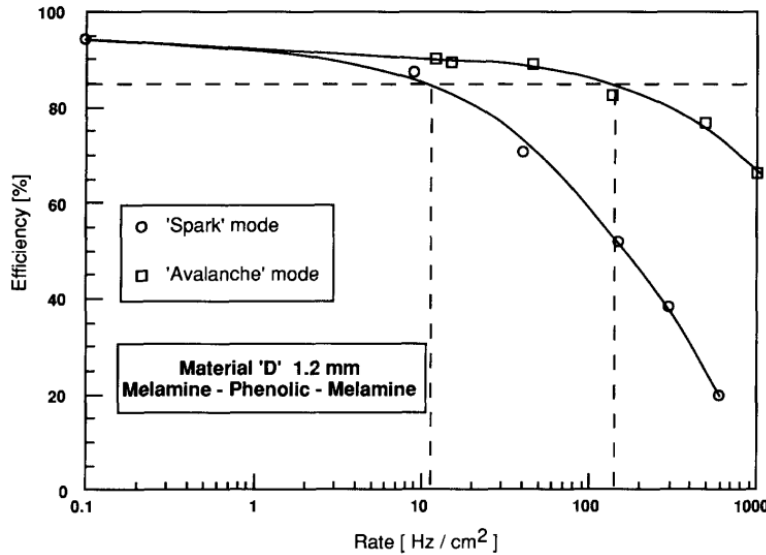


Figure 4.5: Rate capability comparison for the streamer and avalanche mode of operation. An order of magnitude in rate capability for a maximal efficiency drop of 10% is gained by using the avalanche mode over the streamer mode.

This mode offers a higher rate capability by providing smaller discharges that don't affect the electrodes charge and are more locally contained in the gas volume as was demonstrated by Crotty with Figure 4.5 [32]. The detector only stays locally blind the time the charge carriers are recombined and there is no need for electrode recharge which is a long process affecting a large portion of the detector. Another advantage of avalanche signals over streamer is the great time consistency. Figure 4.4 shows very clearly that avalanche signals have a very small time jitter. This is a natural choice for high rate experiments.

4.2.2 Detector designs and performance

Different RPC design have been used and each of them present its own advantages. Historically, the first type of RPC to have been developed is what is referred now to *narrow gap* RPC [29, 48]. After the avalanche mode has been discovered [32], it has been proven that increasing the width of the gas gap lead to higher rate capability, due to lower charge deposition per avalanche, and lower power dissipation [48]. Nevertheless, by increasing the gas gap width, the time resolution of the detector decreases. This is a natural result if the increase of active gas volume in the detector is taken into account. Indeed, for a given threshold, only the small fraction of gas closest to the cathode will provide enough gain to have a detectable signal. In the case of a wider gas volume, the active region is then larger and a larger time jitter is introduced with the variation of starting position of the avalanche, as discussed in [35]. To solve improve both the time resolution and the rate capability, different methods were used trying to get advantages of both narrow and wide gap RPCs.

1724 **4.2.2.1 Double-gap RPC**

1725 Double-gap RPCs are made out of 2 narrow RPC detectors. The 2 RPC gaps are stacked on top of
 1726 each other as shown in Figure 4.6. This detector layout, popularized by the two multipurpose experiments
 1727 CMS [21] and ATLAS [40] at LHC, can be used as an OR system in which each individual
 1728 chamber participates in the output signal. The gain of such a detector is greatly reduced with respect
 1729 to single-gap RPCs with an efficiency plateau reached at lower voltage, as visible on Figure 4.7.

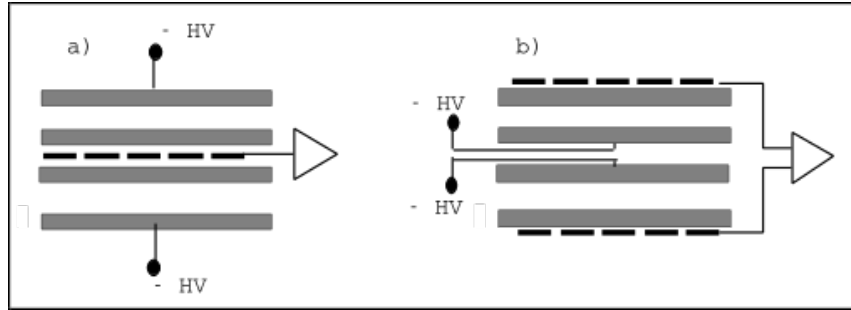


Figure 4.6: Possible double-gap RPC layouts: a) "standard" 1D double-gap RPC, as used in CMS experiment, where the anodes are facing each other and a 1D read-out plane is sandwiched in between them, b) double read-out double-gap RPC as used in ATLAS experiment, where the cathodes are facing each other and 2 read-out planes are used on the outer surfaces. This last layout can offer the possibility to use a 2D reconstruction by using orthogonal read-out planes.

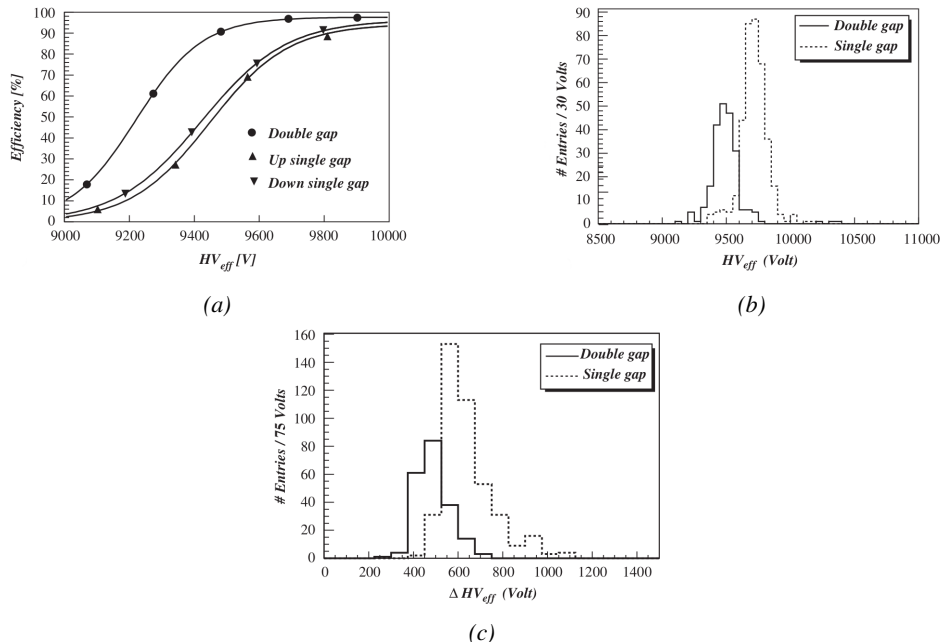


Figure 4.7: Comparison of performance of CMS double and single gap RPCs using cosmic muons [49]. Figure 4.7a: Comparison of efficiency sigmoids. Figure 4.7b: Voltage distribution at 95% of maximum efficiency. Figure 4.7c: $\Delta_{10\%}^{90\%}$ distribution.

4.2.2.2 Multigap RPC (MRPC)

MRPCs are layouts in which floating sub electrode plates are placed into a wide gap RPC to divide the gas volume and create a sum of narrow gaps [35, 36]. The time resolution of such a detector can reach of few tens of ps, with gas gaps of the order of a few hundred μm as shown in Figure 4.8 representing ALICE Time-of-flight (ToF) MRPCs.

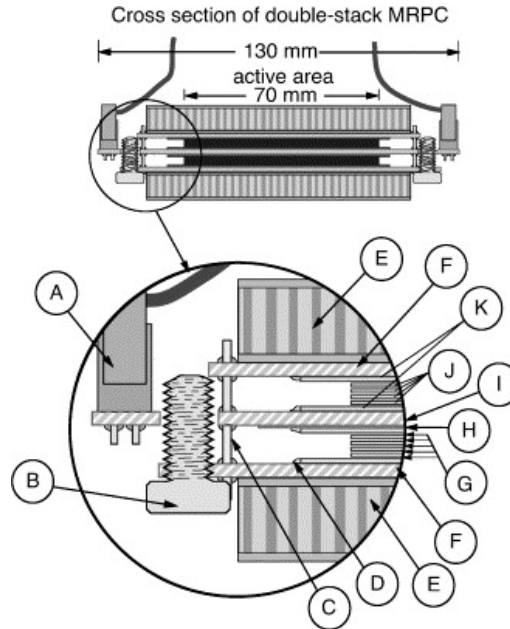


Figure 4.8: Presentation of ALICE MRPC using $250 \mu\text{m}$ gas gaps, $620 \mu\text{m}$ outer glass electrodes and $550 \mu\text{m}$ inner floating electrodes. More details on the labels are given in [50].

Sometimes used as a double multigap RPC, taking advantage of the OR of double gap RPCs, the MRPC is mainly used as ToF detector [50–54] due to its excellent timing properties that allow to perform particle identification as explained by Williams in [55]. The principle of particle identification using ToF is simply the measurement of the velocity of a particle. Indeed, particles are defined by their mass (for the parameter of interest here, their electric charge being measured using the bending angle of the particles traveling through a magnetic field) and this mass can be calculated by measuring the velocity β and momentum of the particle:

$$\beta = \frac{p}{\sqrt{p^2 + m^2}} \quad (4.3)$$

Intuitively, it is trivial to understand that 2 different particles having the same momentum will have a different velocity due to the mass difference and thus a different flight time T_1 and T_2 through the detector and this is used to separate and identify particles. The better the time resolution of the ToF system used, the stronger will the separation be:

$$T = \frac{L}{v} = \frac{L}{c \cdot \beta}, \quad \Delta T = T_1 - T_2 = \frac{L}{c} \left(\sqrt{1 + m_1^2/p^2} - \sqrt{1 + m_2^2/p^2} \right) \cong (m_1^2 - m_2^2) \frac{L}{2cp^2} \quad (4.4)$$

¹⁷⁴⁶ An example of particle identification is given for the case of STAR experiment in Figure 4.9.

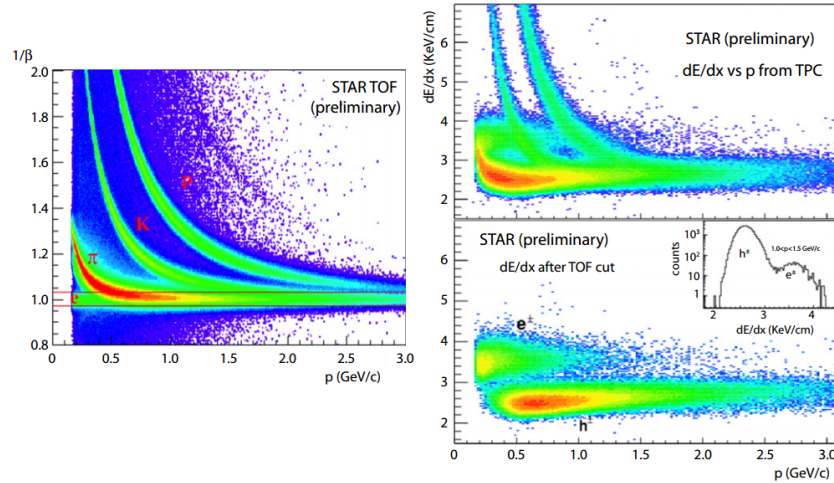


Figure 4.9: Particle identification applied to electrons in the STAR experiment. The identification is performed combining ToF and dE/dx measurements [55].

¹⁷⁴⁷ Another benefice of using such small gas gaps is the strong reduction of the average avalanche
¹⁷⁴⁸ volume and thus of the blind spot on MRPCs leading to an improved rate capability. Multigaps can
¹⁷⁴⁹ sustain backgrounds of several kHz/cm² as demonstrated in Figure 4.10.

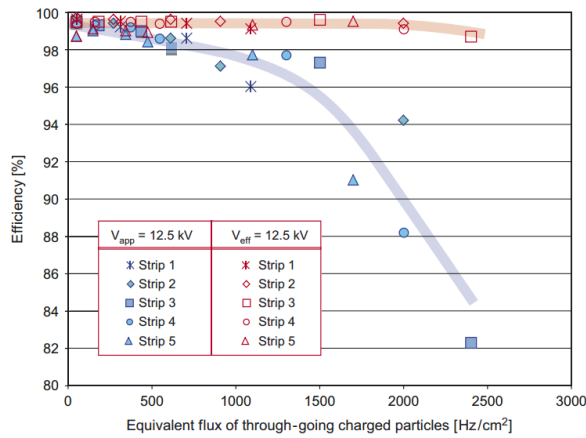


Figure 4.10: Comparison of the detector performance of ALICE ToF MRPC [56] at fixed applied voltage (in blue) and at fixed effective voltage (in red). The effective voltage is kept fixed by increasing the applied voltage accordingly to the current drawn by the detector.

¹⁷⁵⁰ 4.2.2.3 Charge distribution and performance limitations

¹⁷⁵¹ The direct consequence of the different RPC layouts is a variation of intrinsic time resolution of the
¹⁷⁵² RPC as the gap size decreases. An advantage is given to multigaps whose design use sub-millimeter
¹⁷⁵³ gas volumes providing very consistent signals.

1754 On the charge spectrum point of view, each layout has its own advantages. When the double-gap
 1755 has the highest induced over drifting charge ratio, as seen in Figure 4.11, the multigap has a charge
 1756 spectrum strongly detached from the origin, as visible in Figure 4.12. A high induced over drifting
 1757 charge ratio means that the double gap can be safely operated at high threshold or that at similar
 1758 threshold it can be operated with a twice smaller drifting charge, meaning a higher rate capability.
 1759 On the other hand, the strong detachment of the charge spectrum from the origin in the MRPC case
 1760 allows to reach a higher efficiency with increasing threshold as most of the induced charge is not low
 1761 due to the convolution of several single gap spectra. The range of stable efficiency increases with
 1762 the number of gap, as presented in Figure 4.13.

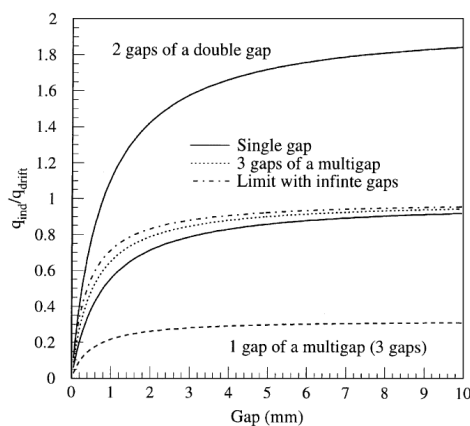


Figure 4.11: Ratio between total induced and drifting charge have been simulated for single gap, double-gap and multigap layouts [57]. The total induced charge for a double-gap RPC is a factor 2 higher than for a multigap.

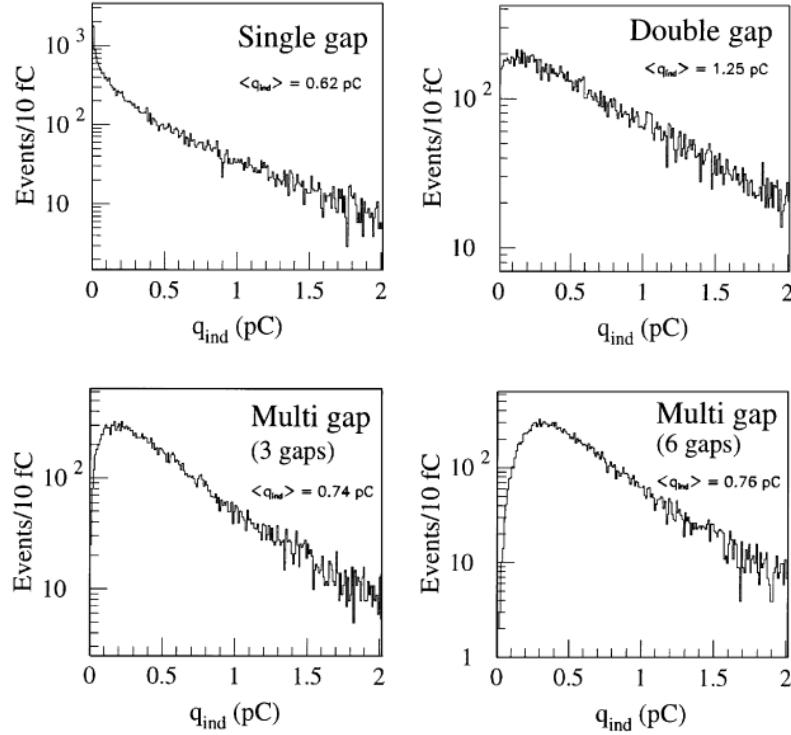


Figure 4.12: Charge spectra have been simulated for single gap, double-gap and multigap layouts [57]. It appears that when single gap shows a decreasing spectrum, double and multigap layouts exhibit a spectrum whose peak is detached from the origin. The detachment gets stronger as the number of gaps increases.

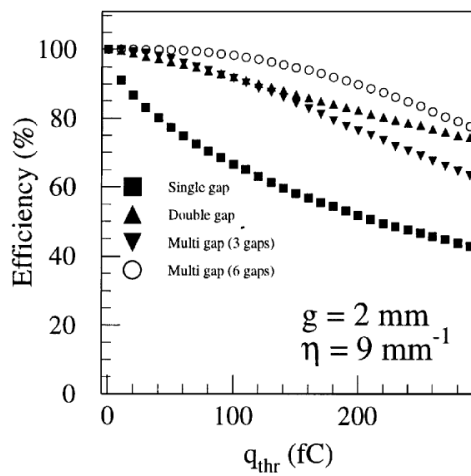


Figure 4.13: The maximal theoretical efficiency is simulated for single gap, double-gap and multigap layouts [57] at a constant gap thickness of 2 mm and using an effective Townsend coefficient of 9 mm^{-1} .

¹⁷⁶³ **4.3 Signal formation**

¹⁷⁶⁴ **4.4 Gas transport parameters**

5

1765

1766

1767

Longevity studies and Consolidation of the present CMS RPC subsystem

5.1 Resistive Plate Chambers at CMS

5.1.1 Overview

1770 The Resistive Plate Chambers (RPC) system, located in both barrel and endcap regions, provides a
1771 fast, independent muon trigger with a looser p_T threshold over a large portion of the pseudorapidity
1772 range ($|\eta| < 1.6$) [add reconstruction].

1773

1774 During High-Luminosity LHC (HL-LHC) operations the expected conditions in terms of back-
1775 ground and pile-up will make the identification and correct P_T assignment a challenge for the Muon
1776 system. The goal of RPC upgrade is to provide additional hits to the Muon system with precise tim-
1777 ing. All these informations will be elaborated by the trigger system in a global way enhancing the
1778 performance of the trigger in terms of efficiency and rate control. The RPC Upgrade is based on two
1779 projects: an improved Link Board System and the extension of the RPC coverage up to $|\eta| = 2.4$.
1780 [FIXME 2.4 or 2.5?]

1781 The Link Board system, that will be described in section xxx, is responsible to process, syn-
1782 chronize and zero-suppress the signals coming from the RPC front end boards. The Link Board
1783 components have been produced between 2006 and 2007 and will be subjected to aging and failure
1784 in the long term. The upgraded Link Board system will overcome the aging problems described in
1785 section xxx and will allow for a more precise timing information to the RPC hits from 25 to 1 ns [ref
1786 section xxx].

1787 The extension of the RPC system up to $|\eta| = 2.1$ was already planned in the CMS TDR [ref
1788 cmstdr] and staged because of budget limitations and expected background rates higher than the rate
1789 capability of the present CMS RPCs in that region. An extensive R&D program has been done in
1790 order to develop an improved RPC that fulfills the CMS requirements. Two new RPC layers in the
1791 innermost ring of stations 3 and 4 will be added with benefits to the neutron-induced background

1792 reduction and efficiency improvement for both trigger and offline reconstruction.

1793 5.1.2 The present RPC system

1794 The RPC system is organized in 4 stations called RB1 to RB4 in the barrel region, and RE1 to RE4
 1795 in the endcap region. The innermost barrel stations, RB1 and RB2, are instrumented with 2 layers
 1796 of RPCs facing the innermost (RB1in and RB2in) and outermost (RB1out and RB2out) sides of the
 1797 DT chambers. Every chamber is then divided from the read-out point of view into 2 or 3 η partitions
 1798 called “rolls”. The RPC system consist of 480 barrel chambers and 576 endcap chambers. Details
 1799 on the geometry are discussed in the paper [ref to geo paper].

1800 The CMS RPC chamber is a double-gap, operated in avalanche mode to ensure reliable operation
 1801 at high rates. Each RPC gap consists of two 2-mm-thick resistive High-Pressure Laminate (HPL)
 1802 plates separated by a 2-mm-thick gas gap. The outer surface of the HPL plates is coated with a thin
 1803 conductive graphite layer, and a voltage is applied. The RPCs are operated with a 3-component,
 1804 non-flammable gas mixture consisting of 95.2% freon ($C_2H_2F_4$, known as R134a), 4.5% isobutane
 1805 ($i-C_4H_{10}$), and 0.3% sulphur hexafluoride (SF_6) with a relative humidity of 40% - 50%. Readout
 1806 strips are aligned in η between the 2 gas gaps. [\[Add a sentence on FEBs.\]](#)

1807 The discriminated signals coming from the Front End boards feed via twisted cables (10 to 20 m
 1808 long) the Link Board System located in UXC on the balconies around the detector. The Link System
 1809 consist of the 1376 Link Boards (LBs) and the 216 Control Boards (CBs), placed in 108 Link Boxes.
 1810 The Link Box is a custom crate (6U high) with 20 slots (for two CBs and eighteen LBs). The Link
 1811 Box contains custom backplane to which the cables from the chambers are connected, as well as the
 1812 cables providing the LBs and CBs power supply and the cables for the RPC FEBs control with use
 1813 of the I2C protocol (trough the CB). The backplane itself contains only connectors (and no any other
 1814 electronic devices).

1815 The Link Board has 96 input channels (one channel corresponds to one RPC strip). The input
 1816 signals are the ~ 100 ns binary pulses which are synchronous to the RPC hits, but not to the LHC
 1817 clock (which drives the entire CMS electronics). Thus the first step of the FEB signals processing
 1818 is synchronization, i.e. assignment of the signals to the BXes (25 ns periods). Then the data are
 1819 compressed with a simple zero-suppressing algorithm (the input channels are grouped into 8 bit
 1820 partitions, only the partitions with at least one nonzero bit are selected for each BX). Next, the non-
 1821 empty partitions are time-multiplexed i.e. if there are more than one such partition in a given BX,
 1822 they are sent one-by-one in consecutive BXes. The data from 3 neighbouring LBs are concentrated
 1823 by the middle LB which contains the optical transmitter for sending them to the USC over a fiber at
 1824 1.6 Gbps.

1825 The Control Boards provide the communication of the control software with the LBs via the
 1826 FEC/CCU system. The CBs are connected into token rings, each ring consists of 12 CBs of one
 1827 detector tower and a FEC mezzanine board placed on the CCS board located in the VME crate in
 1828 the USC. In total, there are 18 rings in the entire Link System. The CBs also perform automatic
 1829 reloading of the LB's firmware which is needed in order to avoid accumulation of the radiation
 1830 induced SEUs in the LBs firmware.

1831 Both LBs and CB are based on the Xilinx Spartan III FPGAs, the CB additionally contains
 1832 radiation-tolerant (FLASH based) FPGA Actel ProAsicPlus.

1833 The High Voltage power system is located in USC, not exposed to radiation and easily accessible
 1834 for any reparation. A single HV channel powers 2 RPC chambers both in the barrel and endcap
 1835 regions. The Low Voltage boards are located in UXC on the balconies and provide the voltage to the

¹⁸³⁶ front end electronics.

¹⁸³⁷ 5.1.3 Pulse processing of CMS RPCs

¹⁸³⁸ Signals induced by cosmic particle in the RPC strips are shaped by standard CMS RPC Front-End
¹⁸³⁹ Electronics (FEE) following the scheme of Figure 5.1. On a first stage, analogic signals are amplified
¹⁸⁴⁰ and then sent to the Constant Fraction Discriminator (CFD) described in Figure 5.2. At the end of
¹⁸⁴¹ the chain, 100 ns long pulses are sent in the LVDS output. These output signal are sent on one side to
¹⁸⁴² a V1190A Time-to-Digital Converter (TDC) module from CAEN and on the other to an OR module
¹⁸⁴³ to count the number of detected signals. Trigger and hit coïncidences are monitored using scalers.
¹⁸⁴⁴ The TDC is used to store the data into ROOT files. These files are thus analysed to understand the
¹⁸⁴⁵ detectors performance.

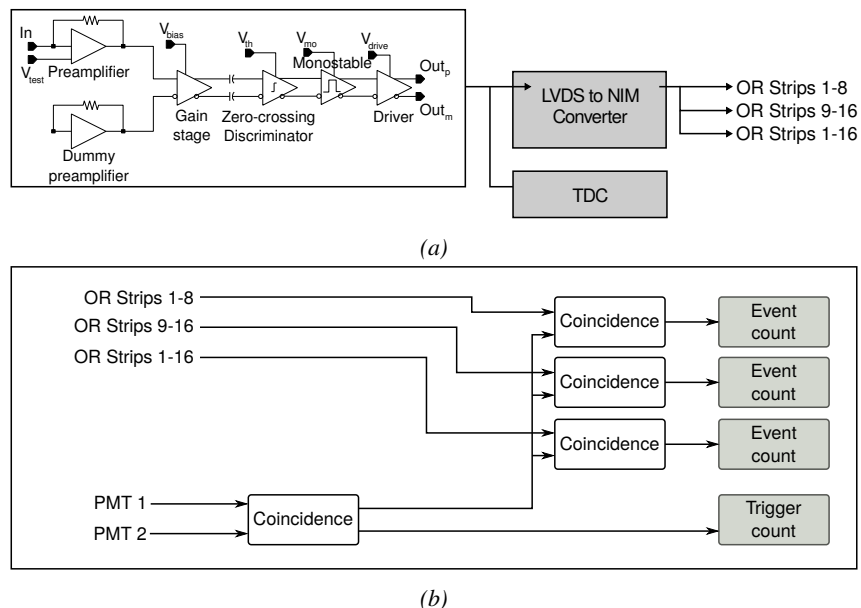


Figure 5.1: Signals from the RPC strips are shaped by the FEE described on Figure 5.1a. Output LVDS signals are then read-out by a TDC module connected to a computer or converted into NIM and sent to scalers. Figure 5.1b describes how these converted signals are put in coincidence with the trigger.

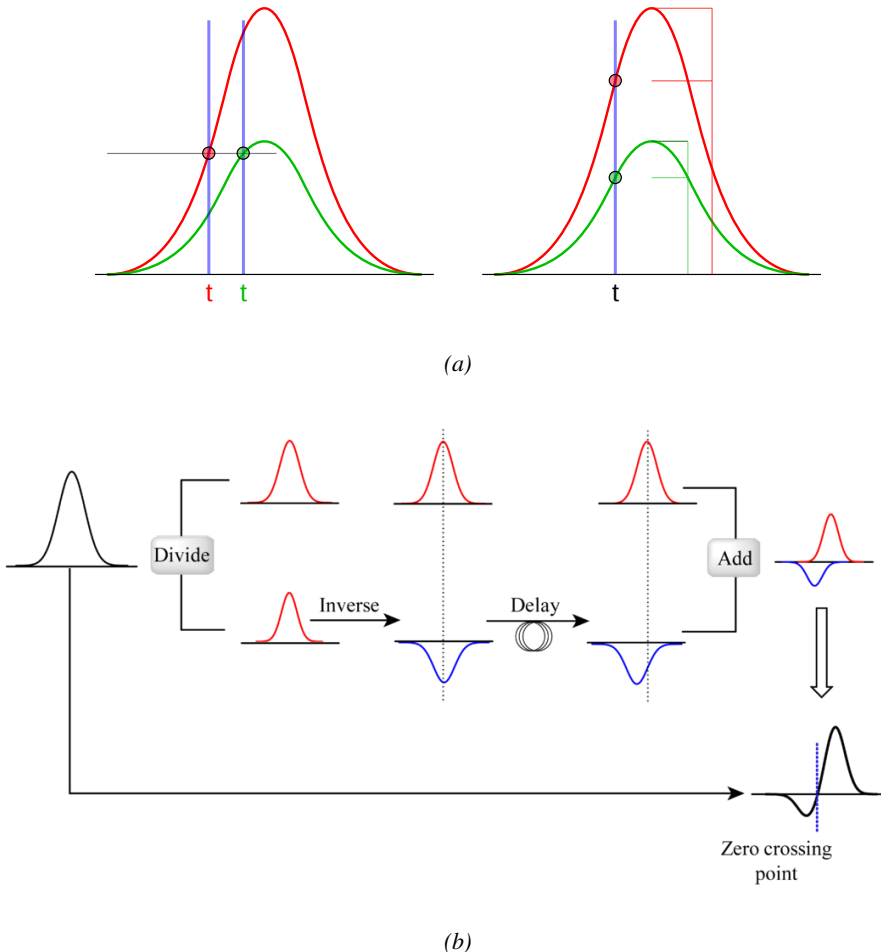


Figure 5.2: Description of the principle of a CFD. A comparison of threshold triggering (left) and constant fraction triggering (right) is shown in Figure 5.2a. Constant fraction triggering is obtained thanks to zero-crossing technique as explained in Figure 5.2b. The signal arriving at the input of the CFD is split into three components. A first one is delayed and connected to the inverting input of a first comparator. A second component is connected to the noninverting input of this first comparator. A third component is connected to the noninverting input of another comparator along with a threshold value connected to the inverting input. Finally, the output of both comparators is fed through an AND gate.

1846 5.2 Testing detectors under extreme conditions

1847 The upgrade from LHC to HL-LHC will increase the peak luminosity from $10^{34} \text{ cm}^{-2} \text{ s}^{-1}$ to reach
 1848 $5 \times 10^{34} \text{ cm}^{-2} \text{ s}^{-1}$, increasing in the same way the total expected background to which the RPC
 1849 system will be subjected to. Composed of low energy gammas and neutrons from $p\text{-}p$ collisions, low
 1850 momentum primary and secondary muons, puch-through hadrons from calorimeters, and particles
 1851 produced in the interaction of the beams with collimators, the background will mostly affect the
 1852 regions of CMS that are the closest to the beam line, i.e. the RPC detectors located in the endcaps.
 1853 [To update.]

1854

1855 The 2016 data allowed to study the values of the background rate in all RPC system. In Figure 5.3, the distribution of the chamber background hit rate per unit area is shown at a luminosity
 1856 of $5 \times 10^{34} \text{ cm}^{-2} \cdot \text{s}^{-1}$ linearly extrapolating from data collected in 2016 [ref mentioning the linear
 1857 dependency of rate vs lumi]. The maximum rate per unit area at HL-LHC conditions is expected to
 1858 be of the order of 600 Hz/cm^2 (including a safety factor 3). Nevertheless, Fluka simulations have
 1859 conducted in order to understand the background at HL-LHC conditions. The comparison to the
 1860 data has shown, in Figure 5.4, a discrepancy of a factor 2 even though the order of magnitude is
 1861 consistent. [Understand mismatch.]
 1862

1863

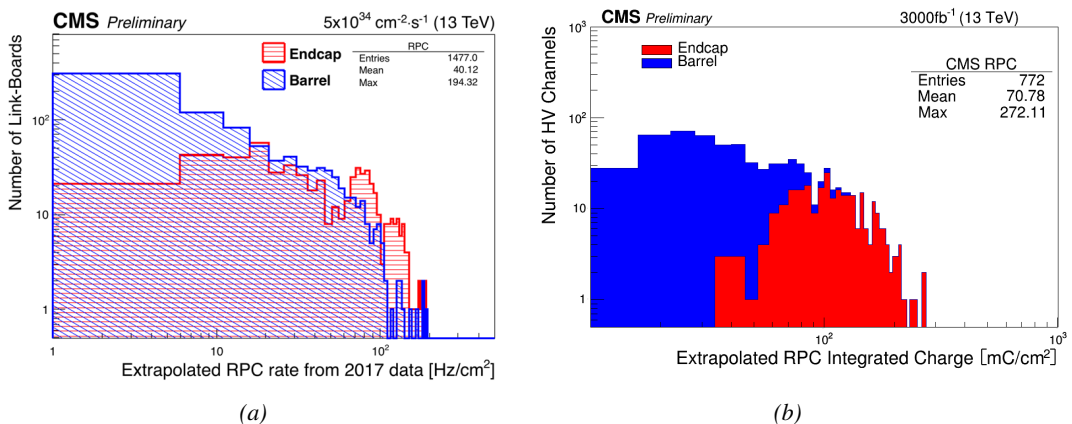


Figure 5.3: Figure 5.3a: The integrated charge per region (Barrel, Endcap) is extrapolated to HL-LHC integrated luminosity (3000 fb^{-1}) using the data accumulated in 2016 in every HV channels. Figure 5.3b: The hit rate per region (Barrel, Endcap) is linearly extrapolated to HL-LHC highest instantaneous luminosity ($5 \times 10^{34} \text{ cm}^{-2} \text{s}^{-1}$) using the rate as a function of instantaneous luminosity recorded by RPCs in 2017 showing a linear dependence.

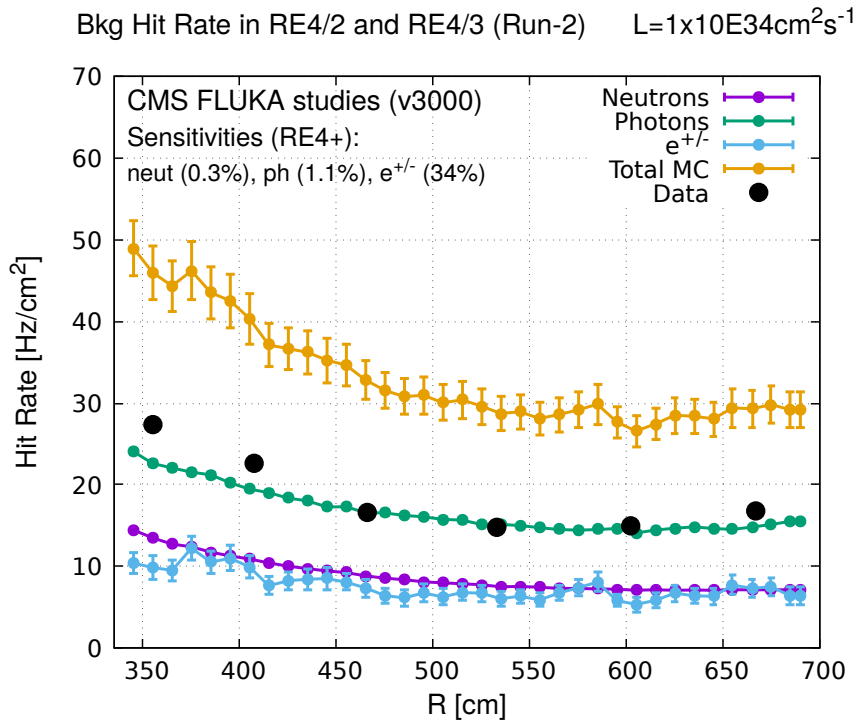


Figure 5.4: Background Fluka simulation compared to 2016 Data at $L = 10^{34}\text{cm}^{-2}\text{s}^{-1}$ in the fourth endcap disk region. A mismatch in between simulation and data can be observed. [\[To be understood.\]](#)

In the past, extensive long-term tests were carried out at several gamma and neutron facilities certifying the detector performance. Both full size and small prototype RPCs have been irradiated with photons up to an integrated charge of $\sim 0.05\text{C}/\text{cm}^2$ and $\sim 0.4\text{C}/\text{cm}^2$, respectively [58, 59]. During Run-I, the RPC system provided stable operation and excellent performance and did not show any aging effects for integrated charge of the order of $0.01\text{C}/\text{cm}^2$. Projections on currents from 2016 Data, has allowed to determine that the total integrated charge, by the end of HL-LHC, would be of the order of $1\text{C}/\text{cm}^2$ (including a safety factor 3). [\[Corresponding figure needed.\]](#)

1871

1872 5.2.1 The Gamma Irradiation Facilities

1873 5.2.1.1 GIF

1874 Located in the SPS West Area at the downstream end of the X5 test beam, the Gamma Irradiation
1875 Facility (GIF) was a test area in which particle detectors were exposed to a particle beam in presence
1876 of an adjustable gamma background [60]. Its goal was to reproduce background conditions these
1877 detectors would suffer in their operating environment at LHC. GIF layout is shown in Figure 5.5.
1878 Gamma photons are produced by a strong ^{137}Cs source installed in the upstream part of the zone
1879 inside a lead container. The source container includes a collimator, designed to irradiate a $6 \times 6\text{ m}^2$
1880 area at 5 m maximum to the source. A thin lens-shaped lead filter helps providing with a uniform
1881 outcoming flux in a vertical plane, orthogonal to the beam direction. The principal collimator hole
1882 provides a pyramidal aperture of $74^\circ \times 74^\circ$ solid angle and provides a photon flux in a pyramidal vol-

ume along the beam axis. The photon rate is controled by further lead filters allowing the maximum rate to be limited and to vary within a range of four orders of magnitude. Particle detectors under test are then placed within the pyramidal volume in front of the source, perpendicularly to the beam line in order to profit from the homogeneous photon flux. Adjusting the background flux of photons can then be done by using the filters and choosing the position of the detectors with respect to the source.

1888

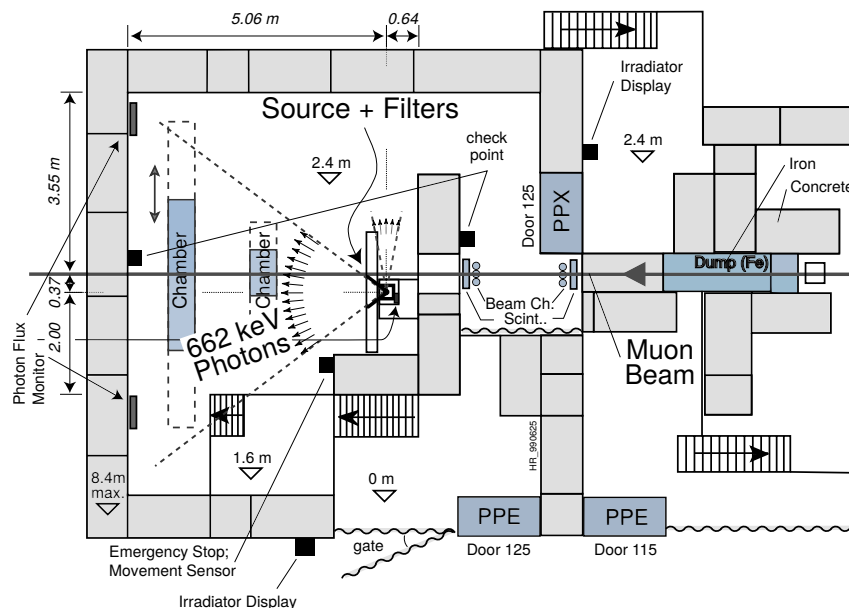


Figure 5.5: Layout of the test beam zone called X5c GIF at CERN. Photons from the radioactive source produce a sustained high rate of random hits over the whole area. The zone is surrounded by 8 m high and 80 cm thick concrete walls. Access is possible through three entry points. Two access doors for personnel and one large gate for material. A crane allows installation of heavy equipment in the area.

1889

As described on Figure 5.6, the ^{137}Cs source emits a 662 keV photon in 85% of the decays. An activity of 740 GBq was measured on the 5th March 1997. To estimate the strength of the flux in 2014, it is necessary to consider the nuclear decay through time assiciated to the Cesium source whose half-life is well known ($t_{1/2} = (30.05 \pm 0.08)$ y). The GIF tests were done in between the 20th and the 31st of August 2014, i.e. at a time $t = (17.47 \pm 0.02)$ y resulting in an attenuation of the activity from 740 GBq in 1997 to 494 GBq in 2014.

1890

1891

1892

1893

1894

1895

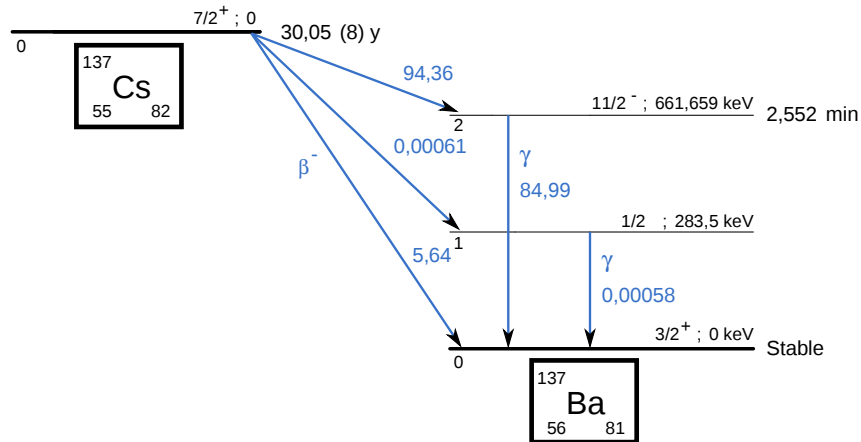


Figure 5.6: ^{137}Cs decays by β^- emission to the ground state of ^{137}Ba ($\text{BR} = 5.64\%$) and via the 662 keV isomeric level of ^{137}Ba ($\text{BR} = 94.36\%$) whose half-life is 2.55 min.

1896 5.2.1.2 GIF++

1897 The new Gamma Irradiation Facility (GIF++), located in the SPS North Area at the downstream end
 1898 of the H4 test beam, has replaced its predecessor during LS1 and has been operational since spring
 1899 2015 [61]. Like GIF, GIF++ features a ^{137}Cs source of 662 keV gamma photons, their fluence being
 1900 controlled with a set of filters of various attenuation factors. The source provides two separated large
 1901 irradiation areas for testing several full-size muon detectors with continuous homogeneous irradiation,
 1902 as presented in Figure 5.7.

1903

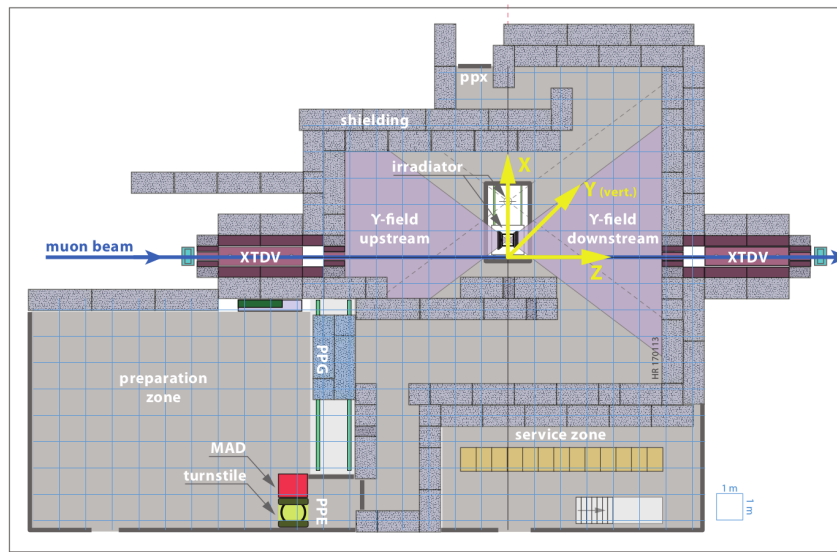


Figure 5.7: Floor plan of the GIF++ facility. When the facility downstream of the GIF++ takes electron beam, a beam pipe is installed along the beam line (z -axis). The irradiator can be displaced laterally (its center moves from $x = 0.65 \text{ m}$ to 2.15 m), to increase the distance to the beam pipe.

1904 The source activity was measured to be about 13.5 TBq in March 2016. The photon flux being
 1905 far greater than HL-LHC expectations, GIF++ provides an excellent facility for accelerated aging
 1906 tests of muon detectors.

1907

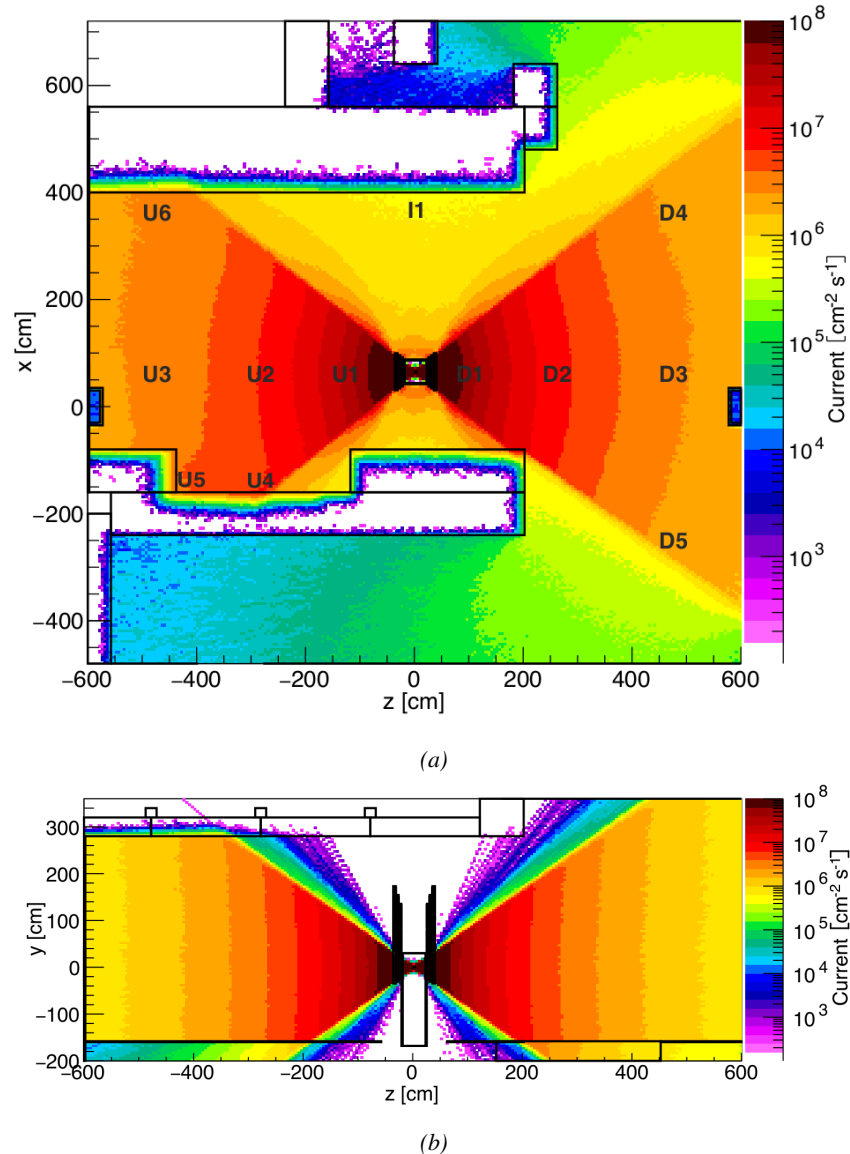


Figure 5.8: Simulated unattenuated current of photons in the xz plane (Figure 5.8a) and yz plane (Figure 5.8b) through the source at $x = 0.65$ m and $y = 0$ m. With angular correction filters, the current of 662 keV photons is made uniform in xy planes.

1908 The source is situated in the muon beam line with the muon beam being available a few times a
 1909 year. The H4 beam, composed of muons with a momentum of about 150 GeV/c, passes through the
 1910 GIF++ zone and is used to study the performance of the detectors. Its flux is of 104 particles/ cm^2

¹⁹¹¹ focused in an area similar to $10 \times 10 \text{ cm}^2$. Therefore, with properly adjusted filters, one can imitate
¹⁹¹² the HL-LHC background and study the performance of muon detectors with their trigger/readout
¹⁹¹³ electronics in HL-LHC environment.

¹⁹¹⁴

¹⁹¹⁵ 5.3 Preliminary tests at GIF

¹⁹¹⁶ 5.3.1 Resistive Plate Chamber test setup

¹⁹¹⁷ During summer 2014, preliminary tests have been conducted in the GIF area on a newly produced
¹⁹¹⁸ RE4/2 chamber labelled RE-4-2-BARC-161. This chamber has been placed into a trolley covered
¹⁹¹⁹ with a tent. The position of the RPC inside the tent and of the tent related to the source is described
¹⁹²⁰ in Figure 5.9. To test this CMS RPC, three different absorber settings were used. First of all,
¹⁹²¹ measurements were done with fully opened source. Then, to complete this preliminary study, the
¹⁹²² gamma flux has been attenuated from a factor 2 and a factor 5. The expected gamma flux at the level
¹⁹²³ of our detector will be discussed in subsection ??.

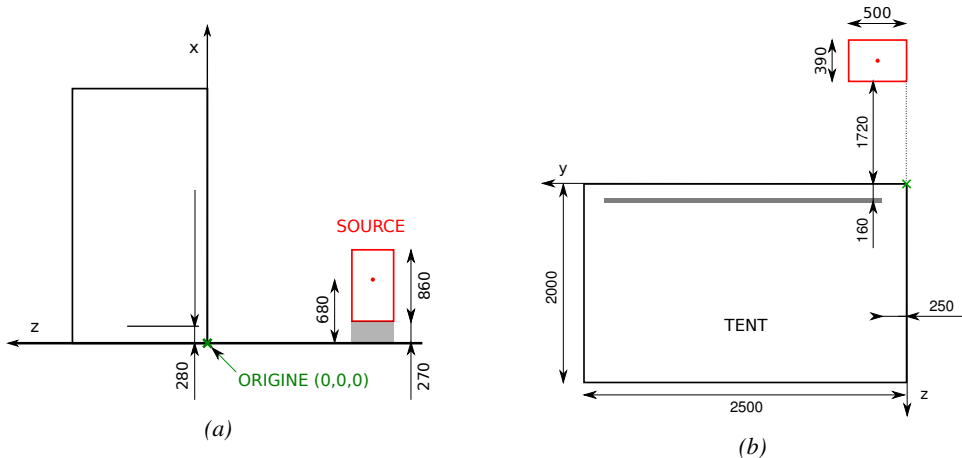


Figure 5.9: Description of the RPC setup. Dimensions are given in mm. A tent containing RPCs is placed at 1720 mm from the source container. The source is situated in the center of the container. RE-4-2-BARC-161 chamber is 160 mm inside the tent. This way, the distance between the source and the chambers plan is 2060 mm. Figure 5.9a provides a side view of the setup in the xz plane while Figure 5.9b shows a top view in the yz plane.



Figure 5.10: RE-4-2-BARC-I61 chamber is inside the tent as described in Figure 5.9. In the top right, the two scintillators used as trigger can be seen. This trigger system has an inclination of 10° relative to horizontal and is placed above half-partition B2 of the RPCs. PMT electronics are shielded thanks to lead blocks placed in order to protect them without stopping photons from going through the scintillators and the chamber.

1924 At the time of the tests, the beam not being operational anymore, a trigger composed of 2 plastic
 1925 scintillators has been placed in front of the setup with an inclination of 10 deg with respect to the
 1926 detector plane in order to look at cosmic muons. Using this particular trigger layout, shown on Fig-
 1927 ure 5.10, leads to a cosmic muon hit distribution into the chamber similar to the one in Figure 5.11.
 1928 Measured without gamma irradiation, two peaks can be seen on the profile of partition B, centered
 1929 on strips 52 and 59. Section ?? will help us understand that these two peaks are due respectively to
 1930 forward and backward coming cosmic particles where forward coming particles are first detected by
 1931 the scintillators and then the RPC while the backward coming muons are first detected in the RPC.

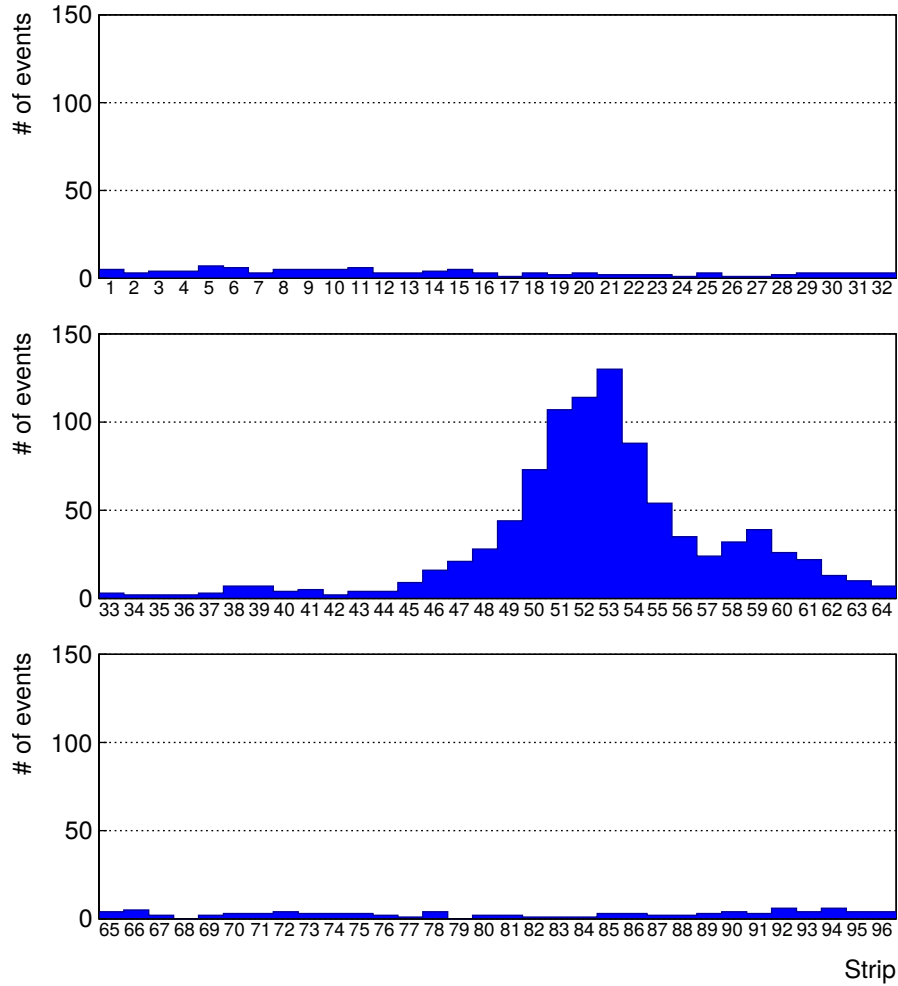


Figure 5.11: Hit distributions over all 3 partitions of RE-4-2-BARC-161 chamber is showed on these plots. Top, middle and bottom figures respectively correspond to partitions A, B, and C. These plots show that some events still occur in other half-partitions than B2, which corresponds to strips 49 to 64, in front of which the trigger is placed, contributing to the inefficiency of detection of cosmic muons. In the case of partitions A and C, the very low amount of data can be interpreted as noise. On the other hand, it is clear that a little portion of muons reach the half-partition B1, corresponding to strips 33 to 48.

5.3.2 Data Acquisition

5.3.3 Geometrical acceptance of the setup layout to cosmic muons

In order to profit from a constant gamma irradiation, the detectors inside of the GIF bunker need to be placed in a plane orthogonal to the beam line. The muon beam that used to be available was meant to test the performance of detectors under test. This beam not being active anymore, another solution to test detector performance had to be used. Thus, it has been decided to use cosmic muons detected through a telescope composed of two scintillators. Lead blocks were used as shielding to

1939 protect the photomultipliers from gammas as can be seen from Figure 5.10.

1940 An inclination has been given to the cosmic telescope to maximize the muon flux. A good com-
 1941 promise had to be found between good enough muon flux and narrow enough hit distribution to
 1942 be sure to contain all the events into only one half partitions as required from the limited available
 1943 readout hardware. Nevertheless, a consequence of the misplaced trigger, that can be seen as a loss
 1944 of events in half-partition B1 in Figure 5.11, is an inefficiency. Nevertheless, the inefficiency of ap-
 1945 proximately 20 % highlighted in Figure 5.12 by comparing the performance of chamber BARC-161
 1946 in 904 and at GIF without irradiation seems too important to be explained only by the geometri-
 1947 cal acceptance of the setup itself. Simulations have been conducted to show how the setup brings
 1948 inefficiency.

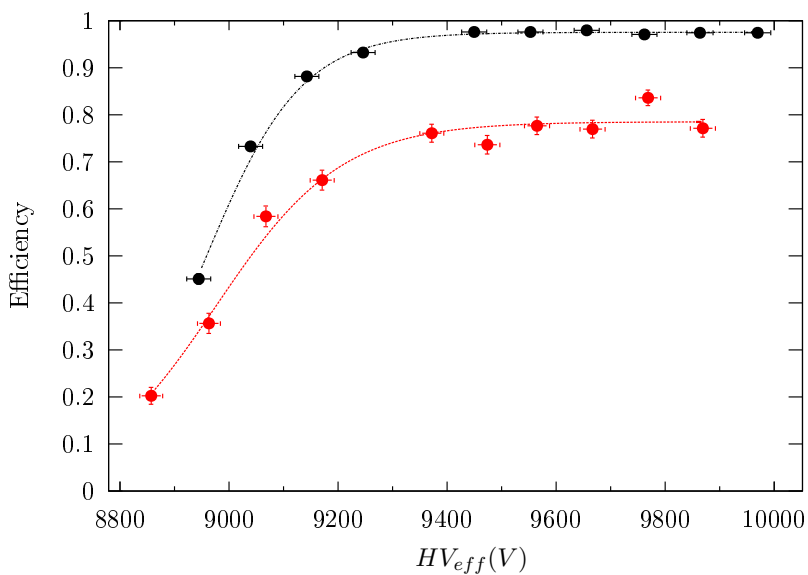


Figure 5.12: Results are derived from data taken on half-partition B2 only. On the 18th of June 2014, data has been taken on chamber RE-2-BARC-161 at building 904 (Prevessin Site) with cosmic muons providing us a reference efficiency plateau of $(97.54 \pm 0.15)\%$ represented by a black curve. A similar measurement has been done at GIF on the 21st of July with the same chamber giving a plateau of $(78.52 \pm 0.94)\%$ represented by a red curve.

1949 5.3.3.1 Description of the simulation layout

1950 The layout of GIF setup has been reproduced and incorporated into a Monte Carlo (MC) simulation
 1951 to study the influence of the disposition of the telescope on the final distribution measured by the
 1952 RPC. A 3D view of the simulated layout is given into Figure 5.13. Muons are generated randomly
 1953 in a horizontal plane located at a height corresponding to the lowest point of the PMTs. This way,
 1954 the needed size of the plane in order to simulate events happening at very big azimuthal angles (i.e.
 1955 $\theta \approx \pi$) can be kept relatively small. The muon flux is designed to follow the usual $\cos^2\theta$ distribution
 1956 for cosmic particle. The goal of the simulation is to look at muons that pass through the muon
 1957 telescope composed of the two scintillators and define their distribution onto the RPC plane. During
 1958 the reconstruction, the RPC plane is then divided into its strips and each muon track is assigned to a
 1959 strip.

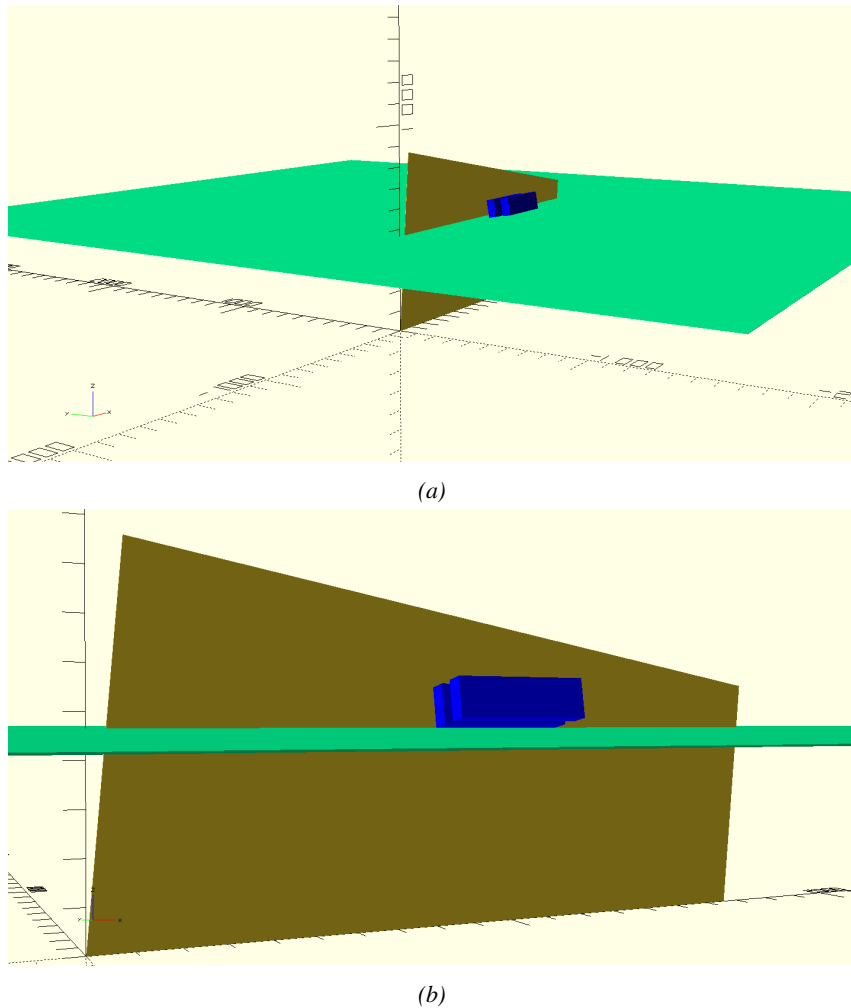


Figure 5.13: Representation of the layout used for the simulations of the test setup. The RPC is represented as a yellow trapezoid while the two scintillators as blue cuboids looking at the sky. A green plane corresponds to the muon generation plane within the simulation. Figure 5.9a shows a global view of the simulated setup. Figure 5.9b shows a zoomed view that allows to see the 2 scintillators as well as the full RPC plane.

1960 In order to further refine the quality of the simulation and understand deeper the results the
 1961 dependance of the distribution has been studied for a range of telescope inclinations. Moreover,
 1962 the threshold applied on the PMT signals has been included into the simulation in the form of a
 1963 cut. In the approximation of uniform scintillators, it has been considered that the threshold can be
 1964 understood as the minimum distance particles need to travel through the scintillating material to give
 1965 a strong enough signal. Particles that travel a distance smaller than the set "threshold" are thus not
 1966 detected by the telescope and cannot trigger the data taking. Finally, the FEE threshold also has
 1967 been considered in a similar way. The mean momentum of horizontal cosmic rays is higher than
 1968 those of vertical ones but the stopping power of matter for momenta ranging from 1 GeV to 1 TeV
 1969 stays comparable. It is then possible to assume that the mean number of primary e^- /ion pairs per
 1970 unit length will stay similar and thus, depending on the applied discriminator threshold, muons with

1971 the shortest path through the gas volume will deposit less charge and induce a smaller signal on the
 1972 pick-up strips that could eventually not be detected. These two thresholds also restrain the overall
 1973 geometrical acceptance of the system.

1974 5.3.3.2 Simulation procedure

1975 The simulation software has been designed using C++ and the output data is saved into ROOT
 1976 histograms. Simulations start for a threshold T_{scint} varying in a range from 0 to 45 mm in steps
 1977 of 5 mm, where $T_{scint} = 0$ mm corresponds to the case where there isn't any threshold apply on
 1978 the input signal while $T_{scint} = 45$ mm, which is the scintillator thickness, is the case where muons
 1979 cannot arrive orthogonally onto the scintillator surface. For a given T_{scint} , a set of RPC thresholds
 1980 are considered. The RPC threshold, T_{RPC} varies from 2 mm, the thickness of the gas volume, to
 1981 3 mm in steps of 0.25 mm. For each $(T_{scint}; T_{RPC})$ pair, $N_\mu = 10^8$ muons are randomly generated
 1982 inside the muon plane described in the previous paragraph with an azimuthal angle θ chosen to follow
 1983 a $\cos^2\theta$ distribution.

1984 Planes are associated to each surface of the scintillators. Knowing muon position into the muon
 1985 plane and its direction allows us, by assuming that muons travel in a straight line, to compute the
 1986 intersection of the muon track with these planes. Applying conditions to the limits of the surfaces
 1987 of the scintillator faces then gives us an answer to whether or not the muon passed through the
 1988 scintillators. In the case the muon has indeed passed through the telescope, the path through each
 1989 scintillator is computed and muons whose path was shorter than T_{scint} are rejected and are thus
 1990 considered as having not interacted with the setup.

1991 On the contrary, if the muon is labeled as good, its position within the RPC plane is computed
 1992 and the corresponding strip, determined by geometrical tests in the case the distance through the
 1993 gas volume was enough not to be rejected because of T_{RPC} , gets a hit and several histograms
 1994 are filled in order to keep track of the generation point on the muon plane, the intersection points
 1995 of the reconstructed muons within the telescope, or on the RPC plane, the path traveled through
 1996 each individual scintillator or the gas volume, as well as other histograms. Moreover, muons fill
 1997 different histograms whether they are forward or backward coming muons. They are discriminated
 1998 according to their direction components. When a muon is generated, an (x, y, z) position is assigned
 1999 into the muon plane as well as a $(\theta; \phi)$ pair that gives us the direction it's coming from. This way,
 2000 muons satisfying the condition $0 \leq \phi < \pi$ are designated as backward coming muons while muons
 2001 satisfying $\pi \leq \phi < 2\pi$ as forward coming muons.

2002 This simulation is then repeated for different telescope inclinations ranging in between 4 and 20°
 2003 and varying in steps of 2°. Due to this inclination and to the vertical position of the detector under
 2004 test, the muon distribution reconstructed in the detector plane is asymmetrical. The choice as been
 2005 made to chose a skew distribution formula to fit the data built as the multiplication of gaussian and
 2006 sigmoidal curves together. A typical gaussian formula is given as 5.1 and has three free parameters
 2007 as A_g , its amplitude, \bar{x} , its mean value and σ , its root mean square. Sigmoidal curves as given by
 2008 formula 5.2 are functions converging to 0 and A_s as x diverges. The inflection point is given as x_i
 2009 and λ is proportional to the slope at $x = x_i$. In the limit where $\lambda \rightarrow \infty$, the sigmoid becomes a
 2010 step function.

$$g(x) = A_g e^{-\frac{(x-\bar{x})^2}{2\sigma^2}} \quad (5.1)$$

$$s(x) = \frac{A_s}{1 + e^{-\lambda(x-x_i)}} \quad (5.2)$$

Finally, a possible representation of a skew distribution is given by formula 5.3 and is the product of 5.1 and 5.2. Naturally, here $A_{sk} = A_g \times A_s$ and represents the theoretical maximum in the limit where the skew tends to a gaussian function.

$$sk(x) = g(x) \times s(x) = A_{sk} \frac{e^{\frac{-(x-\bar{x})^2}{2\sigma^2}}}{1 + e^{-\lambda(x-x_i)}} \quad (5.3)$$

5.3.3.3 Results

Influence of T_{scint} on the muon distribution

Influence of T_{RPC} on the muon distribution

Influence of the telescope inclination on the muon distribution

Comparison to data taken at GIF without irradiation

5.3.4 Photon flux at GIF

5.3.4.1 Expectations from simulations

In order to understand and evaluate the γ flux in the GIF area, simulations had been conducted in 1999 and published by S. Agosteo et al [60]. Table 5.1 presented in this article gives us the γ flux for different distances D to the source. This simulation was done using GEANT and a Monte Carlo N-Particle (MCNP) transport code, and the flux F is given in number of γ per unit area and unit time along with the estimated error from these packages expressed in %.

Nominal ABS	Photon flux F [$s^{-1}cm^{-2}$]			
	at $D = 50$ cm	at $D = 155$ cm	at $D = 300$ cm	at $D = 400$ cm
1	$0.12 \cdot 10^8 \pm 0.2\%$	$0.14 \cdot 10^7 \pm 0.5\%$	$0.45 \cdot 10^6 \pm 0.5\%$	$0.28 \cdot 10^6 \pm 0.5\%$
2	$0.68 \cdot 10^7 \pm 0.3\%$	$0.80 \cdot 10^6 \pm 0.8\%$	$0.25 \cdot 10^6 \pm 0.8\%$	$0.16 \cdot 10^6 \pm 0.6\%$
5	$0.31 \cdot 10^7 \pm 0.4\%$	$0.36 \cdot 10^6 \pm 1.2\%$	$0.11 \cdot 10^6 \pm 1.2\%$	$0.70 \cdot 10^5 \pm 0.9\%$

Table 5.1: Total photon flux ($E\gamma \leq 662$ keV) with statistical error predicted considering a ^{137}Cs activity of 740 GBq at different values of the distance D to the source along the x -axis of irradiation field [60].

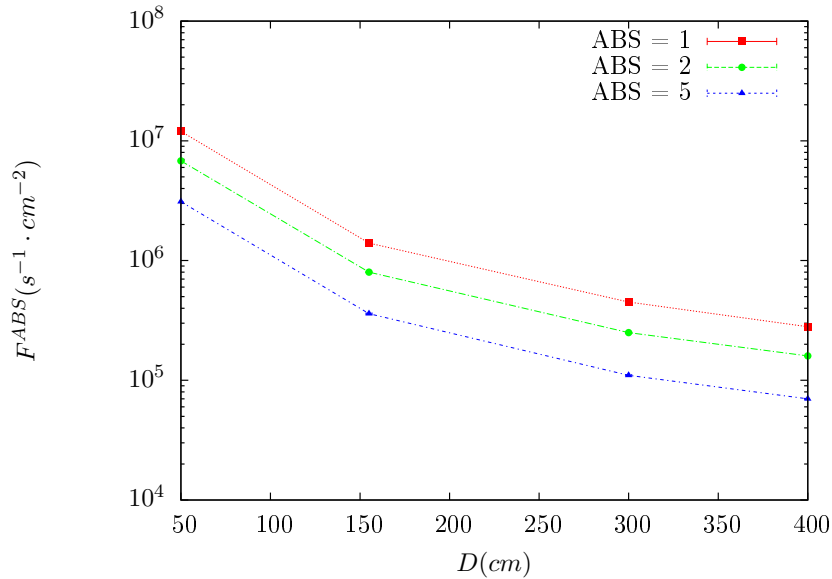


Figure 5.14: γ flux $F(D)$ is plot using values from table 5.1. As expected, the plot shows similar attenuation behaviours with increasing distance for each absorption factors.

The simulation doesn't directly provides us with an estimated flux at the level of our RPC. First of all, it is needed to extract the value of the flux from the available data contained in the original paper and then to estimate the flux in 2014 at the time the experimentation took place. Figure 5.14 that contains the data from Table 5.1. In the case of a pointlike source emitting isotropic and homogeneous gamma radiations, the gamma flux F at a distance D to the source with respect to a reference point situated at D_0 where a known flux F_0 is measured will be expressed like in Equation 5.4, assuming that the flux decreases as $1/D^2$, where c is a fitting factor.

$$F^{ABS} = F_0^{ABS} \times \left(\frac{cD_0}{D} \right)^2 \quad (5.4)$$

By rewriting Equation 5.4, it comes that :

$$c = \frac{D}{D_0} \sqrt{\frac{F^{ABS}}{F_0^{ABS}}} \quad (5.5)$$

$$\Delta c = \frac{c}{2} \left(\frac{\Delta F^{ABS}}{F^{ABS}} + \frac{\Delta F_0^{ABS}}{F_0^{ABS}} \right) \quad (5.6)$$

Finally, using Equation 5.5 and the data in Table 5.1 with $D_0 = 50$ cm as reference point, we can build Table 5.2. It is interesting to note that c for each value of D doesn't depend on the absorption factor.

Nominal ABS	Correction factor c		
	at $D = 155$ cm	at $D = 300$ cm	at $D = 400$ cm
1	$1.059 \pm 0.70\%$	$1.162 \pm 0.70\%$	$1.222 \pm 0.70\%$
2	$1.063 \pm 1.10\%$	$1.150 \pm 1.10\%$	$1.227 \pm 0.90\%$
5	$1.056 \pm 1.60\%$	$1.130 \pm 1.60\%$	$1.202 \pm 1.30\%$

Table 5.2: Correction factor c is computed thanks to formulae 5.5 taking as reference $D_0 = 50$ cm and the associated flux F_0^{ABS} for each absorption factor available in table 5.1.

2037 For the range of D/D_0 values available, it is possible to use a simple linear fit to get the evolution
 2038 of c . The linear fit will then use only 2 free parameters, a and b , as written in Equation 5.7. This gives
 2039 us the results showed in Figure 5.15. Figure 5.15b confirms that using only a linear fit to extract c is
 2040 enough as the evolution of the rate that can be obtained superimposes well on the simulation points.

$$c \left(\frac{D}{D_0} \right) = a \frac{D}{D_0} + b \quad (5.7)$$

$$F^{ABS} = F_0^{ABS} \left(a + \frac{bD_0}{D} \right)^2 \quad (5.8)$$

$$\Delta F^{ABS} = F^{ABS} \left[\frac{\Delta F_0^{ABS}}{F_0^{ABS}} + 2 \frac{\Delta a + \Delta b \frac{D_0}{D}}{a + \frac{bD_0}{D}} \right] \quad (5.9)$$

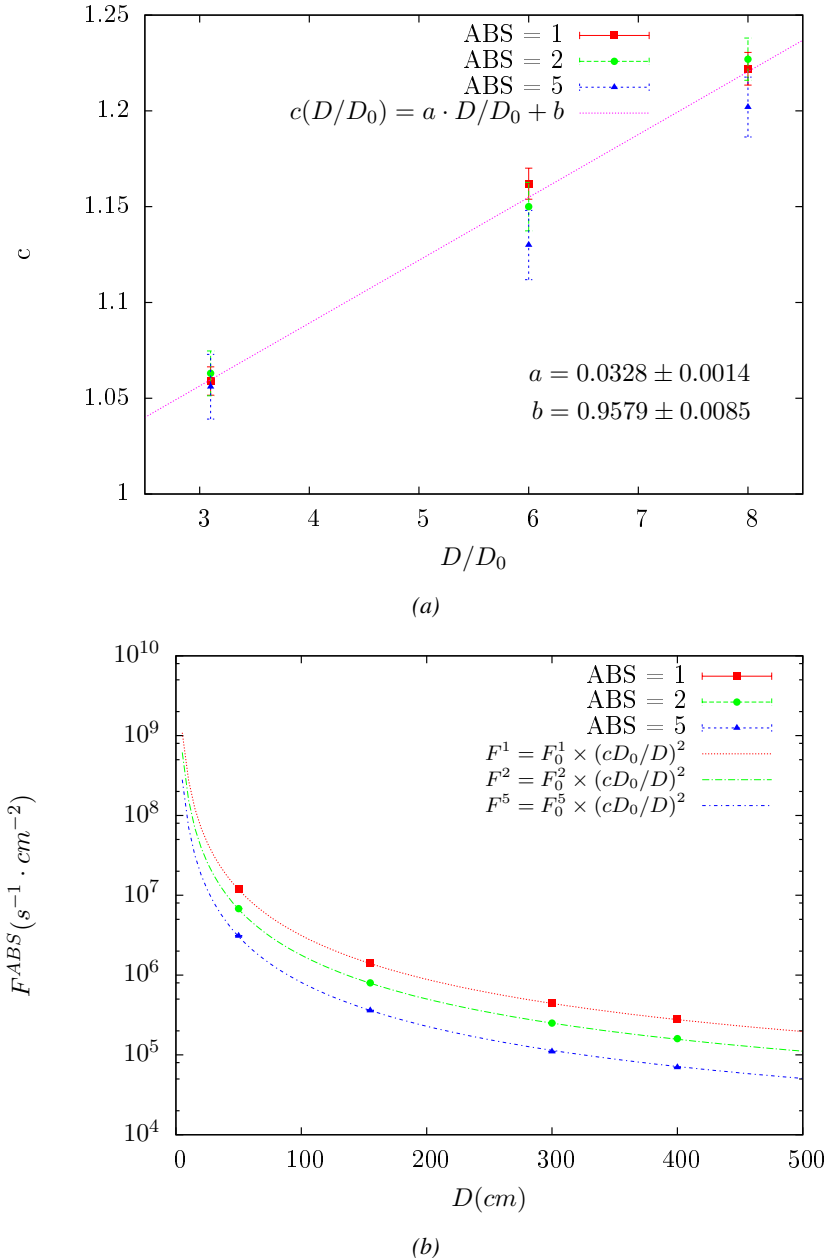


Figure 5.15: Figure 5.15a shows the linear approximation fit done via formulae 5.7 on data from table 5.2. Figure 5.15b shows a comparison of this model with the simulated flux using a and b given in figure 5.15a in formulae 5.4 and the reference value $D_0 = 50\text{cm}$ and the associated flux for each absorption factor F_0^{ABS} from table 5.1

In the case of the 2014 GIF tests, the RPC plane is located at a distance $D = 206\text{ cm}$ to the source.
 Moreover, to estimate the strength of the flux in 2014, it is necessary to consider the nuclear decay through time associated to the Cesium source whose half-life is well known ($t_{1/2} = (30.05 \pm 0.08)\text{ y}$).
 The very first source activity measurement has been done on the 5th of March 1997 while the GIF

2045 tests where done in between the 20th and the 31st of August 2014, i.e. at a time $t = (17.47 \pm 0.02)$ y
 2046 resulting in an attenuation of the activity from 740 GBq in 1997 to 494 GBq in 2014. All the needed
 2047 information to extrapolate the flux through our detector in 2014 has now been assembled, leading
 2048 to the Table 5.3. It is interesting to note that for a common RPC sensitivity to γ of $2 \cdot 10^{-3}$, the
 2049 order of magnitude of the estimated hit rate per unit area is of the order of the kHz for the fully
 2050 opened source. Moreover, taking profit of the two working absorbers, it will be possible to scan
 2051 background rates at 0 Hz, ~ 300 Hz as well as ~ 600 Hz. Without source, a good estimate of the
 2052 intrinsic performance will be available. Then at 300 Hz, the goal will be to show that the detectors
 2053 fulfill the performance certification of CMS RPCs. Then a first idea of the performance of the
 2054 detectors at higher background will be provided with absorption factors 2 (~ 600 Hz) and 1 (no
 2055 absorption). *[Here I will also put a reference to the plot showing the estimated background rate at
 2056 the level of RE3/1 in the case of HL-LHC but this one being in another chapter, I will do it later.]*

Nominal ABS	Photon flux F [$s^{-1}cm^{-2}$]			Hit rate/unit area [$Hz cm^{-2}$] at $D^{2014} = 206$ cm
	at $D_0^{1997} = 50$ cm	at $D^{1997} = 206$ cm	at $D^{2014} = 206$ cm	
1	$0.12 \cdot 10^8 \pm 0.2\%$	$0.84 \cdot 10^6 \pm 0.3\%$	$0.56 \cdot 10^6 \pm 0.3\%$	1129 ± 32
2	$0.68 \cdot 10^7 \pm 0.3\%$	$0.48 \cdot 10^6 \pm 0.3\%$	$0.32 \cdot 10^6 \pm 0.3\%$	640 ± 19
5	$0.31 \cdot 10^7 \pm 0.4\%$	$0.22 \cdot 10^6 \pm 0.3\%$	$0.15 \cdot 10^6 \pm 0.3\%$	292 ± 9

Table 5.3: The data at D_0 in 1997 is taken from [60]. In a second step, using Equations 5.8 and 5.9, the flux at D can be estimated in 1997. Then, taking into account the attenuation of the source activity, the flux at D can be estimated at the time of the tests in GIF in 2014. Finally, assuming a sensitivity of the RPC to γ $s = 2 \cdot 10^{-3}$, an estimation of the hit rate per unit area is obtained.

²⁰⁵⁷ **5.3.4.2 Dose measurements**

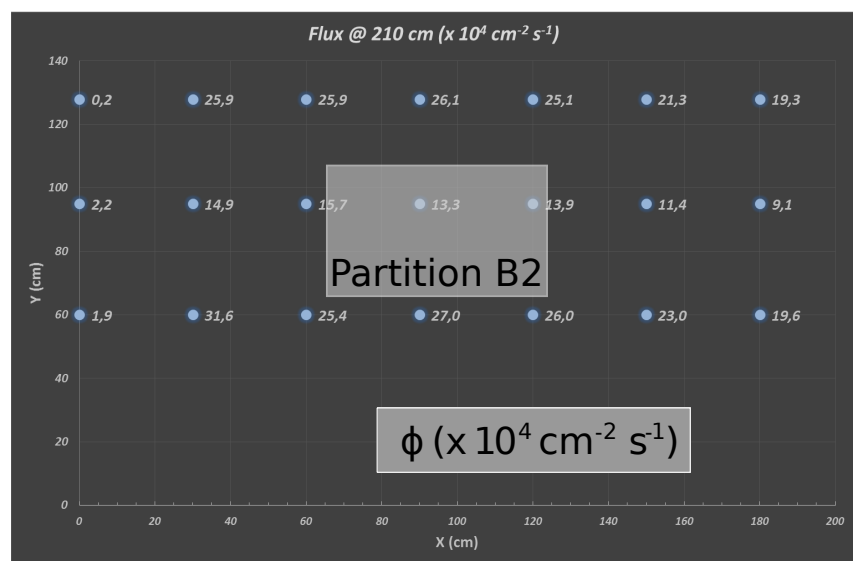


Figure 5.16: Dose measurements has been done in a plane corresponding to the tents front side. This plan is 1900 mm away from the source. As explained in the first chapter, a lens-shaped lead filter provides a uniform photon flux in the vertical plan orthogonal to the beam direction. If the second line of measured fluxes is not taken into account because of lower values due to experimental equipments in the way between the source and the tent, the uniformity of the flux is well showed by the results.

2058 **5.3.5 Results and discussions**

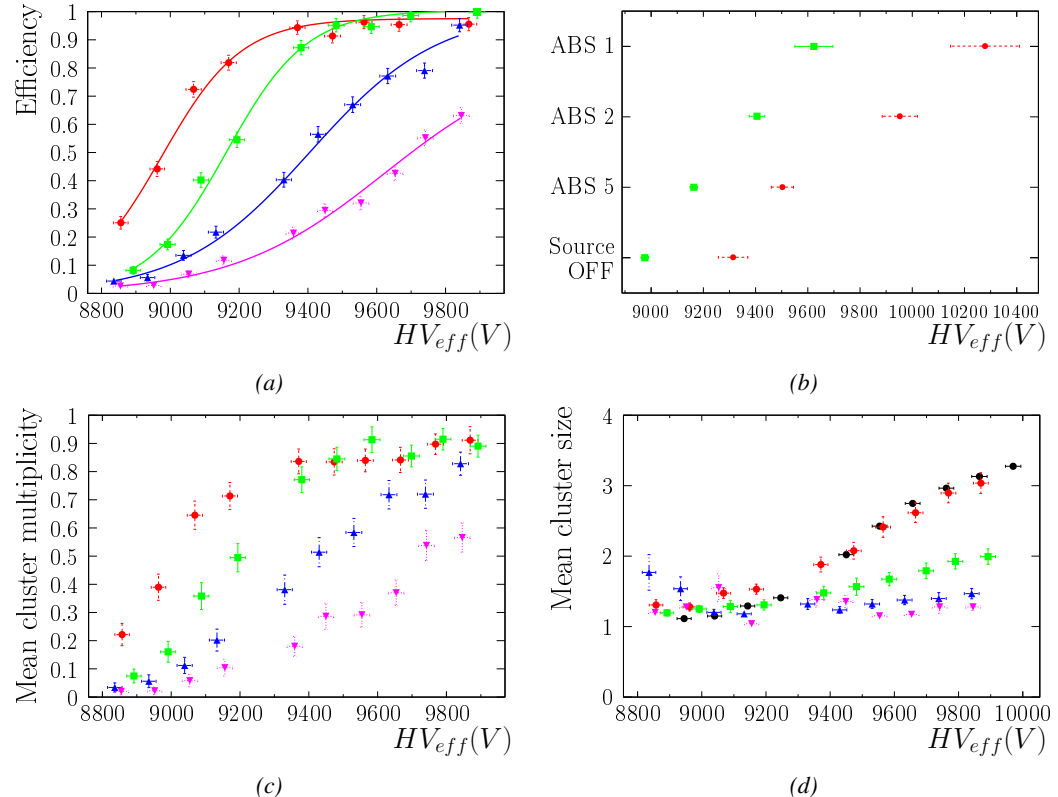


Figure 5.17

2059 5.4 Longevity tests at GIF++

2060 Longevity studies imply a monitoring of the performance of the detectors probed using a high inten-
2061 sity muon beam in a irradiated environment by periodically measuring their rate capability, the dark
2062 current running through them and the bulk resistivity of the Bakelite composing their electrodes.
2063 GIF++, with its very intense ^{137}Cs source, provides the perfect environment to perform such kind
2064 of tests. Assuming a maximum acceleration factor of 3, it is expected to accumulate the equivalent
2065 charge in 1.7 years.

2066 As the maximum background is found in the endcap, the choice naturally was made to focus the
2067 GIF++ longevity studies on endcap chambers. Most of the RPC system was installed in 2007. Nev-
2068 ertheless, the large chambers in the fourth endcap (RE4/2 and RE4/3) have been installed during
2069 LS1 in 2014. The Bakelite of these two different productions having different properties, four spare
2070 chambers of the present system were selected, two RE2,3/2 spares and two RE4/2 spares. Having
2071 two chambers of each type allows to always keep one of them non irradiated as reference, the per-
2072 formance evolution of the irradiated chamber being then compared through time to the performance
2073 of the non irradiated one.

2074 The performance of the detectors under different level of irradiation is measured periodically dur-
2075 ing dedicated test beam periods using the H4 muon beam. In between these test beam periods, the
2076 two RE2,3/2 and RE4/2 chambers selected for this study are irradiated by the ^{137}Cs source in order
2077 to accumulate charge and the gamma background is monitored, as well as the currents. The two
2078 remaining chambers are kept non-irradiated as reference detectors. Due to the limited gas flow in
2079 GIF++, the RE4 chamber remained non-irradiated until end of November 2016 where a new mass
2080 flow controller has been installed allowing for bigger volumes of gas to flow in the system.

2081 Figures 5.18 and 5.19 give us for different test beam periods, and thus for increasing integrated
2082 charge through time, a comparison of the maximum efficiency, obtained using a sigmoid-like func-
2083 tion, and of the working point of both irradiated and non irradiated chambers [49]. No aging is yet
2084 to see from this data, the shifts in γ rate per unit area in between irradiated and non irradiated detec-
2085 tors and RE2 and RE4 types being easily explained by a difference of sensitivity due to the various
2086 Bakelite resistivities of the HPL electrodes used for the electrode production.

2087 Collecting performance data at each test beam period allows us to extrapolate the maximum effi-
2088 ciency for a background hit rate of $300\text{ Hz}/\text{cm}^2$ corresponding to the expected HL-LHC conditions.
2089 Aging effects could emerge from a loss of efficiency with increasing integrated charge over time,
2090 thus Figure 5.20 helps us understand such degradation of the performance of irradiated detectors in
2091 comparison with non irradiated ones. The final answer for an eventual loss of efficiency is given in
2092 Figure 5.21 by comparing for both irradiated and non irradiated detectors the efficiency sigmoids
2093 before and after the longevity study. Moreover, to complete the performance information, the Bake-
2094 lite resistivity is regularly measured thanks to Ag scans (Figure 5.22) and the noise rate is monitored
2095 weekly during irradiation periods (Figure 5.23). At the end of 2016, no signs of aging were observed
2096 and further investigation is needed to get closer to the final integrated charge requirements proposed
2097 for the longevity study of the present CMS RPC sub-system.

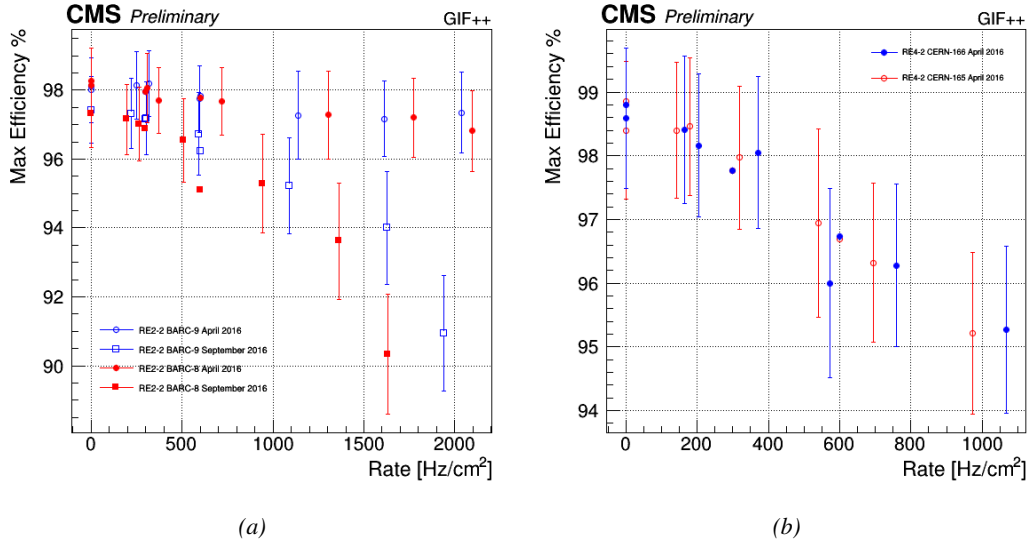


Figure 5.18: Evolution of the maximum efficiency for RE2 (5.18a) and RE4 (5.18b) chambers with increasing extrapolated γ rate per unit area at working point. Both irradiated (blue) and non irradiated (red) chambers are shown.

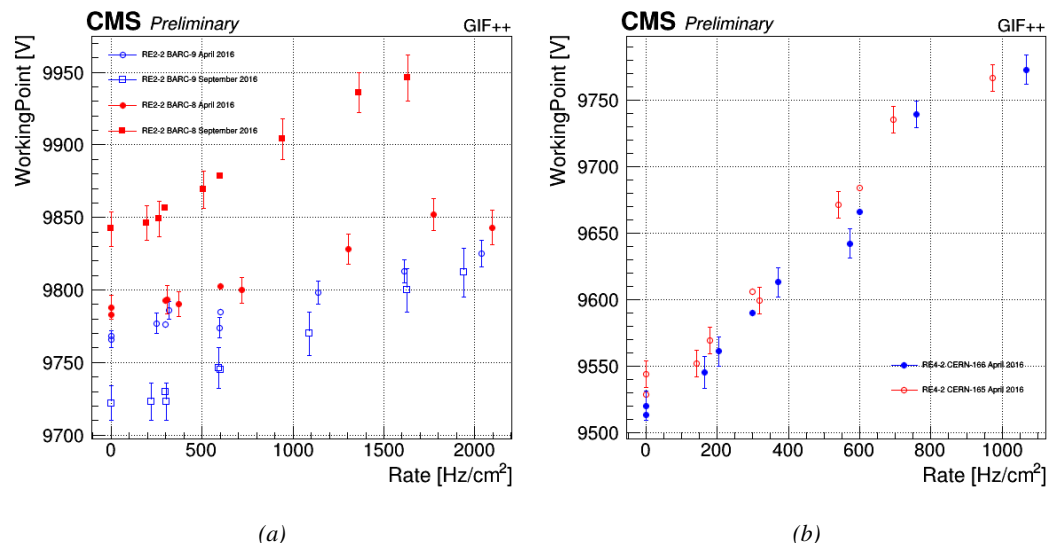


Figure 5.19: Evolution of the working point for RE2 (5.19a) and RE4 (5.19b) with increasing extrapolated γ rate per unit area at working point. Both irradiated (blue) and non irradiated (red) chambers are shown.

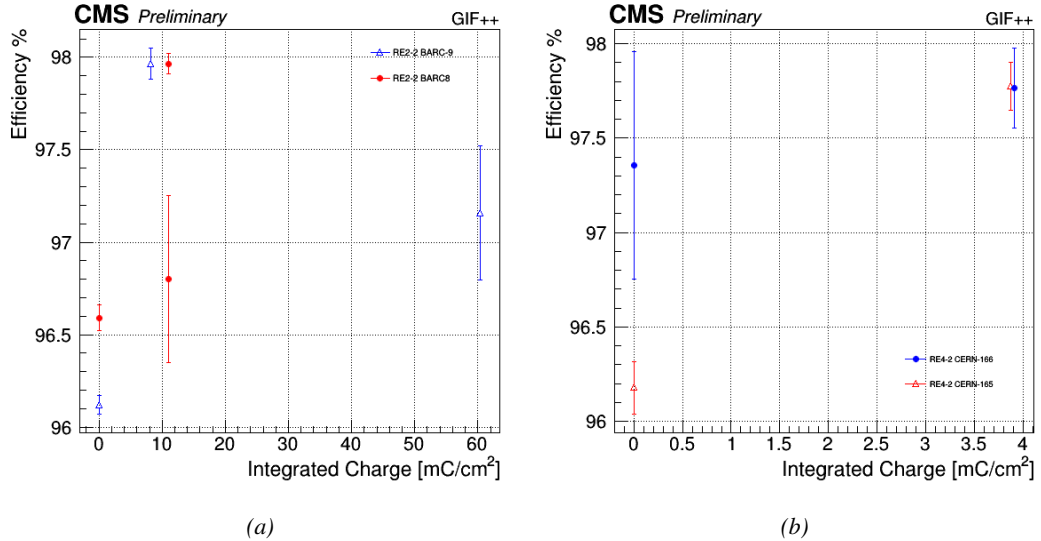


Figure 5.20: Evolution of the maximum efficiency at HL-LHC conditions, i.e. a background hit rate per unit area of 300 Hz/cm², with increasing integrated charge for RE2 (5.20a) and RE4 (5.20b) detectors. Both irradiated (blue) and non irradiated (red) chambers are shown. The integrated charge for non irradiated detectors is recorded during test beam periods and stays small with respect to the charge accumulated in irradiated chambers.

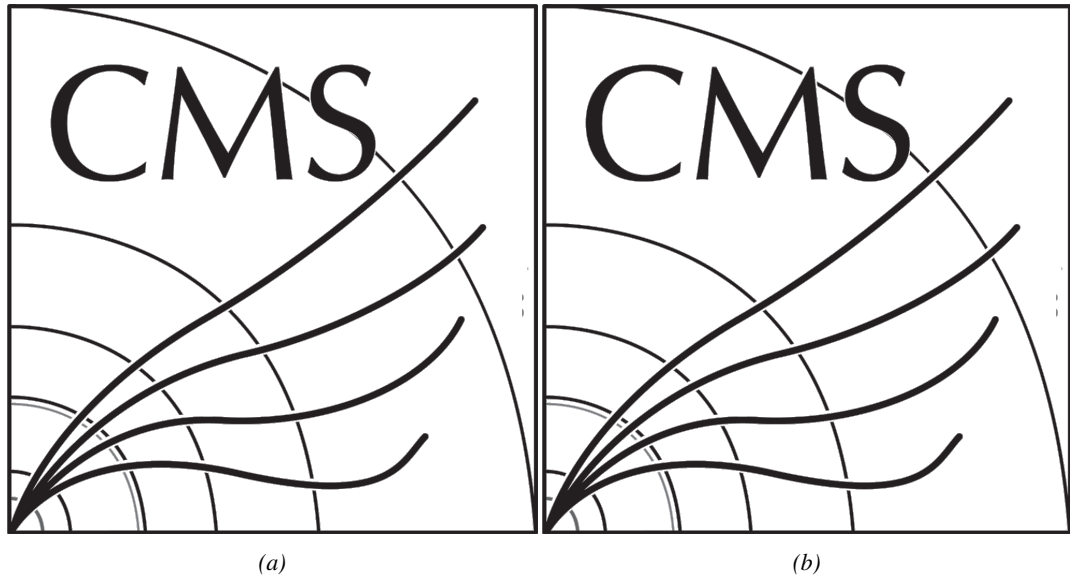


Figure 5.21: Comparison of the efficiency sigmoid before (triangles) and after (circles) irradiation for RE2 (5.21a) and RE4 (5.21b) detectors. Both irradiated (blue) and non irradiated (red) chambers are shown.

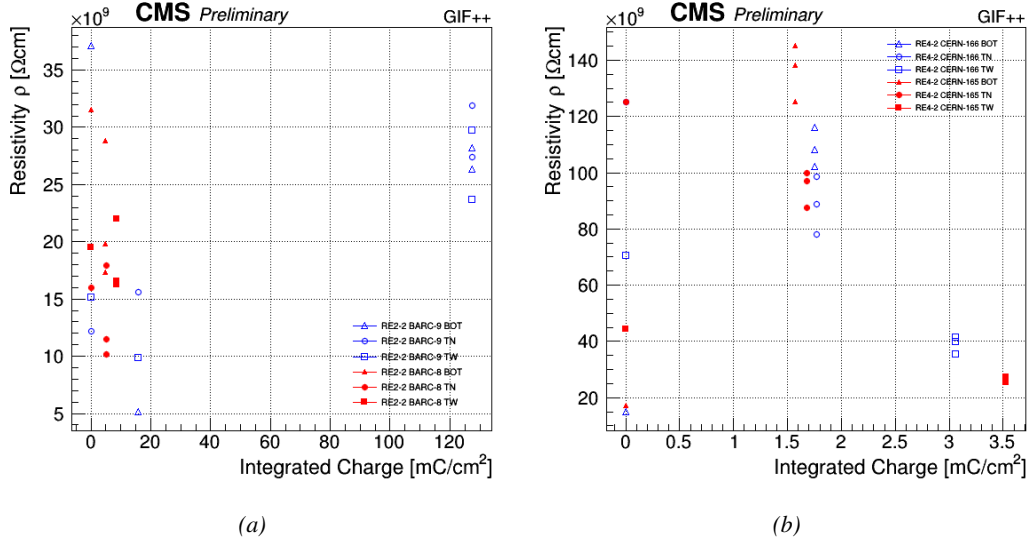


Figure 5.22: Evolution of the Bakelite resistivity for RE2 (5.22a) and RE4 (5.22b) detectors. Both irradiated (blue) and non-irradiated (red) chambers are shown.

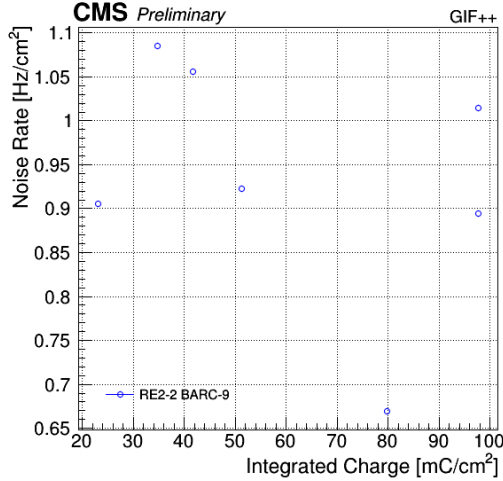


Figure 5.23: Evolution of the noise rate per unit area for the irradiated chamber RE2-2-BARC-9 only.

5.4.1 Description of the Data Acquisition

For the longevity studies, four spare chambers of the present system are used. Two spare RPCs of the RE2,3 stations as well as two spare RPCs from the new RE4 stations have been mounted in a Trolley. Six RE4 gaps are also placed in the trolley. The trolley is placed inside the GIFT++ in the upstream region of the bunker, taking the cesium source as a reference. The trolley is oriented for the detection surface of the chambers to be orthogonal to the beam line. The system can be moved along the orthogonal plane in order to have the beam in all η -partitions. For the aging the trolley is

2106 moved outside the beam line and is placed in a distance of 5.2 m to the source, which irradiates the
 2107 bunker using an attenuation filter of 2.2 which corresponds to a fluence of 10^7 gamma/cm^2 .

2108 During GIF++ operation, the data collected can be divided into different categories as several
 2109 parameters are monitored in addition to the usual RPC performance data. On one hand, to know
 2110 the performance of a chamber, it is need to measure its efficiency and to know the background
 2111 conditions in which it is operated. To do this, the hit signals from the chamber are recorded and
 2112 stored in a ROOT file via a Data Acquisition (DAQ) software. On the other hand, it is also very
 2113 important to monitor parameters such as environmental pressure and temperature, gas temperature
 2114 and humidity, RPC HV, LV, and currents, or even source and beam status. This is done through the
 2115 GIF++ web Detector Control Software (DCS) that stores this information in a database.

2116 Two different types of tests are conducted on RPCs via the DAQ. Indeed, the performance of the
 2117 detectors is measured periodically during dedicated test beam periods using the H4 muon beam. In
 2118 between these test beam periods, when the beam is not available, the chambers are irradiated by the
 2119 ^{137}Cs in order to accumulate deposited charge and the gamma background is measured.

2120 RPCs under test are connected through LVDS cables to V1190A Time-to-Digital Converter
 2121 (TDC) modules manufactured by CAEN. These modules, located in the rack area outside of the
 2122 bunker, get the logic signals sent by the chambers and save them into their buffers. Due to the
 2123 limited size of the buffers, the collected data is regularly erased and replaced. A trigger signal is
 2124 needed for the TDC modules to send the useful data to the DAQ computer via a V1718 CAEN USB
 2125 communication module.

2126 In the case of performance test, the trigger signal used for data acquisition is generated by the
 2127 coincidence of three scintillators. A first one is placed upstream outside of the bunker, a second one
 2128 is placed downstream outside of the bunker, while a third one is placed in front of the trolley, close by
 2129 the chambers. Every time a trigger is sent to the TDCs, i.e. every time a muon is detected, knowing
 2130 the time delay in between the trigger and the RPC signals, signals located in the right time window
 2131 are extracted from the buffers and saved for later analysis. Signals are taken in a time window of
 2132 400 ns centered on the muon peak (here we could show a time spectrum). On the other hand, in the
 2133 case of background rate measurement, the trigger signal needs to be "random" not to measure muons
 2134 but to look at gamma background. A trigger pulse is continuously generated at a rate of 300 Hz using
 2135 a dual timer. To integrate an as great as possible time, all signals contained within a time window of
 2136 10us prior to the random trigger signal are extracted form the buffers and saved for further analysis
 2137 (here another time spectrum to illustrate could be useful, maybe even place both spectrum together
 2138 as a single Figure).

2139 The signals sent to the TDCs correspond to hit collections in the RPCs. When a particle hits
 2140 a RPC, it induce a signal in the pickup strips of the RPC readout. If this signal is higher than the
 2141 detection threshold, a LVDS signal is sent to the TDCs. The data is then organised into 4 branches
 2142 keeping track of the event number, the hit multiplicity for the whole setup, and the time and channel
 2143 profile of the hits in the TDCs.

2144 **5.4.2 RPC current, environmental and operation parameter monitoring**

2145 In order to take into account the variation of pressure and temperature between different data taking
 2146 periods the applied voltage is corrected following the relationship :

$$2147 \quad HV_{eff} = HV_{app} \times \left(0.2 + 0.8 \cdot \frac{P_0}{P} \times \frac{T}{T_0} \right) \quad (5.10)$$

2147 where T_0 (=293 K) and P_0 (=990 mbar) are the reference values.

2148 **5.4.3 Measurement procedure**

2149 Insert a short description of the online tools (DAQ, DCS, DQM).

2150 Insert a short description of the offline tools : tracking and efficiency algorithm.

2151 Identify long term aging effects we are monitoring the rates per strip.

2152 **5.4.4 Longevity studies results**

6

2153

2154

Investigation on high rate RPCs

2155 **6.1 Rate limitations and ageing of RPCs**

2156 **6.1.1 Low resistivity electrodes**

2157 **6.1.2 Low noise front-end electronics**

2158 **6.2 Construction of prototypes**

2159 **6.3 Results and discussions**

7

2160

2161

Conclusions and outlooks

2162 **7.1 Conclusions**

2163 **7.2 Outlooks**

A

2164

2165

A data acquisition software for CAEN VME TDCs

2166

2167 Certifying detectors in the perspective of HL-LHC required to develop tools for the GIF++ experiment.
2168 Among them was the C++ Data Acquisition (DAQ) software that allows to make the communications
2169 in between a computer and TDC modules in order to retrieve the RPC data [62]. In this
2170 appendix, details about this software, as of how the software was written, how it functions and how
2171 it can be exported to another similar setup, will be given.

2172 A.1 GIF++ DAQ file tree

2173 GIF++ DAQ source code is fully available on github at https://github.com/afagot/GIF_DAQ. The software requires 3 non-optional dependencies:

- 2175 • CAEN USB Driver, to mount the VME hardware,
2176 • CAEN VME Library, to communicate with the VME hardware, and
2177 • ROOT, to organize the collected data into a TTree.

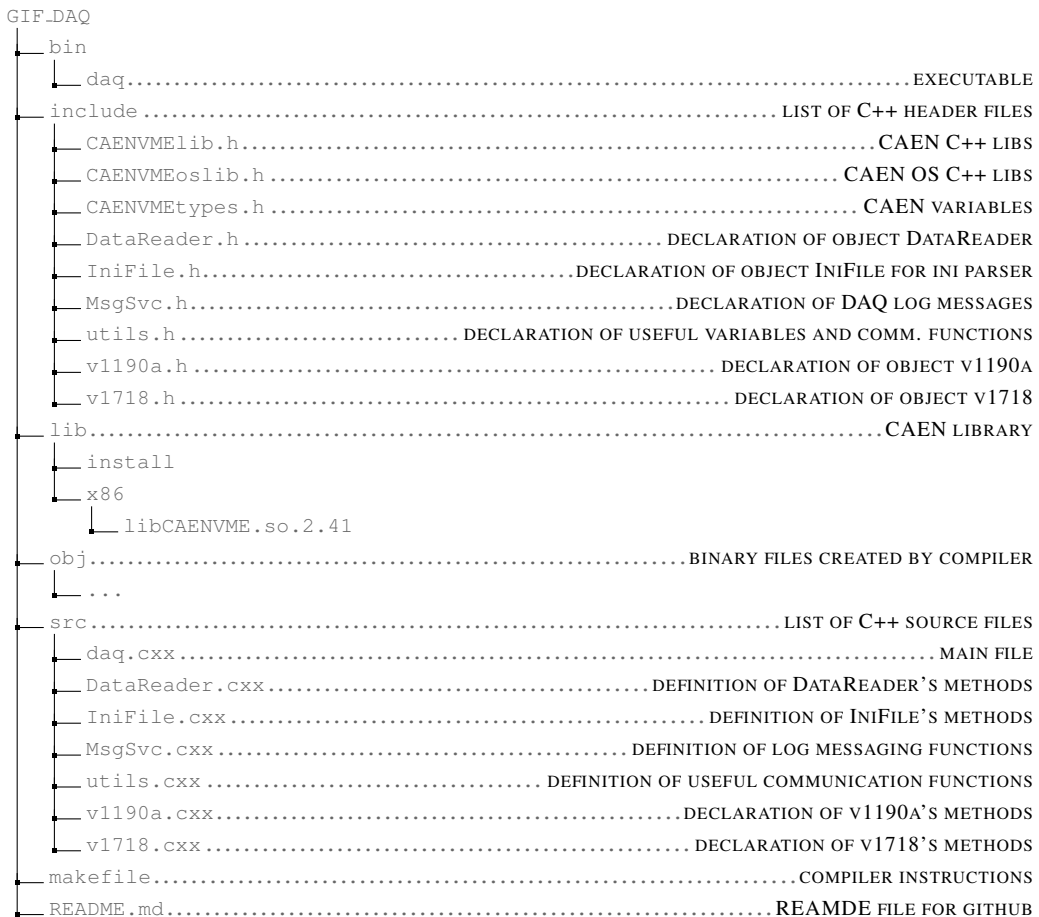
2178 The CAEN VME library will not be packaged by distributions and will need to be installed man-
2179 ually. To compile the GIF++ DAQ project via a terminal, from the DAQ folder use the command:

2180

2181 `make`

2182 The source code tree is provided below along with comments to give an overview of the files' con-
2183 tent. The different objects created for this project (`v1718`, `v1190a`, `IniFile` & `DataReader`) will be
2184 described in details in the following sections.

2185



A.2 Usage of the DAQ

GIF++ DAQ, as used in GIF++, is not a standalone software. Indeed, the system being more complexe, the DAQ only is a sub-layer of the software architecture developped to control and monitor the RPCs that are placed into the bunker for performance study in an irradiated environment. The top layer of GIF++ is a Web Detector Control System (webDCS) application. The DAQ is only called by the webDCS when data needs to be acquired. The webDCS operates the DAQ through command line. To start the DAQ, the webDCS calls:

2193

```
2194     bin/daq /path/to/the/log/file/in/the/output/data/folder
```

2195 where /path/to/the/log/file/in/the/output/data/folder is the only argument required. This
 2196 log file is important for the webDCS as this file contains all the content of the communication of the
 2197 webDCS and the different systems monitored by the webDCS. Its content is constantly displayed
 2198 during data taking for the users to be able to follow the operations. The communication messages
 2199 are normally sent to the webDCS log file via the functions declared in file MsgSvc.h, typically
 2200 MSG_INFO(string message).

2201

2202 A.3 Description of the readout setup

2203 The CMS RPC setup at GIF++ counts 5 V1190A Time-to-Digital Converter (TDC) manufactured
 2204 by CAEN [63]. V1190A are VME units accepting 128 independent Multi-Hit/Multi-Event TDC
 2205 channels whose signals are treated by 4 100 ps high performance TDC chips developed by CERN
 2206 / ECP-MIC Division. The communication between the computer and the TDCs to transfer data is
 2207 done via a V1718 VME master module also manufactured by CAEN and operated from a USB
 2208 port [64]. These VME modules are all hosted into a 6U VME 6021 powered crate manufactured by
 2209 W-Ie-Ne-R than can accommodate up to 21 VME bus cards [65]. These 3 components of the DAQ
 2210 setup are shown in Figure A.1.

2211

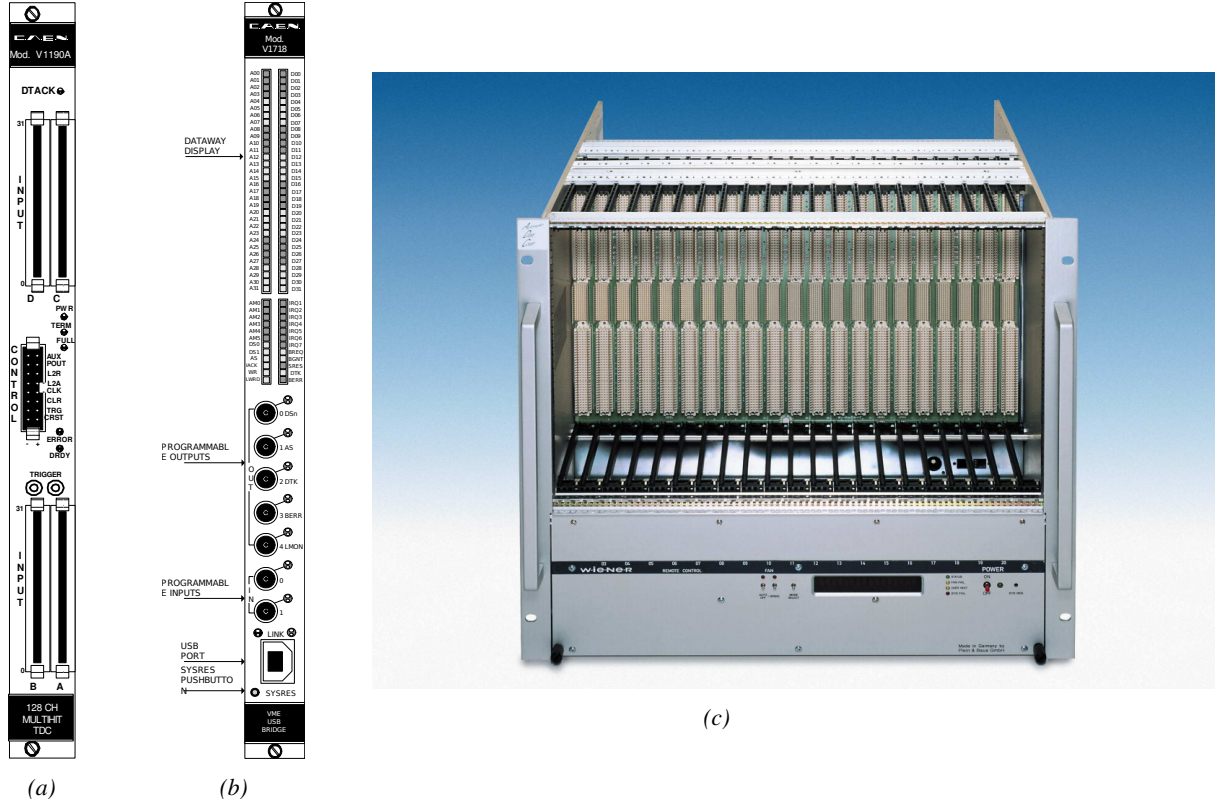


Figure A.1: (A.1a) View of the front panel of a V1190A TDC module [63]. (A.1b) View of the front panel of a V1718 Bridge module [64]. (A.1c) View of the front panel of a 6U 6021 VME crate [65].

2212

A.4 Data read-out

2213 To efficiently perform a data readout algorithm, C++ objects to handle the VME modules (TDCs
 2214 and VME bridge) have been created along with objects to store data and read the configuration file

2215 that comes as an input of the DAQ software.

2216

2217 A.4.1 V1190A TDCs

2218 The DAQ used at GIF takes profit of the *Trigger Matching Mode* offered by V1190A modules.
 2219 This setting is enabled through the method `v1190a::SetTrigMatching (int ntdcs)` where `ntdcs`
 2220 is the total number of TDCs in the setup this setting needs to be enabled for (Source Code A.1). A
 2221 trigger matching is performed in between a trigger time tag, a trigger signal sent into the TRIGGER
 2222 input of the TDC visible on Figure A.1a, and the channel time measurements, signals recorded from
 2223 the detectors under test in our case. Control over this data acquisition mode, explained through
 2224 Figure A.2, is offered via 4 programmable parameters:

- 2225 • **match window:** the matching between a trigger and a hit is done within a programmable time
 2226 window. This is set via the method

2227 `void v1190a::SetTrigWindowWidth(Uint windowHeight, int ntdcs)`

- 2228 • **window offset:** temporal distance between the trigger tag and the start of the trigger matching
 2229 window. This is set via the method

2230 `void v1190a::SetTrigWindowWidth(Uint windowHeight, int ntdcs)`

- 2231 • **extra search margin:** an extended time window is used to ensure that all matching hits are
 2232 found. This is set via the method

2233 `void v1190a::SetTrigSearchMargin(Uint searchMargin, int ntdcs)`

- 2234 • **reject margin:** older hits are automatically rejected to prevent buffer overflows and to speed
 2235 up the search time. This is set via the method

2236 `void v1190a::SetTrigRejectionMargin(Uint rejectMargin, int ntdcs)`

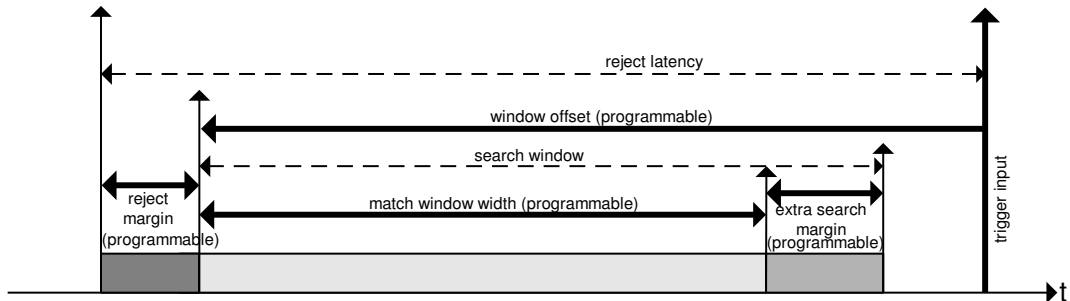


Figure A.2: Module V1190A Trigger Matching Mode timing diagram [63].

2237 Each of these 4 parameters are given in number of clocks, 1 clock being 25 ns long. It is easy to
 2238 understand at this level that there are 3 possible functioning settings:

- 2239 • **1:** the match window is entirely contained after the trigger signal,

- 2240 • **2:** the match window overlaps the trigger signal, or

- 2241 • **3:** the match window is entirely contained before the trigger signal as displayed on Figure A.2.

2242 In both the first and second cases, the sum of the window width and of the offset can be set to
2243 a maximum of 40 clocks, which corresponds to 1 μ s. Evidently, the offset can be negative, allowing
2244 for a longer match window, with the constraint of having the window ending at most 1 μ s after the
2245 trigger signal. In the third case, the maximum negative offset allowed is of 2048 clocks (12 bit) cor-
2246 responding to 51.2 μ s, the match window being strictly smaller than the offset. In the case of GIF++,
2247 the choice has been made to use this last setting by delaying the trigger signal. During the studies
2248 performed in GIF++, both the efficiency of the RPCs, probed using a muon beam, and the noise or
2249 gamma background rate are monitored. The extra search and reject margins are left unused.
2250 To probe the efficiency of RPC detectors, the trigger time tag is provided by the coïncidence of
2251 scintillators when a bunch of muons passes through GIF++ area is used to trigger the data acquisi-
2252 tion. For this measurement, it is useful to reduce the match window width only to contain the muon
2253 information. Indeed, the delay in between a trigger signal and the detection of the corresponding
2254 muon in the RPC being very contant (typically a few tens of ns due to jitter and cable length), the
2255 muon signals are very localised in time. Thus, due to a delay of approximalety 325 ns in between
2256 the muons and the trigger, the settings where chosen to have a window width of 24 clocks (600 ns)
2257 centered on the muon peak thanks to a negative offset of 29 clocks (725 ns).
2258 On the otherhand, monitoring the rates don't require for the DAQ to look at a specific time window.
2259 It is important to integrate enough time to have a robust measurement of the rate as the number of
2260 hits per time unit. The triggerring signal is provided by a pulse generator at a frequency of 300 Hz
2261 to ensure that the data taking occurs in a random way, with respect to beam physics, to probe only
2262 the irradiation spectrum on the detectors. The match window is set to 400 clocks (10 μ s) and the
2263 negative offset to 401 clocks as it needs to exceed the value of the match window.

```

2264
class v1190a
{
    private :
        long             Handle;
        vector<Data32>   Address;
        CVDataWidth      DataWidth;
        CVAddressModifier AddressModifier;

    public:

        v1190a(long handle, IniFile *inifile, int ntdcs);
        ~v1190a();
        Data16 write_op_reg(Data32 address, int code, string error);
        Data16 read_op_reg(Data32 address, string error);
        void Reset(int ntdcs);
        void Clear(int ntdcs);
        void TestWR(Data16 value,int ntdcs);
        void CheckTDCStatus(int ntdcs);
        void CheckCommunication(int ntdcs);
        void SetTDCTestMode(Data16 mode,int ntdcs);
        void SetTrigMatching(int ntdcs);
        void SetTrigTimeSubtraction(Data16 mode,int ntdcs);
        void SetTrigWindowWidth(Uint windowHeight,int ntdcs);
        void SetTrigWindowOffset(Uint windowOffset,int ntdcs);
        void SetTrigSearchMargin(Uint searchMargin,int ntdcs);
        void SetTrigRejectionMargin(Uint rejectMargin,int ntdcs);
        void GetTrigConfiguration(int ntdcs);
        void SetTrigConfiguration(IniFile *inifile,int ntdcs);
        void SetTDCDetectionMode(Data16 mode,int ntdcs);
        void SetTDCResolution(Data16 lsb,int ntdcs);
        void SetTDCDeadTime(Data16 time,int ntdcs);
        void SetTDCHeadTrailer(Data16 mode,int ntdcs);
        void SetTDCEventSize(Data16 size,int ntdcs);
        void SwitchChannels(IniFile *inifile,int ntdcs);
        void SetIRQ(Data32 level, Data32 count,int ntdcs);
        void SetBlockTransferMode(Data16 mode,int ntdcs);
        void Set(IniFile *inifile,int ntdcs);
        void CheckStatus(CVErrorCodes status) const;
        int ReadBlockD32(Uint tdc, const Data16 address,
                         Data32 *data, const Uint words, bool ignore_berr);
        Uint Read(RAWData *DataList,int ntdcs);
};

2265

```

2266 *Source Code A.1: Description of C++ object v1190a.*

2267 The v1190a object, defined in the DAQ software as in Source Code A.1, offers the possibility to
 2268 concatenate all TDCs in the readout setup into a single object containing a list of hardware addresses
 2269 (addresses to access the TDCs' buffer through the VME crate) and each constructor and method acts
 2270 on the list of TDCs.

2271

2272 A.4.2 DataReader

2273 Enabled thanks to v1190a::SetBlockTransferMode(Data16 mode, int ntdcs), the data transfer
 2274 is done via Block Transfer (BLT). Using BLT allows to tranfer a fixed number of events called a
 2275 *block*. This is used together with an Almost Full Level (AFL) of the TDCs' output buffers, defined

2276 through `v1190a::SetIRQ(Data32 level, Data32 count, int ntdcs)`. This AFL gives the maximum amount of 32735 words (16 bits, corresponding to the depth of a TDC output buffer) that can
 2277 written in a buffer before an Interrupt Request (IRQ) is generated and seen by the VME Bridge,
 2278 stopping the data acquisition to transfer the content of each TDC buffers before resuming. For each
 2280 trigger, 6 words or more are written into the TDC buffer:

- 2281 • a **global header** providing information of the event number since the beginning of the data
 acquisition,
- 2283 • a **TDC header**,
- 2284 • the **TDC data** (*if any*), 1 for each hit recorded during the event, providing the channel and the
 time stamp associated to the hit,
- 2286 • a **TDC error** providing error flags,
- 2287 • a **TDC trailer**,
- 2288 • a **global trigger time tag** that provides the absolute trigger time relatively to the last reset,
 and
- 2290 • a **global trailer** providing the total word count in the event.

2291 As previously described in Section ??, CMS RPC FEEs provide us with 100 ns long LVDS output
 2292 signals that are injected into the TDCs' input. Any avalanche signal that gives a signal above the
 2293 FEEs threshold is thus recorded by the TDCs as a hit within the match window. Each hit is assigned
 2294 to a specific TDC channel with a time stamp, with a precision of 100 ps. The reference time, $t_0 = 0$,
 2295 is provided by the beginning of the match window. Thus for each trigger, coming from a scintillator
 2296 coïncidence or the pulse generator, a list of hits is stored into the TDCs' buffers and will then be
 2297 transferred into a ROOT Tree.

2298 When the BLT is used, it is easy to understand that the maximum number of words that have
 2299 been set as ALF will not be a finite number of events or, at least, the number of events that would
 2300 be recorded into the TDC buffers will not be a multiple of the block size. In the last BLT cycle to
 2302 tranfer data, the number of events to transfer will most probably be lower than the block size. In that
 2303 case, the TDC can add fillers at the end of the block but this option requires to send more data to the
 2304 computer and is thus a little slower. Another solution is to finish the transfer after the last event by
 2305 sending a bus error that states that the BLT reached the last event in the pile. This method has been
 2306 chosen in GIF++.

2307 Due to irradiation, an event in GIF++ can count up to 300 words per TDC. A limit of 4096 words
 2308 (12 bits) has been set to generate IRQ which represent from 14 to almost 700 events depending on
 2309 the average of hits collected per event. Then the block size has been set to 100 events with enabled
 2311 bus errors. When an AFL is reached for one of the TDCs, the VME bridge stops the acquisition by
 2312 sending a BUSY signal.

2313

```

2314     The data is then transferred one TDC at a time into a structure called RAWData (Source Code A.2).
2315
2316 struct RAWData{
2317     vector<int>           *EventList;
2318     vector<int>           *NHitsList;
2319     vector<int>           *QFlagList;
2320     vector<vector<int> >   *Channellist;
2321     vector<vector<float> > *TimeStampList;
2322 };

```

2317 *Source Code A.2: Description of data holding C++ structure `RAWData`.*

2318 In order to organize the data transfer and the data storage, an object called `DataReader` was
2319 created (Source Code A.3). On one hand, it has `v1718` and `v1190a` objects as private members for
2320 communication purposes, such as VME modules settings via the configuration file `*iniFile` or data
2321 read-out through `v1190a::Read()` and on the other hand, it contains the structure `RAWData` that allows
2322 to organise the data in vectors reproducing the tree structure of a ROOT file.

```

2323
2324 class DataReader
2325 {
2326     private:
2327     bool      StopFlag;
2328     IniFile *iniFile;
2329     Data32   MaxTriggers;
2330     v1718   *VME;
2331     int       nTDCs;
2332     v1190a  *TDCs;
2333     RAWData TDCData;
2334
2335     public:
2336     DataReader();
2337     virtual ~DataReader();
2338     void      SetIniFile(string inifilename);
2339     void      SetMaxTriggers();
2340     Data32  GetMaxTriggers();
2341     void      SetVME();
2342     void      SetTDC();
2343     int       GetQFlag(UInt it);
2344     void      Init(string inifilename);
2345     void      FlushBuffer();
2346     void      Update();
2347     string  GetFileName();
2348     void      WriteRunRegistry(string filename);
2349     void      Run();
2350 };

```

2325 *Source Code A.3: Description of C++ object `DataReader`.*

2326 Each event is transferred from `TDCData` and saved into branches of a ROOT `TTree` as 3 integers
2327 that represent the event ID (`EventCount`), the number of hits read from the TDCs (`nHits`), and the
2328 quality flag that provides information for any problem in the data transfer (`qflag`), and 2 lists of
2329 `nHits` elements containing the fired TDC channels (`TDCCh`) and their respective time stamps (`TDCTS`),
2330 as presented in Source Code A.4. The ROOT file file is named using information contained into
2331 the configuration file, presented in section A.5.2. The needed information is extracted using method
2332 `DataReader::GetFileName()` and allow to build the output filename format `ScanXXXXXX_HVX_DAQ.root`

2333 where ScanXXXXXX is a 6 digit number representing the scan number into GIFT++ database and HVX
 2334 the HV step within the scan that can be more than a single digit. An example of ROOT data file is
 2335 provided with Figure A.3.

```
2336
RAWData TDCData;
TFile *outputFile = new TFile(outputFileName.c_str(),"recreate");
TTree *RAWDataTree = new TTree("RAWData","RAWData");

int EventCount = -9;
int nHits = -8;
int qflag = -7;
vector<int> TDCCh;
vector<float> TDCTS;

RAWDataTree->Branch("EventNumber",&EventCount, "EventNumber/I");
RAWDataTree->Branch("number_of_hits",&nHits,"number_of_hits/I");
RAWDataTree->Branch("Quality_flag",&qflag,"Quality_flag/I");
RAWDataTree->Branch("TDC_channel",&TDCCh);
RAWDataTree->Branch("TDC_TimeStamp",&TDCTS);

2337
//...
//Here read the TDC data using v1190a::Read() and place it into
//TDCData for as long as you didn't collect the requested amount
//of data.
//...

for(Uint i=0; i<TDCData.EventList->size(); i++){
    EventCount = TDCData.EventList->at(i);
    nHits = TDCData.NHitsList->at(i);
    qflag = TDCData.QFlagList->at(i);
    TDCCh = TDCData.ChannelList->at(i);
    TDCTS = TDCData.TimeStampList->at(i);
    RAWDataTree->Fill();
}
```

2338 *Source Code A.4: Highlight of the data transfer and organisation within DataReader::Run() after the data has been collected into TDCData.*

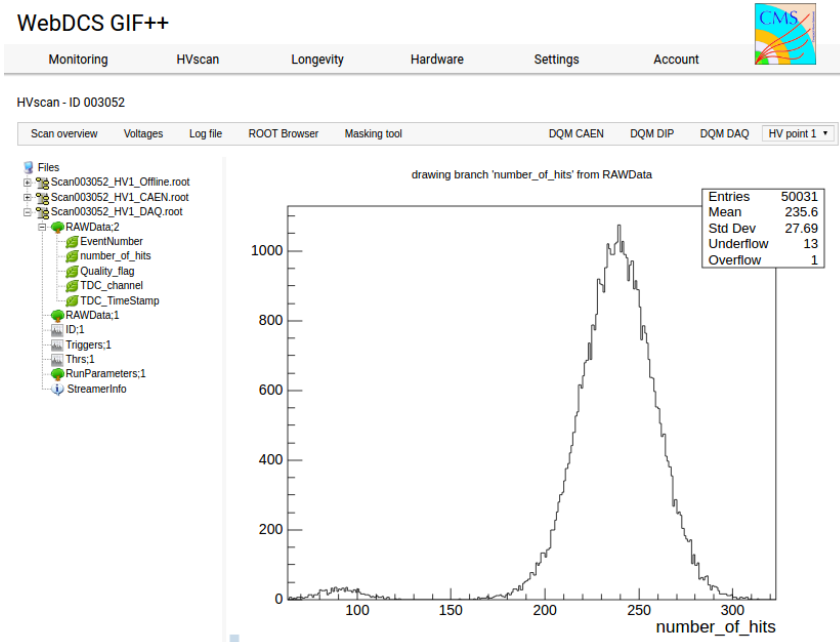


Figure A.3: Structure of the ROOT output file generated by the DAQ. The 5 branches (EventNumber, number_of_hits, Quality_flag, TDC_channel and TDC_TimeStamp) are visible on the left panel of the ROOT browser. On the right panel is visible the histogram corresponding to the variable nHits. In this specific example, there were approximately 50k events recorded to measure the gamma irradiation rate on the detectors. Each event is stored as a single entry in the TTree.

2339 A.4.3 Data quality flag

2340 Among the parameters that are recorded for each event, the quality flag, defined in Source Code A.5,
 2341 is determined on the fly by checking the data recorded by every single TDC. From method `v1190a::Read()`,
 2342 it can be understood that the content of each TDC buffer is readout one TDC at a time. Entries are
 2343 created in the data list for the first TDC and then, when the second buffer is readout, events corre-
 2344 sponding to entries that have already been created to store data for the previous TDC are added to
 2345 the existing list element. On the contrary, when an event entry has not been yet created in the data
 2346 list, a new entry is created.

```
2347
typedef enum _QualityFlag {
    GOOD      = 1,
    CORRUPTED = 0
} QualityFlag;
```

2349 *Source Code A.5: Definition of the quality flag `enum`.*

2350 It is possible that each TDC buffer contains a different number of events. In cases where the first
 2351 element in the buffer list is an event for corresponds to a new entry, the difference in between the
 2352 entry from the buffer and the last entry in the data list is recorded and checked. If it is greater than 1,
 2353 what should never be the case, the quality flag is set to CORRUPTED for this TDC and an empty entry
 2354 is created in the place of the missing ones. Missing entries are believe to be the result of a bad hold

2355 on the TDC buffers at the moment of the readout. Indeed, the software hold is effective only on 1
 2356 TDC at a time and no solution as been found yet to completely block the writting in the buffers when
 2357 an IRQ is received.

2358 At the end of each BLT cycle, the ID of the last entry stored for each TDC buffer is not recorded.
 2359 When starting the next cycle, if the first entry in the pile corresponds to an event already existing
 2360 in the list, the readout will start from this list element and will not be able to check the difference
 2361 in between this entry's ID and the one of the last entry that was recorded for this TDC buffer in
 2362 the previous cycle. In the case events were missing, the flag stays at its initial value of 0, which is
 2363 similar to CORRUPTED and it is assumed that then this TDC will not contribute to `number_of_hits`,
 2364 `TDC_channel` or `TDC_TimeStamp`.

2365 Finally, since there will be 1 `RAWData` entry per TDC for each event (meaning `nTDCs` entries,
 2366 referring to `DataReader` private attribute), the individual flags of each TDC will be added together.
 2367 The final format is an integer composed `nTDCs` digits where each digit is the flag of a specific TDC.
 2368 This is constructed using powers of 10 like follows:

```
2369 TDC 0: QFlag = 100 × _QualityFlag
2370 TDC 1: QFlag = 101 × _QualityFlag
2371 ...
2372 TDC N: QFlag = 10N × _QualityFlag
```

2373 and the final flag to be with N digits:

```
2374 QFlag = n....3210
```

2375 each digit being 1 or 0. Below is given an example with a 4 TDCs setup.

2376 If all TDCs were good : `QFlag = 1111`,

2377 but if TDC 2 was corrupted : `QFlag = 1011`.

2378 When data taking is over and the data contained in the dynamical `RAWData` structure is transferred
 2379 to the ROOT file, all the 0s are changed into 2s by calling the method `DataReader::GetQFlag()`.
 2380 This will help translating the flag without knowing the number of TDCs beforehand. Indeed, a flag
 2381 111 could be due to a 3 TDC setup with 3 good individual TDC flags or to a more than 3 TDC setup
 2382 with TDCs those ID is greater than 2 being CORRUPTED, thus giving a 0.

2383 The quality flag has been introduced quite late, in October 2017 only, to the list of GIFT++ DAQ
 2384 parameters to be recorded into the output ROOT file. Before this addition, the missing data, corrupting
 2385 the quality for the offline analysis, was contributing to artificially fill data with lower multiplicity.
 2386 Looking at `TBranch number_of_hits` provides an information about the data of the full GIFT++
 2387 setup. When a TDC is not able to transfer data for a specific event, the effect is a reduction of the
 2388 total number of hits recorded in the full setup, this is what can be seen from Figure A.4. After offline
 2389 reconstruction detector by detector, the effect of missing events can be seen in the artificially filled
 2390 bin at multiplicity 0 shown in Figure A.5. Nonetheless, for data with high irradiation levels, as it is
 2391 the case for Figure A.5a, discarding the fake multiplicity 0 data can be done easily during the offline
 2392 analysis. At lower radiation, the missing events contribution becomes more problematic as the mul-
 2393 tiplicity distribution overlaps the multiplicity 0 and that in the same time the proportion of missing

2394 events decreases. Attempts to fit the distribution with a Poisson or skew distribution function were
 2395 not conclusive and this very problem has been at the origin of the quality flag that allows to give a
 2396 non ambiguous information about each event quality.

2397

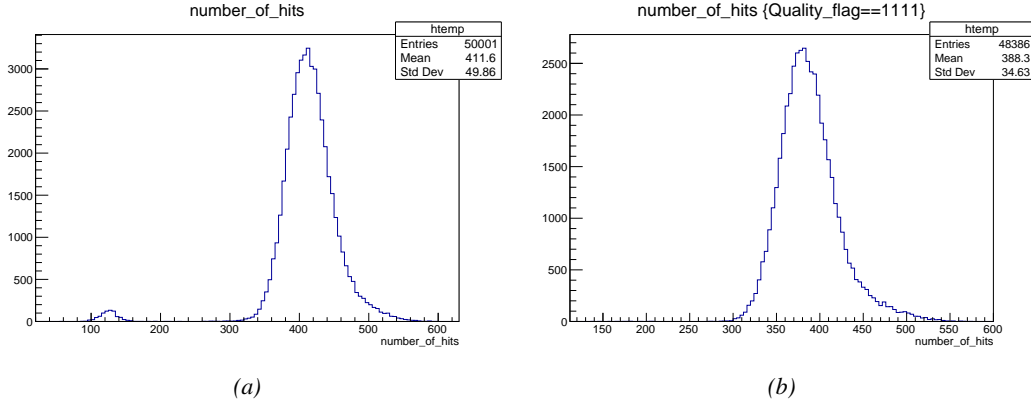


Figure A.4: The effect of the quality flag is explained by presenting the content of TBranch `number_of_hits` of a data file without `Quality_flag` in Figure A.4a and the content of the same TBranch for data corresponding to a `Quality_flag` where all TDCs were labelled as `GOOD` in Figure A.4b taken with similar conditions. It can be noted that the number of entries in Figure A.4b is slightly lower than in Figure A.4a due to the excluded events.

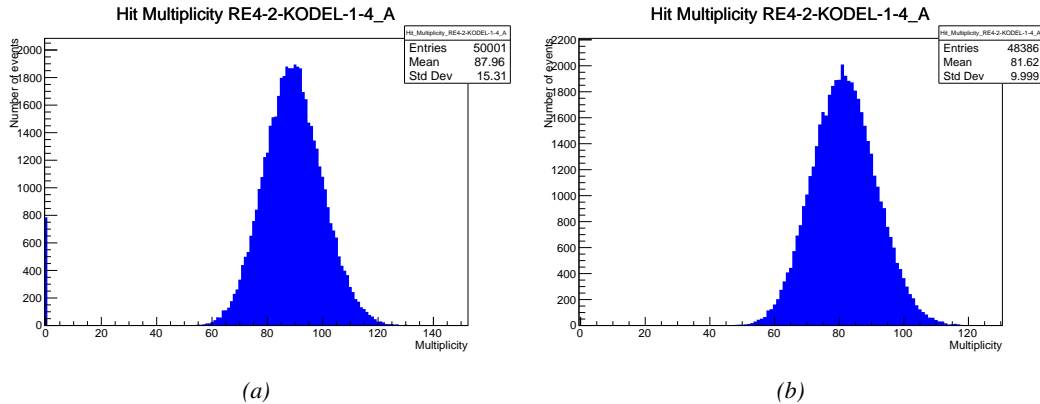


Figure A.5: Using the same data as previously showed in Figure A.4, the effect of the quality flag is explained by presenting the reconstructed hit multiplicity of a data file without `Quality_flag` in Figure A.5a and the reconstructed content of the same RPC partition for data corresponding to a `Quality_flag` where all TDCs were labelled as `GOOD` in Figure A.5b taken with similar conditions. The artificial high content of bin 0 is completely suppressed.

A.5 Communications

2398 To ensure data readout and dialog in between the machine and the TDCs or in between the webDCS
 2399 and the DAQ, different communication solutions were used. First of all, it is important to have a
 2400

2401 module to allow the communication in between the TDCs and the computer from which the DAQ
 2402 operates. When this communication is effective, shifters using the webDCS to control data taking
 2403 can thus send instructions to the DAQ.

2404

2405 A.5.1 V1718 USB Bridge

2406 In the previous section, the data transfer has been discussed. The importance of the `v1718` object
 2407 (Source Code A.6), used as private member of `DataReader`, was not explicated. VME master
 2408 modules are used for communication purposes as they host the USB port that connects the pow-
 2409 ered crate buffer to the computer where the DAQ is installed. From the source code point of view,
 2410 this object is used to control the communication status, by reading the returned error codes with
 2411 `v1718::CheckStatus()`, or to check for IRQs coming from the TDCs through `v1718::CheckIRQ()`.
 2412 Finally, to ensure that triggers are blocked at the hardware level, a NIM pulse is sent out of one of the
 2413 5 programmable outputs (`v1718::SendBUSY()`) to the VETO of the coincidence module where the
 2414 trigger signals originate from. As long as this signal is ON, no trigger can reach the TDCs anymore.
 2415

```
2416
  class v1718{
    private:
      int Handle;
      Data32 Data;           // Data
      CVIRQLevels Level;    // Interrupt level
      CVAddressModifier AM;   // Addressing Mode
      CVDataWidth dataSize;  // Data Format
      Data32 BaseAddress;    // Base Address

    public:
      v1718(IniFile *inifile);
      ~v1718();
      long GetHandle(void) const;
      int SetData(Data16 data);
      Data16 GetData(void);
      int SetLevel(CVIRQLevels level);
      CVIRQLevels GetLevel(void);
      int SetAM(CVAddressModifier am);
      CVAddressModifier GetAM(void);
      int SetDatasize(CVDataWidth datasize);
      CVDataWidth GetDataSize(void);
      int SetBaseAddress(Data16 baseaddress);
      Data16 GetBaseAddress(void);
      void CheckStatus(CVErrorCodes status) const;
      void CheckIRQ();
      void SetPulsers();
      void SendBUSY(BusyLevel level);
  };

```

2417 *Source Code A.6: Description of C++ object v1718.*

2418 A.5.2 Configuration file

2419 The DAQ software takes as input a configuration file written using INI standard [66]. This file is
 2420 partly filled with the information provided by the shifters when starting data acquisition using the
 2421 webDCS, as shown by Figure A.6. This information is written in section [`General`] and will later

2422 be stored in the ROOT file that contains the DAQ data as can be seen from Figure A.3. Indeed,
 2423 another `TTree` called `RunParameters` as well as the 2 histograms `ID`, containing the scan number,
 2424 start and stop time stamps, and `Triggers`, containing the number of triggers requested by the shifter,
 2425 are available in the data files. Moreover, `ScanID` and `HV` are then used to construct the file name
 2426 thanks to the method `DataReader::GetFileName()`.

Chamber	RE2-2-NPD-BARC-8	RE4-2-CERN-106	RE2-3-NPD-BARC-9	RE4-2-CERN-105	RE4-2-KODEL-1-4	Max triggers
HV _{eff} 1	8600	8500	8600	8500	6500	
HV _{eff} 2	8700	8600	8700	8600	6600	
HV _{eff} 3	8800	8700	8800	8700	6700	
HV _{eff} 4	8900	8800	8900	8800	6800	
HV _{eff} 5	9000	8900	9000	8900	6900	
HV _{eff} 6	9100	9000	9100	9000	7000	
HV _{eff} 7	9200	9100	9200	9100	7100	
HV _{eff} 8	9300	9200	9300	9200	7200	
HV _{eff} 9	9400	9300	9400	9300	7300	
HV _{eff} 10	9500	9400	9500	9400	7400	

Figure A.6: WebDCS DAQ scan page. On this page, shifters need to choose the type of scan (Rate, Efficiency or Noise Reference scan), the gamma source configuration at the moment of data taking, the beam configuration, and the trigger mode. These information will be stored in the DAQ ROOT output. Are also given the minimal measurement time and waiting time after ramping up of the detectors is over before starting the data acquisition. Then, the list of HV points to scan and the number of triggers for each run of the scan are given in the table underneath.

2427 The rest of the information is written beforehand in the configuration file template, as explicated
 2428 in Source Code A.7, and contains the hardware addresses to the different VME modules in the
 2429 setup as well as settings for the TDCs. As the TDC settings available in the configuration file are not
 2430 supposed to be modified, an improvement would be to remove them from the configuration file and
 2431 to hardcode them inside of the DAQ code itself or to place them into a different INI file that would
 2432 host only the TDC settings to lower the probability for a bad manipulation of the configuration file
 2433 that can be modified from one of webDCS' menus.

2434

```

[General]
TdcS=4
ScanID=$scanid
HV=$HV
RunType=$runtype
MaxTriggers=$maxtriggers
Beam=$beam
[VMEInterface]
Type=V1718
BaseAddress=0xFF0000
Name=VmeInterface
[TDC0]
Type=V1190A
BaseAddress=0x00000000
Name=Tdc0
StatusA00-15=1
StatusA16-31=1
StatusB00-15=1
StatusB16-31=1
StatusC00-15=1
StatusC16-31=1
StatusD00-15=1
StatusD16-31=1
[TDC1]
Type=V1190A
BaseAddress=0x11110000
Name=Tdc1
StatusA00-15=1
StatusA16-31=1
StatusB00-15=1
StatusB16-31=1
StatusC00-15=1
StatusC16-31=1
StatusD00-15=1
StatusD16-31=1
[TDC2]
Type=V1190A
BaseAddress=0x22220000
Name=Tdc2
StatusA00-15=1
StatusA16-31=1
StatusB00-15=1
StatusB16-31=1
StatusC00-15=1
StatusC16-31=1
StatusD00-15=1
StatusD16-31=1
[TDC3]
Type=V1190A
BaseAddress=0x44440000
Name=Tdc3
StatusA00-15=1
StatusA16-31=1
StatusB00-15=1
StatusB16-31=1
StatusC00-15=1
StatusC16-31=1
StatusD00-15=1
StatusD16-31=1
[TDCSettings]
TriggerExtraSearchMargin=0
TriggerRejectMargin=0
TriggerTimeSubtraction=0b1
TdcDetectionMode=0b01
TdcResolution=0b10
TdcDeadTime=0b00
TdcHeadTrailer=0b1
TdcEventSize=0b1001
TdcTestMode=0b0
BLTMode=1

```

2435

Source Code A.7: INI configuration file template for 4 TDCs. In section [General], the number of TDCs is explicitated and information about the ongoing run is given. Then, there are sections for each and every VME modules. There buffer addresses are given and for the TDCs, the list of channels to enable is given. Finally, in section [TDCSettings], a part of the TDC settings are given.

2437 In order to retrieve the information of the configuration file, the object `IniFile` has been developed
 2438 to provide an INI parser, presented in Source Code A.8. It contains private methods returning a
 2439 boolean to check the type of line written in the file, whether a comment, a group header or a key line
 2440 (`IniFile::CheckIfComment()`, `IniFile::CheckIfGroup()` and `IniFile::CheckIfToken()`). The
 2441 key may sometimes be referred to as *token* in the source code. Moreover, the private element
 2442 `FileData` is a map of `const string` to `string` that allows to store the data contained inside the
 2443 configuration file via the public method `IniFile::GetFileData()` following the formatting (see
 2444 method `IniFile::Read()`):

```
2445
 2446     string group, token, value;
 2447     // Get the field values for the 3 strings.
 2448     // Then concatenate group and token together as a single string
 2449     // with a dot separation.
 2450     token = group + "." + token;
 2451     FileData[token] = value;
```

2447 More methods have been written to translate the different keys into the right variable format
 2448 when used by the DAQ. For example, to get a `float` value out of the configuration file data, knowing
 2449 the group and the key needed, the method `IniFile::floatType()` can be used. It takes 3 arguments
 2450 being the group name and key name (both `string`), and a default `float` value used as exception in
 2451 the case the expected combination of group and key cannot be found in the configuration file. This
 2452 default value is then used and the DAQ continues on working after sending an alert in the log file for
 2453 further debugging.

```

2454 typedef map< const string, string > IniFileData;
2455
class IniFile{
    private:
        bool          CheckIfComment (string line);
        bool          CheckIfGroup(string line, string& group);
        bool          CheckIfToken(string line, string& key, string& value);
        string         FileName;
        IniFileData   FileData;
        int           Error;

    public:
        IniFile();
        IniFile(string filename);
        virtual      ~IniFile();

        // Basic file operations
        void          SetFileName(string filename);
        int           Read();
        int           Write();
        IniFileData GetFileData();

        // Data readout methods
        Data32         addressType (string groupname, string keyname, Data32
→     defaultvalue);
        long          intType     (string groupname, string keyname, long
→     defaultvalue);
        long long    longType    (string groupname, string keyname, long long
→     defaultvalue );
        string         stringType  (string groupname, string keyname, string
→     defaultvalue );
        float         floatType   (string groupname, string keyname, float
→     defaultvalue );

        // Error methods
        string         GetErrorMsg();
    };

```

2456 *Source Code A.8: Description of C++ object `IniFile` used as a parser for INI file format.*

2457 A.5.3 WebDCS/DAQ intercommunication

2458 When shifters send instructions to the DAQ via the configuration file, it is the webDCS itself that
 2459 gives the start command to the DAQ and then the 2 softwares use inter-process communication
 2460 through file to synchronise themselves. This communication file is represented by the variable **const**
 2461 **string** __runstatuspath.

2462 On one side, the webDCS sends commands or status that are readout by the DAQ:

- 2463 ● INIT, status sent when launching a scan and read via function `CtrlRunStatus(...)`,
- 2464 ● START, command to start data taking and read via function `CheckSTART()`,
- 2465 ● STOP, command to stop data taking at the end of the scan and read via function `CheckSTOP()`,
 2466 and
- 2467 ● KILL, command to kill data taking sent by user and read via function `CheckKILL()`

2468 and on the other, the DAQ sends status that are controled by the webDCS:

- 2469 ● `DAQ_RDY`, sent with `SendDAQReady()` to signify that the DAQ is ready to receive commands
2470 from the webDCS,
- 2471 ● `RUNNING`, sent with `SendDAQRunning()` to signify that the DAQ is taking data,
- 2472 ● `DAQ_ERR`, sent with `SendDAQError()` to signify that the DAQ didn't receive the expected com-
2473 mand from the webDCS or that the launch command didn't have the right number of argu-
2474 ments,
- 2475 ● `RD_ERR`, sent when the DAQ wasn't able to read the communication file, and
- 2476 ● `WR_ERR`, sent when the DAQ wasn't able to write into the communication file.

2477 **A.5.4 Example of inter-process communication cycle**

2478 Under normal conditions, the webDCS and the DAQ processes exchange commands and status via
2479 the file hosted at the address `__runstatuspath`, as explained in subsection A.5.3. An example of
2480 cycle is given in Table A.1. In this example, the steps 3 to 5 are repeated as long as the webDCS tells
2481 the DAQ to take data. A data taking cycle is the equivalent as what is called a *Scan* in GIFT++ jargon,
2482 referring to a set a runs with several HV steps. Each repetition of steps 3 to 5 is then equivalent to a
2483 single *Run*.

2484 At any moment during the data taking, for any reason, the shifter can decide that the data taking
2485 needs to be stopped before it reached the end of the scheduled cycle. Thus at any moment on the
2486 cycle, the content of the inter-process communication file will be changed to `KILL` and the DAQ will
2487 shut down right away. The DAQ checks for `KILL` signals every 5s after the TDCs configuration is
2488 over. So far, the function `CheckKILL()` has been used only inside of the data taking loop of method
2489 `DataReader::Run()` and thus, if the shifter decides to KILL the data taking during the TDC con-
2490 figuration phase or the HV ramping in between 2 HV steps, the DAQ will not be stopped smoothly
2491 and a *force kill* command will be sent to stop the DAQ process that is still awake on the computer.
2492 Improvements can be brought on this part of the software to make sure that the DAQ can safely
2493 shutdown at any moment.

2496 **A.6 Software export**

2497 In section A.2 was discussed the fact that the DAQ as written in its last version is not a standalone
2498 software. It is possible to make it a standalone program that could be adapted to any VME setup
2499 using V1190A and V1718 modules by creating a GUI for the software or by printing the log mes-
2500 sages that are normally printed in the webDCS through the log file, directly into the terminal. This
2501 method was used by the DAQ up to version 3.0 moment where the webDCS was completed. Also, it
2502 is possible to check branches of DAQ v2.X to have example of communication through a terminal.

2503
2504 DAQ v2.X is nonetheless limited in it's possibilities and requires a lot of offline manual interven-
2505 tions from the users. Indeed, there is no communication of the software with the detectors' power
2506 supply system that would allow for a user a predefine a list of voltages to operate the detectors at

step	actions of webDCS	status of DAQ	__runstatuspath
1	launch DAQ ramp voltages ramping over wait for currents stabilization	readout of IniFile configuration of TDCs	INIT
2		configuration done send DAQ ready wait for START signal	DAQ_RDY
3	waiting time over send START		START
4	wait for run to end monitor DAQ run status	data taking ongoing check for KILL signal	RUNNING
5		run over send DAQ_RDY wait for next DCS signal	DAQ_RDY
6	ramp voltages ramping over wait for currents stabilization		DAQ_RDY
3	waiting time over send START		START
4	wait for run to end monitor DAQ run status	update IniFile information data taking ongoing check for KILL signal	RUNNING
5		run over send DAQ_RDY wait for next DCS signal	DAQ_RDY
7	send command STOP	DAQ shuts down	STOP

Table A.1: Inter-process communication cycles in between the webDCS and the DAQ through file string signals.

2507 and loop over to take data without any further manual intervention. In v2.X, the data is taken for a
2508 single detector setting and at the end of each run, the softwares asks the user if he intends on taking
2509 more runs. If so, the software invites the user to set the operating voltages accordingly to what is
2510 necessary and to manual update the configuration file in consequence. This working mode can be a
2511 very first approach before an evolution and has been successfully used by colleagues from different
2512 collaborations.

2513
2514 For a more robust operation, it is recommended to develop a GUI or a web application to inter-
2515 face the DAQ. Moreover, to limit the amount of manual interventions, and thus the probability to
2516 make mistakes, it is also recommended to add an extra feature into the DAQ by installing the HV
2517 Wrapper library provided by CAEN of which an example of use in a similar DAQ software devel-
2518 opped by a master student of UGent, and called TinyDAQ, is provided on UGent's github. Then, this
2519 HV Wrapper will help you communicating with and give instructions to a CAEN HV powered crate
2520 and can be added into the DAQ at the same level where the communication with the user was made
2521 in DAQ v2.X. In case you are using another kind of power system for your detectors, it is stringly
2522 adviced to use HV modules or crates that can be remotely controled via a using C++ libraries.
2523

B

2524

2525

Details on the offline analysis package

2526 The data collected in GIF++ thanks to the DAQ described in Appendix A is difficult to interpret by
2527 a human user that doesn't have a clear idea of the raw data architecture of the ROOT data files. In
2528 order to render the data human readable, a C++ offline analysis tool was designed to provide users
2529 with detector by detector histograms that give a clear overview of the parameters monitored during
2530 the data acquisition [67]. In this appendix, details about this software in the context of GIF++, as of
2531 how the software was written and how it functions will be given.

2532 **B.1 GIF++ Offline Analysis file tree**

2533 GIF++ Offline Analysis source code is fully available on github at https://github.com/afagot/GIF_OfflineAnalysis. The software requires ROOT as non-optionnal dependency
2534 as it takes ROOT files in input and write an output ROOT file containing histograms. To compile the
2535 GIF++ Offline Analysis project is compiled with cmake. To compile, first a build/ directory must
2536 be created to compile from there:

```
2538 mkdir build
2539 cd build
2540 cmake ..
2541 make
2542 make install
```

2540 To clean the directory and create a new build directory, the bash script cleandir.sh can be used:

```
2541
2542 ./cleandir.sh
```

2543 The source code tree is provided below along with comments to give an overview of the files' con-
2544 tent. The different objects created for this project (`Infrastructure`, `Trolley`, `RPC`, `Mapping`, `RPCHit`,
2545 `RPCCluster` and `Inifile`) will be described in details in the following sections.

2546

```

GIF_OfflineAnalysis
├── bin
│   └── offlineanalysis ..... EXECUTABLE
├── build..... CMAKE COMPILATION DIRECTORY
└── ...
    ├── include..... LIST OF C++ HEADER FILES
    │   ├── Cluster.h..... DECLARATION OF OBJECT RPCCLUSTER
    │   ├── Current.h..... DECLARATION OF GETCURRENT ANALYSIS MACRO
    │   ├── GIFTrolley.h..... DECLARATION OF OBJECT TROLLEY
    │   ├── Infrastructure.h..... DECLARATION OF OBJECT INFRASTRUCTURE
    │   ├── IniFile.h..... DECLARATION OF OBJECT INI FILE FORINI PARSER
    │   ├── Mapping.h..... DECLARATION OF OBJECT MAPPING
    │   ├── MsgSvc.h..... DECLARATION OF OFFLINE LOG MESSAGES
    │   ├── OfflineAnalysis.h..... DECLARATION OF DATA ANALYSIS MACRO
    │   ├── RPCTracker.h..... DECLARATION OF OBJECT RPC
    │   ├── RPCHit.h..... DECLARATION OF OBJECT RPCHIT
    │   ├── types.h..... DEFINITION OF USEFUL VARIABLE TYPES
    │   └── utils.h..... DECLARATION OF USEFUL FUNCTIONS
    ├── obj..... BINARY FILES CREATED BY COMPILER
    └── ...
        ├── src..... LIST OF C++ SOURCE FILES
        │   ├── Cluster.cc..... DEFINITION OF OBJECT RPCCLUSTER
        │   ├── Current.cc..... DEFINITION OF GETCURRENT ANALYSIS MACRO
        │   ├── GIFTrolley.cc..... DEFINITION OF OBJECT TROLLEY
        │   ├── Infrastructure.cc..... DEFINITION OF OBJECT INFRASTRUCTURE
        │   ├── IniFile.cc..... DEFINITION OF OBJECT INI FILE FORINI PARSER
        │   ├── main.cc..... MAIN FILE
        │   ├── Mapping.cc..... DEFINITION OF OBJECT MAPPING
        │   ├── MsgSvc.cc..... DECLARATION OF OFFLINE LOG MESSAGES
        │   ├── OfflineAnalysis.cc..... DECLARATION OF DATA ANALYSIS MACRO
        │   ├── RPCTracker.cc..... DECLARATION OF OBJECT RPC
        │   ├── RPCHit.cc..... DECLARATION OF OBJECT RPCHIT
        │   └── utils.cc..... DEFINITION OF USEFUL FUNCTIONS
        ├── cleandir.sh..... BASH SCRIPT TO CLEAN BUILD DIRECTORY
        ├── CMakeLists.txt..... SET OF INSTRUCTIONS FOR CMAKE
        ├── config.h.in..... DEFINITION OF VERSION NUMBER
        └── README.md..... README FILE FOR GITHUB

```

2547

B.2 Usage of the Offline Analysis

2548

In order to use the Offline Analysis tool, it is necessary to know the Scan number and the HV Step of the run that needs to be analysed. This information needs to be written in the following format:

2550

2551

```
Scan00XXXX_HVY
```

2552

where XXXX is the scan ID and Y is the high voltage step (in case of a high voltage scan, data will be taken for several HV steps). This format corresponds to the base name of data files in the database

2553

2554 of the Gif++ webDCS. Usually, the offline analysis tool is automatically called by the webDCS at
 2555 the end of data taking or by a user from the webDCS panel if an update of the tool was brought.
 2556 Nonetheless, an expert can locally launch the analysis for tests on the Gif++ computer, or a user can
 2557 get the code on its local machine from github and download data from the webDCS for its own anal-
 2558 ysis. To launch the code, the following command can be used from the `GIF_OfflineAnalysis` folder:

2559
 2560 `bin/offlineanalysis /path/to/Scan00XXXX_HVY`

2561 where, `/path/to/Scan00XXXX_HVY` refers to the local data files. Then, the offline tool will by itself
 2562 take care of finding all available ROOT data files present in the folder, as listed below:

- 2563
 - 2564 ● `Scan00XXXX_HVY_DAQ.root` containing the TDC data as described in Appendix ?? (events, hit
 and timestamp lists), and
 - 2565 ● `Scan00XXXX_HVY_CAEN.root` containing the CAEN mainframe data recorded by the monitor-
 ing tool webDCS during data taking (HVs and currents of every HV channels). This file is
 created independently of the DAQ.

2568 **B.2.1 Output of the offline tool**

2569 **B.2.1.1 ROOT file**

2570 The analysis gives in output ROOT datafiles that are saved into the data folder and called using the
 2571 naming convention `Scan00XXXX_HVY_Offline.root`. Inside those, a list of `TH1` histograms can be
 2572 found. Its size will vary as a function of the number of detectors in the setup as each set of histograms
 2573 is produced detector by detector. For each partition of each chamber, can be found:

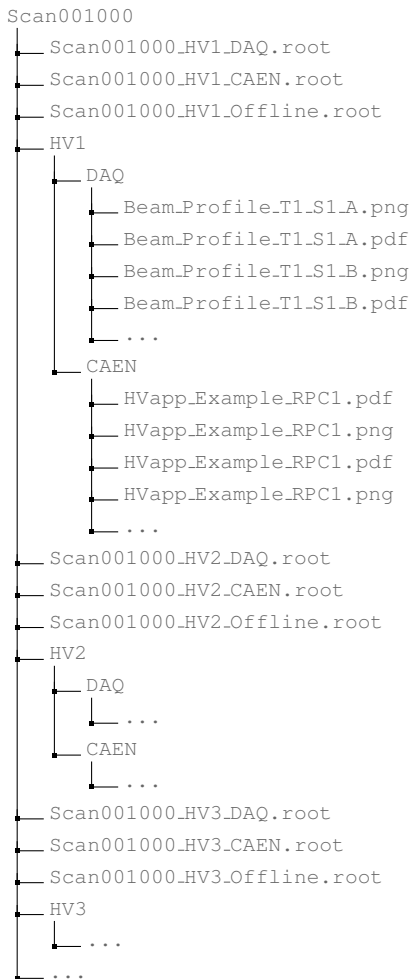
- 2574
 - 2575 ● `Time_Profile_Tt_Sc_p` shows the time profile of all recorded events (number of events per
 time bin),
 - 2576 ● `Hit_Profile_Tt_Sc_p` shows the hit profile of all recorded events (number of events per chan-
 nel),
 - 2578 ● `Hit_Multiplicity_Tt_Sc_p` shows the hit multiplicity (number of hits per event) of all recorded
 events (number of occurrences per multiplicity bin),
 - 2580 ● `Strip_Mean_Noise_Tt_Sc_p` shows noise/gamma rate per unit area for each strip in a se-
 lected time range. After filters are applied on `Time_Profile_Tt_Sc_p`, the filtered version
 of `Hit_Profile_Tt_Sc_p` is normalised to the total integrated time and active detection area
 of a single channel,
 - 2584 ● `Strip_Activity_Tt_Sc_p` shows noise/gamma activity for each strip (normalised version of
 previous histogram - strip activity = strip rate / average partition rate),
 - 2586 ● `Strip_Homogeneity_Tt_Sc_p` shows the *homogeneity* of a given partition ($\text{homogeneity} = \exp(-\text{strip rates standard deviation(strip rates in partition/average partition rate)})$),
 - 2588 ● `mask_Strip_Mean_Noise_Tt_Sc_p` shows noise/gamma rate per unit area for each masked
 strip in a selected time range. Offline, the user can control the noise/gamma rate and decide to
 mask the strips that are judged to be noisy or dead. This is done via the *Masking Tool* provided
 by the webDCS,

- 2592 ● `mask_Strip_Activity_Tt_Sc_p` shows noise/gamma activity per unit area for each masked
2593 strip with respect to the average rate of active strips,
- 2594 ● `NoiseCSize_H_Tt_Sc_p` shows noise/gamma cluster size, a cluster being constructed out of
2595 adjacent strips giving a signal at the *same time* (hits within a time window of 25 ns),
- 2596 ● `NoiseCMult_H_Tt_Sc_p` shows noise/gamma cluster multiplicity (number of reconstructed
2597 clusters per event),
- 2598 ● `Chip_Mean_Noise_Tt_Sc_p` shows the same information than `Strip_Mean_Noise_Tt_Scp` us-
2599 ing a different binning (1 chip corresponds to 8 strips),
- 2600 ● `Chip_Activity_Tt_Sc_p` shows the same information than `Strip_Activity_Tt_Scp` using
2601 chip binning,
- 2602 ● `Chip_Homogeneity_Tt_Sc_p` shows the homogeneity of a given partition using chip binning,
- 2603 ● `Beam_Profile_Tt_Sc_p` shows the estimated beam profile when taking efficiency scan. This
2604 is obtained by filtering `Time_Profile_Tt_Sc_p` to only consider the muon peak where the
2605 noise/gamma background has been subtracted. The resulting hit profile corresponds to the
2606 beam profile on the detector channels,
- 2607 ● `L0_Efficiency_Tt_Sc_p` shows the level 0 efficiency that was estimated **without** muon track-
2608 ing,
- 2609 ● `MuonCSize_H_Tt_Sc_p` shows the level 0 muon cluster size that was estimated **without** muon
2610 tracking, and
- 2611 ● `MuonCMult_H_Tt_Sc_p` shows the level 0 muon cluster multiplicity that was estimated **without**
2612 muon tracking.

2613 In the histogram labels, t stands for the trolley number (1 or 3), c for the chamber slot label in
2614 trolley t and p for the partition label (A, B, C or D depending on the chamber layout) as explained
2615 in Chapter 5.4.

2616 In the context of GIF++, an extra script called by the webDCS is called to extract the histograms
2617 from the ROOT files. The histograms are then stored in PNG and PDF formats into the correspond-
2618 ing folder (a single folder per HV step, so per ROOT file). the goal is to then display the histograms
2619 on the Data Quality Monitoring (DQM) page of the webDCS in order for the users to control the
2620 quality of the data taking at the end of data taking. An example of histogram organisation is given
2621 below:

2622



2624 *Here can put some screens from the webDCS to show the DQM and the plots available to users.*
 2625

2626 **B.2.1.2 CSV files**

2627 Moreover, up to 3 CSV files can be created depending on which ones of the 3 input files were in the
 2628 data folder:

- 2629 • `Offline-Corrupted.csv`, is used to keep track of the amount of data that was corrupted and
 2630 removed from old data format files that don't contain any data quality flag.
- 2631 • `Offline-Current.csv`, contains the summary of the currents and voltages applied on each
 2632 RPC HV channel.
- 2633 • `Offline-L0-EffC1.csv`, is used to write the efficiencies, cluster size and cluster multiplicity
 2634 of efficiency runs. Note that `L0` refers here to *Level 0* and means that the results of efficiency and
 2635 clusterization are a first approximation calculated without performing any muon tracking in

2636 between the different detectors. This offline tool provides the user with a preliminar calculation
 2637 of the efficiency and of the muon event parameters. Another analysis software especially
 2638 dedicated to muon tracking is called on selected data to retrieve the results of efficiency and
 2639 muon clusterization using a tracking algorithm to discriminate noise or gamma from muons
 2640 as muons are the only particles that pass through the full setup, leaving hits than can be used
 2641 to reconstruct their tracks.

- 2642 • `Offline-Rate.csv`, is used to write the noise or gamma rates measured in the detector readout
 2643 partitions.

2644 Note that these 4 CSV files are created along with their *headers* (`Offline-[...]-Header.csv`
 2645 containing the names of each data columns) and are automatically merged together when the offline
 2646 analysis tool is called from the webDCS, contrary to the case where the tool is runned locally from
 2647 the terminal as the merging bash script is then not called. Thus, the resulting files, used to make
 2648 official plots, are:

- 2649 • `Corrupted.csv`,
 2650 • `Current.csv`,
 2651 • `L0-EffCl.csv`.
 2652 • `Rate.csv`.

2653 B.3 Analysis inputs and information handling

2654 The usage of the Offline Analysis tool as well as its output have been presented in the previous section.
 2655 It is now important to dig further and start looking at the source code and the inputs necessary
 2656 for the tool to work. Indeed, other than the raw ROOT data files that are analysed, more information
 2657 needs to be imported inside of the program to perform the analysis such as the description of the
 2658 setup inside of GIFT++ at the time of data taking (number of trolleys, of RPCs, dimensions of the
 2659 detectors, etc...) or the mapping that links the TDC channels to the coresponding RPC channels in
 2660 order to translate the TDC information into human readable data. 2 files are used to transmit all this
 2661 information:
 2662

- 2663 • `Dimensions.ini`, that provides the necessary setup and RPC information, and
 2664 • `ChannelsMapping.csv`, that gives the link between the TDC and RPC channels as well as the
 2665 *mask* for each channel (masked or not?).

2666 B.3.1 Dimensions file and InFile parser

2667 This input file, present in every data folder, allows the analysis tool to know of the number of active
 2668 trolleys, the number of active RPCs in those trolleys, and the details about each RPCs such as
 2669 the number of RPC gaps, the number of pseudo-rapidity partitions (for CMS-like prototypes), the
 2670 number of strips per partion or the dimensions. To do so, there are 3 types of groups in the INI file
 2671 architecture. A first general group, appearing only once at the head of the document, gives information
 2672 about the number of active trolleys as well as their IDs, as presented in Source Code B.1. For

2673 each active trolley, a group similar to Source Code B.2 can be found containing information about
 2674 the number of active detectors in the trolley and their IDs. Each trolley group as a `Tt` name format,
 2675 where `t` is the trolley ID. Finally, for each detector stored in slots of an active trolley, there is a group
 2676 providing information about their names and dimensions, as shown in Source Code B.3. Each slot
 2677 group as a `TtSs` name format, where `s` is the slot ID of trolley `t` where the active RPC is hosted.

```
2678 [General]
2679 nTrolleys=2
TrolleysID=13
```

2680 *Source Code B.1: Example of `[General]` group as might be found in `Dimensions.ini`. In Gif++, only 2 trolleys are available to hold RPCs and place them inside of the bunker for irradiation. The IDs of the trolleys are written in a single string as "13" and then read character by character by the program.*

```
2681 [T1]
nSlots=4
SlotsID=1234
```

2682 *Source Code B.2: Example of trolley group as might be found in `Dimensions.ini`. In this example, the file tells that there are 4 detectors placed in the holding slots of the trolley `T1` and that their IDs, written as a single string variable, are 1, 2, 3 and 4.*

```
2683 [T1S1]
Name=RE2-2-NPD-BARC-8
Partitions=3
Gaps=3
Gap1=BOT
Gap2=TN
Gap3=TW
AreaGap1=11694.25
AreaGap2=6432
AreaGap3=4582.82
Strips=32
ActiveArea-A=157.8
ActiveArea-B=121.69
ActiveArea-C=93.03
```

2684 *Source Code B.3: Example of slot group as might be found in `Dimensions.ini`. In this example, the file provides information about a detector named `RE2-2-NPD-BARC-8`, having 3 pseudo-rapidity readout partitions and stored in slot `S1` of trolley `T1`. This is a CMS RE2-2 type of detector. This information will then be used for example to compute the rate per unit area calculation.*

2685 This information is readout and stored in a C++ object called `IniFile`, that parses the information
 2686 in the INI input file and stores it into a local buffer for later use. This INI parser is the exact same
 2687 one that was previously developed for the Gif++ DAQ and described in Appendix A.5.2.

2688 B.3.2 TDC to RPC link file and Mapping

2689 The same way the INI dimension file information is stored using `map`, the channel mapping and mask
 2690 information is stored and accessed through `map`. First of all, the mapping CSV file is organised into
 2691 3 columns separated by tabulations (and not by commas, as expected for CSV files as it is easier using
 2692 streams to read tab or space separated data using C++):

2693

2694 RPC_channel TDC_channel mask

2695 using as formatting for each field:

2696
2697 TSCCC TCCC M

2698 TSCCC is a 5-digit integer where T is the trolley ID, s the slot ID in which the RPC is held insite
2699 the trolley T and ccc is the RPC channel number, or *strip* number, that can take values up to
2700 3-digits depending on the detector,

2701 TCCC is a 4 digit integer where T is the TDC ID, ccc is the TDC channel number that can take values
2702 in between 0 and 127, and

2703 M is a 1-digit integer indicating if the channel should be considered ($M = 1$) or discarded ($M = 0$)
2704 during analysis.

2705 This mapping and masking information is readout and stored thanks to the object `Mapping`, pre-
2706 sented in Source Code B.4. Similarly to `IniFile` objects, this class has private methods. The first
2707 one, `Mapping::CheckIfNewLine()` is used to find the newline character '`\n`' or return character
2708 '`\r`' (depending on which kind of operating system interacted with the file). This is used for the
2709 simple reason that the masking information has been introduced only during the year 2017 but the
2710 channel mapping files exist since 2015 and the very beginning of data taking at GIF++. This means
2711 that in the older data folders, before the upgrade, the channel mapping file only had 2 columns, the
2712 RPC channel and the TDC channel. For compatibility reasons, this method helps controling the
2713 character following the readout of the 2 first fields of a line. In case any end of line character is
2714 found, no mask information is present in the file and the default $M = 1$ is used. On the contrary, if
2715 the next character was a tabulation or a space, the mask information is present.

2716 Once the 3 fields have been readout, the second private method `Mapping::CheckIfTDCCh()` is
2717 used to control that the TDC channel is an existing TDC channel. Finally, the information is stored
2718 into 3 different maps (`Link`, `ReverseLink` and `Mask`) thanks to the public method `Mapping::Read()`.
2719 `Link` allows to get the RPC channel by knowing the TDC channel while `ReverseLink` does the op-
2720 posite by returning the TDC channel by knowing the RPC channel. Finally, `Mask` returns the mask
2721 associated to a given RPC channel.

```

2722 typedef map<Uint,Uint> MappingData;

2723 class Mapping {
    private:
        bool          CheckIfNewLine(char next);
        bool          CheckIfTDCCh(Uint channel);
        string         FileName;
        MappingData   Link;
        MappingData   ReverseLink;
        MappingData   Mask;
        int           Error;

    public:
        Mapping();
        Mapping(string baseName);
        ~Mapping();

        void SetFileName(const string filename);
        int Read();
        Uint GetLink(Uint tdcchannel);
        Uint GetReverse(Uint rpcchannel);
        Uint GetMask(Uint rpcchannel);
};


```

2724 *Source Code B.4: Description of C++ object Mapping used as a parser for the channel mapping and mask file.*

B.4 Description of GIF++ setup within the Offline Analysis tool

2726 In the previous section, the tool input files have been discussed. The dimension file information is
 2727 stored in a map hosted by the `IniFile` object. But this information is then used to create a series of
 2728 new objects that helps defining the GIF++ infrastructure directly into the Offline Analysis. Indeed,
 2729 from the `RPC`, to the more general `Infrastructure`, every element of the GIF++ infrastrucutre is
 2730 recreated for each data analysis based on the information provided in input. All this information
 2731 about the infrastructure will be used to assign each hit signal to a specific strip channel of a specific
 2732 detector, and having a specific active area. This way, rate per unit area calculation is possible.
 2733

B.4.1 RPC objects

2735 `RPC` objects have been developped to represent physical active detectors in GIF++ at the moment
 2736 of data taking. Thus, there are as many `RPC` objects created during the analysis than there were
 2737 active RPCs tested during a run. Each `RPC` hosts the information present in the corresponding INI
 2738 slot group, as shown in B.3, and organises it using a similar architecture. This can be seen from
 2739 Source B.5.

2740 To make the object more compact, the lists of gap labels, of gap active areas and strip active
 2741 areas are stored into `vector` dynamical containers. `RPC` objects are always contructed thanks to the
 2742 dimension file information stored into the `IniFILE` and their ID, using the format `TtSs`. Using the
 2743 `RPC` ID, the constructor calls the methods of `IniFILE` to initialise the `RPC`. The other constructors
 2744 are not used but exist in case of need. Finally, some getters have been written to access the different
 2745 private parameters storing the detector information.

```

2746 class RPC{
2747     private:
        string      name;           //RPC name as in webDCS database
        Uint        nGaps;          //Number of gaps in the RPC
        Uint        nPartitions;    //Number of partitions in the RPC
        Uint        nStrips;         //Number of strips per partition
        vector<string> gaps;       //List of gap labels (BOT, TOP, etc...)
        vector<float>  gapGeo;        //List of gap active areas
        vector<float>  stripGeo;      //List of strip active areas

        public:
        RPC();
        RPC(string ID, IniFile* geofile);
        RPC(const RPC& other);
        ~RPC();
        RPC& operator=(const RPC& other);

        string GetName();
        Uint GetNGaps();
        Uint GetNPartitions();
        Uint GetNStrips();
        string GetGap(Uint g);
        float GetGapGeo(Uint g);
        float GetStripGeo(Uint p);
    };

```

2748 *Source Code B.5: Description of C++ objects RPC that describe each active detectors used during data taking.*

2749 B.4.2 Trolley objects

2750 Trolley objects have been developped to represent physical active trolleys in GIFT++ at the moment
 2751 of data taking. Thus, there are as many trolley objects created during the analysis than there were
 2752 active trolleys hosting tested RPCs during a run. Each Trolley hosts the information present in the
 2753 corresponding INI trolley group, as shown in B.2, and organises it using a similar architecture. In
 2754 addition to the information hosted in the INI file, these object have a dynamical container of RPC
 2755 objects, representing the active detectors the active trolley was hosting at the time of data taking.
 2756 This can been seen from Source Code B.6.

2757 Trolley objects are always contructed thanks to the dimension file information stored into the
 2758 IniFILE and their ID, using the format Tt. Using the Trolley ID, the constructor calls the methods
 2759 of IniFILE to initialise the Trolley. Retrieving the information of the RPC IDs via SlotsID, a new
 2760 RPC is constructed and added to the container RPCs for each character in the ID string. The other
 2761 constructors are not used but exist in case of need. Finally, some getters have been written to access
 2762 the different private parameters storing the trolley and detectors information.

```

2763
class Trolley{
    private:
        Uint          nSlots; //Number of active RPCs in the considered trolley
        string        SlotsID; //Active RPC IDs written into a string
        vector<RPC*> RPCs;   //List of active RPCs

    public:
        //Constructors, destructor and operator =
        Trolley();
        Trolley(string ID, IniFile* geofile);
        Trolley(const Trolley& other);
        ~Trolley();
        Trolley& operator=(const Trolley& other);

        //Get GIFTrolley members
        Uint  GetNSlots();
        string GetSlotsID();
        Uint   GetSlotID(Uint s);

        //Manage RPC list
        RPC*  GetRPC(Uint r);
        void  DeleteRPC(Uint r);

        //Methods to get members of RPC objects stored in RPCs
        string GetName(Uint r);
        Uint   GetNGaps(Uint r);
        Uint   GetNPartitions(Uint r);
        Uint   GetNStrips(Uint r);
        string GetGap(Uint r, Uint g);
        float  GetGapGeo(Uint r, Uint g);
        float  GetStripGeo(Uint r, Uint p);
    };

```

Source Code B.6: Description of C++ objects `Trolley` that describe each active trolley used during data taking.

2766 B.4.3 Infrastructure object

2767 The `Infrastructure` object has been developped to represent the GIFT++ bunker area dedicated to
 2768 CMS RPC experiments. With this very specific object, all the information about the CMS RPC
 2769 setup within GIFT++ at the moment of data taking is stored. It hosts the information present in the
 2770 corresponding INI general group, as shown in B.1, and organises it using a similar architecture. In
 2771 addition to the information hosted in the INI file, this object have a dynamical container of `Trolley`
 2772 objects, representing the active tolleys in GIFT++ area. This can be seen from Source Code B.7.

2773 The `Infrastructure` object is always contructed thanks to the dimension file information stored
 2774 into the `IniFILE`. Retrieving the information of the trolley IDs via `TrolleysID`, a new `Trolley` is
 2775 constructed and added to the container `Trolleys` for each character in the ID `string`. By extension,
 2776 it is easy to understand that the process described in Section B.4.2 for the construction of RPCs
 2777 takes place when a trolley is constructed. The other constructors are not used but exist in case of
 2778 need. Finally, some getters have been written to access the different private parameters storing the
 2779 infrastructure, tolleys and detectors information.

```

2780
class Infrastructure {
    private:
        Uint             nTrolleys;   //Number of active Trolleys in the run
        string          TrolleysID; //Active trolley IDs written into a string
        vector<Trolley*> Trolleys; //List of active Trolleys (struct)

    public:
        //Constructors and destructor
        Infrastructure();
        Infrastructure(IniFile* geofile);
        Infrastructure(const Infrastructure& other);
        ~Infrastructure();
        Infrastructure& operator=(const Infrastructure& other);

        //Get Infrastructure members
        Uint  GetNTrolleys();
        string GetTrolleysID();
        Uint  GetTrolleyID(Uint t);

2781
        //Manage Trolleys
        Trolley* GetTrolley(Uint t);
        void     DeleteTrolley(Uint t);

        //Methods to get members of GIFTrolley objects stored in Trolleys
        Uint  GetNSlots(Uint t);
        string GetSlotsID(Uint t);
        Uint  GetSlotID(Uint t, Uint s);
        RPC*  GetRPC(Uint t, Uint r);

        //Methods to get members of RPC objects stored in RPCs
        string GetName(Uint t, Uint r);
        Uint  GetNGaps(Uint t, Uint r);
        Uint  GetNPartitions(Uint t, Uint r);
        Uint  GetNStrips(Uint t, Uint r);
        string GetGap(Uint t, Uint r, Uint g);
        float  GetGapGeo(Uint t, Uint r, Uint g);
        float  GetStripGeo(Uint t, Uint r, Uint p);
    };

```

Source Code B.7: Description of C++ object *Infrastructure* that contains the full information about CMS RPC experiment in GIF++.

2783 B.5 Handeling of data

2784 As discussed in Appendix A.4.2, the raw data as a `TTree` architecture where every entry is related to
 2785 a trigger signal provided by a muon or a random pulse, whether the goal of the data taking was to
 2786 measure the performance of the detector or the noise/gamma background respectively. Each of these
 2787 entries, referred also as events, contain a more or less full list of hits in the TDC channels to which
 2788 the detectors are connected. To this list of hits corresponds a list of time stamps, marking the arrival
 2789 of the hits within the TDC channel.

2790 The infrastructure of the CMS RPC experiment within GIF++ being defined, combining the
 2791 information about the raw data with the information provided by both the mapping/mask file and the
 2792 dimension file allows to build new physical objects that will help in computing efficiency or rates.

2793 B.5.1 RPC hits

2794 The raw data stored in the ROOT file as output of the GIFT++ DAQ, is readout by the analysis tool
 2795 using the structure `RAWData` presented in Source Code B.9 that differs from the structure presented
 2796 in Appendix A.4.2 as it is not meant to hold all of the data contained in the ROOT file. In this sense,
 2797 this structure is in the case of the offline analysis tool not a dynamical object and will only be storing
 2798 a single event contained in a single entry of the `TTree`.

```
2799
  class RPCHit {
    private:
      Uint Channel;      //RPC channel according to mapping (5 digits)
      Uint Trolley;     //0, 1 or 3 (1st digit of the RPC channel)
      Uint Station;     //Slot where is held the RPC in Trolley (2nd digit)
      Uint Strip;       //Physical RPC strip where the hit occurred (last 3
→   digits)
      Uint Partition;   //Readout partition along eta segmentation
      float TimeStamp; //Time stamp of the arrival in TDC

    public:
      //Constructors, destructor & operator =
      RPCHit();
      RPCHit(Uint channel, float time, Infrastructure* Infra);
      RPCHit(const RPCHit& other);
      ~RPCHit();
      RPCHit& operator=(const RPCHit& other);

      //Get RPCHit members
      Uint GetChannel();
      Uint GetTrolley();
      Uint GetStation();
      Uint GetStrip();
      Uint GetPartition();
      float GetTime();
    };

    typedef vector<RPCHit> HitList;
    typedef struct GIFHitList { HitList rpc[NTROLLEYS][NSLOTS][NPARTITIONS]; }
→   GIFHitList;

    bool SortHitbyStrip(RPCHit h1, RPCHit h2);
    bool SortHitbyTime(RPCHit h1, RPCHit h2);
  
```

2801 *Source Code B.8: Description of C++ object `RPCHit`.*

```
2802
  struct RAWData{
    int iEvent;        //Event i
    int TDCNHits;    //Number of hits in event i
    int QFlag;         //Quality flag list (1 flag digit per TDC)
    vector<Uint> *TDCCh; //List of channels giving hits per event
    vector<float> *TDCTS; //List of the corresponding time stamps
  };

```

2803 *Source Code B.9: Description of C++ structure `RAWData`.*

2804 Each member of the structure is then linked to the corresponding branch of the ROOT data tree,
 2805 as shown in the example of Source Code B.10, and using the method `GetEntry(int i)` of the ROOT
 2806 class `TTree` will update the state of the members of `RAWData`.

```

2807   TTree* dataTree = (TTree*)dataFile.Get("RAWData");
2808   RAWData data;
2809
2810   dataTree->SetBranchAddress("EventNumber", &data.iEvent);
2811   dataTree->SetBranchAddress("number_of_hits", &data.TDCNHits);
2812   dataTree->SetBranchAddress("Quality_flag", &data.QFlag);
2813   dataTree->SetBranchAddress("TDC_channel", &data.TDCCh);
2814   dataTree->SetBranchAddress("TDC_TimeStamp", &data.TDCTS);

```

2809 *Source Code B.10: Example of link in between RAWData and TTree.*

2810 The data is then analysed entry by entry and to each element of the TDC channel list, a `RPCHit` is
2811 constructed by linking each TDC channel to the corresponding RPC channel thanks to the `Mapping`
2812 object. The information carried by the RPC channel format allows to easily retrieve the trolley and
2813 slot from which the hit was recorded (see section B.3.2). Using these 2 values, the readout partition
2814 can be found by knowing the strip channel and comparing it with the number of partitions and strips
2815 per partition stored into the `Infrastructure` object.

2816 Thus `RPCHit` objects are then stored into 3D dynamical list called `GIFHitList` (Source Code B.9)
2817 where the 3 dimensions refer to the 3 layers of the readout in `GIF++` : in the bunker there are *trolleys*
2818 (τ) holding detectors in *slots* (s) and each detector readout is divided into 1 or more pseudo-rapidity
2819 *partitions* (p). Using these 3 information allows to assign an address to each readout partition and
2820 this address will point to a specific hit list.

2821

2822 B.5.2 Clusters of hits

2823 All the hits contained in the ROOT file have been sorted into the different hit lists through the
2824 `GIFHitList`. At this point, it is possible to start looking for clusters. A cluster is a group of adjacent
2825 strips getting hits within a time window of 25 ns. These strips are then assumed to be part of the same
2826 physical avalanche signal generated by a muon passing through the chamber or by the interaction of
2827 a gamma stopping into the electrodes of the RPCs.

2828 To keep the cluster information, `RPCCluster` objects have been defined as shown in Source
2829 Code B.11. Using the information of each individual `RPCHit` taken out of the hit list, it stores
2830 the cluster size (number of adjacent strips composing the cluster), the first and last hit, the center for
2831 spatial reconstruction and finally the start and stop time stamps as well as te time spread in between
2832 the first and last hit.

```

2833
class RPCCluster{
    private:
        Uint ClusterSize; //Size of cluster #ID
        Uint FirstStrip; //First strip of cluster #ID
        Uint LastStrip; //Last strip of cluster #ID
        float Center; //Center of cluster #ID ((first+last)/2)
        float StartStamp; //Time stamp of the earliest hit of cluster #ID
        float StopStamp; //Time stamp of the latest hit of cluster #ID
        float TimeSpread; //Time difference between earliest and latest hits
                           //of cluster #ID
    public:
        //Constructors, destructor & operator =
        RPCCluster();
        RPCCluster(HitList List, Uint cID, Uint cSize, Uint first, Uint firstID);
        RPCCluster(const RPCCluster& other);
        ~RPCCluster();
        RPCCluster& operator=(const RPCCluster& other);

        //Get Cluster members
        Uint GetID();
        Uint GetSize();
        Uint GetFirstStrip();
        Uint GetLastStrip();
        float GetCenter();
        float GetStart();
        float GetStop();
        float GetSpread();
    };

typedef vector<RPCCluster> ClusterList;

//Other functions to build cluster lists out of hit lists
void BuildClusters(HitList &cluster, ClusterList &clusterList);
void Clusterization(HitList &hits, TH1 *hcSize, TH1 *hcMult);

```

2835 *Source Code B.11: Description of C++ object Cluster.*

2836 To investigate the hit list of a given detector partition, the function `Clusterization()` defined
2837 in `include/Cluster.h` needs the hits in the list to be time sorted. This is achieved by calling func-
2838 tion `sort()` of library `<algorithm>` using the comparator `SortHitbyTime(RPCHit h1, RPCHit h2)`
2839 defined in `include/RPCHit.h` that returns `true` if the time stamp of hit `h1` is lower than that of `h2`.
2840 A first isolation of strips is made only based on time information. All the hits within the 25 ns win-
2841 dow are taken separately from the rest. Then, this sub-list of hits is sorted this time by ascending
2842 strip number, using this time the comparator `SortHitbyStrip(RPCHit h1, RPCHit h2)`. Finally, the
2843 groups of adjacent strips are used to construct `RPCCluster` objects that are then stored in a temporary
2844 list of clusters that is at the end of the process used to know how many clusters were reconstructed
2845 and to fill their sizes into an histogram that will allows to know the mean size of muon or gamma
2846 clusters.

2847

2848 B.6 DAQ data Analysis

2849 All the ingredients to analyse GIF++ data have been defined. This section will focus on the different
2850 part of the analysis performed on the data, from determining the type of data the tool is dealing with

2851 to calculating the rate in each detector or reconstructing muon or gamma clusters.

2852 B.6.1 Determination of the run type

2853 In GIF++, both the performance of the detectors in detecting muons in an irradiated environment and
 2854 the gamma background can be independantly measured. These corresponds to different run types
 2855 and thus, to different TDC settings giving different data to look at.

2856
 2857 In the case of performance measurements, the trigger for data taking is provided by the coïncidence
 2858 of several scintillators when muons from the beam passing through the area are detected. Data
 2859 is collected in a 600 ns wide window around the arrival of muons in the RPCs. The expected time
 2860 distribution of hits is shown in Figure B.1a. The muon peak is clearly visible in the center of the
 2861 distribution and is to be extracted from the gamma background that composes the flat part of the
 2862 distribution.

2863 On the other hand, gamma background or noise measurements are focussed on the non muon
 2864 related physics and the trigger needs to be independant from the muons to give a good measurement
 2865 of the gamma/noise distribution as seen by the detectors. The trigger is then provided by a pulse
 2866 generator at a frequency of 300 Hz whose pulse is not likely to be on time with a muon. In order
 2867 to increase the integrated time without increasing the acquisition time too much, the width of the
 2868 acquisition windows are increased to 10 μ s. The time distribution of the hits is expected to be flat, as
 2869 shown by Figure B.1b.

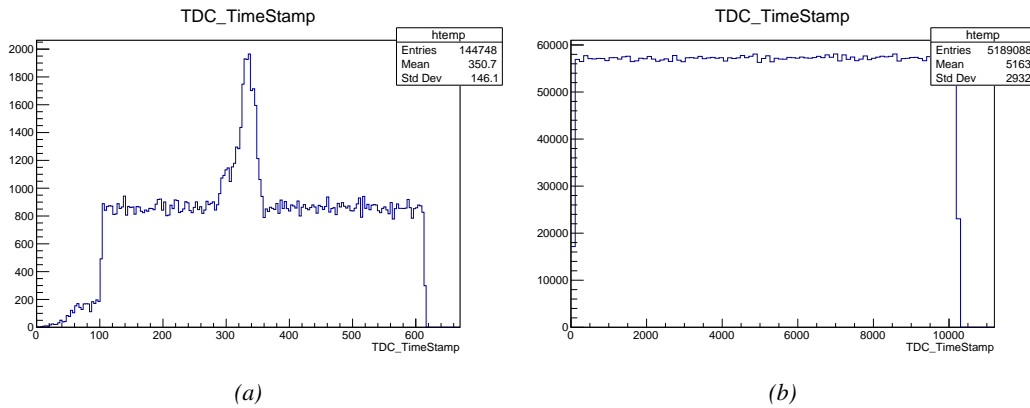


Figure B.1: Example of expected hit time distributions in the cases of efficiency (Figure B.1a) and noise/gamma rate per unit area (Figure B.1b) measurements as extracted from the raw ROOT files. The unit along the x-axis corresponds to ns. The fact that "the" muon peak is not well defined in Figure B.1a is due to the contribution of all the RPCs being tested at the same time that don't necessarily have the same signal arrival time. Each individual peak can have an offset with the ones of other detectors. The inconsistency in the first 100 ns of both time distributions is an artefact of the TDCs and are systematically rejected during the analysis.

2870 The ROOT files include a TTree called RunParameters containing, among other things, the in-
 2871 formation related to the type of run. The run type can then be accessed as described by Source
 2872 Code B.12 and the function IsEfficiencyRun() is then used to determine if the run file is an effi-
 2873 ciency run or, on the contrary, another type of run (noise or gamma measurement).

```

2874     TTree* RunParameters = (TTree*)dataFile.Get("RunParameters");
2875     TString* RunType = new TString();
2876     RunParameters->SetBranchAddress("RunType", &RunType);
2877     RunParameters->GetEntry(0);

```

2876 *Source Code B.12: Access to the run type contained in TTree* RunParameters.*

2877 Finally, the data files will have a slightly different content whether it was collected before or after
 2878 October 2017 and the upgrade of the DAQ software that brought a new information into the ROOT
 2879 output. This is discussed in Appendix A.4.3 and implies that the analysis will differ a little depending
 2880 on the data format. Indeed, as no information on the data quality is stored, in older data files, the cor-
 2881 rections for missing events has to be done at the end of the analysis. The information about the type
 2882 of data format is stored in the variable **bool** `isNewFormat` by checking the list of branches contained
 2883 in the data tree via the methods `TTree::GetListOfBranches()` and `TCollection::Contains()`.

2884 **B.6.2 Beam time window calculation for efficiency runs**

2885 Knowing the run type is important first of all to know the width of the acquisition window to be used
 2886 for the rate calculation and finally to be able to seek for muons. Indeed, the peak that appears in the
 2887 time distribution for each detectors is then fitted to extract the most probable time window in which
 2888 the tool should look for muon hits. The data outside of this time window is then used to evaluate the
 2889 noise or gamma background the detector was subjected to during the data taking. Computing the
 2890 position of the peak is done calling the function `SetBeamWindow()` defined in file `src/RPCHit.cc` that
 2891 loops a first time on the data. The data is first sorted in a 3D array of 1D histograms (`GIFH1Array`, see
 2892 `include/types.h`). Then the location of the highest bin is determined using `TH1::GetMaximumBin()`
 2893 and is used to define a window in which a gaussian fit will be applied to compute the peak width.
 2894 This window is a 80 ns defined by Formula B.1 around the central bin.

$$t_{center}(ns) = \text{bin} \times \text{width}_{\text{bin}}(ns) \quad (\text{B.1a})$$

$$[t_{low}; t_{high}] = [t_{center} - 40; t_{center} + 40] \quad (\text{B.1b})$$

2895 Before the fit is performed, the average number of noise/gamma hits per bin is evaluated using
 2896 the data outside of the fit window. Excluding the first 100 ns, the average number of hits per bin
 2897 due to the noise or gamma is defined by Formula B.2 after extracting the amount of hits in the time
 2898 windows $[100; t_{low}]$ and $[t_{high}; 600]$ thanks to the method `TH1::Integral()`. This average number
 2899 of hits is then subtracted to every bin of the 1D histogram, in order to *clean* it from the noise or
 2900 gamma contribution as much as possible to improve the fit quality. Bins where $\langle n_{\text{hits}} \rangle$ is greater
 2901 than the actual bin content are set to 0.

$$\Delta t_{noise}(ns) = 600 \overbrace{-t_{high} + t_{low}}^{-80ns} - 100 = 420ns \quad (\text{B.2a})$$

$$\langle n_{\text{hits}} \rangle = \text{width}_{\text{bin}}(ns) \times \frac{\sum_{t=100}^{t_{low}} + \sum_{t=t_{high}}^{600}}{\Delta t_{noise}(ns)} \quad (\text{B.2b})$$

2902 Finally, the fit parameters are extracted and saved for each detector in 3D arrays of **float**
 2903 (`muonPeak`, see `include/types.h`), a first one for the mean arrival time of the muons, `PeakTime`,

2904 and a second one for the width of the peak, `PeakWidth`. The width is defined as 6σ of the gaussian
 2905 fit. The same settings are applied to every partitions of the same detector. To determine which one
 2906 of the detector's partitions is directly illuminated by the beam, the peak height of each partition is
 2907 compared and the highest one is then used to define the peak settings.

2908 B.6.3 Data loop and histogram filling

2909 3D arrays of histogram are created to store the data and display it on the DQM of GIF++ webDCS
 2910 for the use of shifters. These histograms, presented in section B.2.1.1, are filled while looping on
 2911 the data. Before starting the analysis loop, it is necessary to control the entry quality for the new
 2912 file formats featuring `QFlag`. If the `QFlag` value for this entry shows that 1 TDC or more have a
 2913 `CORRUPTED` flag, then this event is discarded. The loss of statistics is low enough to be neglected.
 2914 `QFlag` is controled using the function `IsCorruptedEvent()` defined in `src/utils.cc`. As explained
 2915 in Appendix A.4.3, each digit of this integer represent a TDC flag that can be 1 or 2. Each 2 is
 2916 the sign of a `CORRUPTED` state. Then, the data is accessed entry by entry in the ROOT `TTree` using
 2917 `RAWData` and each hit in the hit list is assigned to a detector channel and saved in the corresponding
 2918 histograms. In the first part of the analysis, in which the loop over the ROOT file's content is
 2919 performed, the different steps are:

2920 **1- RPC channel assignment and control:** a check is done on the RPC channel extracted thanks
 2921 to the mapping via the method `Mapping::GetLink()`. If the channel is not initialised and is 0, or if
 2922 the TDC channel was greater than 5127, the hit is discarded. This means there was a problem in the
 2923 mapping. Often a mapping problem leads to the crash of the offline tool.

2924 **2- Creation of a `RPCHit` object:** to easily get the trolley, slot and partition in which the hit has
 2925 been assigned, this object is particularly helpful.

2926 **3- General histograms are filled:** the hit is filled into the time distribution and the general hit
 2927 distribution histograms, and if the arrival time is within the first 100 ns, it is discarded and nothing
 2928 else happens and the loop proceeds with the next hit in the list.

2929 **4- Multiplicity counter:** the hit multiplicity counter of the corresponding detectors incremented.

2930 **5-a- Efficiency runs - Is the hit within the peak window? :** if the peak is contained in the peak
 2931 window previously defined in section B.6.2, the hit is filled into the beam hit profile histogram of
 2932 the corresponding chamber, added into the list of muon hits and increments the counter of *in time*
 2933 hits. The term *in time* here refers to the hits that are likely to be muons by arriving in the expected
 2934 time window. If the hit is outside of the peak window, it is filled into the noise profile histogram
 2935 of the corresponding detector, added into the list of noise/gamma hits and increments the counter of
 2936 noise/gamma hits.

2937 **5-b- Noise/gamma rate runs - Noise histograms are filled:** the hit is filled into the noise profile
 2938 histogram of the corresponding detector, added into the list of noise/gamma hits and increments the
 2939 counter of noise/gamma hits.

2940

2941 After the loop on the hit list of the entry is over, the next step is to clusterize the 3D lists filled
 2942 in the previous steps. A 3D loop is then started over the active trolley, slot and RPC partitions to
 2943 access these objects. Each `NoiseHitList` and `MuonHitList`, in case of efficiency run, are clusterized
 2944 as described in section B.5.2. There corresponding cluster size and multiplicity histograms are filled
 2945 at the end of the clustering process. Then, the efficiency histogram is filled in case of efficiency run.
 2946 The selection is simply made by checking whether the RPC detected signals in the peak window
 2947 during this event. Nevertheless, it is useful to highlight that at this level, it is not possible yet to
 2948 discriminate in between a muon hit and noise or gamma hit. Thus, `MuonCSize_H`, `MuonCMult_H`
 2949 and `Efficiency0_H` are subjected to noise and gamma contamination. This contamination will be
 2950 estimated and corrected at the moment the results will be written into output CSV files. Finally, the
 2951 loop ends on the filling of the general hit multiplicity histogram.

2952 **B.6.4 Results calculation**

2953 As mentioned in section B.2.1, the analysis of DAQ data provides the user with 3 CSV files and
 2954 a ROOT file associated to each and every ROOT data file. The fourth CSV file is provided by the
 2955 extraction of the CEAN main frame data monitored during data taking and will be discussed later.
 2956 After looping on the data in the previous part of the analysis macro, the output files are created and a
 2957 3D loop on each RPC readout partitions is started to extract the histograms parameters and compute
 2958 the final results.

2959

2960 **B.6.4.1 Rate normalisation**

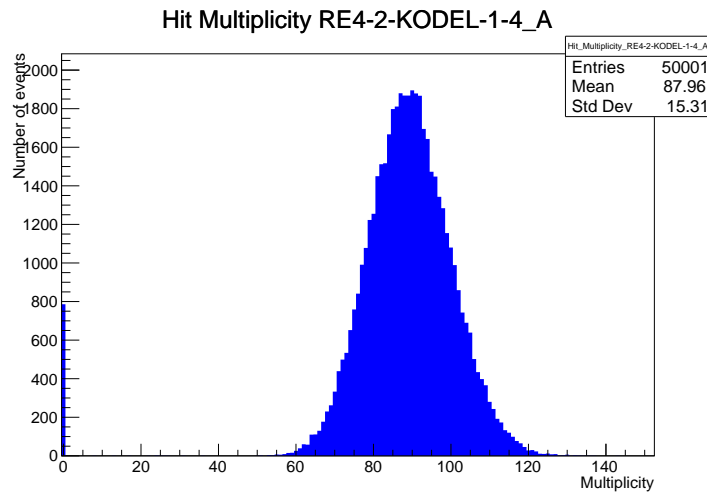


Figure B.2: The effect of the quality flag is explained by presenting the reconstructed hit multiplicity of a data file without `Quality_flag`. The artificial high content of bin 0 is the effect of corrupted data.

2961 To analyse old data format files, not containing any quality flag, it is needed to estimate the amount
 2962 of corrupted data via a fit as the corrupted data will always fill events with a fake "0 multiplicity".
 2963 Indeed, as no hits were stored in the DAQ ROOT files, these events artificially contribute to fill
 2964 the bin corresponding to a null multiplicity, as shown in Figure B.2. In the case the mean of the

hit multiplicity distribution is high, the contribution of the corrupted data can easily be evaluated for later correction by comparing the level of the bin at multiplicity 0 and of a skew fit curve that should indicate a value consistent with 0. A skew fit has been chosen over a Poisson fit as it was giving better results for lower mean multiplicity values. Nevertheless, for low irradiation cases, as explained in Appendix A.4.3, the hit multiplicity distribution mean is, on the contrary, rather small and the probability to record events without hits can't be considered small anymore, leading to a difficult and non-reliable estimation of the corruption. As can be seen in Source Code B.13, conditions have been applied to prevent bad fits and wrong corruption estimation in cases where :

- The difference in between the data for multiplicity 1 and the corresponding fit value should be lower than 1% of the total amount of data : $\frac{|n_{m=1} - sk(1)|}{N_{tot}} < 0.01$ where $n_{m=1}$ is the number of entries with multiplicity 1, $sk(1)$ the value of the skew fit, as defined by Formula 5.3, for multiplicity 1 and N_{tot} the total number of entries.

- The amount of data contained in the multiplicity 0 bin should not exceed 40% : $\frac{n_{m=0}}{N_{tot}} \leq 0.4$ where $n_{m=0}$ is the number of entries with multiplicity 0. This number has been determined to be the maximum to be able to separate the excess of data due to corruption from the hit multiplicity distribution.

Those 2 conditions need to be fulfilled to estimate the corruption of old data format files. If the fit was successful, the level of corruption is written in `Offline-Corrupted.csv` and the number of corrupted entries, refered as the integer `nEmptyEvent`, is subtracted from the total number of entries when the rate normalisation factor is computed as explicit in Source Code B.13. Note that for new data format files, the number of corrupted entries being set to 0, the definition of `rate_norm` stays valid.

```

2987
if(!isNewFormat){
    TF1* GaussFit = new TF1("gaussfit","[0]*exp(-0.5*((x-[1])/[2])**2)",0,Xmax);
    GaussFit->SetParameter(0,100);
    GaussFit->SetParameter(1,10);
    GaussFit->SetParameter(2,1);
    HitMultiplicity_H.rpc[T][S][p]->Fit(GaussFit,"LIQR","",0.5,Xmax);

    TF1* SkewFit = new TF1("skewfit","[0]*exp(-0.5*((x-[1])/[2])**2) / (1 +
→ exp(-[3]*(x-[4])))",0,Xmax);
    SkewFit->SetParameter(0,GaussFit->GetParameter(0));
    SkewFit->SetParameter(1,GaussFit->GetParameter(1));
    SkewFit->SetParameter(2,GaussFit->GetParameter(2));
    SkewFit->SetParameter(3,1);
    SkewFit->SetParameter(4,1);
    HitMultiplicity_H.rpc[T][S][p]->Fit(SkewFit,"LIQR","",0.5,Xmax);

    double fitValue = SkewFit->Eval(1,0,0,0);
    double dataValue = (double)HitMultiplicity_H.rpc[T][S][p]->GetBinContent(2);
    double difference = TMath::Abs(dataValue - fitValue);
    double fitTOdataVSentries_ratio = difference / (double)nEntries;
    bool isFitGOOD = fitTOdataVSentries_ratio < 0.01;

2988
    double nSinglehit = (double)HitMultiplicity_H.rpc[T][S][p]->GetBinContent(1);
    double lowMultRatio = nSinglehit / (double)nEntries;
    bool isMultLOW = lowMultRatio > 0.4;

    if(isFitGOOD && !isMultLOW){
        nEmptyEvent = HitMultiplicity_H.rpc[T][S][p]->GetBinContent(1);
        nPhysics = (int)SkewFit->Eval(0,0,0,0);
        if(nPhysics < nEmptyEvent)
            nEmptyEvent = nEmptyEvent-nPhysics;
    }
}

double corrupt_ratio = 100.*(double)nEmptyEvent / (double)nEntries;
outputCorrCSV << corrupt_ratio << '\t';

float rate_norm = 0.;
float stripArea = GIFIInfra->GetStripGeo(tr,sl,p);

if(IsEfficiencyRun(RunType)){
    float noiseWindow = BMTDCWINDOW - TIMEREJECT - 2*PeakWidth.rpc[T][S][p];
    rate_norm = (nEntries-nEmptyEvent)*noiseWindow*1e-9*stripArea;
} else
    rate_norm = (nEntries-nEmptyEvent)*RDMNOISEWDW*1e-9*stripArea;

```

Source Code B.13: Definition of the rate normalisation variable. It takes into account the number of non corrupted entries and the time window used for noise calculation, to estimate the total integrated time, and the strip active area to express the result as rate per unit area.

2990 B.6.4.2 Rate and activity

2991 At this point, the strip rate histograms, StripNoiseProfile_H.rpc[T][S][p], only contain an in-
2992 formation about the total number of noise or rate hits each channel received during the data taking.
2993 As described in Source Code B.14, a loop on the strip channels will be used to normalise the content
2994 of the rate distribution histogram for each detector partitions. The initial number of hits recorded for
2995 a given bin will be extracted and 2 values will be computed:

- 2996 ● the strip rate, defined as the number of hits recorded in the bin normalised like described in
 2997 the previous section, using the variable `rate_norm`, and

- 2998 ● the strip activity, defined as the number of hits recorded in the bin normalised to the average
 2999 number of hits per bin contained in the partition histogram, using the variable `averageNhit`.
 3000 This value provides an information on the homogeneity of the detector response to the gamma
 3001 background or of the detector noise. An activity of 1 corresponds to an average response.
 3002 Above 1, the channel is more active than the average and bellow 1, the channel is less active.

```

int nNoise = StripNoiseProfile_H.rpc[T][S][p]->GetEntries();
float averageNhit = (nNoise>0) ? (float)(nNoise/nStripsPart) : 1.;

for(Uint st = 1; st <= nStripsPart; st++) {
    float stripRate =
        StripNoiseProfile_H.rpc[T][S][p]->GetBinContent(st)/rate_norm;
    float stripAct =
        StripNoiseProfile_H.rpc[T][S][p]->GetBinContent(st)/averageNhit;

    StripNoiseProfile_H.rpc[T][S][p]->SetBinContent(st,stripRate);
    StripActivity_H.rpc[T][S][p]->SetBinContent(st,stripAct);
}

```

3004 *Source Code B.14: Description of the loop that allows to set the content of each strip rate and strip activity
 channel for each detector partition.*

3005 On each detector partitions, which are readout by a single FEE, all the channels are not processed
 3006 by the same chip. Each chip can give a different noise response and thus, histograms using a chip
 3007 binning are used to investigate chip related noise behaviours. The average values of the strip rate
 3008 or activity grouped into a given chip are extracted using the using the function `GetChipBin()` and
 3009 stored in dedicated histograms as described in Source Codes B.15 and B.16 respectively.

```

float GetChipBin(TH1* H, Uint chip){
    Uint start = 1 + chip*NSTRIPSCHIP;
    int nActive = NSTRIPSCHIP;
    float mean = 0.;

    for(Uint b = start; b <= (chip+1)*NSTRIPSCHIP; b++) {
        float value = H->GetBinContent(b);
        mean += value;
        if(value == 0.) nActive--;
    }

    if(nActive != 0) mean /= (float)nActive;
    else mean = 0.;

    return mean;
}

```

3012 *Source Code B.15: Function used to compute the content of a bin for an histogram using chip binning.*

```

3013   for(UInt ch = 0; ch < (nStripsPart/NSTRIPSCHIP); ch++) {
      ChipMeanNoiseProf_H.rpc[T][S][p]->
          SetBinContent(ch+1,GetChipBin(StripNoiseProfile_H.rpc[T][S][p],ch));
      ChipActivity_H.rpc[T][S][p]->
          SetBinContent(ch+1,GetChipBin(StripActivity_H.rpc[T][S][p],ch));
}

```

Source Code B.16: Description of the loop that allows to set the content of each chip rate and chip activity bins for each detector partition knowing the information contained in the corresponding strip distribution histograms.

The activity variable is used to evaluate the homogeneity of the detector response to background or of the detector noise. The homogeneity h_p of each detector partition can be evaluated using the formula $h_p = \exp(-\sigma_p^R / \langle R \rangle_p)$, where $\langle R \rangle_p$ is the partition mean rate and σ_p^R is the rate standard deviation calculated over the partition channels. The more homogeneously the rates are distributed and the smaller will σ_p^R be, and the closer to 1 will h_p get. On the contrary, if the standard deviation of the channel's rates is large, h_p will rapidly get to 0. This value is saved into histograms as shown in Source Code B.17 and could in the future be used to monitor through time, once extracted, the evolution of every partition homogeneity. This could be of great help to understand the apparition of eventual hot spots due to ageing of the chambers subjected to high radiation levels. The monitored homogeneity information could then be combined with a monitoring of the activity of each individual channel in order to have a finer information. Monitoring tools have been suggested and need to be developed for this purpose.

```

3027   float MeanPartSDev = GetTH1StdDev(StripNoiseProfile_H.rpc[T][S][p]);
   float strip_homog = (MeanPartRate==0)
     ? 0.
     : exp(-MeanPartSDev/MeanPartRate);
   StripHomogeneity_H.rpc[T][S][p]->Fill("exp -#left(#frac{\#sigma_{Strip
     \rightarrow Rate}}{\#mu_{Strip Rate}}\#right)",strip_homog);
   StripHomogeneity_H.rpc[T][S][p]->GetYaxis()->SetRangeUser(0.,1.);

3028   float ChipStDevMean = GetTH1StdDev(ChipMeanNoiseProf_H.rpc[T][S][p]);
   float chip_homog = (MeanPartRate==0)
     ? 0.
     : exp(-ChipStDevMean/MeanPartRate);
   ChipHomogeneity_H.rpc[T][S][p]->Fill("exp -#left(#frac{\#sigma_{Chip
     \rightarrow Rate}}{\#mu_{Chip Rate}}\#right)",chip_homog);
   ChipHomogeneity_H.rpc[T][S][p]->GetYaxis()->SetRangeUser(0.,1.);

```

Source Code B.17: Storage of the homogeneity into dedicated histograms.

3030 B.6.4.3 Strip masking tool

The offline tool is automatically called at the end of each data taking to analyse the data and offer the shifter DQM histograms to control the data quality. After the histograms have been published online in the DQM page, the shifter can decide to mask noisy or dead channels that will contribute to bias the final rate calculation by editing the mask column of `ChannelsMapping.csv` as can be seen in Figure B.3.

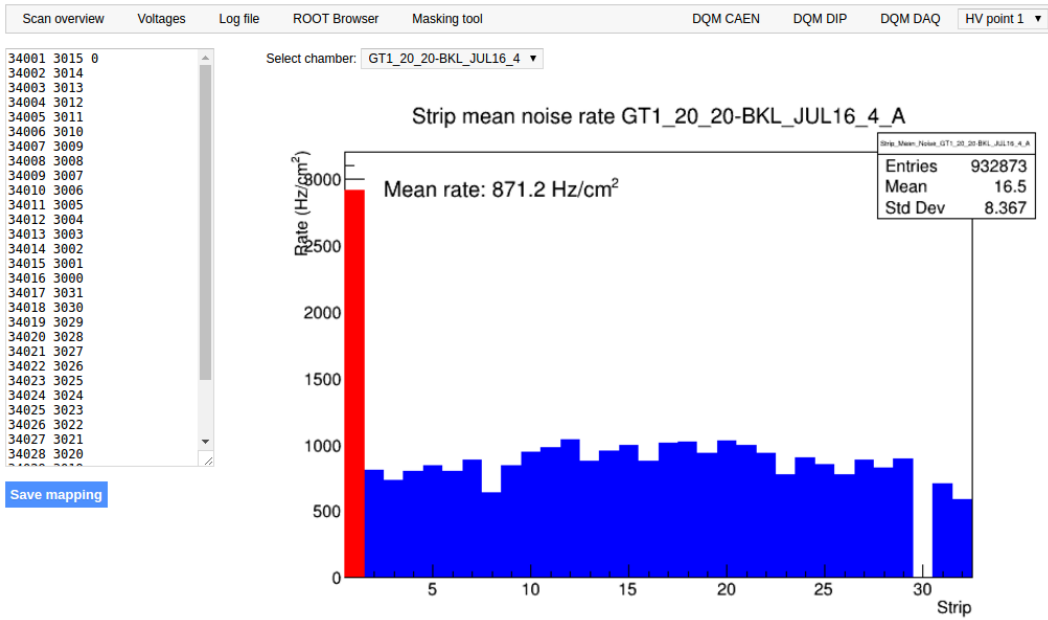


Figure B.3: Display of the masking tool page on the webDCS. The window on the left allows the shifter to edit ChannelsMapping.csv. To mask a channel, it only is needed to set the 3rd field corresponding to the strip to mask to 0. It is not necessary for older mapping file formats to add a 1 for each strip that is not masked as the code is versatile and the default behaviour is to consider missing mask fields as active strips. The effect of the mask is directly visible for noisy channels as the corresponding bin turns red. The global effect of masking strips will be an update of the rate value showed on the histogram that will take into consideration the rejected channels.

3036 From the code point of view, the function `GetTH1Mean()` is used to retrieve the mean rate par-
 3037 tition by partition after the rates have been calculated strip by strip and filled into the histograms
 3038 `StripNoiseProfile_H.rpc[T][S][p]`, as described through Source Code B.18.

3039 Once the mask for each rejected channel has been updated, the shifter can manually run the of-
 3040 fline tool again to update the DQM plots, now including the masked strips, as well the rate results
 3041 written in the output CSV file `Offline-Rate.csv`. If not done during the shifts, the strip masking
 3042 procedure needs to be carefully done by the person in charge of data analysis on the scans that were
 3043 selected to produce the final results.

```

3044
3045     float GetTH1Mean(TH1* H) {
3046         int nBins = H->GetNbinsX();
3047         int nActive = nBins;
3048         float mean = 0.;

3049         for(int b = 1; b <= nBins; b++) {
3050             float value = H->GetBinContent(b);
3051             mean += value;
3052             if(value == 0.) nActive--;
3053         }

3054         if(nActive != 0) mean /= (float)nActive;
3055         else mean = 0.;

3056         return mean;
3057     }

```

Source Code B.18: The function `GetTH1Mean()` is used to return the mean along the y-axis of `TH1` histograms containing rate information. In order to take into account masked strips whose rate is set to 0, the function looks for masked channels and decrement the number of active channels for each null value found.

3047 B.6.4.4 Output CSV files filling

3048 All the histograms have been filled. Parameters will then be extracted from them to compute the
 3049 final results that will later be used to produce plots. Once the results have been computed, the very
 3050 last step of the offline macro is to write these values into the corresponding CSV outputs. Aside of
 3051 the file `Offline-Corrupted.csv`, 2 CSV files are being written by the macro `offlineAnalysis()`,
 3052 `Offline-Rates.csv` and `Offline-L0-EffCl.csv` that respectively contain information about noise
 3053 or gamma rates, cluster size and multiplicity, and about level 0 reconstruction of the detector effi-
 3054 ciency, muon cluster size and multiplicity. Details on the computation and file writing are respec-
 3055 tively given in Sources Codes B.19 and B.20.

3056 **Noise/gamma background variables** are computed and written in the output file for each detector
 3057 partitions. A detector average of the hit and cluster rate is also provided, as shown through Sources
 3058 Code B.19. The variables that are written for each partition are:

- 3059 • The mean partition hit rate per unit area, `MeanPartRate`, that is extracted from the histogram
 3060 `StripNoiseProfile_H` as the mean value along the y-axis, as described in section B.6.4.3. No
 3061 error is recorded for the hit rate as this is considered a single measurement. No statistical error
 3062 can be associated to it and the systematics are unknown.
- 3063 • The mean cluster size, `cSizePart`, is extracted from the histogram `NoiseCSize_H` and it's
 3064 statistical error, `cSizePartErr`, is taken to be 2σ of the total distribution.
- 3065 • The mean cluster multiplicity per trigger, `cMultPart`, is extracted from the histogram `NoiseCMult_H`
 3066 and it's statistical error, `cMultPartErr`, is taken to be 2σ of the total distribution. It is impor-
 3067 tant to point to the fact that this variable gives an information that is dependent on the buffer
 3068 window width used for each trigger for the calculation.
- 3069 • The mean cluster rate per unit area, `ClustPartRate`, is defined as the mean hit rate normalised

3070 to the mean cluster size and it's statistical error, `ClustPartRateErr`, is then obtained using the
 3071 relative statistical error on the mean cluster size.

```

for (UInt tr = 0; tr < GIFInfra->GetNTrolleys(); tr++) {
  UInt T = GIFInfra->GetTrolleyID(tr);

  for (UInt sl = 0; sl < GIFInfra->GetNSlots(tr); sl++) {
    UInt S = GIFInfra->GetSlotID(tr,sl) - 1;

    float MeanNoiseRate = 0.;
    float ClusterRate = 0.;
    float ClusterSDev = 0.;

    for (UInt p = 0; p < GIFInfra->GetNPartitions(tr,sl); p++) {
      float MeanPartRate = GetTH1Mean(StripNoiseProfile_H.rpc[T][S][p]);
      float cSizePart = NoiseCSIZE_H.rpc[T][S][p]->GetMean();
      float cSizePartErr = (NoiseCSIZE_H.rpc[T][S][p]->GetEntries()==0)
        ? 0.
        : 2*NoiseCSIZE_H.rpc[T][S][p]->GetStdDev() /
          sqrt(NoiseCSIZE_H.rpc[T][S][p]->GetEntries());
      float cMultPart = NoiseCMult_H.rpc[T][S][p]->GetMean();
      float cMultPartErr = (NoiseCMult_H.rpc[T][S][p]->GetEntries()==0)
        ? 0.
        : 2*NoiseCMult_H.rpc[T][S][p]->GetStdDev() /
          sqrt(NoiseCMult_H.rpc[T][S][p]->GetEntries());
      float ClustPartRate = (cSizePart==0) ? 0.
        : MeanPartRate/cSizePart;
      float ClustPartRateErr = (cSizePart==0) ? 0.
        : ClustPartRate * cSizePartErr/cSizePart;

      outputRateCSV << MeanPartRate << '\t'
        << cSizePart << '\t' << cSizePartErr << '\t'
        << cMultPart << '\t' << cMultPartErr << '\t'
        << ClustPartRate << '\t' << ClustPartRateErr << '\t';

      RPCarea += stripArea * nStripsPart;
      MeanNoiseRate += MeanPartRate * stripArea * nStripsPart;
      ClusterRate += ClustPartRate * stripArea * nStripsPart;
      ClusterSDev += (cSizePart==0)
        ? 0.
        : ClusterRate*cSizePartErr/cSizePart;
    }

    MeanNoiseRate /= RPCarea;
    ClusterRate /= RPCarea;
    ClusterSDev /= RPCarea;

    outputRateCSV << MeanNoiseRate << '\t'
      << ClusterRate << '\t' << ClusterSDev << '\t';
  }
}

```

3073 *Source Code B.19: Description of rate result calculation and writing into the CSV output Offline-Rate.csv. Are saved into the file for each detector, the mean partition rate, cluster size and cluster mutiplicity, along with their errors, for each partition and as well as a detector average.*

3074 **Muon performance variables** are computed and written in the output file for each detector parti-
 3075 tions as shown through Sources Code B.20. The variables that are written for each partition are:

- 3076 ● The muon efficiency, `eff`, extracted from the histogram `Efficiency0_H`. It is reminded that
3077 this offline tool doesn't include any tracking algorithm to identify muons from the beam and
3078 only relies on the hits arriving in the time window corresponding to the beam time. The con-
3079 tent of the efficiency histogram is thus biased by the noise/gamma background contribution
3080 into this window and is thus corrected by estimating the muon data content in the peak re-
3081 gion knowing the noise/gamma content in the rate calculation region. Both time windows
3082 being different, the choice was made to normalise the noise/gamma background calculation
3083 window to it's equivalent beam window in order to have comparable values using the variable
3084 `windowRatio`. Finally, to estimate the data ratio in the peak region, the variable `DataRatio`
3085 is defined as the ratio in between the estimated mean cluster multiplicity of the muons in the
3086 peak region, `MuonCM`, and of the total mean cluster multiplicity in the peak region, `PeakCM`.
3087 `MuonCM` is itself defined as the difference in between the total mean cluster multiplicity in the
3088 peak region and the normalised mean noise/gamma cluster multiplicity calculated outside of
3089 the peak region. The statistical error related to the efficiency, `eff_err`, is computed using a
3090 binomial distribution, as the efficiency measure the probability of "success" and "failure" to
3091 detect muons.
- 3092 ● The mean muon cluster size, `MuonCS`, is calculated using the total mean cluster size and multi-
3093 plicity in the peak region, respectively extracted from histograms `MuonCSize_H` and `MuonCMult_H`,
3094 the noise/gamma background mean cluster size and normalised multiplicity, extracted from
3095 `NoiseCSize_H` and `NoiseCMult_H`, and of the estimated muon cluster multiplicity `MuonCM` pre-
3096 viously explicated. The associated statistical error, `MuonCM_err`, is calculated using the propa-
3097 gation of errors of the mentioned variables.
- 3098 ● The mean muon cluster multiplicity in the peak region, `MuonCM`, explicated above whose sta-
3099 tistical error, `MuonCM_err`, is the sum of statistical error associated to the total mean clus-
3100 ter multiplicity in the peak reagion, `PeakCM_err`, and of the mean noise/gamma cluster size,
3101 `NoiseCM_err`.

3102 In addition to these 2 CSV files, the histograms are saved in ROOT file `Scan00XXXX_HVY_Offline.root`
3103 as explained in section B.2.1.1.

3104

```

for (UInt tr = 0; tr < GIFInfra->GetNTrolleys(); tr++) {
    UInt T = GIFInfra->GetTrolleyID(tr);
    for (UInt sl = 0; sl < GIFInfra->GetNSlots(tr); sl++) {
        UInt S = GIFInfra->GetSlotID(tr,sl) - 1;
        for (UInt p = 0; p < GIFInfra->GetNPartitions(tr,sl); p++) {
            float noiseWindow =
                BMTDCWINDOW - TIMEREJECT - 2*PeakWidth.rpc[T][S][p];
            float peakWindow = 2*PeakWidth.rpc[T][S][p];
            float windowRatio = peakWindow/noiseWindow;

            float PeakCM = MuonCMult_H.rpc[T][S][p]->GetMean();
            float PeakCS = MuonCSize_H.rpc[T][S][p]->GetMean();
            float NoiseCM = NoiseCMult_H.rpc[T][S][p]->GetMean() *windowRatio;
            float NoiseCS = NoiseCSize_H.rpc[T][S][p]->GetMean();
            float MuonCM = (PeakCM<NoiseCM) ? 0. : PeakCM-NoiseCM;
            float MuonCS = (MuonCM==0 || PeakCM*PeakCS<NoiseCM*NoiseCS)
                ? 0.
                : (PeakCM*PeakCS-NoiseCM*NoiseCS) / MuonCM;
            float PeakCM_err = (MuonCMult_H.rpc[T][S][p]->GetEntries()==0.)
                ? 0.
                : 2*MuonCMult_H.rpc[T][S][p]->GetStdDev() /
                    sqrt(MuonCMult_H.rpc[T][S][p]->GetEntries());
            float PeakCS_err = (MuonCSize_H.rpc[T][S][p]->GetEntries()==0.)
                ? 0.
                : 2*MuonCSize_H.rpc[T][S][p]->GetStdDev() /
                    sqrt(MuonCSize_H.rpc[T][S][p]->GetEntries());
            float NoiseCM_err = (NoiseCMult_H.rpc[T][S][p]->GetEntries()==0.)
                ? 0.
                : windowRatio*2*NoiseCMult_H.rpc[T][S][p]->GetStdDev() /
                    sqrt(NoiseCMult_H.rpc[T][S][p]->GetEntries());
            float NoiseCS_err = (NoiseCSize_H.rpc[T][S][p]->GetEntries()==0.)
                ? 0.
                : 2*NoiseCSize_H.rpc[T][S][p]->GetStdDev() /
                    sqrt(NoiseCSize_H.rpc[T][S][p]->GetEntries());
            float MuonCM_err = (MuonCM==0) ? 0. : PeakCM_err+NoiseCM_err;
            float MuonCS_err = (MuonCS==0 || MuonCM==0) ? 0.
                : (PeakCS*PeakCM_err + PeakCM*PeakCS_err +
                    NoiseCS*NoiseCM_err + NoiseCM*NoiseCS_err +
                    MuonCS*MuonCM_err) / MuonCM;

            float DataRatio = MuonCM/PeakCM;
            float DataRatio_err = (MuonCM==0) ? 0.
                : DataRatio*(MuonCM_err/MuonCM + PeakCM_err/PeakCM);
            float eff = DataRatio*Efficiency0_H.rpc[T][S][p]->GetMean();
            float eff_err = DataRatio*2*Efficiency0_H.rpc[T][S][p]->GetStdDev() /
                sqrt(Efficiency0_H.rpc[T][S][p]->GetEntries()) +
                Efficiency0_H.rpc[T][S][p]->GetMean()*DataRatio_err;

            outputEffCSV << eff << '\t' << eff_err << '\t'
                << MuonCS << '\t' << MuonCS_err << '\t'
                << MuonCM << '\t' << MuonCM_err << '\t';
        }
    }
}

```

3105

Source Code B.20: Description of efficiency result calculation and writing into the CSV output Offline-L0-EffCl.csv. Are saved into the file for each detector, the efficiency, corrected taking into account the background in the peak window of the time profile, muon cluster size and muon cluster multiplicity, along with their errors, for each partition and as well as a detector average.

3106

3107 B.7 Current data Analysis

3108 Detectors under test at GIF++ are connected both to a CAEN HV power supply and to a CAEN
3109 ADC that reads the currents inside of the RPC gaps bypassing the supply cable. During data tak-
3110 ing, the webDCS records into a ROOT file called `Scan00XXXX_HVY_CAEN.root` histograms with the
3111 monitored parameters of both CAEN devices. Are recorded for each RPC channels (in most cases,
3112 a channel corresponds to an RPC gap):

- 3113 • the effective voltage, HV_{eff} , set by the webDCS using the PT correction on the CAEN power
3114 supply,
- 3115 • the applied voltage, HV_{app} , monitored by the CAEN power supply, and the statistical error
3116 related to the variations of this value through time to follow the variation of the environmental
3117 parameters defined as the RMS of the histogram divided by the square root of the number of
3118 recorded points,
- 3119 • the monitored current, I_{mon} , monitored by the CAEN power supply, and the statistical error
3120 related to the variations of this value through time to follow the variation of the environmental
3121 parameters defined as the RMS of the histogram divided by the square root of the number of
3122 recorded points,
- 3123 • the corresponding current density, J_{mon} , defined as the monitored current per unit area,
3124 $J_{mon} = I_{mon}/A$, where A is the active area of the corresponding gap,
- 3125 • the ADC current, I_{ADC} , recorded through the CAEN ADC module that monitors the dark
3126 current in the gap itself. First of all, the resolution of such a module is better than that of
3127 CAEN power supplies and moreover, the current is not read-out through the HV supply line
3128 but directly at the chamber level giving the real current inside of the detector. The statistical
3129 error is defined as the RMS of the histogram distribution divided by the square root of the
3130 number of recorded points.

3131 Once extracted through a loop over the element of GIF++ infrastructure via the C++ macro
3132 `GetCurrent()`, these parameters, organised in 9 columns per detector HV supply line, are written in
3133 the output CSV file `Offline-Current.csv`. The macro can be found in the file `Current.cc`.

References

- 3135 [1] T. Massam et al. “Experimental observation of antideuteron production”. In: *Il Nuovo Cimento A* 63 (1965), pp. 10–14.
- 3136
- 3137 [2] UA1 Collaboration. “Experimental observation of isolated large transverse energy electrons with associated missing energy at $s = 540 \text{ GeV}$ ”. In: *Physics Letters B* 122 (1983), pp. 103–116.
- 3138
- 3139
- 3140 [3] UA2 Collaboration. “Observation of single isolated electrons of high transverse momentum in events with missing transverse energy at the CERN pp collider”. In: *Physics Letters B* 122 (1983), pp. 476–485.
- 3141
- 3142
- 3143 [4] UA1 Collaboration. “Experimental observation of lepton pairs of invariant mass around $95 \text{ GeV}/c^2$ at the CERN SPS collider”. In: *Physics Letters B* 126 (1983), pp. 398–410.
- 3144
- 3145 [5] UA2 Collaboration. “Evidence for $Z_0 \rightarrow e^+e^-$ at the CERN pp collider”. In: *Physics Letters B* 129 (1983), pp. 130–140.
- 3146
- 3147 [6] ALEPH Collaboration. “Determination of the number of light neutrino species”. In: *Physics Letters B* 231 (1989), pp. 519–529.
- 3148
- 3149 [7] CERN, ed. (1985).
- 3150 [8] CERN, ed. (1986).
- 3151 [9] CERN, ed. (1994).
- 3152 [10] CERN, ed. (1998).
- 3153 [11] CERN, ed. (1999).
- 3154 [12] CERN. Geneva. LHC Experiments Committee. *Letter of Intent for A Large Ion Collider Experiment [ALICE]*, note = CERN-LHCC-93-016. Tech. rep. ALICE Collaboration, 1993.
- 3155
- 3156 [13] CERN. Geneva. LHC Experiments Committee. *ATLAS : technical proposal for a general-purpose pp experiment at the Large Hadron Collider at CERN*, note = CERN-LHCC-94-43. Tech. rep. ATLAS Collaboration, 1994.
- 3157
- 3158
- 3159 [14] CERN. Geneva. LHC Experiments Committee. *CMS : letter of intent by the CMS Collaboration for a general purpose detector at LHC*, note = CERN-LHCC-92-003. Tech. rep. CMS Collaboration, 1992.
- 3160
- 3161
- 3162 [15] CERN. Geneva. LHC Experiments Committee. *LHCb : letter of intent*. Tech. rep. CERN-LHCC-95-5. LHCb Collaboration, 1995.
- 3163
- 3164 [16] L. Evans and P. Bryant. “LHC Machine”. In: *JINST* 3 (2008). S08001.
- 3165 [17] CMS Collaboration ATLAS Collaboration. “Combined Measurement of the Higgs Boson Mass in pp Collisions at $\sqrt{s} = 7$ and 8 TeV with the ATLAS and CMS Experiments”. In: *Physical Review Letters* 114 (2015). 191803.
- 3166
- 3167
- 3168 [18] LHCb Collaboration. “Observation of $J/\psi p$ Resonances Consistent with Pentaquark States in $\Lambda_b^0 \rightarrow J/\psi K^- p$ Decays”. In: *Physical Review Letters* 115 (2015). 072001.
- 3169

- 3170 [19] LHCb Collaboration. “Observation of $J/\psi\phi$ Structures Consistent with Exotic States from
3171 Amplitude Analysis of $B^+ \rightarrow J/\psi\phi K^+$ Decays”. In: *Physical Review Letters* 118 (2017).
3172 022003.
- 3173 [20] CERN. Geneva. *High-Luminosity Large Hadron Collider (HL-LHC) Technical Design Re-*
3174 *port V. 0.1*. Tech. rep. CERN-2017-007-M. 2017.
- 3175 [21] CERN. Geneva. LHC Experiments Committee. *The CMS muon project : Technical Design*
3176 *Report*. Tech. rep. CERN-LHCC-97-032. CMS Collaboration, 1997.
- 3177 [22] CERN. Geneva. LHC Experiments Committee. *CMS, the Compact Muon Solenoid : technical*
3178 *proposal*. Tech. rep. CERN-2015-005. 2015.
- 3179 [23] CERN. Geneva. LHC Experiments Committee. *The Phase-2 Upgrade of the CMS Muon*
3180 *Detectors*. Tech. rep. CERN-LHCC-2017-012, CMS-TDR-016. CMS Collaboration, 2017.
- 3181 [24] CERN. Geneva. LHC Experiments Committee. *High-Luminosity Large Hadron Collider*
3182 *(HL-LHC) Preliminary Design Report*. Tech. rep. CERN-LHCC-94-38. CMS Collaboration,
3183 1994.
- 3184 [25] CERN. Geneva. LHC Experiments Committee. *The Phase-2 Upgrade of the CMS Level-1*
3185 *Trigger - Interim Report to the LHCC*. Tech. rep. CERN-LHCC-2017-013, CMS-TDR-017.
3186 CMS Collaboration, 2017.
- 3187 [26] CERN. Geneva. LHC Experiments Committee. *Technical Proposal for the Phase-II Upgrade*
3188 *of the CMS Detector*. Tech. rep. CERN-LHCC-2015-010, CMS-TDR-15-02. CMS Collabora-
3189 ration, 2015.
- 3190 [27] F.Sauli. “GEM: A new concept for electron amplification in gas detectors”. In: *Nucl. Instr.*
3191 *Meth. Phys. Res.* 386 (1997), pp. 531–534.
- 3192 [28] CERN. Geneva. LHC Experiments Committee. *CMS Technical Design Report for the Muon*
3193 *Endcap GEM Upgrade*. Tech. rep. CERN-LHCC-2015-012, CMS-TDR-013. CMS Collabo-
3194 ration, 2015.
- 3195 [29] R. Santonico and R. Cardarelli. “Development of resistive plate counters”. In: *Nucl. Instr.*
3196 *Meth. Phys. Res.* 187 (1981), pp. 377–380.
- 3197 [30] Yu.N. Pestov and G.V. Fedotovich. *A picosecond time-of-flight spectrometer fot eh VEPP-2M*
3198 *based on local-discharge spark counter*. Tech. rep. SLAC-TRANS-0184. SLAC, 1978.
- 3199 [31] W.W. Ash, ed. *Spark Counter With A Localized Discharge*. Vol. SLAC-R-250. 1982, pp. 127–
3200 131.
- 3201 [32] I. Crotty et al. “The non-spark mode and high rate operation of resistive parallel plate cham-
3202 bers”. In: *NIMA* 337 (1993), pp. 370–381.
- 3203 [33] I. Crotty et al. “Further studies of avalanche mode operation of resistive parallel plate cham-
3204 bers”. In: *NIMA* 346 (1994), pp. 107–113.
- 3205 [34] R. Cardarelli et al. “Avalanche and streamer mode operation of resistive plate chambers”. In:
3206 *NIMA* 382 (1996), pp. 470–474.
- 3207 [35] E. Cerron Zeballos et al. “A new type of resistive plate chamber: The multigap RPC”. In:
3208 *NIMA* 374 (1996), pp. 132–135.
- 3209 [36] M.C.S. Williams. “The development of the multigap resistive plate chamber”. In: *Nucl. Phys.*
3210 *B* 61 (1998), pp. 250–257.
- 3211 [37] H. Czyrkowski et al. “New developments on resistive plate chambers for high rate operation”.
3212 In: *NIMA* 419 (1998), pp. 490–496.

BIBLIOGRAPHY

- [38] P. Camarri et al. “Streamer suppression with SF₆ in RPCs operated in avalanche mode”. In: *NIMA* 414 (1998), pp. 317–324.
- [39] E. Cerron Zeballos et al. “Effect of adding SF₆ to the gas mixture in a multigap resistive plate chamber”. In: *NIMA* 419 (1998), pp. 475–478.
- [40] CERN. Geneva. LHC Experiments Committee. *ATLAS muon spectrometer: Technical design report*. Tech. rep. CERN-LHCC-97-22. ATLAS Collaboration, 1997.
- [41] CERN. Geneva. LHC Experiments Committee. *ALICE Time-Of-Flight system (TOF) : Technical Design Report*. Tech. rep. CERN-LHCC-2000-012. ALICE Collaboration, 2000.
- [42] The CALICE collaboration. “First results of the CALICE SDHCAL technological prototype”. In: *JINST* 11 (2016).
- [43] PoS, ed. *Density Imaging of Volcanoes with Atmospheric Muons using GRPCs*. International Europhysics Conference on High Energy Physics - HEP 2011. 2011.
- [44] C. Lippmann. “Detector Physics of Resistive Plate Chambers”. PhD thesis. Johann Wolfgang Goethe-Universität, 2003.
- [45] M. Abbrescia et al. “Properties of C₂H₂F₄-based gas mixture for avalanche mode operation of resistive plate chambers”. In: *NIMA* 398 (1997), pp. 173–179.
- [46] G. Battistoni et al. “Sensitivity of streamer mode to single ionization electrons”. In: *NIMA* 235 (1985), pp. 91–97.
- [47] W. Riegler. “Induced signals in resistive plate chambers”. In: *NIMA* 491 (2002), pp. 258–271.
- [48] E. Cerron Zeballos et al. “A comparison of the wide gap and narrow gap resistive plate chamber”. In: *NIMA* 373 (1996), pp. 35–42.
- [49] M. Abbrescia et al. “Cosmic ray tests of double-gap resistive plate chambers for the CMS experiment”. In: *NIMA* 550 (2005), pp. 116–126.
- [50] ALICE Collaboration. “A study of the multigap RPC at the gamma irradiation facility at CERN”. In: *NIMA* 490 (2002), pp. 58–70.
- [51] B. Bonner et al. “A multigap resistive plate chamber prototype for time-of-flight for the STAR experiment at RHIC”. In: *NIMA* 478 (2002), pp. 176–179.
- [52] S. Yang et al. “Test of high time resolution MRPC with different readout modes for the BESIII upgrade”. In: *NIMA* 763 (2014), pp. 190–196.
- [53] A. Akindinov et al. “RPC with low-resistive phosphate glass electrodes as a candidate for the CBM TOF”. In: *NIMA* 572 (2007), pp. 676–681.
- [54] JINST, ed. *Development of the MRPC for the TOF system of the MultiPurpose Detector*. RPC2016: XII Workshop on Resistive Plate Chambers and Related Detectors. 2016.
- [55] M.C.S. Williams. “Particle identification using time of flight”. In: *Journal of Physics G* 39 (2012).
- [56] A. Alici et al. “Aging and rate effects of the Multigap RPC studied at the Gamma Irradiation Facility at CERN”. In: *NIMA* 579 (2007), pp. 979–988.
- [57] M. Abbrescia et al. “The simulation of resistive plate chambers in avalanche mode: charge spectra and efficiency”. In: *NIMA* 431 (1999), pp. 413–427.
- [58] M. Abbrescia et al. “Study of long-term performance of CMS RPC under irradiation at the CERN GIF”. In: *NIMA* 533 (2004), pp. 102–106.
- [59] H.C. Kim et al. “Quantitative aging study with intense irradiation tests for the CMS forward RPCs”. In: *NIMA* 602 (2009), pp. 771–774.

- 3256 [60] S. Agosteo et al. “A facility for the test of large-area muon chambers at high rates”. In: *NIMA*
3257 452 (2000), pp. 94–104.
- 3258 [61] PoS, ed. *CERN GIF ++ : A new irradiation facility to test large-area particle detectors for*
3259 *the high-luminosity LHC program*. Vol. TIPP2014. 2014, pp. 102–109.
- 3260 [62] A. Fagot. *GIF++ DAQ v4.0*. 2017. URL: https://github.com/afagot/GIF_DAQ.
- 3261 [63] CAEN. *Mod. V1190-VX1190 A/B, 128/64 Ch Multihit TDC*. 14th ed. 2016.
- 3262 [64] CAEN. *Mod. V1718 VME USB Bridge*. 9th ed. 2009.
- 3263 [65] W-Ie-Ne-R. *VME 6021-23 VXI*. 5th ed. 2016.
- 3264 [66] Wikipedia. *INI file*. 2017. URL: https://en.wikipedia.org/wiki/INI_file.
- 3265 [67] S. Carrillo A. Fagot. *GIF++ Offline Analysis v6*. 2017. URL: <https://github.com/>
3266 [afagot/GIF_OfflineAnalysis](https://github.com/afagot/GIF_OfflineAnalysis).